

AD-A118 398

TECHNICAL  
LIBRARY

AD A-118 398

CONTRACT REPORT ARBRL-CR-00485

BRL PARTICLE SIZING INTERFEROMETER

Prepared by

The University of Tennessee Space Institute  
Tullahoma, TE 37388

July 1982



**US ARMY ARMAMENT RESEARCH AND DEVELOPMENT COMMAND**  
**BALLISTIC RESEARCH LABORATORY**  
ABERDEEN PROVING GROUND, MARYLAND

Approved for public release; distribution unlimited.

Destroy this report when it is no longer needed.  
Do not return it to the originator.

Secondary distribution of this report is prohibited.

Additional copies of this report may be obtained  
from the National Technical Information Service,  
U. S. Department of Commerce, Springfield, Virginia  
22161.

The findings in this report are not to be construed as  
an official Department of the Army position, unless  
so designated by other authorized documents.

*The use of trade names or manufacturers' names in this report  
does not constitute indorsement of any commercial product.*

REPORT DOCUMENTATION PAGE		READ INSTRUCTIONS BEFORE COMPLETING FORM
1. REPORT NUMBER Contract Report ARBRL-CR-00485	2. GOVT ACCESSION NO.	3. RECIPIENT'S CATALOG NUMBER
4. TITLE (and Subtitle) BRL PARTICLE SIZING INTERFEROMETER		5. TYPE OF REPORT & PERIOD COVERED Contract
		6. PERFORMING ORG. REPORT NUMBER
7. AUTHOR(s) J.W. FARMER		8. CONTRACT OR GRANT NUMBER(s) DAADO5-79-C-1004
9. PERFORMING ORGANIZATION NAME AND ADDRESS The University of Tennessee Space Institute Tullahoma, TE 37388		10. PROGRAM ELEMENT, PROJECT, TASK AREA & WORK UNIT NUMBERS
11. CONTROLLING OFFICE NAME AND ADDRESS US Army Armament Research and Development Command US Army Ballistic Research Laboratory (DRDAR-BL) Aberdeen Proving Ground, MD 21005		12. REPORT DATE July 1982
		13. NUMBER OF PAGES 232
14. MONITORING AGENCY NAME & ADDRESS (if different from Controlling Office)		15. SECURITY CLASS. (of this report) UNCLASSIFIED
		15a. DECLASSIFICATION/DOWNGRADING SCHEDULE
16. DISTRIBUTION STATEMENT (of this Report) Approved for public release; distribution unlimited		
17. DISTRIBUTION STATEMENT (of the abstract entered in Block 20, if different from Report)		
18. SUPPLEMENTARY NOTES		
19. KEY WORDS (Continue on reverse side if necessary and identify by block number) Interferometer Particles Droplets Jet Spray Laser Velocimeter		
20. ABSTRACT (Continue on reverse side if necessary and identify by block number) raj <p>A particle sizing interferometer designed to measure particle sizes from 0.3 to 500 micrometres has been constructed for the Ballistics Research Laboratory. The device was constructed to measure droplet size distributions produced by high pressure pneumatic nozzles. This report describes the expected operational response of this instrument in high density liquid sprays. Additionally, discussion is provided of theoretical concepts which are required for data interpretation when the interferometer sample volume depends on droplet sizes.</p>		

## TABLE OF CONTENTS

	PAGE
I. INTRODUCTION. . . . .	7
II. FUEL SPRAY CHARACTERISTICS EXPECTED TO AFFECT PSI PERFORMANCE. . . . .	13
III. PSI DESIGN LIMITATIONS IMPOSED BY FUEL SPRAY REQUIREMENTS. . . . .	23
IV. CALIBRATION. . . . .	32
V. DATA SOFTWARE. . . . .	42
REFERENCES. . . . .	58
APPENDIX I. . . . .	59
APPENDIX II. . . . .	99
APPENDIX III. . . . .	143
APPENDIX IV. . . . .	185
NOMENCLATURE. . . . .	225
DISTRIBUTION LIST. . . . .	229

# LIST OF ILLUSTRATIONS

FIGURE	PAGE
1. PRINCIPLE OF THE PARTICLE SIZING INTERFEROMETER.....	8
2. VISIBILITY AS A FUNCTION OF PARTICLE SIZE FOR A CYLINDER AND SPHERE.....	11
3. UNCERTAINTY IN SPHERICAL PARTICLE DIAMETERS FOR VARIOUS VALUES OF UNCERTAINTY IN THE VISIBILITY.....	12
4. ASSUMED SPRAY NOZZLE GEOMETRY.....	14
5. PROBABILITY DENSITY DISTRIBUTION FOR THE ASSUMED BIMODAL LOG-NORMAL DISTRIBUTIONS.....	20
6. EXAMPLE OF ON AXIS PSI VIEWING GEOMETRY.....	21
7. EXAMPLE OF POSSIBLE PSI OFF AXIS VIEWING DIRECTIONS.....	22
8. EXPLODED VIEW OF BEAM INTERSECTION POINT SHOWING HOW RECEIVER LENS ORIENTATION LIMITS PSI SAMPLE VOLUME.....	25
9. EXAMPLE OF ACCEPTANCE RATIO AS A FUNCTION OF NUMBER DENSITY FOR ON AXIS AND OFF AXIS.....	26
10. EXAMPLES OF MICROPHOTOGRAPHS OF THE DROPLET STREAM FROM THE VIBRATING ORIFICE MONODISPERSE GENERATOR.....	34
11. MONODISPERSE GENERATOR WITH SYNCHRONIZED PARTICLE SEPARATION AND STROBOSCOPIC MICROSCOPE OBSERVATION.....	35
12. METHOD FOR GLASS BEAD DISPERSAL THROUGH PSI SAMPLE VOLUME.....	43

## 1.0 INTRODUCTION

The Gas Diagnostics Division of The University of Tennessee Space Institute has constructed and delivered to the U. S. Army Ballistics Research Laboratory (BRL) a Particle Sizing Interferometer (PSI) designed to measure droplet sizes over ranges from 0.3 to greater than 1000 micrometres. The PSI is perhaps the only nonintrusive diagnostic instrument which can obtain time histories of particle or droplet size distributions in hostile environments. While the PSI is simple in concept, its successful utilization and application requires a good understanding of many subtle points pertinent to the particles being measured and their effects on instrument operation. Therefore, the purpose of this report is to 1) describe the expected operation of the system in realistic injector sprays (a subject for study at BRL), 2) develop in greater detail theoretical references alluded to in previous reports, and 3) provide suggestions for extending the application to other potential applications such as burning powders.

### 1.1 Theoretical Synopsis

Consider the optical system shown in figure 1. A beam from a laser is split into two equal intensity beams. A lens system makes the beams cross and focus at a common origin called the geometric center. Define the included angle between the beams as  $\alpha$ . Near the geometric center the wavefronts are planar. A Huygen's diagram of the wavefronts shows that planar interference fringes are formed which are perpendicular to the plane defined by the beam centerlines and are parallel to the bisector between the beams. The distance  $\delta$  between the periodic fringes is given by

$$\delta = \lambda/2\sin(\alpha/2) \quad (1)$$

where  $\lambda$  is the wavelength of the coherent light. At this point it is convenient to divide the particles which may interact with the interference fringes into two classes. Class I particles are "small" (diameters comparable to an optical wavelength) scattering particles with scattering characteristics which can be described by Fraunhofer diffraction or Lorenz-Mie scattering theory. The light scattered by these particles is assumed to be observed with a scattered light collection lens centered on the bisector between the beam in the forward direction. Class II particles are "large" (diameters much greater than a wavelength) refracting or reflecting particles with scattering characteristics which can be described using geometric optics. Light scattered from these particles is observed at some angle off the bisector between the beams with the scattered light collection lens centered in a plane perpendicular to the plane of the beams. The following discussion presents two simple models for understanding the signal generated by the two classes of particles.

### 1.2 Class I Particles

When a particle (assumed spherical) much less than  $\delta$  in diameter crosses the fringe pattern, it can be assumed to be uniformly illuminated across its



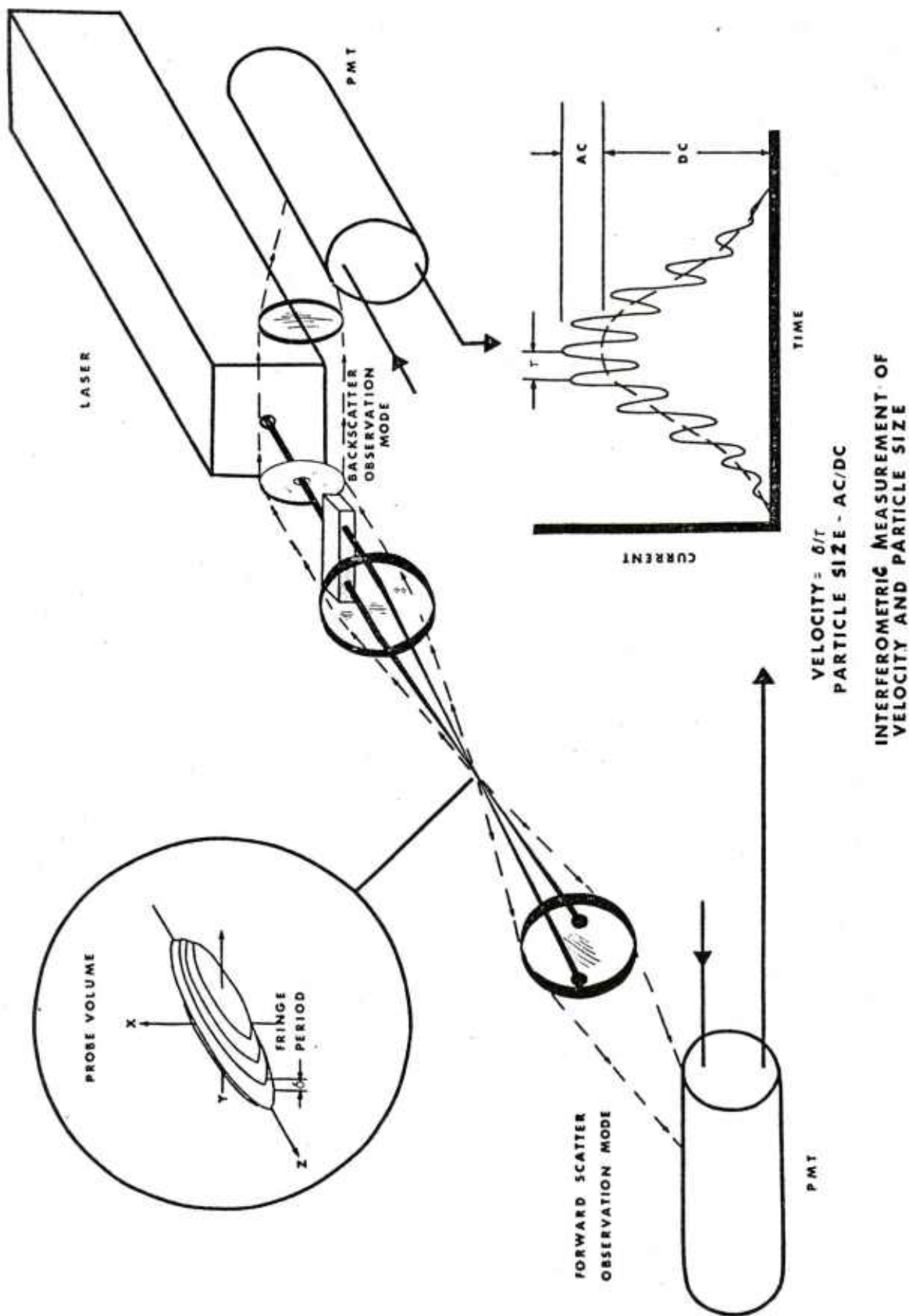


FIGURE 1. PRINCIPLE OF THE PARTICLE SIZING INTERFEROMETER.

diameter at all points along its path through the fringe pattern. The light which is scattered by the particle is proportional to the observable flux illuminating it. Thus, measurement of the time period,  $\tau$ , of the scattered light is related to the velocity,  $v$ , of the particle through the relationship

$$v = \delta/\tau \quad . \quad (2)$$

As the size of the scattering particle increases relative to  $\delta$ , the illumination of the particle is no longer uniform and must be averaged over the cross-sectional area of the particle. The non-uniform illumination of the particle results in a reduction of the contrast or visibility of the scattered light signal. Let  $I_{\max}$  be the maximum value in intensity in a period of the scattered light from a particle and  $I_{\min}$  the next successive minimum. The visibility,  $V$ , can then be defined as

$$V = \frac{I_{\max} - I_{\min}}{I_{\max} + I_{\min}} \quad . \quad (3)$$

It is straightforward to show that  $V$  is fully equivalent to the ratio of AC amplitude divided by the DC amplitude of the scattered light signal. The high frequency "Doppler" portion of the signal is defined as the "AC". It usually has many cycles of information relative to that of the DC component (the DC component refers to the Gaussian shaped low frequency term describing the signal). Analytically, the visibility may be written as

$$V \approx \frac{\int_{A_p} I_o \cos(2\pi y/\delta) dA_p}{\int_{A_p} I_o dA_p} \quad (4)$$

where  $A_p$  is the cross-sectional area of the particle,  $I_o$  is intensity distribution across one of the illuminating beams, and  $y$  is the coordinate normal to the fringe planes. When  $I_o$  is a Gaussian function ( $TEM_{00q}$ \* laser beam - the subscripts indicate the order of the Hermite polynomial used to describe the oscillation mode of the laser cavity), it can be shown that Equation 4 is an accurate approximation over a depth of field,  $\ell$ , given by

$$\ell \approx 0.8 b_o/\alpha \quad (5)$$

where  $b_o$  is the radius of the  $e^{-2}$  intensity point in the illumination beam. For depths of field greater than  $\ell$ , the signal visibility is a function of particle size and position in the illumination. In order to simplify Equation 4 for Gaussian beams and still maintain accuracy, it is required that the particle diameter,  $D$ , satisfy the relationship

$$D \leq 0.2b_o \quad (6)$$



and for  $\delta$  to satisfy

$$\delta \leq 0.2b_0 \quad (7)$$

Under these conditions,  $V$  for a sphere can be written as

$$V \approx 2J_1(\pi D/\delta)/(\pi D/\delta) \quad (8)$$

where  $J_1$  is a Bessel function of the first kind. For a cylinder,  $V$  can be written as

$$V = \sin(\pi L_c/\delta)/(\pi L_c/\delta) \quad (9)$$

where  $L_c$  is the length of a cylinder of diameter  $D \ll \delta$ . Equations 8 and 9 are plotted in figure 2 to illustrate the salient features of the visibility in particle size measurement.

Figure 2 shows that for spherical particles, the visibility function is not monotonic for sizes greater than about  $1.05 \delta$ . This value fixes the upper limit of the PSI size range. The lower limit results from the acceptable error in the particle size measurements. Since particle size is a non-linear function of visibility, a 1% uncertainty in visibility gives a 1% uncertainty in  $D$  when  $D/\delta$  is about 1, but  $\pm 30\%$  when  $D/\delta$  is about 0.1. Acceptable sizing uncertainty and signal processor accuracy thus limit the low end of the PSI size range to about  $0.05 D/\delta$ . Hence, the PSI can cover about 20:1 size range for a given  $\delta$ . Figure 3 shows the uncertainty in particle diameter as a function of  $D/\delta$  for fixed uncertainty values of  $V$ .

### 1.3 Class II Particles

These particles may be imagined to be small spherical lenses or mirrors. As the particle enters the fringe pattern, it causes the incident beams to focus to two point sources immediately in front of the particle. The separation of the point sources is a function of the particle size and index of refraction. The light from the two point sources generates a set of interference fringes which follow hyperbolic contours in the plane of the observation lens. By keeping the observation lens in the plane perpendicular to the plane of the beams and intersecting the bisector, these fringes will be nearly constant across the lens aperture. The observed signal visibility will thus be a function of the separation of the point sources and the aperture used to detect the refracted or reflected light from the particle. Analysis shows (see Appendix I) that the resulting visibility may be written as

$$V = \frac{2J_1(\pi D/\delta_e)}{\pi D/\delta_e} \quad (10)$$

where  $\delta_e$  is the "effective" fringe period of the system. For example, for scatter in the near forward direction

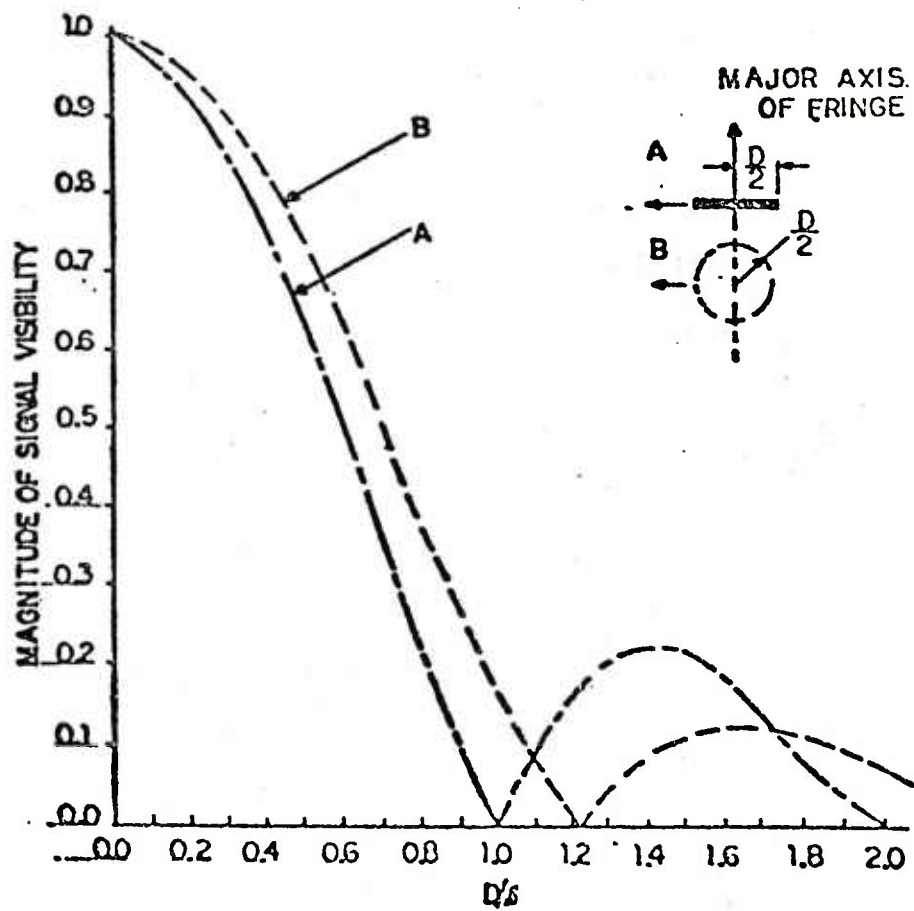


FIGURE 2. VISIBILITY AS A FUNCTION OF PARTICLE SIZE FOR A CYLINDER AND SPHERE.

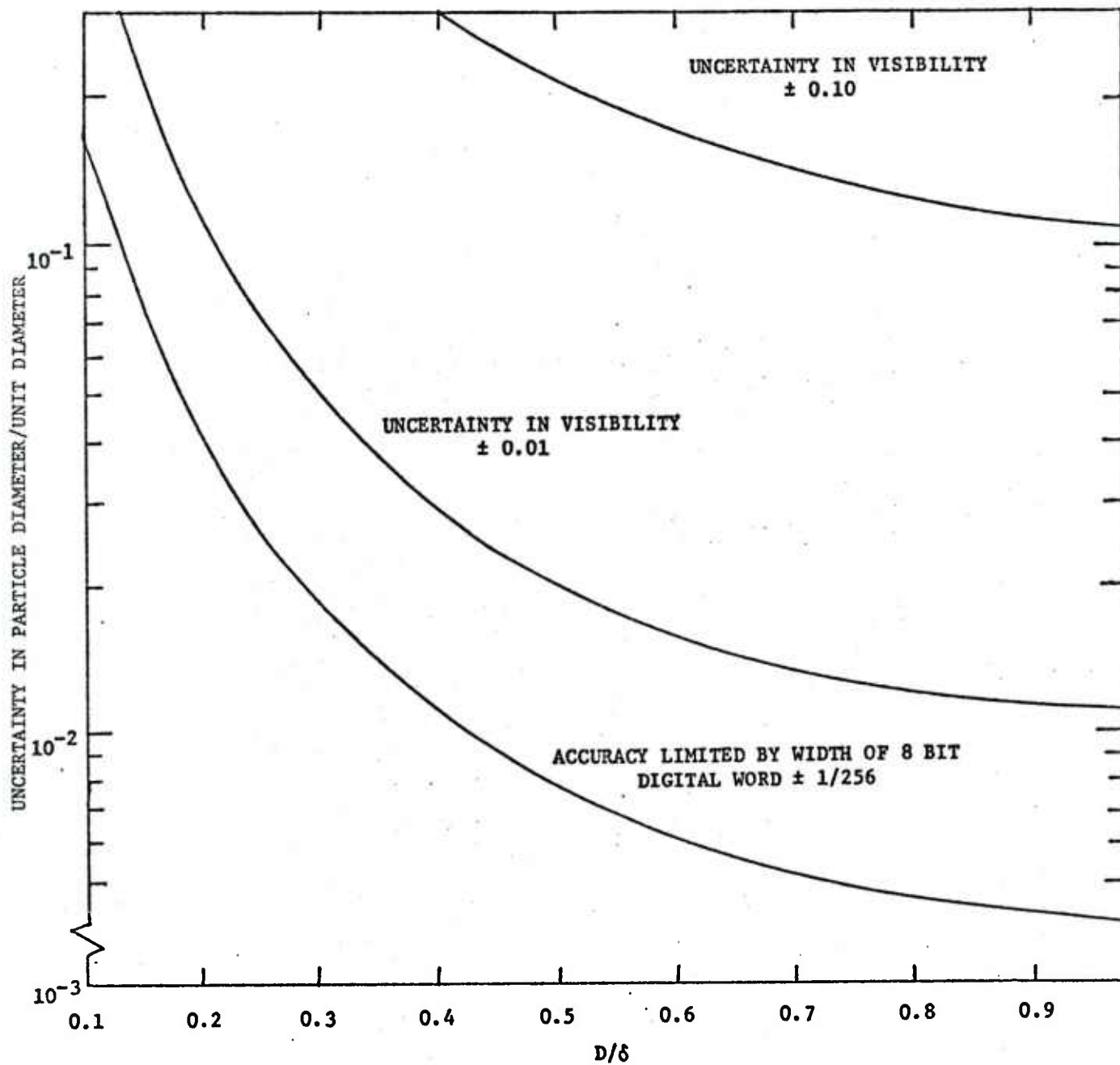


FIGURE 3. UNCERTAINTY IN SPHERICAL PARTICLE DIAMETERS FOR VARIOUS VALUES OF UNCERTAINTY IN THE VISIBILITY.

$$\delta_e = 4F\delta \left[ 1 + \frac{1}{2} \tan^2 \beta \right] \frac{m'-1}{m'} \quad (11)$$

where  $F$  is the  $F$  number subtended by the scattered light receiver,  $\beta$  is the observation angle, and  $m'$  is the index of refraction. Thus, the same visibility function as for Class I particles still applies. However, the fringe period is scaled as shown in Equation 11. Equation 11 shows that the size range which can be covered for a given fringe period and particle index of refraction can be adjusted through adjustment of the scattered light collector  $F$  number.

## 2.0 FUEL SPRAY CHARACTERISTICS EXPECTED TO AFFECT PSI PERFORMANCE

The purpose of this section is to develop simple parametric equations which can be used to illustrate the expected performance of a PSI system under possible operational conditions. The parameters associated with a fuel spray which may be expected to have a significant impact on PSI performance are:

1. Droplet number density
2. Droplet size range
3. Droplet size distribution
4. Droplet index of refraction
5. Material density of the fuel.

These factors are discussed separately in the following subsections.

### 2.1 Droplet Number Density

Consider figure 4 which shows the geometry used to estimate droplet number density as a function of position in the spray. Assume the spray has a divergence angle given by  $\theta$ . The mass flow rate,  $\dot{M}$ , crossing a plane in the spray is given by

$$\dot{M} = \frac{\pi}{6} \rho_o \mu_3 \dot{N} \quad (12)$$

where  $\rho_o$  = material density of fuel,  $\mu_3$  = third moment of size distributions, and  $N$  = number of particles per second crossing the plane. The droplet number density  $\rho_N$  can be written as

$$\rho_N = \frac{N}{V_z a_s \Delta t} \quad (13)$$

where  $a_s$  = cross-sectional area of the spray,  $V_z$  = spray droplet velocity normal to  $a_s$ ,  $\Delta t$  = observation time during which  $\rho_N$  is detected, and  $N$  = number of particles crossing  $a_s$  during  $\Delta t$ . If  $\rho_N$  is constant during  $\Delta t$  then  $N = \rho_N \Delta t$ . For some axial position,  $Z$ , in the spray  $a_s$  is given by

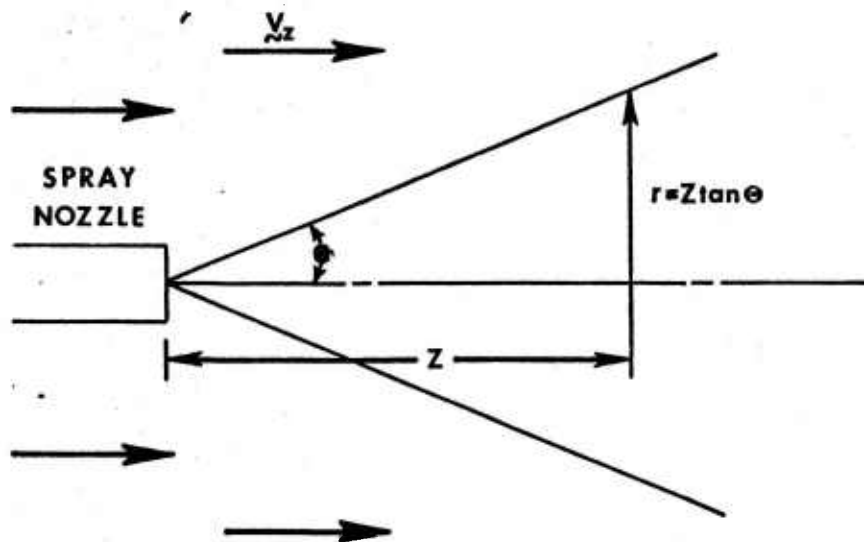


Fig. 4. Assumed spray nozzle geometry.

$$a_s = \pi Z^2 \tan^2 \theta \quad (14)$$

where  $\theta$  is spray cone half angle. Using Equations 12 and 14 in Equation 13 yields

$$\rho_N = \frac{\dot{M}}{\frac{\pi^2}{6} \rho_o \mu_3 v_z Z^2 \tan^2 \theta} \quad (15)$$

Equation 15 shows that  $\rho_N$  can be expected to vary inversely as  $Z^2$ . This implies that as  $Z$  decreases,  $\rho_N$  will eventually reach a point where the PSI cannot function. The factors affecting this limitation will be discussed in detail in a later section. It should be clearly understood that Equation 15 is an approximate relationship which assumes that the droplets have all assumed the same  $v_z$  value. In general, this will not be the case. A velocity distribution will exist which depends on the droplets angular trajectory and variations in background air and nozzle pressure during the sample interval.

## 2.2 Droplet Size Range

A PSI can accommodate a size range of approximately 10-20:1 for any one optical setting. If the nozzle produces particles over a size range greater than this then it is necessary to recognize and correct for the fact that a number of overlapping size ranges may be necessary to properly describe the size distribution.

## 2.3 Droplet Size Distribution

The shape of the droplet size distribution can directly affect the operating characteristics of the PSI system. To illustrate these effects, consider the following possible size distributions.

1. Monodisperse size distribution
2. Single mode log-normal size distribution
3. Bimodal log-normal size distribution.

It is assumed for simplicity that the range of the log-normal distributions is 0 to  $\infty$ . These distributions are chosen for simplicity and because they are known to characterize many droplet and particle processes. Before proceeding, it will be convenient to define the moments of the distributions. The  $k$ th sample moment,  $\mu_k$ , of a droplet distribution expressed as a size histogram is defined by

$$\mu_k = \frac{1}{N_t} \sum_{i=1}^n f_i D_i^k \quad (16)$$

where  $N_t$  is the total number of measurements for the histograms and it is assumed that there are  $n$  size increments with  $f_i$  measurements in the  $i$ th size



interval.  $D_i$  is assumed to be the largest diameter in the  $i$ th increment. Note that

$$N_t = \sum_{i=1}^n f_i \quad (17)$$

Log-normal distributions are characterized by two parameters: 1) geometric mean diameter,  $D_g$ , and 2) the geometric standard deviation  $\sigma_g$ .  $D_g$  and  $\sigma_g$  are defined according to

$$D_g = \exp\left\{ \frac{1}{N_t} \sum_{i=1}^n f_i \ln D_i \right\} \quad (18)$$

$$\sigma_g = \exp\left\{ \frac{1}{N_t} \sum_{i=1}^n f_i \ln^2(D_i/D_g) \right\} \quad (19)$$

A log-normal probability density distribution may be written as

$$P(D) = \frac{1}{\sqrt{2\pi} \ln \sigma_g} \exp\left( - \left[ \frac{\ln(D/D_g)}{\sqrt{2} \ln \sigma_g} \right]^2 \right) \quad (20)$$

The first four moments of the distribution may be written as<sup>1</sup>

$$\mu_1 = D_g \exp\left(\frac{1}{2} \ln^2 \sigma_g\right) \quad (21)$$

$$\mu_2 = D_g^2 \exp(2 \ln^2 \sigma_g) \quad (22)$$

$$\mu_3 = D_g^3 \exp(4.5 \ln^2 \sigma_g) \quad (23)$$

$$\mu_4 = D_g^4 \exp(8 \ln^2 \sigma_g) \quad (24)$$

The first four moments are used to express various mean diameters which have appeared in the literature and have been used to characterize nozzles. For example, the volume to area diameter often called the "Sauter" mean diameter,  $D_s$ , may be expressed as

$$D_s = \mu_3/\mu_2 \quad (25)$$

$$D_s = D_g \exp(2.5 \ln^2 \sigma_g) \quad (26)$$

The volumetric mean diameter  $D_v$  is defined as

$$D_v = \mu_3^{1/3} \quad (27)$$

$$D_v = D_g \exp(1.5 \ln^2 \sigma_g) \quad (28)$$

Also found is the mass mean diameter  $D_{mm}$  given by

$$D_{mm} = \mu_4 / \mu_3 \quad (29)$$

$$D_{mm} = D_g \exp(3.5 \ln^2 \sigma_g) \quad (30)$$

It is often found that bimodal distributions exist in smokes and in some sprays. In this case, the total distribution may be viewed as the sum of two weighted distributions. One distribution contributes a fraction  $fN$  to the total number of particles while a second contributes  $(1-f)N$ . If such a distribution is considered to be the sum of two log-normal distributions, then the resulting probability density will be of the form

$$P(D) = \frac{f}{\sqrt{2\pi} \ln \sigma_{g1}} \exp\left(-\frac{\ln(D/D_{g1})^2}{2 \ln \sigma_{g1}}\right) + \frac{(1-f)}{\sqrt{2\pi} \ln \sigma_{g2}} \exp\left(-\frac{\ln(D/D_{g2})^2}{2 \ln \sigma_{g2}}\right) \quad (31)$$

where  $D_{gi}$ ,  $\sigma_{gi}$   $i=1, 2$  indicates the geometric mean and standard deviation for distributions 1 and 2. Now consider how the special cases of interest affect the expected number density.

### 2.3.1 Monodisperse Size Distribution of Diameter $D$

In this case,  $\mu_3 = D^3$ . Equation 15 becomes

$$\rho_N(0) = \frac{\dot{M}}{\frac{\pi}{6} D^3 V_z^2 \tan^2 \theta} \quad (32)$$

where  $\rho_N(0)$  is the number density for a monodisperse size distribution. The following parameters are typically found in a fuel spray nozzle.

$$D = 50 \text{ } \mu\text{m}$$

$$V_z = 1524 \text{ cm/sec.}$$

$$\theta = 70^\circ$$

$$\dot{M} = 667 \text{ lb/hour}$$

$$\dot{M} = 84.11 \text{ gm/sec.}$$

Assume  $\rho_o = 0.9$  gm/cc, then equation 32 yields

$$\rho_N(0) = \frac{4 \cdot 10^4}{z^2} \text{ cc}^{-1} \quad (33)$$

### 2.3.2 Single Mode Log-Normal Size Distribution

In this case, Equation 15 when used with Equation 23 yields

$$\rho_N(1) = \frac{\dot{M}_e^{-4.51 \ln^2 \sigma_g}}{\frac{\pi}{6} \rho_o D_g^3 V_z^2 \tan^2 \theta} \quad (34)$$

where  $\rho_N(1)$  is understood to mean the number density resulting from a single mode log-normal size distribution. If  $D_g$  is taken to be 50  $\mu\text{m}$  and the parameters used to compute  $\rho_N(0)$  are used in Equation 34, then

$$\rho_N(1) \approx \frac{4 \cdot 10^4 e^{-4.51 \ln^2 \sigma_g}}{z^2} \text{ cc}^{-1} \quad (35)$$

Equation 35 shows the result that as  $\sigma_g$  increases, the number density decreases. This should be expected since  $\sigma_g$  increasing corresponds to a broader distribution containing increased numbers of large particles carrying significant fractions of the total mass.

### 2.3.3 Bimodal Log-Normal Distribution

For this illustration, it will be assumed that the following parameters apply to the distribution function described by Equation 31:

$$D_{g1} = 10 \mu\text{m} \quad (36)$$

$$D_{g2} = 100 \mu\text{m} \quad (37)$$

$$\sigma_{g1} = 1.64 \quad (\ln \sigma_{g1} = 0.5) \quad (38)$$

$$\sigma_{g2} = 1.105 \quad (\ln \sigma_{g2} = 0.1) \quad (39)$$

To examine a case that might cause particular difficulty with a PSI, consider the situation where the largest numbers of particles are in the small size mode but the greatest portion of the mass is in the large size mode. The parameters in Equation 31 have been chosen such that numerically 92% of the total number of particles in the distribution reside in the small mode. However, this mode contributes only about 2% of the total mass. Let  $f$  represent the numeric fraction of particles in the first size distribution. Using Equation 13 and 32 and the parameters in Equations 36-39, there results for the third moment

of the bimodal size distribution

$$\mu_3 = fD_{g1}^3 e^{4.5 \ln^2 \sigma_{g1}} + (1-f)D_{g2}^3 e^{4.5 \ln^2 \sigma_{g2}} \quad (40)$$

$$\mu_3 = 0.92(10)^3 e^{4.5(0.25)} + 0.08(10^2)^3 e^{4.5(0.01)} \quad (41)$$

$$\mu_3 = 8.39 \cdot 10^4 \mu\text{m}^3 \quad (42)$$

$$D_v = 43.78 \mu\text{m} \quad (43)$$

Using Equation 42 along with the parameters used in section 2.3.1 (Equation 32) yields for the number density

$$\rho_N \approx \frac{6 \cdot 10^4}{z^2} \quad (44)$$

where  $\mu_3$  has been substituted for  $D^3$ . Equation 44 shows that roughly a 50% increase in  $\rho_N$  results from the parameters chosen for the bimodal distribution even though the volumetric mean diameter is nearly the same as that for the monodisperse case. Figure 5 plots the numeric distribution for the parameters assumed to obtain equation 44. As the figure shows, the PSI would need to count large numbers of particles very accurately if accurate  $\rho_N$  and hence mass concentrations are to be obtained.

## 2.4 Droplet Index of Refraction

There are two observation modes which have been found to be useful with the PSI. These are called the "on axis" (for Class I particles) and "off axis" (for Class II particles) viewing modes. The "on axis" viewing mode requires that the scattered light collection system be centered on the bisector between the beams forming the PSI sample volume. (A discussion of the theoretical interpretation and operating principles of the PSI in this mode is given in reference 5.) Figure 6 illustrates this viewing mode. In this configuration, it has been found that the PSI size parameter is independent of the droplet index of refraction when the particle absorbs a small fraction of the incident light. In this case, the visibility function is monotonic when the particle diameter is less than about 1 fringe period,  $\delta$ , in diameter. Hence, the PSI measurement is independent of index of refraction and covers a size range between roughly 0.05-1.0  $\delta$  when used in the axis viewing mode.

In the off axis viewing mode shown in figure 7, the PSI signal is obtained by collecting the scattered light at some angle off the bisector between the beams. Appendix I discusses how index of refraction affects the PSI signal and presents a simple model for understanding why this is so. In the off axis viewing mode, the particle size range is shifted. A 10-1

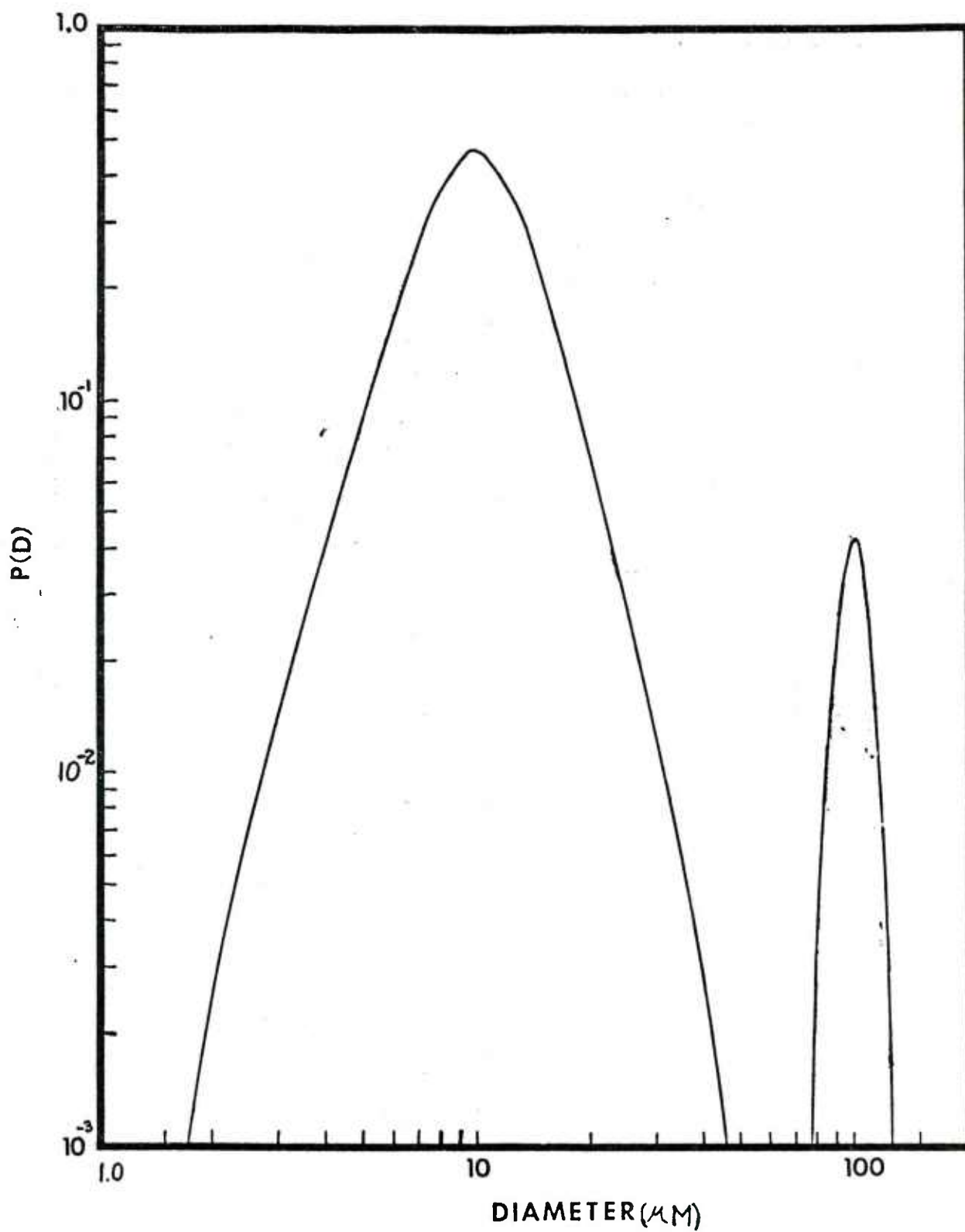


Fig. 5. Probability density distribution for the assumed bimodal log-normal distribution.

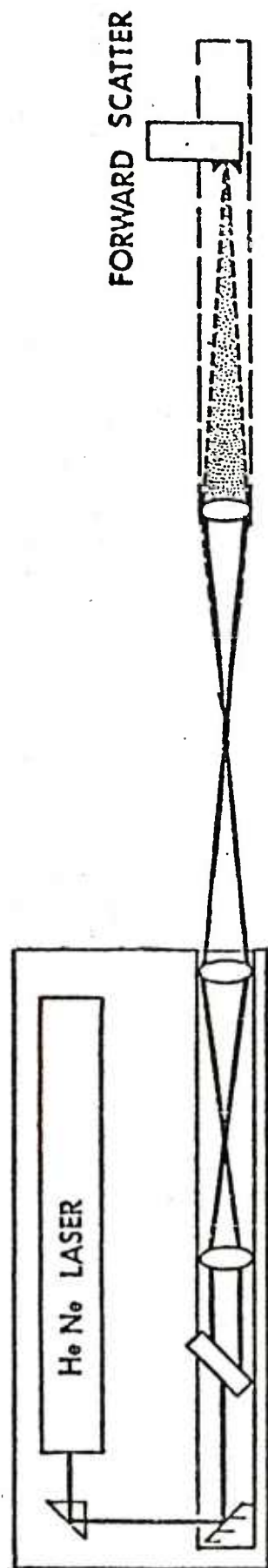


Fig. 6. Example of on axis PSI viewing geometry.



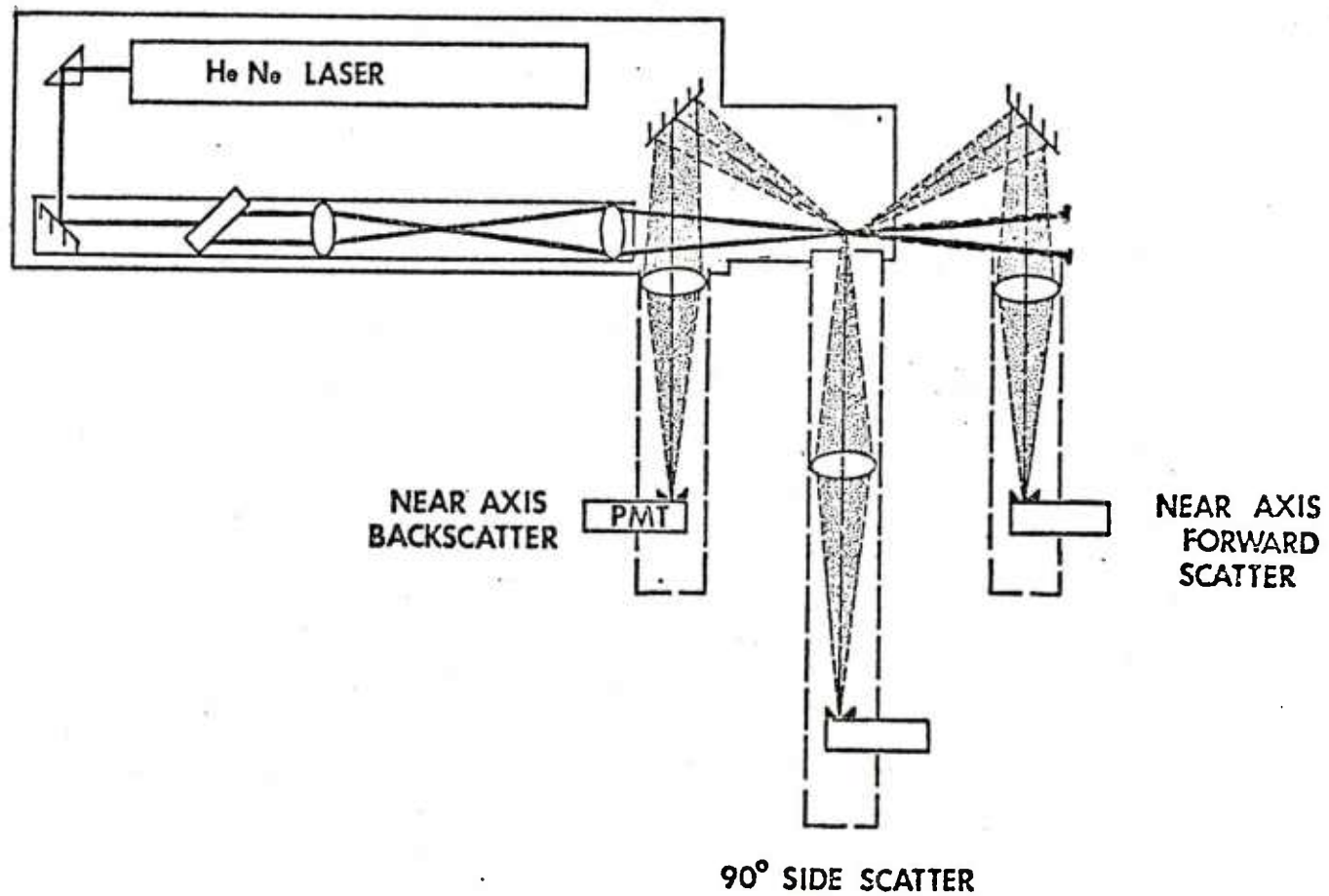


Fig. 7. Example of possible PSI off axis viewing directions.

or 20-1 size range is still covered but the location of the size range will depend on the droplet index of refraction and the F number of the scattered light collector. When droplets are opaque the discussion in reference 5 applies.

## 2.5 Material Density of the Fuel

The PSI produces sufficient information to compute the time average mass concentration  $\langle C \rangle$  or mass flow rate  $\dot{M}$  at a particular point in the spray.  $\langle C \rangle$  can be written as

$$C = \frac{\pi}{6} \rho_o \langle \mu_3 \rho_N \rangle \quad (45)$$

where  $\langle \mu_3 \rho_N \rangle$  is the time averaged value of the third moment and number density of the size distribution.  $\rho_o$  is the material density of the fuel. Equation 45 shows that if absolute values of  $\langle C \rangle$  are computed, then  $\rho_o$  must be known. Equation 15 also shows that if  $\dot{M}$  is computed from PSI data that  $\rho_o$  is a fundamental parameter which must be known.

## 3.0 PSI DESIGN LIMITATIONS IMPOSED BY FUEL SPRAY REQUIREMENTS

Section 2.0 discussed the spray characteristics which will affect the performance and accuracy of a PSI. In this section, the results of section 2.0 are supplied to the response parameters which define the operational characteristics of the PSI.

### 3.1 Number Density Limitations

#### 3.1.1 Data Acquisition Limitations

Determination of number density with any optical instrument is difficult and subject to numerous errors. This is especially true for a PSI. In estimating number density with a PSI, at least two different approaches have been developed. The first approach is to attempt to make the sample volume so small that virtually no signals are ever seen from more than one particle. Then counts of individual particles can be correlated with the total volume of fluid sampled. This approach can only be valid when particle number density is so low that the average number of particles in the sample volume is much less than 1. In sprays where the number density may fluctuate, erroneous counts may result from the presence of more than one particle in the sample volume. The second approach recognizes this fact and attempts to make use of the multiple particle detection capability of the PSI and statistical models to estimate particle number density. Appendix II presents a discussion of the model employed in the second approach for estimating number density. This is the method used by UTSI to estimate number density and it has been found to yield surprisingly good results. The PSI parameter used to estimate number density is called the acceptance ratio A. A is the ratio of the number

of single particle signals (with aperiodicity less than 50%) detected to the total number of signals detected. Appendix II shows that A can be written as

$$A = 1 - \left[ \left(1 - \exp \frac{-\rho_N^{1/3} \Delta x^2}{\pi \delta}\right) \left(1 - \exp \frac{-\rho_N^{1/3} \Delta y^2}{\pi \delta}\right) \left(1 - \exp \frac{-\rho_N^{1/3} \Delta z^2}{\pi \delta}\right) \right]^{1/2} \quad (46)$$

where  $\delta$  is the fringe period of the system and  $\Delta x$ ,  $\Delta y$ ,  $\Delta z$  are the rectangular spatial measures of the PSI sample volume. For purpose of illustration, we will consider two extremes in the optical viewing geometry. These two cases are illustrated in figure 8. In the first case, we consider an on axis viewing geometry in which  $\Delta x = \Delta y$  and  $\Delta x \Delta y$  is the sample volume cross-section normal to the bisector between the beams. In this geometry  $\Delta z \gg \Delta x$ ,  $\Delta y$ . Equation 46 then becomes

$$A = \exp \left( \frac{-\rho_N^{1/3} \Delta x^2}{\pi \delta} \right) \quad (47)$$

If it is assumed that the particles generate a certain number of cycles in the signal,  $N_L$ , before they are measured, then  $\Delta x$  can be written as

$$\Delta x = N_L \delta \quad (48)$$

Using Equation 48 in Equation 47 yields

$$A = \exp \left( \frac{-\rho_N^{1/3} N_L^2 \delta}{\pi} \right) \quad (49)$$

In the second case, it is assumed that the scattered light receiver is positioned  $90^\circ$  off the bisector between the beams. This case would correspond to roughly the smallest possible sample volume. In this case,  $\Delta x = \Delta y = \Delta z$  and use of Equation 48 reduces equation 46 to

$$A = 1 - \left( 1 - \exp \left( \frac{-\rho_N^{1/3} N_L^2 \delta}{\pi} \right) \right)^{3/2} \quad (50)$$

Equations 49 and 50 indicate the extremes in A that could be obtained for two possible viewing geometries. As Appendix II points out, A can be increased by using slit apertures to reduce  $\Delta x$ . In this way, increased number density response can be obtained. To illustrate the PSI operating characteristics indicated by Equations 49 and 50, assume  $N_L = 10$  and  $\delta = 30 \mu\text{m}$ . ( $N_L = 10$  has been found to yield reasonable results in previous applications and  $\delta = 30 \mu\text{m}$  will yield a size range of  $1.5 - 30 \mu\text{m}$  for on axis viewing and a  $15 - 300 \mu\text{m}$  size range for the case of  $90^\circ$  off axis observation and an F/3.5 receiver. See Table I in Appendix I.) Figure 9 plots A for the two cases of interest. The figure shows, for example, that when  $\rho_N = 10^5$ , that the PSI will measure between 1 and 2% of the total number of

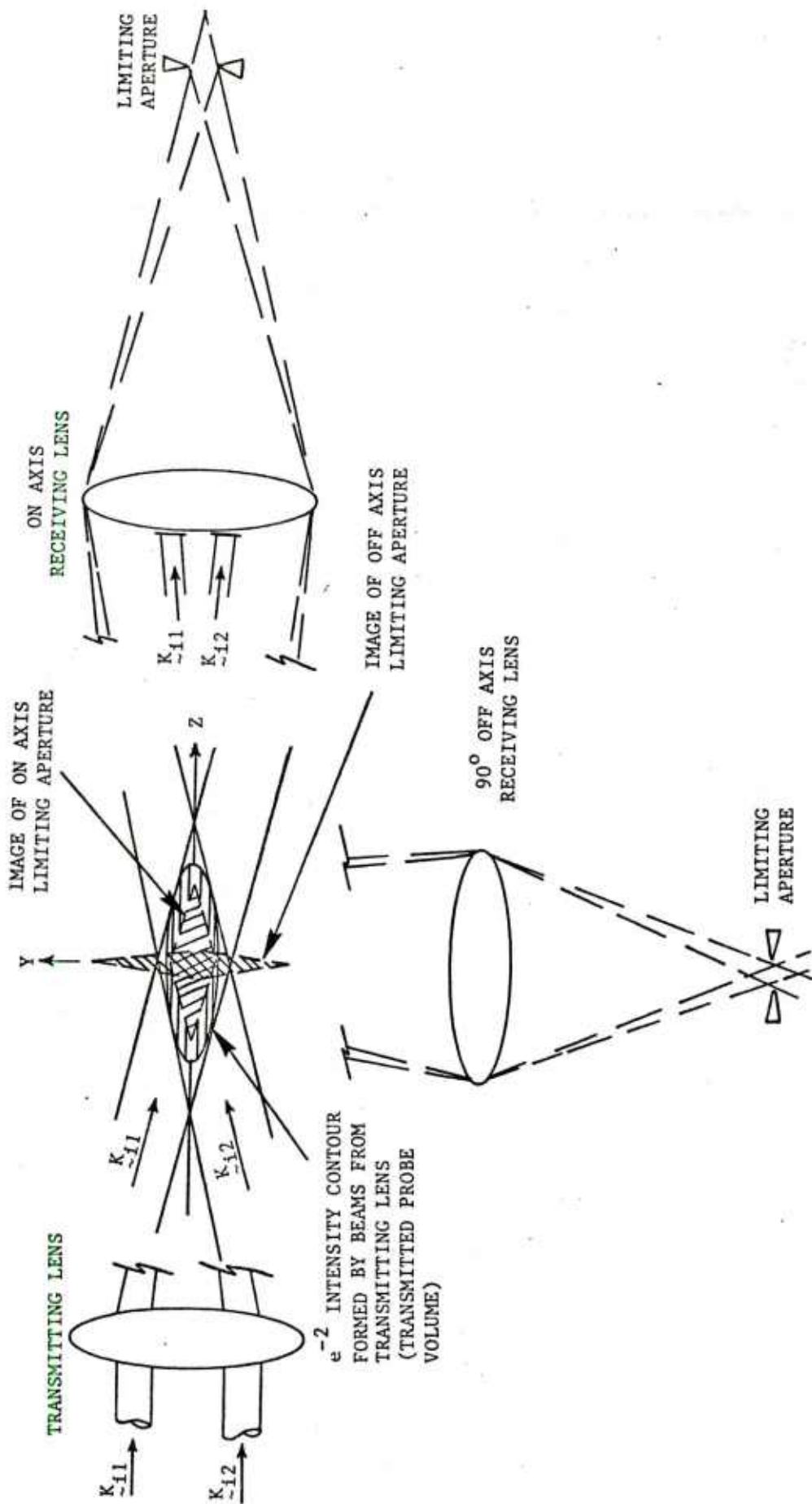


Fig. 8. Exploded View of Beam Intersection Point Showing How Receiver Lens Orientation Limits PSI Sample Volume.

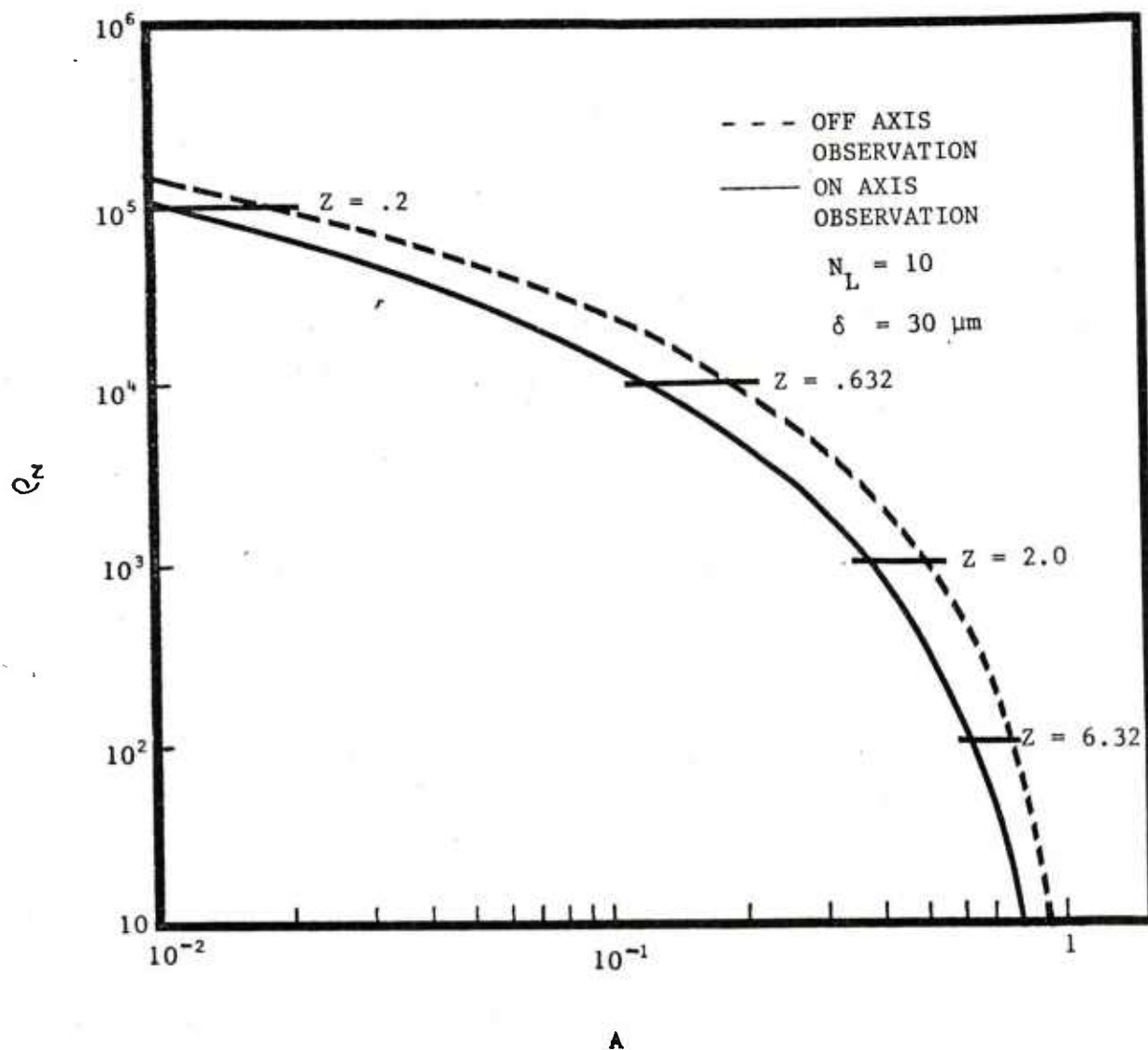


Fig. 9. Example of acceptance ratio as a function of number density for on axis and off axis viewing geometry.  $Z$  values correspond to  $Z$  positions (cm) in a  $50 \mu m$  diameter monodisperse spray with mass flow of 667 lbs/hr. (84.11 gm/sec).

particles detected and that  $90^\circ$  off axis observation does not give that much better response for  $\rho_N$  than the on axis geometry. Also plotted in figure 9 are the corresponding Z positions in the model spray described for a monodisperse size distribution. (Note, however, that in case 2 spatial resolution will be significantly better than for case 1.)

Past experience has shown that when A reaches a value of 0.1 that data acquisition with the PSI is too slow to obtain a statistically significant data set in a reasonable length of time. If  $A = 0.1$  is chosen as the limiting criteria for data acquisition, then equations 49 and 50 can be solved to specify the required  $N_L$  and  $\delta$  values to obtain a reasonable optical geometry for an estimated limiting number density. Solving Equations 49 and 50 for these cases yields

$$\rho_N \Big|_{\max} = \frac{3.78 \cdot 10^2}{N_L^6 \delta^3} \quad \text{case 1} \quad (51)$$

$$\rho_N \Big|_{\max} = \frac{6.04 \cdot 10^2}{N_L^6 \delta^3} \quad \text{case 2} \quad (52)$$

Suppose the spray produced  $\rho_N$  values up to  $10^6$  particles  $\text{cc}^{-1}$ .  $N_L = 10$  is approximately as small as desirable for successful operation of the PSI. Equation 51 in that case yields a  $\delta$  value of  $7.23 \mu\text{m}$  for the on axis case while Equation 52 shows that the smallest acceptable fringe period in case 2 is  $8.45 \mu\text{m}$ . This means that for  $\rho_N = 10^6 \text{ cc}^{-1}$ , the size range achievable for the on axis case is about  $0.36$  to  $7.23 \mu\text{m}$ . In the  $90^\circ$  off axis case, Table I in Appendix I shows that an F/12.6 scattered light receiver would yield a size range of approximately  $30$ – $300 \mu\text{m}$  for a  $\rho_N$  value of  $10^6 \text{ cc}^{-1}$ . While these calculations seem to indicate that the PSI would function for number densities of the order of  $10^6 \text{ cc}^{-1}$  over the required size range for a  $90^\circ$  off axis viewing geometry, the reader should be cautioned that UTSI has not attempted such measurements ( $90^\circ$  off axis) on number densities this high and cannot be certain that such measurements are possible. However, measurements have been obtained for hygroscopic smokes with reasonable success in the on axis case with fringe periods similar to those calculated for case 1. These results are described in Appendix III. Table III.1 summarizes the results of these computations.

### 3.1.2 Optical Transmission Limitations

Optical transmission is a fundamental limitation imposed by particle number density of PSI operation. In this area, the spray density and droplet scattering cross-section must be sufficiently small that adequate beam transmission can be obtained through the spray. During the work reported in Appendix III, it was found (but not reported) that when the optical



TABLE III.1

PSI CHARACTERISTICS REQUIRED  
FOR RESPONSE TO  $\rho_N = 10^6 \text{ cc}^{-1}$   
FOR AN ACCEPTANCE RATIO OF 0.1

	ON AXIS OBSERVATION	90° OFF AXIS OBSERVATION
Required Signal Cycles	10	10
Maximum Fringe Period ( $\mu\text{m}$ )	7.23	8.45
10:1 Particle Size Range for F/12.6 Receiver ( $\mu\text{m}$ )	0.723 - 7.23	30 - 300
Velocity Range for Simultaneous Velocity- Particle Size Measurement (0.5% Uncertainty)	2.17 - 25.3	2.54 - 29.6
Velocity Range Without Particle Size (5% Uncertainty)	2.17 - 253	2.54 - 296

transmittance fell below about 0.8, the PSI data rate fell to an unusably low value. Thus, in this section, PSI operational limitations are examined in light of this transmittance limit. The Beer-Bougher transmission law may be written as

$$T = \exp(-\bar{\sigma}\rho_N L) \quad (53)$$

where  $\bar{\sigma}$  is the mean extinction cross-section and  $L$  is the transmission path length. For a polydispersion,  $\bar{\sigma}$  can be written as

$$\bar{\sigma} = \int_0^{\infty} Q_E(D) D^2 \frac{\pi}{4} \frac{d\rho_N(D)}{\rho_N} \quad (54)$$

where  $Q_E$  is the extinction efficiency and  $d\rho_N/\rho_N$  is the numeric size distribution. The extinction efficiency is defined as  $4\sigma/\pi D^2$  where  $\sigma$  is the extinction cross-section.<sup>2</sup> When  $D \gg \lambda$  (the optical wavelength)  $Q_E \approx 2$  independent of  $D$ .<sup>2</sup> This is assumed to be the case for fuel spray. Then Equation 54 reduces to

$$\bar{\sigma} \approx \frac{\pi}{2} \mu_2 \quad (55)$$

where  $Q_E = 2$  has been substituted into Equation 54 and  $\mu_2$  is understood to represent the second moment of the size distribution.

$$\rho_N \Big|_{\text{max. tran.}} = \frac{1.42 \cdot 10^7}{\mu_{2\mu\text{m}} L} \text{ cc}^{-1} \quad (56)$$

where  $\mu_{2\mu\text{m}}$  is the second moment of the size distribution expressed in  $\mu\text{m}^2$  and  $L$  is in cm.

For the monodisperse size distribution described by Equation 33, Equation 56 reduces to

$$\rho_N(0) \Big|_{\text{max. tran.}} = \frac{5.68 \cdot 10^3}{L} \text{ cc}^{-1} \quad (57)$$

Comparison of Equations 33 and 57 shows that two competing effects exist to limit the PSI operation - either the number density may be too high to obtain a useable data rate or the transmission path through the spray may be too long even at reduced number densities. An estimate of the maximum value of  $Z$  in the monodisperse spray can be obtained by letting  $L = 2Z \tan \theta$  and equating Equations 33 and 57. The result is

$$Z(0) \approx 38.7 \text{ cm} \quad (58)$$

max

For the single mode log-normal distribution with  $D_g = 50 \mu\text{m}$ , Equations 22 and 56 show that  $\rho_N(1)_{\text{max.tran.}}$  is given by

$$\rho_N(1)_{\text{max.tran.}} = \frac{5.68 \cdot 10^3}{L} e^{-2 \ln^2 \sigma_g} \quad (59)$$

Using Equations 33, 35, 57, and 59,  $Z_{\text{max}}(1)$  thus can be written as

$$\frac{\rho_N(0)}{\rho_N(1)}_{\text{max.tran.}} = \frac{Z(1)}{Z(0)} e^{2 \ln^2 \sigma_g} \quad (60a)$$

$$Z_{\text{max}}(1) = Z_{\text{max}}(0) e^{-2.5 \ln^2 \sigma_g} \quad (60b)$$

Hence, for the single mode log-normal distribution the transmission path decreases because the particle number density increases. For example, if  $\ln \sigma_g = 0.5$ , then  $Z_{\text{max}}(1)$  is about 50% of  $Z_{\text{max}}(0)$ . For the bimodal distribution specified by Equations 36-39 and a small particle fraction of 92%, the second moment is computed to be

$$\mu_{2\mu\text{m}} = 9.68 \cdot 10^2 \mu\text{m}^2 \quad (61)$$

$\rho_N_{\text{max.tran.}}$  as expressed in Equation 56 thus becomes for the bimodal distribution:

$$\rho_N(2)_{\text{max.tran.}} = \frac{1.46 \cdot 10^4}{L} \quad (62)$$

Using Equation 44 with Equation 62 yields

$$Z_{\text{max}}(2) \approx 22.6 \text{ cm} \quad (63)$$

These examples clearly show that the size distribution characteristics of the spray can significantly affect the operational performance of the PSI. As a result, specification of number density operating characteristics for the PSI must be dependent on the spray to be measured.

### 3.2 Velocity Limitations

The PSI signal processing system imposes velocity limits which depend on fringe period used in the optical system. The minimum velocity measurable by the PSI can be derived from the equation

$$V_{z \min} = \delta v_{Dmin} \quad (64)$$

where  $v_{Dmin}$  is the minimum Doppler frequency acceptable by the data acquisition system. UTSI has supplied an optical system which produces a minimum fringe period of 6  $\mu\text{m}$ .  $v_{Dmin}$  for the PSI signal processing electronics is limited by the high pass filter and is 30 KHz. Hence,

$$V_{z \min} = 0.18 \text{ m/sec.} \quad (65)$$

The maximum Doppler frequency obtainable with the signal processing electronics is approximately 3.5 MHz and is limited by acceptable signal distortions introduced by the full wave rectifier as the signal frequency increases. This leads to a maximum measurable velocity  $V_{z \max}$  for the small particle size range ( $\delta = 6 \mu\text{m}$ ) of

$$V_{z \max} = 21 \text{ m/sec.} \quad (66)$$

The largest fringe period for the PSI system is 100  $\mu\text{m}$ . In this case, the maximum and minimum velocities correspond to

$$V_{z \min} = 3 \text{ m/sec.} \quad (67)$$

$$V_{z \max} = 350 \text{ m/sec.} \quad (68)$$

However, as figure 9 shows, the maximum number density will correspond to approximately  $10^4 \text{ cc}^{-1}$  for an intermediate fringe period of 30  $\mu\text{m}$ . For a 100  $\mu\text{m}$  fringe period the maximum number density will correspond to about  $370 \text{ cc}^{-1}$  as estimated using Equation 51. Table III.1 summarizes the velocity limitations. It should be noted that if only velocity and number density are to be measured then the maximum measurable Doppler frequency is about 35 MHz (upper frequency response of the Doppler processor) leading to maximum velocities of 210 m/sec ( $\delta = 6 \mu\text{m}$ ) and 3500 m/sec ( $\delta = 100 \mu\text{m}$ ).

### 3.3 Particle Size Range Limitations

It has already been indicated in previous sections that the particle size range is a function of viewing geometry and fringe period. Appendix I and reference 5 detail how these factors directly affect the size range. The ultimate limitations of the size range depend on two factors: acceptable error for the small size measurements and the monotonic limit in the visibility when the particle sizes become larger than a fringe period (or equivalent fringe period). In the latter case, the error in diameter will be of the same order as that for the visibility. On the other hand, when the diameter to fringe period ratio is about 0.1, the uncertainty in diameter is about 30 times that of the visibility (see figure 3). As a result, a 10:1 size range is achievable with these devices for a 30% uncertainty in the smallest sizes and 20:1 (as extrapolated from figure 3) when errors greater than about 60% are acceptable.

## 4.0 CALIBRATION STANDARDS AND METHODS

Calibration of the PSI system falls into two categories: 1) optical, and 2) electronics. The electronics system calibration is dependent on a straightforward operational procedure which is detailed in the PSI Electronics Operations Manual.<sup>3</sup> The optical system calibration procedures are discussed here.

### 4.1 Optical Calibration Procedures

Three different calibration procedures should be performed on the optical system. These are:

1. Fringe period calibration
2. Checks of visibility as a function of particle size
3. Depth of field and probe volume diameter calibration.

The following sections describe how these calibrations have been performed in past tests and the results of such calibrations are described.

### 4.2 Fringe Period Calibration

The electronics measure the Doppler time period,  $\tau$ , or Doppler frequency  $1/\tau$ ,  $\nu_D$ , and the deviations in frequency for a set of measurements. Equation 2 shows that the fringe period  $\delta$  can be written as

$$\delta = \tau V \quad . \quad (69)$$

Hence, for a known velocity and measured  $\tau$ ,  $\delta$  can be computed. The known velocity is typically generated by a synchronous motor which spins a small wire mounted on a wheel attached to the motor shaft. The radius,  $r$ , from the center of the shaft to the center position of the wire is measured with a micrometer calipers to the nearest 0.001". A typical value of  $r$  is  $2.125 \pm 0.001$ ". Commercial power is regulated to a frequency of 60 Hz with precision and accuracy typically better than 0.1%. By placing the wheel such that its tangent is perpendicular to the fringe planes the wire velocity can be computed from

$$V = 2\pi r 60 \text{ cm/sec.} \quad (70)$$

where  $r$  is expressed in cm. By using the PSI system to measure  $\tau$ ,  $\delta$  can be computed from

$$\delta = 120 \pi r \tau \text{ cm} \quad (71)$$

where  $\tau$  is expressed in seconds. 0.5% uncertainty or better in the calibrated  $\delta$  values can be achieved using this method to determine the fringe period.

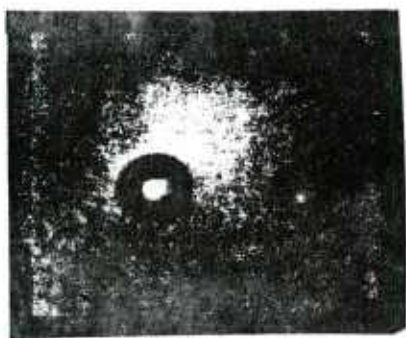
### 4.3 Visibility as a Function of Particle Size

To obtain this calibration, UTSI normally uses a vibrating orifice monodisperse generator to produce a stream of droplets with sizes in the range of 60 to 100 micrometers or greater. The droplet diameter can be computed with less than 5% uncertainty from the fluid flow rate and orifice vibration frequency. To further reduce this uncertainty, a microscope and strobe light system is used to photograph the droplets at the same time they were measured with the PSI. Because the droplets are typically separated by 4-5 diameters, multiple particles may be present in the probe volume from the initial output stream. This is overcome by using a droplet charging and deflection system. By charging, say, every 64th drop and passing the drop stream through a high static electric field (typically 2000 volts/cm) the charged drops can be directed through the sample volume while the main stream follows a different trajectory. Figure 10 shows photographs taken with the microscope system of the droplet stream. The estimated particle diameter from flow rate-frequency calculation and the visual diameter are compared under each. Figure 11 shows the particle deflection system and experimental arrangement.

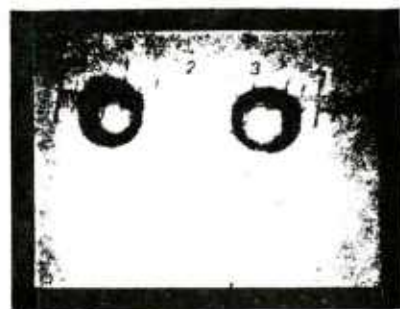
### 4.4 Probe Volume Calibration

In this section, the pertinent parameters required for probe volume calibration are described. The value of the probe volume is required if particle number density estimates or volume normalized size distributions are to be obtained. Two possible probe volumes should be considered. These will be referred to as the "High Density Probe Volume" (HIRO) and the "Low Density Probe Volume" (LORO). The HIRO volume corresponds to the volume defined by the localized region where the beams cross. It is a function of the incident beam intensities, optical viewing system and particle scattering cross-section, and signal processing logic.<sup>4</sup> Table IV shows the basic geometry of some possible HIRO probe volumes commonly encountered in PSI application and the formulas used to compute these volumes. The LORO probe volume is the cylindrical volume defined by the cross-sectional area of the HIRO volume normal to the mean flow direction and a height,  $h$ , defined by the mean velocity and the total sample time, i.e.  $h = \bar{v}_z t$ . Table IV.1 illustrates the LORO probe volumes and the appropriate formulas for computing the volumes associated with a particular viewing geometry. The calibration factor common to both volumes is the maximum number of signal cycles,  $N_0$ , detectable by the system. Once this value is known, then the HIRO volume can be directly estimated. In the LORO case, the length of the sample volume for a given maximum width can be a calibration factor. Table IV.2 illustrates depth of field calibration results using the arrangement shown in figure 11. The droplet stream was positioned down the probe volume axis until no more signals were read by the processor. The tabulated parameter was then changed and the measurement repeated. The calculated values with respect to the measured values were within  $\pm 1$  cycle of that predicted using the formulas used to compute the probe volumes. The choice of a particular probe volume is somewhat arbitrary. However, a reasonable "rule of thumb" is to use the





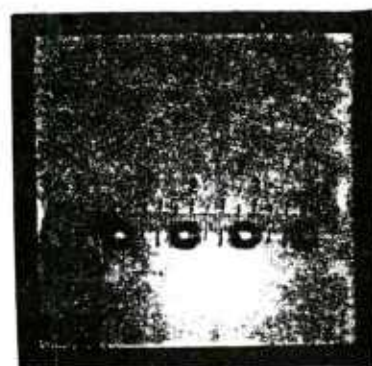
VISUAL MICROSCOPIC DIAMETER = **166  $\mu\text{m}$**



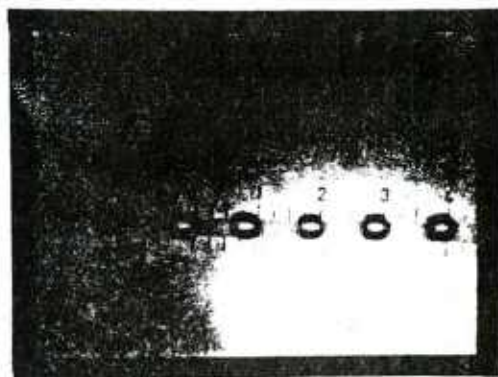
VISUAL MICROSCOPIC DIAMETER = **151  $\mu\text{m}$**



MONODISPERSE CALCULATED DIAMETER = **68  $\mu\text{m}$**   
VISUAL MICROSCOPIC DIAMETER = **74  $\mu\text{m}$**



MONODISPERSE CALCULATED DIAMETER = **59  $\mu\text{m}$**   
VISUAL MICROSCOPIC DIAMETER = **64  $\mu\text{m}$**



MONODISPERSE CALCULATED DIAMETER = **60  $\mu\text{m}$**   
VISUAL MICROSCOPIC DIAMETER = **57  $\mu\text{m}$**



MONODISPERSE CALCULATED DIAMETER = **64  $\mu\text{m}$**   
VISUAL MICROSCOPIC DIAMETER = **72  $\mu\text{m}$**

Figure 10. Examples of microphotographs of the droplet stream from the vibrating orifice monodisperse generator.

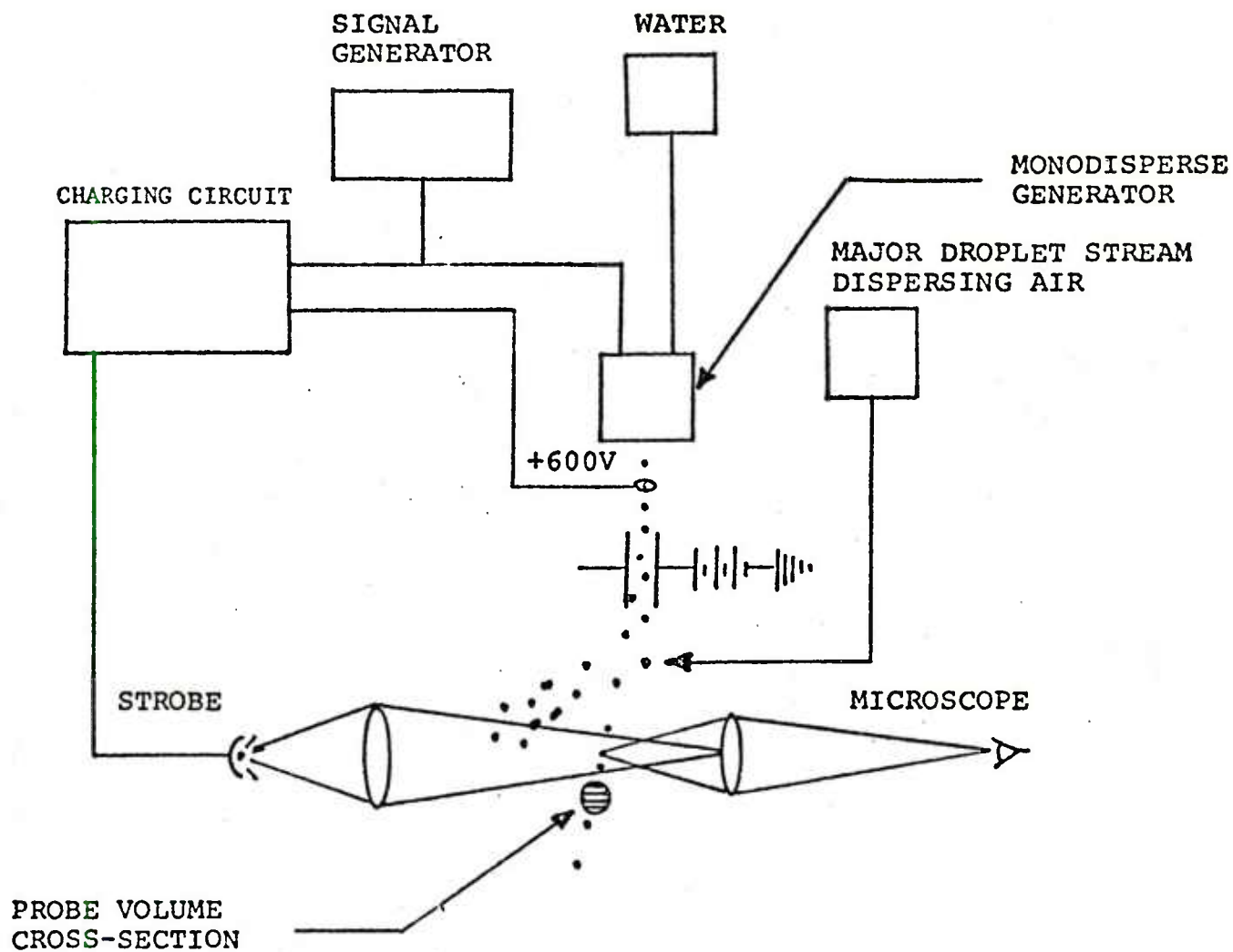
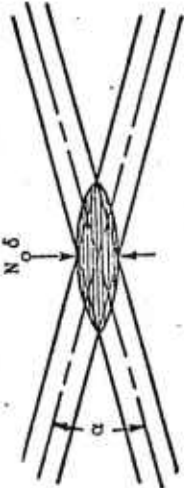
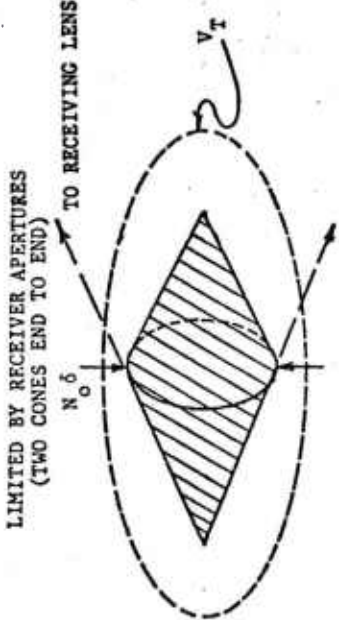
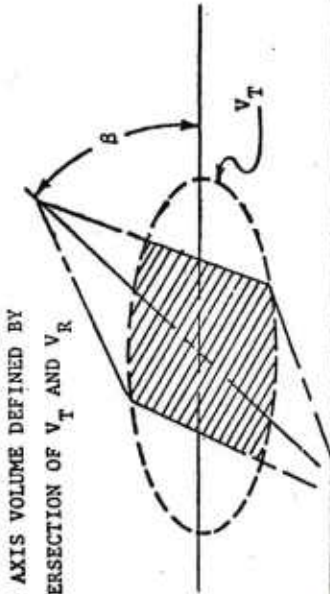


FIGURE 11. MONODISPERSE GENERATOR WITH SYNCHRONIZED PARTICLE SEPARATION AND STROBOSCOPIC MICROSCOPE OBSERVATION.

TABLE IV  
HIRO PROBE VOLUME SUMMARY

PROBE VOLUME GEOMETRY	PROBE VOLUME
<p>LIMITED BY TRANSMITTED BEAMS (ELLIPSOID OF REVOLUTION)</p> 	$V_T = \frac{\pi}{3} N_0^3 \delta^3$
<p>LIMITED BY RECEIVER APERTURES (TWO CONES END TO END)</p> 	$V_R = \frac{\pi}{6} N_0^3 \delta^3$
<p>OFF AXIS VOLUME DEFINED BY INTERSECTION OF <math>V_T</math> AND <math>V_R</math></p> 	$V_O = \frac{16}{3} \frac{N_0^3 \delta^3}{\sin \theta}$

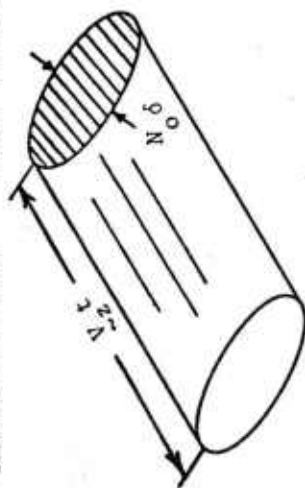
NOTE:  $N_0$  = Number of interference fringes  
included inside the  $\alpha^2$  intensity  
contour

TABLE IV.1  
LORO PROBE VOLUME SUMMARY

PROBE VOLUME

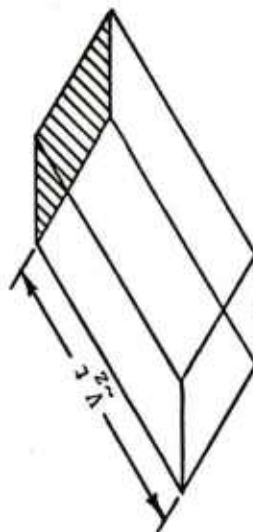
PROBE VOLUME GEOMETRY

TRANSMITTED BEAM CROSS SECTION



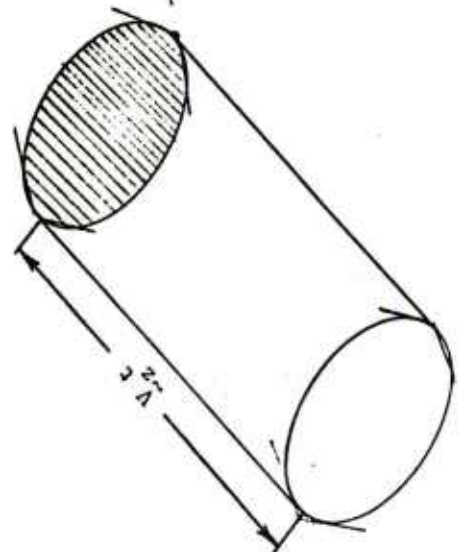
$$V_t = \frac{\pi}{2} \frac{N^2 \delta_o^2}{\alpha} V_t z_t$$

RECEIVER APERTURE  
CROSS-SECTION



$$V_R = V_t \frac{N^2 \delta_o^2}{\alpha} z_r$$

OFF AXIS VOLUME



$$V_o = \frac{\pi}{4} V_t \frac{N^2 \delta_o^2}{\alpha} z_o \sin \beta$$

TABLE IV.2  
DEPTH OF FIELD CALIBRATION

FRAME PERIOD (1-μ)	PARTICLE DIAMETER (μm)	PMT GAIN (VOLTS)	(1)	REQUIRED SIGNAL (2) CYCLES	SIGNAL PROCESSOR THRESHOLD	SCATTER DIRECTION	DEPTH OF FIELD (mm)
100	62	300		9	0	0	48
100	90.8	600		5	0	173.3	9
100	90.7	700		7	0	173.3	14.5
50	90.7	500		8	0	173.3	8
50	90.7	600		8	0	173.3	19
50	69.1	500		5	1.0	90°	2
20	69	500		9	0	173.3	8.5
20	69	600		9	0	173.3	8.5
20	69	500		9	0.6	90°	2
20	69	350		9	1.25	14.7°	10
6	67	500		9	1.0	14.7°	1.0
6	67	500		9	2.5	14.7°	1.0
6	72	500		9	1.5	90°	1.25

1) PMT GAIN =  $8.3 \cdot 10^5 \left( \frac{V}{630} \right)^{6.3}$  (WHERE V = PMT VOLTAGE SETTING)

2) REQUIRED SIGNAL CYCLES = LONG COUNT + PRECOUNT



HIRO volume when signal separation is much less than signal duration and LORO when signal separation is much greater than signal duration.

#### 4.5 Histogram Weighting Factors

A fundamental use of the probe volume calibration is for the estimation of a volume normalized particle size distribution. This is necessary to account for the fact that the size of the probe volume depends on particle scattering cross-section (all other parameters being constant) and the variation in fringe contrast throughout the probe volume.<sup>4</sup>

This concept is straightforward if one imagines a large box containing a broad range of particle sizes. If a scattered light detector with limited sensitivity such as the eye or a lens-phototube arrangement is used at a fixed position to observe the particles, the smaller particles will be detectable over a smaller distance away from the detector than the larger particles. Hence, if a particle size distribution were determined by the detector the smaller particles would be counted in a smaller volume than the larger particles -- the number of small particles would in effect be undersampled by the ratio of volumes in which the particles could be detected. Multiplying the small particle count by this ratio would thus weight the count to correspond to the same volume as the larger particles. It should also be borne in mind that the probe volumes described thus far have been somewhat arbitrary (in the sense that the threshold level of the detector was not specified) for purposes of modeling the function of the instrument.

##### 4.5.1 Fringe Contrast Weighting Factors

The fringe contrast weighting factors account for the possibility that the measured signal visibility may be lower than that predicted on the basis of its particle size relative to a fringe period. This reduction arises because of the incident fringe contrast reduction away from the geometric center of the probe volume (the interfering beams no longer have equal amplitudes). Table IV.3 lists these weighting factors as a function of  $D/\delta$ , and the length of the probe volume,  $m$ , relative to the  $e^{-2}$  length,  $2b_0/\alpha$ , where  $\alpha$  is the angle between the beams. When the length of the sample volume is determined, then these weighting factors should be used for correction up to that length only. For example, suppose the maximum Z axis trajectory which could be observed was 0.2 times the  $e^{-2}$  length. Then no weighting factors would be needed since Table IV.3 shows all weighting factors for all observable trajectories  $0 \leq m \leq 0.2$  are 1, i.e. the histogram bins containing sizes corresponding to low visibilities would be known not to contain particle counts resulting from small particles with low visibilities due to a Z axis trajectory corresponding to  $m=1$ . This case would occur for  $90^\circ$  viewing. On the other hand, if all Z trajectories could be detected and measured then the bins corresponding to low visibilities would be multiplied by the appropriate weighting factor to reduce an incorrect number of counts resulting from point particles passing near  $m=1$  values.

TABLE IV.3  
FRINGE CONTRAST WEIGHTING FACTORS

Z AXIS TRAJECTORY LOCATION (m) (1)	VISIBILITY FOR A POINT PARTICLE WITH CORRESPONDING Z AXIS TRAJECTORY	EQUIVALENT $D/\delta$ VALUE FOR $Z = 0$	HISTOGRAM BIN NUMBER FOR CORRESPONDING VISIBILITY	WEIGHTING FACTORS
0.0	1.0	0.05	1	1
0.1	0.983	0.15	3	1
0.2	0.94	0.25	5	1
0.3	0.871	0.35	7	0.976
0.4	0.785	0.45	9	0.944
0.5	0.689	0.55	11	0.896
0.6	0.591	0.65	13	0.841
0.7	0.495	0.75	15	0.76
0.8	0.407	0.80	16	0.66
0.9	0.326	0.90	18	0.593
1.0	0.259	0.95	19	0.293

1.  $Z = m (2N\delta/\alpha)$



#### 4.5.2 Particle Size Weighting Factors

These weighting factors can be extremely complicated to compute. Experience has shown that reasonable results are obtained using the following approximate results.

##### 4.5.2.1 On Axis Measurements

In this case, the weighting factors are computed for HIRO and LORO conditions using:

$$\text{HIRO: } W_i = W_f G_o^2 D_o^2 / G_i^2 D_i^2 \quad (72)$$

$$\text{LORO: } W_i = W_f G_o^{1/2} D_o^{1/2} / G_i^{1/2} D_i^{1/2} \quad (73)$$

where  $W_i$  is the weighting factor for the  $i$ th histogram bin,  $D_i$  is the largest particle in the  $i$ th histogram increment,  $D_o$  is the largest particle in the "largest resolvable size" histogram bin, and  $G_o$ ,  $G_i$  are the scattering gain function for the  $D_o$ ,  $D_i$  th particle size and  $W_f$  is the fringe contrast weighting factor. These functions may be computed from the equation

$$G_i = J_0^2(\beta' \epsilon) - J_0^2(\beta') + J_1^2(\beta' \epsilon) - J_1^2(\beta') \quad (74)$$

$$\beta' = \pi D_i / \lambda F \quad (75)$$

where  $J_0$ ,  $J_1$  are zeroth and first order Bessel functions of the first kind.  $\epsilon$  is the fraction of the collection aperture radius obscured by a circular beam stop and  $F$  is the receiver F number. Reference 4 provides additional discussion and insight into the computation of the weighting factors and detailed tabulation of  $G_i$  for the PSI system were provided upon system delivery.

##### 4.5.2.2 Off Axis Measurements

The computations in this case (both for Class I and Class II particles) are generally more complicated. In this case, both simple models and a sophisticated Mie scatter program developed at UTSI for this purpose should be used as deemed necessary from calibration measurements with the mono-disperse generator. A discussion of some aspects of this program are described in Appendix IV. In the special case of droplets greater than about 10 micrometers in diameter and observation angles less than  $30^\circ$ ,  $G_i \approx G_o$  for all viewing angles and  $F$  numbers. Equations 72 and 73 apply with  $G_o/G_i = 1$ . Reference 4 provides a general discussion of the theory behind the development of the probe volume as a function of particle size and the resulting weighting factors.

## 4.6 Glass Bead Calibration

Glass beads offer a convenient means for in house calibration tests. Such particles should be understood to be poor measures of system performance because of non-spheristy and inhomogenities. However, these particles can be used as an indication of proper system performance. UTSI uses such calibration beads in 4 size ranges (ranging from roughly 60  $\mu\text{m}$  to several hundred microns) and a device to disperse the beads through the sample volume similar to that shown in figure 12. These may be purchased from Duke Standards Inc. or the Cataphote Corporation. (See the list of references for appropriate addresses.)

## 5.0 DATA SOFTWARE PROGRAMS

Normally the data reduction programs used in the UTSI PSI are recorded on floppy disks and are used to manipulate data recorded in memory. Since program requirements tend to vary with applications, the development of a specialized program for BRL is offered as an option. A program commonly used by UTSI is included in order to illustrate system capability. It uses a 21 bin size histogram and computes numeric and mass probability density functions. It is possible (and has been used in previous research) for forming histograms of up to 100 bins or to distribute the bins logarithmically in size.

### 5.1 Current UTSI Data Reduction Program

In this section, examples of current UTSI PSI software programs and their interpretation are presented. Section 5.3 provides data examples from a program used in a number of obscurant tests. Section 5.3 also shows the results from a program which totals or summarizes data from a number of individual data files.

#### 5.1.1 Interpreting PSI Data Printouts

The following is intended to instruct the reader in interpreting data printouts from the Particle Sizing Interferometer. In examining a data sheet, the reader will observe that the information is presented in eight blocks with a space between each block. The first block of information which begins "Long Fringe Count" specifies the logic parameters which were used to control the signal processor during data acquisition, to specify the size of the sample which was recorded in memory, and to indicate a run number which is also operator generated. The second block contains three lines for operator generated messages which pertain to experimental conditions or instrument parameters not covered in the first block. The third block of data which begins "Data Read From Diskette File ..." contains the following information. The

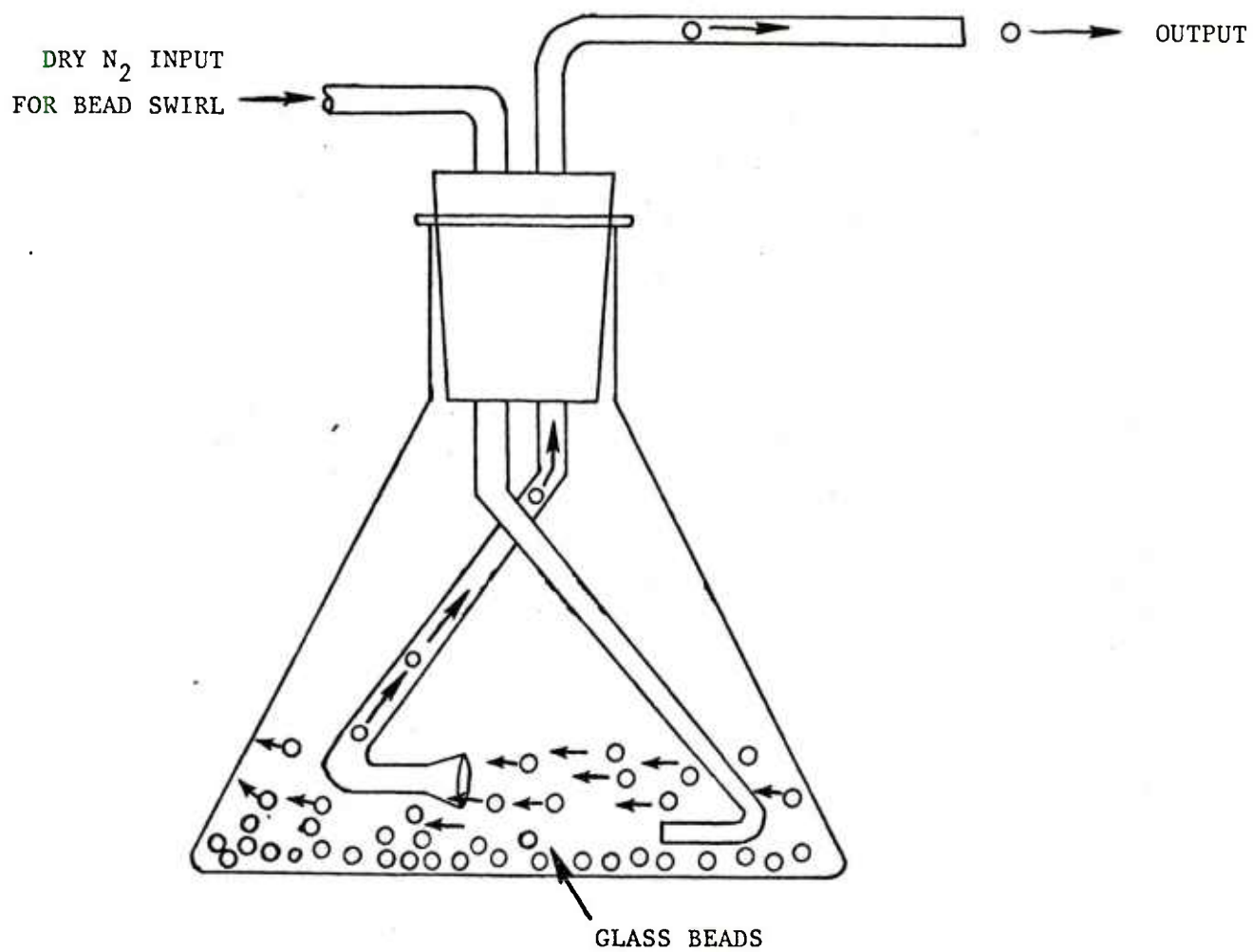


Fig. 12. Method for Glass Bead Dispersal Through PSI Sample Volume.

diskette file number identifies the location of the complete data set recorded on the magnetic disk. The second line provides the mean particle velocity in m/s, the standard deviation in m/s and the turbulence intensity (velocity distribution standard deviation relative to the mean velocity) in percent. The line containing "frequency" gives the mean Doppler frequency from which the mean velocity was computed. "Aperiodicity Accepted" and "aperiodicity Failures" indicate the number of signals in the total sample size which the control logic indicated was either that resulting from a single particle (Aperiodicity Accepted) or those resulting from two or more particles (Aperiodicity Failures). High pass failures indicate the number of signals which had frequencies that were above the high pass filter limit set in block one. Acquisition time is the time in seconds required to obtain the sample size being analyzed. The next line shows IRIG-B time at which the sample acquisition was initiated. The next block indicates the number of measurements which passed tests imposed on the signal in order that it be accepted for a size measurement. The first two parameters indicate the number of particles which generated signals that were beyond the resolution capability of the instrument (either too small or too large). The "Pedestal Under Range" shows the number of signals which were detected but too small to measure. "Ped Amp Saturation" indicates the number of signals which produced scatter magnitudes large enough to drive the system amplifiers into nonlinear operation. "Doppler Under Range" shows the number of signals with Doppler signal components too small for measurement. The next block of data is a summary of the statistical parameters for the measured size distribution. The "Mean Diameter" is the geometric mean diameter. "Sigma G" is the geometric standard deviation and the resulting moments are computed using the generally accepted equations from statistics. The sixth block computes particle number density and aerosol mass concentration using the model described in Appendix II. Inputs required are relative slit width  $Kappa$ , and observed average  $N_L$ . The material density is computed for orthophosphoric acid with relative humidities an input. The seventh block labeled "Visibility Calibration Coefficient" contains the exponents and coefficients for a least squares curve fit correction for input data which has been degraded due to long transmission line losses. For cable lengths less than 50m between processor and interferometer, this correction has not been found necessary. The eighth block is the computed histogram information from the number of measurements indicated in the size accepted statement. The "Bin" column identifies a particular particle size increment with a bin number. The "Diameter" column lists the largest particle diameter associated with a given bin. The "Probability" column lists the accumulative probability as the bin number increases. "WTPOP" lists the weighted population associated with the measurements. The weighted population is the population which is computed to exist for a common volume for the entire particle size range. It is computed in order to accommodate the fact that the sampling volume of the PSI depends on particle size. Hence, large particles may be observed over a larger volume than the smaller particles. The "Weight" column indicates the normalization factors used for each bin increment in order to normalize the measured population to a common volume. The column listed "VIS" indicates the cut point in the visibility function for a particle bin as computed from Equation 8.

The column listed "POP" is the actual measured particle population. The page immediately following this data shows the probability density distribution and is intended only to give the reader some idea of the shape of the distribution. The amplitudes of the probability density plot are relative. The largest amplitude is chosen to fit a convenient scale on the paper. The first column indicates the largest particle size for a given probability density amplitude. The second column gives the accumulated probability density.

## 5.2 DEFINITIONS OF COMPUTED VALUES \*

**ACCEPTANCE RATIO** --- The number of signals accepted for measurement with respect to the number of signals detected which satisfy the counting constraints required for entry into the Histogram Counter.

**ACQUISITION TIME** --- The time which elapsed during data acquisition. Does not include data reduction time.

**APERIODICITY ACCEPTED** --- The number of velocity measurements which passed the aperiodicity test.

**APERIODICITY FAILURES** --- The number of velocity readings which failed the aperiodicity test.

**ARITHMETIC MEAN** --- The arithmetic mean of the particle size distribution.

$$= \frac{1}{N} \sum_{i=1}^n f_i D_i$$

where  $f_i$  = weighted #/bin  
 $D_i$  = largest particle diameter in a bin.  
 $N$  = total weighted bins

**BIN** --- The bin number in a size histogram.

**COEFFICIENT** --- A coefficient of the visibility versus frequency calibration.

**DIAH** --- Particle diameter. The units are micron (i.e., micrometers) if the fringe Period is in microns.

**DOPP** --- The measured mean Doppler component of the signal.

**DOPPLER UNDER RANGE** --- The number of measurements for which the Doppler component of the signal was too small to measure accurately.

**DR** --- The integrator range (0,1,2,3) for the Doppler signal channel, where Range 0 = Time constant of 1E-6, Range 1 = Time constant of 1E-5, Range 2 = Time constant of 1E-4, Range 3 = Time constant of 1E-3.

**DIFF %** --- Numeric frequency of occurrence per unit size interval in percent.



EXP --- The exponent of frequency in a visibility versus frequency calibration.

FIRST MOMENT --- The first moment of the particle size distribution.

$$\mu_1 = \frac{1}{N} \sum_{i=1}^n f_i D_i$$

where  $f_i$ =weighted #/bin  
 $D_i$ =largest particle diameter  
in a bin.  
 $N$ =total weighted bins

FOURTH MOMENT --- The fourth moment of the particle size distribution.

$$\mu_4 = \frac{1}{N} \sum_{i=1}^n f_i D_i^4$$

where  $f_i$ =weighted #/bin  
 $D_i$ =largest particle diameter  
in a bin  
 $N$ =total weighted bins

FREQUENCY --- Doppler signal frequency.

GAMMA --- A dimensionless constant proportional to the Number Density. It is a function of the average number of cycles in a signal and the fringe period.

GEOMETRIC MEAN --- The Geometric mean is defined as:

$$D_g = \exp\left(\frac{1}{N} \sum_{i=1}^n f_i \ln D_i\right)$$

HIGH PASS FAILURES --- The number of measurements whose frequency was less than the high pass filter setting in the parameter list.

KAPPA --- An experimental constant which is the ratio of the x dimension to the y dimension in the probe volume.

$K^{th}$  MOMENT --- 
$$\mu_k = \frac{1}{N} \sum_{i=1}^n f_i D_i^k$$

LCC --- The long clock count. An integer between 1 and 65535.

Z MASS --- Mass frequency of occurrence per unit size interval.

$$= \frac{f_i D_i^3}{\sum f_i D_i^3}$$

where  $f_i$ =weighted #/bin  
 $D_i$ =largest particle  
diameter in a bin



MASS CONCENTRATION --- Aerosol mass contained in a unit volume of aerosol.

MASS MEAN --- Ratio of the Fourth to the Third Moment in the particle size distribution.

MATERIAL DENSITY --- Mass per unit volume of a material.

MEAN VELOCITY --- The mean particle velocity.

NUMBER DENSITY --- Number of aerosol particles per unit volume

$$= \left( \frac{2\pi\Gamma}{NL^2\delta} \right)^3 \quad \text{where } NL = \text{long count} + \text{precount} + 2$$

$\delta = \text{delta} = \text{fringe period}$

OVT --- The timer over-range counter. This is a software counter and is in error if the hardware timer overflowed more than once between two successive data readings.

PED --- The measured mean pedestal component of the signal.

PEDESTAL UNDER RANGE --- The number of readings for which the pedestal component of the signal was too small to measure accurately.

POP --- The population (i.e., the number of counts) in a bin of the particle size histogram.

PR --- The integrator range (0,1,2,3) for the pedestal signal channel.

PROBABILITY --- The cumulative probability corresponding to the  $i^{\text{th}}$  consecutive bin beginning from the smallest particle size bin.

RUN NUMBER --- The number used by the operator to identify a data set.

SCC --- The short clock count.

SECOND MOMENT --- The second moment of the particle size distribution.

$$\mu_2 = \frac{1}{N} \sum_{i=1}^n f_i D_i^2$$

SIGMA --- The standard deviation of a measurement (i.e., the square root of the variance).

SIGMA G --- The standard deviation of the geometric mean of the particle size distribution.

$$\sigma_g = \exp \left\{ \left( \frac{f_i \ln^2 (D_i / D_g)}{N} \right)^{\frac{1}{2}} \right\}$$

SIZE --- Particle diameter measured in the units in which the fringe period is expressed.

SIZE ACCEPTED --- The number of measurements which passed all tests applied to the size data.

THIRD MOMENT --- The third moment of the particle size distribution.

$$\mu_3 = \frac{1}{N} \sum_{i=1}^n f_i D_i^3$$

TIME --- Time in seconds measured from that time at which the operator struck the space bar to take data.

TIME AVERAGED MOMENTS AND MASS CONCENTRATION --- Time averages of the ensemble of the measurements entered into the computations.

TIME AVERAGED MASS CONCENTRATION ---

$$= \frac{\sum_{\beta=1}^n \frac{m_{\beta} \Delta t_{\beta}}{n}}{\sum_{\beta=1}^n \Delta t_{\beta}}$$

TIME AVERAGED MOMENTS ---

$$\frac{\sum_{\beta=1}^n \mu_{k\beta} \Delta t_{\beta}}{\sum_{\beta=1}^n \Delta t_{\beta}}$$

where  $\mu_k = k^{\text{th}}$  moment

$m_{\beta}$  = mass concentration/trial

$\Delta t$  = acquisition time/trial

TOTALIZED HISTOGRAM --- Ensemble average of all histograms entered into computations.

VEL --- Measured particle velocity.

VIS --- Measured particle visibility.

VISIBILITY CALIBRATION CONSTANTS --- The coefficients and corresponding exponents in a visibility versus frequency calibration.

VOLUME/AREA MEAN --- Mean particle of the volume to area ratio.

$$= \frac{\mu_3}{\mu_2}$$

VOLUMETRIC MEAN --- Mean particle volume.

$$= \sqrt[3]{\mu_3}$$

WEIGHT --- The weighting factor for a bin in the particle size histogram.

WTPOP --- The weighted population (i.e., measured population times the weighting factor) of a bin in the particle size histogram acquisition. Does not include data reduction time.

\* NOTE: Some of these values are available on a total data printout which is not present in the data example summaries.

### 5.3 PSI Data Examples

# UTSI GAS DIAGNOSTICS DIVISION

LONG FRINGE COUNT 12  
 SHORT FRINGE COUNT 9  
 PRECOUNT 3  
 CLOCK FREQUENCY 70.00 MHZ  
 HIGH PASS FILTER .2000 MHZ  
 FRINGE PERIOD 6.000  
 MAXIMUM APERIODICITY 1.0000 %  
 DC OFFSET 4.900 VOLTS  
 DC OFFSET 4.900 PED ADJUST OFFSET 42.0  
 TIMER RATE 1000.0 HZ IRIG CLOCK ON  
 SYSTEM VOLTAGE GAIN 40.0 HISTOGRAM NOT PRINTED  
 SAMPLE SIZE 3000  
 RUN NUMBER 1  
 PARTICLE SIZING MODE  
 AUGUST 16, 1980 DATA FROM PSI #2 ON PAD  
 TRIAL #25 XM825 WP  
 SMOKE WEEK III EGLIN AFB  
 FMT=600 SLIT=100 LPF=2.0MHZ ZCD=3.7

DATA READ FROM DISKETTE FILE TRIAL25 1

MEAN VELOCITY= 2.672 SIGMA= .4670 = 17. %

FREQUENCY = .4453 MHZ

APERIODICITY ACCEPTED = 1320 = 44.0 %

APERIODICITY FAILURES = 1680 = 56.0 %

HIGH PASS FAILURES = 0 = 0.00 %

ACQUISITION TIME = 95.14

HOURS = 21 MINUTES = 46 SECONDS = 3

SIZE ACCEPTED = 828 = 27.6 %

VISIBILITY TOO SMALL = 3 = .100 %

VISIBILITY TOO BIG = 43 = 1.43 %

PEDESTAL UNDER RANGE = 425 = 14.2 %

DOPPLER UNDER RANGE = 67 = 2.23 %

GEOMETRIC MEAN = .593

SIGMA G = 1.98

FIRST MOMENT = 1.09

SECOND MOMENT = 2.95

THIRD MOMENT = 10.6

FOURTH MOMENT = 42.0

ARITHMETIC MEAN = 1.09

VOLUME/AREA MEAN = 3.60

VOLUMETRIC MEAN = 2.20

MASS MEAN = .3.95

GAMMA = 1.54 ACCEPTANCE RATIO = .440 KAPPA = .360

NUMBER DENSITY (N/CC) = 1.228E+05 MATERIAL DENSITY = 1.45

MASS CONCENTRATION (GM/CUBIC METER) = .991 WHEN NL = 18

ALPHA EXTINCTION = .6113 SIGMA BAR = 4.931

VISIBILITY CALIBRATION CONSTANTS

EXP = 0 COEFFICIENT = 8.77333E-01

EXP = 1 COEFFICIENT = 3.47290E-01

EXP = 2 COEFFICIENT = -5.79147E-01

RUN NUMBER= 1  
AUGUST 16, 1980 DATA FROM PSI #2 ON PAD  
TRIAL #25 XM825 WP  
SMOKE WEEK III EGLIN AFB  
PMT=600 SLIT=100 LPF=2.0MHZ ZCD=3.7

# NUMBER DISTRIBUTION

BIN	DIAM	DIFF %	PROBABILITY	WTPOP	WEIGHT	VIS	POP
1	.30	.646	.646	2.002E+03	45.5	.997	44
2	.60	5.873E-02	.705	182.	45.5	.988	4
3	.90	2.033E-02	.725	63.0	12.6	.972	5
4	1.20	1.569E-02	.741	48.6	6.08	.951	8
5	1.50	1.775E-02	.758	55.0	3.93	.925	14
6	1.80	1.355E-02	.772	42.0	2.80	.893	15
7	2.10	1.897E-02	.791	58.8	2.10	.856	28
8	2.40	2.502E-02	.816	77.5	1.65	.815	47
9	2.70	2.465E-02	.841	76.4	1.34	.770	57
10	3.00	3.331E-02	.874	103.	1.11	.722	93
11	3.30	2.420E-02	.898	75.0	1.000	.670	75
12	3.60	2.689E-02	.925	83.3	.896	.617	93
13	3.90	2.804E-02	.953	86.9	.790	.562	110
14	4.20	1.999E-02	.973	62.0	.765	.506	81
15	4.50	1.047E-02	.984	32.4	.676	.449	48
16	4.80	6.165E-03	.990	19.1	.579	.393	33
17	5.10	4.654E-03	.994	14.4	.577	.337	25
18	5.40	2.741E-03	.997	8.50	.531	.283	16
19	5.70	1.850E-03	.999	5.73	.273	.231	21
20	6.00	7.305E-04	1.000	2.26	.283	.181	8
21	6.30	2.836E-04	1.000	.879	.293	0.00	3

# MASS DISTRIBUTION

BIN	DIAM	% MASS	PROBABILITY	WTPOP	WEIGHT	VIS	POP
1	.30	1.639E-03	1.639E-03	2.002E+03	45.5	.997	44
2	.60	1.192E-03	2.831E-03	182.	45.5	.988	4
3	.90	1.393E-03	4.223E-03	63.0	12.6	.972	5
4	1.20	2.548E-03	6.772E-03	48.6	6.08	.951	8
5	1.50	5.630E-03	1.240E-02	55.0	3.93	.925	14
6	1.80	7.427E-03	1.983E-02	42.0	2.80	.893	15
7	2.10	1.651E-02	3.634E-02	58.8	2.10	.856	28
8	2.40	3.250E-02	6.884E-02	77.5	1.65	.815	47
9	2.70	4.558E-02	.114	76.4	1.34	.770	57
10	3.00	8.451E-02	.199	103.	1.11	.722	93
11	3.30	8.172E-02	.281	75.0	1.000	.670	75
12	3.60	.118	.399	83.3	.896	.617	93
13	3.90	.156	.555	86.9	.790	.562	110
14	4.20	.139	.694	62.0	.765	.506	81
15	4.50	8.965E-02	.784	32.4	.676	.449	48
16	4.80	6.407E-02	.848	19.1	.579	.393	33
17	5.10	5.802E-02	.906	14.4	.577	.337	25
18	5.40	4.056E-02	.946	8.50	.531	.283	16
19	5.70	3.219E-02	.979	5.73	.273	.231	21
20	6.00	1.483E-02	.993	2.26	.283	.181	8
21	6.30	6.664E-03	1.000	.879	.293	0.00	3

RUN NUMBER= 1  
 AUGUST 16, 1980 DATA FROM PSI #2 ON PAD  
 TRIAL #25 XM825 WP  
 SMOKE WEEK III EGLIN AFB  
 PMT=600 SLIT=100 LPF=2.0MHZ ZCD=3.7

=====

NUMERIC SIZE DISTRIBUTION

.300	.646	X*****
.600	5.873E-02	X****
.900	2.033E-02	X*
1.20	1.569E-02	X*
1.50	1.775E-02	X*
1.80	1.355E-02	X*
2.10	1.897E-02	X*
2.40	2.502E-02	X*
2.70	2.465E-02	X*
3.00	3.331E-02	X**
3.30	2.420E-02	X*
3.60	2.689E-02	X**
3.90	2.804E-02	X**
4.20	1.999E-02	X*
4.50	1.047E-02	X
4.80	6.165E-03	X
5.10	4.654E-03	X
5.40	2.741E-03	X
5.70	1.850E-03	X
6.00	7.305E-04	X
6.30	2.836E-04	X

=====

MASS DISTRIBUTION

.300	1.639E-03	X
.600	1.192E-03	X
.900	1.393E-03	X
1.20	2.548E-03	X
1.50	5.630E-03	X*
1.80	7.427E-03	X**
2.10	1.651E-02	X*****
2.40	3.250E-02	X*****
2.70	4.558E-02	X*****
3.00	8.451E-02	X*****
3.30	8.172E-02	X*****
3.60	.118	X*****
3.90	.156	X*****
4.20	.139	X*****
4.50	8.965E-02	X*****
4.80	6.407E-02	X*****
5.10	5.802E-02	X*****
5.40	4.056E-02	X*****
5.70	3.219E-02	X*****
6.00	1.483E-02	X****
6.30	6.664E-03	X**

=====



=====

T O T A L E D   D I S T R I B U T I O N   H I S T O G R A M S

=====

RUN NUMBERS FOR TOTALED HISTOGRAM

2   3   4   5   6

AUGUST 16, 1980   DATA FROM PSI #2 ON PAD

TRIAL #24   5" ZUNI WP

SMOKE WEEK III   EGLIN AFB

PMT=600   SLIT=100   LPF=2.0MHZ   ZCD=3.7

TOTAL SAMPLE SIZE = 6154  
APERIODICITY ACCEPTED = 3525  
TOTAL ACQUISITION TIME = 226.0  
TOTAL SIZE ACCEPTED = 2903

GEOMETRIC MEAN = .387

FIRST MOMENT = .555

THIRD MOMENT = 2.82

SIGMA G = 1.59

SECOND MOMENT = .912

FOURTH MOMENT = 10.4

ARITHMETIC MEAN = .555

VOLUME/AREA MEAN = 3.10

VOLUMETRIC MEAN = 1.41

MASS MEAN = 3.69

GAMMA = .937   ACCEPTANCE RATIO = .573   KAPPA = .360

NUMBER DENSITY (N/CC) = 2.777E+04   MATERIAL DENSITY = 1.43

MASS CONCENTRATION (GM/CUBIC METER) = 5.864E-02 WHEN NL = 18

ALPHA EXTINCTION = .6262   SIGMA BAR = 1.322

VISIBILITY CALIBRATION CONSTANTS

EXP = 0   COEFFICIENT = 8.77333E-01

EXP = 1   COEFFICIENT = 3.47290E-01

EXP = 2   COEFFICIENT = -5.79147E-01

=====

\*\*TIME AVERAGED STATISTICS\*\*

=====

GEOMETRIC MEAN = .389

FIRST MOMENT = .559

THIRD MOMENT = 2.84

SIGMA G = 1.59

SECOND MOMENT = .920

FOURTH MOMENT = 10.5

ARITHMETIC MEAN = .559

VOLUME/AREA MEAN = 3.09

VOLUMETRIC MEAN = 1.42

MASS MEAN = 3.69

MASS CONCENTRATION (GM/CUBIC METER) = .108   WHEN NL = 18

ALPHA EXTINCTION COEFF.   SIGMA BAR  
.631135   1.33207

# RUN NUMBERS FOR TOTALED HISTOGRAM

2 3 4 5 6  
AUGUST 16, 1980 DATA FROM PSI #2 ON PAD  
TRIAL #24 5" ZUNI WP  
SMOKE WEEK III EGLIN AFB  
PMT=600 SLIT=100 LFF=2.0MHZ ZCD=3.7

## NUMBER DISTRIBUTION

BIN	DIAM	DIFF %	PROBABILITY	WTPOP	WEIGHT	VIS	POP
1	.30	.844	.844	2.621E+04	45.5	.997	576
2	.60	3.955E-02	.883	1.228E+03	45.5	.988	27
3	.90	1.663E-02	.900	517.	12.6	.972	41
4	1.20	1.155E-02	.912	359.	6.08	.951	59
5	1.50	1.240E-02	.924	385.	3.93	.925	98
6	1.80	8.745E-03	.933	272.	2.80	.893	97
7	2.10	8.993E-03	.942	279.	2.10	.856	133
8	2.40	9.403E-03	.951	292.	1.65	.815	177
9	2.70	8.284E-03	.959	257.	1.34	.770	192
10	3.00	7.684E-03	.967	239.	1.11	.722	215
11	3.30	7.856E-03	.975	244.	1.000	.670	244
12	3.60	7.616E-03	.983	237.	.896	.617	264
13	3.90	6.512E-03	.989	202.	.790	.562	256
14	4.20	4.508E-03	.994	140.	.765	.506	183
15	4.50	3.025E-03	.997	94.0	.676	.449	139
16	4.80	1.622E-03	.998	50.4	.579	.393	87
17	5.10	1.003E-03	.999	31.2	.577	.337	54
18	5.40	4.958E-04	1.000	15.4	.531	.283	29
19	5.70	1.406E-04	1.000	4.37	.273	.231	16
20	6.00	8.201E-05	1.000	2.55	.283	.181	9
21	6.30	5.660E-05	1.000	1.76	.293	0.00	6

## MASS DISTRIBUTION

BIN	DIAM	% MASS	PROBABILITY	WTPOP	WEIGHT	VIS	POP
1	.30	8.073E-03	8.073E-03	2.621E+04	45.5	.997	576
2	.60	3.028E-03	1.110E-02	1.228E+03	45.5	.988	27
3	.90	4.297E-03	1.540E-02	517.	12.6	.972	41
4	1.20	7.072E-03	2.247E-02	359.	6.08	.951	59
5	1.50	1.483E-02	3.730E-02	385.	3.93	.925	98
6	1.80	1.807E-02	5.537E-02	272.	2.80	.893	97
7	2.10	2.951E-02	8.488E-02	279.	2.10	.856	133
8	2.40	4.606E-02	.131	292.	1.65	.815	177
9	2.70	5.778E-02	.189	257.	1.34	.770	192
10	3.00	7.352E-02	.262	239.	1.11	.722	215
11	3.30	.100	.362	244.	1.000	.670	244
12	3.60	.126	.488	237.	.896	.617	264
13	3.90	.137	.625	202.	.790	.562	256
14	4.20	.118	.743	140.	.765	.506	183
15	4.50	9.769E-02	.841	94.0	.676	.449	139
16	4.80	6.356E-02	.905	50.4	.579	.393	87
17	5.10	4.716E-02	.952	31.2	.577	.337	54
18	5.40	2.767E-02	.979	15.4	.531	.283	29
19	5.70	9.229E-03	.989	4.37	.273	.231	16
20	6.00	6.277E-03	.995	2.55	.283	.181	9
21	6.30	5.015E-03	1.000	1.76	.293	0.00	6

# RUN NUMBERS FOR TOTALED HISTOGRAM

2 3 4 5 6  
AUGUST 16, 1980 DATA FROM PSI #2 ON PAD  
TRIAL #24 5" ZUNI WP  
SMOKE WEEK III EGLIN AFB  
PMT=600 SLIT=100 LPF=2.0MHZ ZCD=3.7

## NUMERIC SIZE DISTRIBUTION

.300	.844	X*****
.600	3.955E-02	X**
.900	1.663E-02	X
1.20	1.155E-02	X
1.50	1.240E-02	X
1.80	8.745E-03	X
2.10	8.993E-03	X
2.40	9.403E-03	X
2.70	8.284E-03	X
3.00	7.684E-03	X
3.30	7.856E-03	X
3.60	7.616E-03	X
3.90	6.512E-03	X
4.20	4.508E-03	X
4.50	3.025E-03	X
4.80	1.622E-03	X
5.10	1.003E-03	X
5.40	4.958E-04	X
5.70	1.406E-04	X
6.00	8.201E-05	X
6.30	5.660E-05	X

## MASS DISTRIBUTION

.300	8.073E-03	X**
.600	3.028E-03	X*
.900	4.297E-03	X*
1.20	7.072E-03	X**
1.50	1.483E-02	X*****
1.80	1.807E-02	X*****
2.10	2.951E-02	X*****
2.40	4.606E-02	X*****
2.70	5.778E-02	X*****
3.00	7.352E-02	X*****
3.30	.100	X*****
3.60	.126	X*****
3.90	.137	X*****
4.20	.118	X*****
4.50	9.769E-02	X*****
4.80	6.356E-02	X*****
5.10	4.716E-02	X*****
5.40	2.767E-02	X*****
5.70	9.229E-03	X***
6.00	6.277E-03	X**
6.30	5.015E-03	X*

## REFERENCES

1. Cadle, R. D. Particle Size Determination, Interscience Publishers, Inc. New York, pp. 39-56 (1955).
2. Kerker, M. "The Scattering Light and Other Electromagnetic Radiation" Academic Press, (1969).
3. "BRL PSI Electronic Operations Manual" U. T. Space Institute No. 80-4.
4. Farmer, W. M. "Sample Space for Particle Size and Velocity Measuring Interferometers" Applied Optics, Vol. 15, p. 1984, August (1976).
5. Farmer, W. M. "Measurement of Particle Size, Number Density, and Velocity Using a Laser Interferometer" Appl. Opt. 11, 1603, (1972).

Cataphote Corporation, Microbeads Division, Jackson, Mississippi, 39205.

Duke Standards Company, 445 Sherman Avenue, Palo Alto, California, 94306.

## APPENDIX I

A SIMPLE MODEL FOR THE VISIBILITY OF LARGE  
SPHERES OBSERVED WITH A LASER VELOCIMETER

W. M. Farmer  
The University of Tennessee Space Institute  
Gas Diagnostics Research Division  
Tullahoma, Tennessee

ABSTRACT

A model is developed to express the signal visibility for large refracting or reflecting spheres observed with a fringe type laser velocimeter. The model yields a closed form solution for the visibility when scattering is observed off axis in the near forward,  $90^\circ$ , or near backward direction. Results show that particle size range can be adjusted by aperture adjustments at the scattered light receiver. Comparison of model predictions with recently published numerical computations shows good agreement.

INTRODUCTION

Considerable effort has been given to the measurement of particle size using the optical system of differential Doppler laser velocimeters (see for example references 1-7). Three basic approaches to this problem can be identified: 1) correlation of particle velocity with aerodynamic particle diameter in a known velocity field,<sup>1</sup> 2) correlation of scattered irradiance with particle diameter,<sup>2</sup> and 3) correlation of signal visibility or contrast with particle diameter.<sup>3-7</sup> Much of the research involving the

latter method has been concerned with particle diameters comparable to the wavelength illuminating it. An approximate model which relates particle diameter to signal visibility appears to correlate experimental data with theoretical predictions surprisingly well when the constraints imposed by the model are carefully followed.<sup>8</sup> This model requires that the scattered light be observed with a large receiver aperture centered on the symmetry axis of the transmitting optical system. Measurement of spherical particles with this model requires that the particle diameter be less than an illuminating fringe period if unambiguous measurements are to be obtained. Early research with particles much greater than a wavelength in diameter showed that receiver alignment was very critical if agreement with the approximate model was to be obtained.<sup>4</sup> It was also found that when the particle diameter was greater than a fringe period and the scattered light observed at some angle off the axis of symmetry, the measured visibility was usually much higher than predicted by the approximate model. Thus it was concluded that a visibility measurement could not be used for particle diameter estimates.<sup>2</sup> However recently published calculations have shown this conclusion to be incorrect.<sup>9</sup> Bachalo has shown that for particles much greater than a wavelength in diameter and at viewing angles where the reflected or refracted component of the scattered light is greater than the diffracted component, particle diameter can be related to a visibility function which is monotonic over a significant size range. This work shows that the visibility function is monotonic when particle diameter is greater than a fringe period and that the visibility function depends on the receiving optics F number, particle index-of-refraction, and viewing angle. The analysis performed by Bachalo consisted of numerical integrations of the



classical electromagnetic field equations describing refraction and reflection by homogeneous spheres illuminated by plane waves. As such, this work is acceptably rigorous. However, because of the approach taken and the numerical integration, it is difficult to discern or physically visualize the scaling laws which relate visibility to particle index-of-refraction, receiver F number or viewing angle. The purpose of this paper is to develop a simple model which elucidates the results obtained by Bachalo and yields simple scaling laws which can be used to configure optical systems for measuring a broad range of particle sizes for a fixed fringe period.

#### SCATTERED IRRADIANCE APPROXIMATION FOR REFRACTING OR REFLECTING SPHERES ILLUMINATED BY TWO COHERENT BEAMS.

A classical approximation for the electric fields scattered by a large (relative to the wavelength) homogeneous sphere involves separating the scattered field  $E_s$ , into three contributions

$$E_s = E_D + E_t + E_R \quad (1)$$

where  $E_D$  is the field component due to diffraction,  $E_t$  is that due to refraction and  $E_R$  is that due to reflection.<sup>10</sup> Hodgkinson's work can be manipulated to show that the mean value of  $E_t$  will be the predominant field component in the forward scatter direction (rather than diffraction) when the scatter angle,  $\beta$  is such that:

$$\beta \geq \left( \frac{\lambda}{4\pi^2 D} \right)^{1/3} \left( \frac{m+1}{m} \right) \quad (2)$$

where  $\lambda$  is the illuminating wavelength,  $D$  is the particle diameter and  $m$  is the index of refraction (assumed real). For the near axis backscatter the reflected field is predominant when

$$\beta \ll \gamma \quad (3)$$

where  $\gamma$  is the rainbow angles and  $n$ th order refraction in the back direction is ignored.

For this analysis the geometry shown in figure 1 will be assumed. The centerlines of two coherent beams cross at the center of an XYZ coordinate system. The beam centerlines are separated by an angle  $\alpha$ . The Z axis is parallel to the bisector between the beams. Y is perpendicular to Z and lies in the plane of the beam centerlines and X is perpendicular to YZ. A scattered light collection aperture is centered at some viewing angle  $\beta$  and subtends a collection angle defined by the F number of the receiver. Into this coordinate system a large homogeneous sphere of radius  $r_s$  is placed at some position  $X = 0$ , Y and Z = 0 as shown in figure 2. The sphere in the limit  $D \gg \lambda$  may be imagined to function as a spherical lens. Those rays having angles of incidence near zero will be predominantly refracted by two refractions (ray entrance and ray exit). These rays will appear to focus at some distance,  $f$ , from the center of the sphere. For angles of incidence less than about  $20^\circ$ ,  $f$  is nearly independent of the angle of incidence. Differences in reflection due to different values

of the Fresnel reflection coefficients are also minimal. Rays contained within this angle of incidence will all appear to diverge from  $f$  and form a spherical wave with radius of curvature measured from  $f$ . As the angle of incidence increases  $f$  is reduced and spherical aberration becomes significant. Furthermore rays undergoing more than two refractions may be observed. It will be assumed that the refracted light observations are made with an observation aperture and observation angle which is small enough to preclude these effects thus allowing  $f$  to be uniquely specified. Experimentally these assumptions are found not to be too restrictive. Consider figure 3a which is a photograph of a 114 micrometre diameter crown glass (index of refraction  $\sim 1.5$ ) sphere illuminated by two coherent beams. The central portion of the sphere images the interference fringes produced by the incident beams. A large portion of the sphere cross-section is shadowed indicating that rays refracted by this portion of the sphere did not pass through the  $F/2$  camera lens used to obtain the photograph. If it is assumed that rays reaching the photograph are only twice refracted by the sphere, then a ray trace for this geometry will show that the angle of incidence could not have been more than about  $21^\circ$ , which is sufficiently small for the approximations to be used here. With these assumptions it is clear that if two angularly separated plane waves illuminate the sphere, two focus points will be obtained. These foci produce two spherical waves which produce nonlocalized interference fringes. The fringe contours are identical in shape to those observed in Young's experiment using two circular point sources. As is well known, the fringe contours are hyperboles and are beautifully illustrated in figure 5 of Bachalo's work. Figure 3b

shows the resulting fringe contours for the sphere shown in figure 3a. The model to be used in this analysis contains assumptions radically different from those made originally for a visibility analysis where diffraction is predominant.<sup>3</sup> In that analysis it was assumed that the spherical waves scattered by the particle illuminated by two beams have a common center. In the case where scatter is predominantly from the edge of the particle and the angle between the illuminating beams is small this is a reasonable assumption. When refraction or reflection is the dominant mechanism through which light reaches the collecting aperture, this model shows that such an assumption is no longer valid.

With the assumption that only twice refracted light reaches the collecting aperture, the electric fields originating from the refracted foci may be written by assuming spherical waves and the geometry shown in figure 2. These fields are

$$E_{t1} = \frac{E_{01}}{r_1} \exp(i(k_{t1}r_1 - \omega_{t1}t)) \quad (4)$$

$$E_{t2} = \frac{E_{02}}{r_2} \exp(i(K_{t2}r_2 - \omega_{t2}t)) \quad (5)$$

where the  $E_{oi}$  ( $i=1,2$ ) are the incident field amplitudes for beams 1 and 2.

$K_{ti}$  are the wave vector magnitudes

$$K_{ti} = 2\pi/\lambda_i \quad (6)$$

and  $\omega_{ti}$  are the Doppler shifted optical frequencies given by:

$$\omega_{t1} = \omega_o + \vec{V} \cdot (\vec{K}_{t1} - \vec{K}_{o1}) \quad (7)$$

$$\omega_{t2} = \omega_o + \vec{V} \cdot (\vec{K}_{t2} - \vec{K}_{o2}) \quad (8)$$

$\vec{V}$  is the particle velocity.  $\vec{K}_{oi}$  is the incident wave vector for the  $i$ th beam. It will be assumed that the receiver aperture is small enough to approximate  $\vec{K}_{ti}$  as  $\vec{K}_o$ . The geometry in figure 2 shows that  $r_1$  and  $r_2$  can be written as

$$r_1^2 = r_o^2 + (X_o + X')^2 + (Y_o + Y' + \Delta/2)^2 \quad (9)$$

$$r_2^2 = r_o^2 + (X_o + X')^2 + (Y_o + Y' - \Delta/2)^2 \quad (10)$$

where the  $X'$ ,  $Y'$  coordinate system is centered in the scattered light collection aperture. The coordinates of a point in a circular aperture coordinate system are given by

$$X' = \rho \sin \theta \quad (11)$$

$$Y' = \rho \cos \theta \quad (12)$$

The total field at the aperture point defined by  $r_1$  and  $r_2$  is

$$E_t = E_{t1} + E_{t2} \quad (13)$$

The irradiance resulting from  $E_t$  is approximately given by

$$I_t = \frac{c}{8\pi Z'} |E_t|^2 \quad (14)$$

where  $Z'$  is the impedance of the medium in which the observations are made and  $c$  is the speed of light in vacuum. Using equation 13 in equation 14 results in the well known form for the scattered irradiance from two coherent beams.

$$I_t = \frac{c}{8\pi Z} \{ |E_{t1}|^2 + |E_{t2}|^2 + 2\text{Re}(E_{t1}E_{t2}^*) \} \quad (15)$$

For simplicity assume that  $E_{01} = E_{02} = E_o$ .  $|E_{t1}|^2$  and  $|E_{t2}|^2$  are thus constants and

$$|E_{t1}|^2 = |E_{t2}|^2 = |E_t|^2 \quad (16)$$

$$|E_t|^2 = |E_o|^2 / r_o^2 \quad (17)$$

The last term in brackets in equation 15 is the so called interference term. Use of equations 4, 5, 7 and 8 allows the interference term to be written as

$$2\text{Re}(E_{t1}E_{t2}^*) = \frac{2|E_o|^2}{r_1 r_2} \cos(K_t(r_1 - r_2) + \vec{v} \cdot ((\vec{K}_{t2} - \vec{K}_{t1} + (\vec{K}_{02} - \vec{K}_{01}))) \quad (18)$$

to obtain  $r_1 - r_2$  use is made of equations 9 and 10 to compute



$$r_1^2 - r_2^2 = 2(Y_0 + \rho \cos \theta) \Delta \quad (19)$$

for the case when  $r_1, r_2 \gg \Delta$  and  $r_1 \approx r_2 = r_0 [1 + \frac{1}{2} \tan^2 \beta]$   
equation 19 reduces to

$$r_1 - r_2 \approx \frac{\Delta(Y_0 + \rho \cos \theta)}{r_0 [1 + \frac{1}{2} \tan^2 \beta]} \quad (20)$$

where  $\tan^2 \beta = (X_0^2 + Y_0^2)/r_0^2$  arises from the second order terms in the Taylor's series expansion of  $r_1$  and  $r_2$ . It is important to note that since spherical waves are assumed to originate from point sources in the X,Y co-ordinate system any results involving  $r_1, r_2$  are invariant to simple rotation about the Y axis ( $\beta > 0, X_0 = 0$ ). This means that if  $X', Y'$  is kept perpendicular to  $r'_0$  and the origin of  $X', Y'$  kept in the  $X_0, Y_0$  plane, then the only angular dependence on  $\beta$  should arise from a lengthening of  $r'_0$  as  $\beta$  increases. The  $(1 + \frac{1}{2} \tan^2 \beta)$  factor accounts for this increase. Hence, no angular correction is necessary to account for aperture ellipticity as might be expected if the  $X', Y'$  plane were held in the  $X_0, Y_0$  plane. It is straightforward to show that the terms in equation 18 resulting from the Doppler shift can be written as

$$\vec{v} \cdot (\vec{k}_{t1} - \vec{k}_{t2}) = v_y k_o \Delta/R \quad (21)$$

$$\vec{v} \cdot (\vec{k}_{o2} - \vec{k}_{o1}) = v_y k_o 2\sin(\alpha/2) \quad (22)$$

R is the distance from the particle centered coordinate system to a point of interest in the aperture. In previous calculations the term expressed by equation 21 was neglected on the basis that  $\vec{v} \cdot (\vec{k}_{t1} - \vec{k}_{t2})$  was proportional to  $\Delta\lambda/\lambda$  where  $\Delta\lambda$  is the difference in optical wavelengths resulting from the Doppler shift.  $\Delta\lambda/\lambda$  is of the order of  $10^{-6}$  or less in nearly all cases of interest and hence can be reasonably neglected. In most cases  $\Delta/R$  is also small although cases can be envisioned where it might be significant. This analysis will assume that this term is negligible. Equations 20 and 22 result in the interference term being written as

$$2\text{Re}(E_{t1} E_{t2}^*) = \frac{2|E_o|^2}{r_o^2} \cos(k_t \frac{\Delta(Y + \rho \cos\theta)}{r_o [1 + \frac{1}{2} \tan^2 \beta]} + 2\pi Y/\delta) \quad (23)$$

$$\delta = \lambda/2\sin(\alpha/2) \quad (24)$$

$$Y = v_y t \quad (25)$$

$\delta$  is the fringe period generated by the beams striking the particle.

#### IRRADIANCE COLLECTED BY A CIRCULAR APERTURE

The photodetector used to detect light scattered by the particle is assumed to respond to the total irradiance,  $I_R$ , incident on the scattered light collection aperture. For a circular collection aperture,  $I_R$  is given by

$$I_R = \int_0^a \int_0^{2\pi} I_t \rho d\rho d\theta \quad (26)$$

Using equations 17 and 23 in equation 26 results in an integral with a closed form solution given by

$$I_R = \frac{ca^2 I_0}{4Z'r_0^2} \left[ 1 + \frac{2J_1(K_0 \Delta a / r'_0)}{K_0 \Delta a / r'_0} \cos (2\pi Y / \delta + K \Delta Y_0 / r'_0) \right] \quad (27)$$

where  $r'_0 = r_0 [1 + \frac{1}{2} \tan^2 \beta]$   
function of the first kind.

and  $J_1$  is a first order Bessel

## VISIBILITY FUNCTION FOR A CIRCULAR APERTURE

It is straightforward to show that the relative amplitude of the interference term in equation 27 is identical to the signal visibility function,  $V$ , as defined in previous research. In this case equation 27 shows that  $V$  is given by

$$V = 2J_1(K\Delta a/r_o')/K\Delta a/r_o' \quad (28)$$

The visibility function in equation 28 is identical in form to that calculated previously for circular diffracting particles and a sufficiently large aperture centered on the bisector between the incident beams. However, comparison shows there are important differences between the two cases. Equation 28 shows that in the case of refraction the visibility depends directly on the angular extent  $a/r_o'$  of the collection aperture, its angular position and the separation,  $\Delta$ , of the two point sources generated by incident beams focused by the particle. As will be shown,  $\Delta$  depends on both the diameter of the particle and its index-of-refraction. It is interesting to note that a phase term  $K y_o/r_o$  is predicted for the Doppler signal portion of  $I_R$ . This phase term depends on the viewing angle,  $y_o/r_o$  in the plane of the incident beams, the particle size, and index-of-refraction. These dependences have not been calculated by the more rigorous solution to the problem posed by Bachalo. (There was no apparent need to do so.)

Similar effects using Mie scattering theory have also been predicted for scattered light observations involving particles comparable to a wavelength in diameter.

#### VISIBILITY FOR NEAR-AXIS FORWARD SCATTER

The geometry shown in figure 4 can be used to express  $\Delta$  as a function of beam intersection angle,  $\alpha$ , and the focal lengths developed by the sphere for the individual beams. Inspection of figure 4 shows that

$$\Delta/2f = \sin(\alpha/2) \quad (29)$$

$$\Delta = f(2\sin\alpha/2) \quad (30)$$

$f$  may be obtained by simple ray traces through the sphere with an application of Snell's law assuming that the angle of incidence  $\theta_i \ll 1$ . Appendix 1, using this approach, shows that  $f$  can be written as

$$f = \frac{Dm}{4(m-1)} \quad (31)$$

where  $m$  is the particle index of refraction,  $D$  is its diameter, and it is assumed that the refractive index of the medium surrounding the particle is 1.

The F number of the scattered light collection aperture is defined as

$$F = r_o / 2a \quad (32)$$

Equations 24, 30, 31, and 32 may be used to express the argument of the visibility function in 28 as

$$K_o \Delta a / r_o' = \frac{\pi (D/\delta) m}{4F [1 + \frac{1}{2} \tan^2 \beta] (m - 1)} \quad (33)$$

Thus the receiver aperture and index of ~~refraction~~ of the particle scale the range over which a particle size measurement can be obtained from a visibility measurement. This result agrees with conclusions drawn by Bachalo from his numerical integration studies of the problem. Resolution of the visibility measuring electronics limits the smallest measurable value of equation 33 to about  $0.1 \pi$ . The visibility is a monotonic function of its argument for values up to about  $1.0 \pi$ . Since the  $D/\delta$  (ultimately  $D$  is measured in terms of a known  $\delta$ ) is usually the parameter to be determined, the size range limits for a given value of  $F$  and  $m$  are

$$(D/\delta)_{\min} \approx 0.4F \frac{(m-1)}{m} [1 + \frac{1}{2} \tan^2 \beta] \quad (34)$$

$$D/\delta)_{\max} = \frac{4F(m-1)}{m} [1 + \frac{1}{2} \tan^2 \beta] \quad (35)$$

These equations show that with a fixed fringe period,  $\delta$ , and particles all having the same index-of-refraction, the size range covered is easily varied by adjusting the F number of the receiving aperture.

These results suggest that when  $D/\delta$  is known, the index of refraction of the particle can be measured. For example, suppose liquid droplets of a known size were produced with a monodisperse generator and the measured visibility corresponded to an argument  $\eta$ . Solution of equation 33 for the index-of-refraction yields

$$m = \frac{4F\eta}{4F\eta - \pi D/\delta} \quad (36)$$

Equations 30 - 32 shows that the phase shift,  $\psi$ , in the signal for this case is given by

$$\psi = K\Delta y_o / r_o \quad (37)$$

$$\psi = 2\pi \left[ \frac{(D/\delta)m}{4(m-1)} \right] \beta_y \quad (38)$$



$$\beta_y = Y_o/r_o$$

(39)

The relative phase of the signal is seen to depend on the aperture position  $\beta_y$  only and not on the aperture size. It is linearly proportional to  $D/\delta$ . Figure 5 shows the phase shift effect as  $D/\delta$  increases from 1 to 10 for an F/10 aperture located at  $\beta_y = 0.1$  and an index of refraction of 4/3. This result suggests that particle size could be obtained by measuring the phase shift,  $\psi$ , rather than the visibility  $v$ .

#### VISIBILITY FOR NEAR AXIS BACKSCATTER

Previous numerical studies by Bachalo suggested that this approach could also be used to measure  $D/\delta$  from off axis backscatter measurements of highly reflecting or absorbing particles. Assume that the observation angle is far removed from any glory or rainbow angles. The previous results can be modified in a straightforward fashion to show this. In this case the particle is no longer assumed to be a refractive lens but a spherical mirror. The focal length of a spherical mirror is half the radius of curvature. Equation 30 then shows that  $\Delta$  for backscatter,  $\Delta_B$ , is given by

$$\Delta_B = \frac{D}{4} (2\sin(\alpha/2))$$

(40)

The argument for the visibility in the backscatter case may thus be written as:

$$K_o \Delta a / r_o' = \pi(D/\delta)/4F[1 + \frac{1}{2} \tan^2 \beta] \quad (41)$$

The phase shift in the Doppler signal for backscatter,  $\psi_B$  can be computed from equation 37 and 40 as

$$\psi_B = 2\pi(D/\delta)\beta_y/4 \quad (42)$$

Equation 41 shows that a much greater range in  $D/\delta$  can be covered in backscatter measurements since the size range is independent of the index of refraction. For example when near axis forward and backscatter measurements are compared for water drops ( $m = 4/3$ ), the maximum value of  $D/\delta$  which can be measured in the forward scatter direction is  $F$  while in the backscatter direction it is  $4F$ . This result suggests that backscatter measurements over the same size range as forward scatter may give accurate results even for highly refracting particles since the collection aperture may be significantly reduced thereby eliminating rays resulting from multiple refractions toward the backward direction.

#### VISIBILITY FOR $90^\circ$ SIDE SCATTER

The simple model used for analysis of near-axis forward and backscatter measurements may also be used to develop an approximate expression for the

visibility function for light scattered  $90^\circ$  relative to the bisector between the incident beams. Light reaching the collection aperture in this case results predominantly from reflection. For observations made at  $90^\circ$  with respect to the bisector between the beams, reflected rays originate for angles of incidence of  $\frac{\pi}{4} - \alpha/2$  and  $\frac{\pi}{4} + \alpha/2$  for beams separated by an angle  $\alpha$ . The lateral separation of the reflected light sources on the sphere is thus given by

$$\Delta_{90} = \frac{D}{2} (\cos(\pi/4 - \alpha/2) - \cos(\pi/4 + \alpha/2)) \quad (43)$$

$$\Delta_{90} = D \sin(\pi/4) \sin \alpha/2 \quad (44)$$

Fig. 6 illustrates the coordinate geometry for the estimation of  $\Delta_{90}$ . The collection aperture again can be modeled as one observing two point sources separated by a distance  $\Delta_{90}$ . The visibility function for a circular aperture is thus given by equation 28. The argument of the visibility function in this case is thus found from equation 44 to be

$$k\Delta a/r_o = \frac{\sqrt{2}}{4F} \pi D/\delta \quad (45)$$

The phase shift observed in the Doppler signal for  $90^\circ$  side scatter  $\psi_{90}$  is found using equations 37 and 44 to be

$$\psi_{90} = 2\pi \left( \frac{\sqrt{2}}{4} (D/\delta) \right) \beta_y \quad (46)$$

These results apply to the experimental case of the highest possible spatial resolution which can be achieved with an instrument of this type.

#### THE GENERALIZED VISIBILITY FUNCTION

The previous results for a circular aperture may be generalized to apertures of virtually any shape. The approach is similar to that followed by Robinson and Chu in analyzing the visibility function for diffraction<sup>5</sup> only. With assumptions made previously, the intensity distribution in the plane of the collection aperture may be written using equations 15, and 18 - 22 as

$$I_t = I_o (1 + \cos((k\Delta Y'/r'_o) + \phi)) \quad (47)$$

$$\phi = k\Delta Y_o/r'_o + 2\pi Y/\delta \quad (48)$$

where  $I_o$  includes all necessary constants and it is assumed that the waves incident on the particle are equal in amplitude. The irradiance collected by the receiving aperture is given by

$$I_R = I_o \int_{A_p} dA_p + I_o \int_{A_p} \cos\left(\frac{k\Delta Y'}{r'_o} + \phi\right) dA_p \quad (49)$$

where  $A_p$  is the area of the receiving lens. It is convenient to define a pupil function  $P(X,Y)$  such that

$$\begin{aligned} P(X,Y) &= 1 \text{ for all } x, y \text{ falling inside } A_p \\ &= 0 \text{ otherwise} \end{aligned}$$

$I_R$  can be written as

$$I_R = I_o \int_{\infty} P(X,Y) dA_p + I_o \int_{\infty} P(X,Y) \cos\left(\frac{k\Delta Y'}{r_o'} + \phi\right) dA_p \quad (50)$$

The integrals in equation 50 may be recognized as the Fourier Transforms of the pupil function evaluated at spatial frequencies  $f_{x_o}$ , and  $f_{y_o}$ , where

$$f_{y_o} = k\Delta/r_o' \quad (a)$$

(51)

$$f_{x_o} = 0 \quad (b)$$

with this identification, equation 50 may be written as:

$$I_R = I_o \tilde{P}(0,0) \left[ 1 + \frac{\tilde{P}(0,f_y)}{\tilde{P}(0,0)} \cos(\phi) \right] \quad (52)$$

where  $P(f_x, f_y)$  is understood to represent the Fourier transform of the pupil function  $P(X, Y)$ . From equation 52 it is clear that the visibility function is given by

$$v = \tilde{P}(0, f_y) / \tilde{P}(0, 0) \quad (53)$$

Equation 53 shows how the visibility function varies as a function collection aperture geometry. For example, a rectangular aperture of width  $2L$  and "arbitrary length" oriented with sides parallel to the interference fringes in the reception plane requires a visibility function given by

$$v = \frac{\sin(k\Delta L / r_o)}{k\Delta L / r_o} \quad (54)$$

The arguments of the visibility functions for spherical particles developed for circular apertures transpose directly with the understanding that the F number of the receiver is now defined as  $r_o / 2L$ . Equation 53 also indicates the possibility of aperture shaping to achieve increased resolution at the small or large ends of the particle size range. For example, a square aperture oriented with its diagonal perpendicular to the planes defined by the sample space interference fringes requires a visibility function given by

$$v = \frac{\sin^2(k\Delta L \sqrt{2} / 2r_o)}{(k\Delta L \sqrt{2} / r_o)^2} \quad (55)$$

In this case the large size limits of the visibility function are extended over those required by the one dimensional aperture described by equation 54

because the visibility is monotonic over a larger range (the first zero in the visibility is extended by a factor of  $\sqrt{2}$ ). The small size limit is also increased but because the visibility is squared the small size resolution limit can be decreased from about  $0.1 \pi$  in the limiting argument of the visibility to about  $0.075 \pi$  to obtain the same limiting value of visibility. This represents an approximate reduction in the smallest resolvable particle size of about 25%.

#### COMPARISON WITH NUMERICAL COMPUTATIONS

Bachalo's approach to the solution of this problem is to use more exact expressions for the refracted waves and to numerically integrate the resulting expressions to obtain the visibility. As such this method should yield more precise results than those of the approximate model developed here. Thus, it is of interest to compare results from the two approaches to determine how well the approximate model compares with the numerical calculations.

Table I summarizes the results of the approximate solution for circular apertures and near forward,  $90^\circ$ , and near backscatter estimates. When the approximate model results are compared with Bachalo's calculations it is immediately seen that both agree in predicting that the same functional form will result as the particle index of refraction or aperture size is varied. A reasonable point of comparison for the two results is the prediction of the value of  $D/\delta$  for the first zero in the visibility function. Table II shows the results of comparing the two predictions for the index-of-refraction and F number values used in Bachalo's numerical calculations.



In view of the assumptions made for the approximate model evaluation, the agreement is quite good. The comparison shows the essential correctness of the scaling relationship effects on the visibility resulting from changes in viewing angle, collection aperture, or index-of-refraction. Note also that as the index-of-refraction increases, the approximation becomes better.

#### SUMMARY AND CONCLUSIONS

A simple model has been developed which gives in closed form solution a prediction of the visibility dependence on particle index-of-refraction, receiver F number, and viewing angle for large refracting particles. The analysis also shows the effects of these parameters on the phase of the Doppler signal and how receiving apertures can be shaped to obtain visibility functions which are consistent with a desired size range for a given fringe period. Comparison of the model results with recently published results obtained by numerical integration shows reasonable agreement.

The ability to adjust the measurable size range by simply adjusting an iris in front of the receiving lens is a significant operational simplification over past paraxial interferometers which were designed to produce very large fringe periods for large particle measurements.

Results in this analysis help to qualitatively explain the alignment sensitivity problem described in past work for the measurement of large refracting particles paraxially.<sup>8</sup> When optical alignment is such that refractive amplitudes are greater than diffracted amplitudes, the visibility can be expected to increase. Hence, paraxial observations of particles

producing diffracted components which are effectively blocked by beam stops can lead to visibilities of the magnitude predicted here.

The method developed here may also be used for predicting visibility functions for non-spherical particles. The parameter measured by the visibility function is  $\Delta$ . Hence, as the particle shape becomes non-spherical, geometric ray traces can be used to relate  $\delta$  to a particle size parameter.

TABLE I  
RESULTS FROM APPROXIMATE MODEL FOR CIRCULAR APERTURES

OBSERVATION DIRECTION	ARGUMENT OF VISIBILITY FUNCTION	VALUE OF $D/\delta$ FOR FIRST ZERO IN VISIBILITY	APPROXIMATE LIMITS IN PARTICLE SIZE RANGE	
			MINIMUM	MAXIMUM
NEAR FORWARD SCATTER ( $\beta \leq 30^\circ$ )	$\frac{\pi (D/\delta) (m/m - 1)}{4F(1 + \frac{1}{2} \tan^2 \beta)}$	$4.88 (m - 1)/m F(1 + \frac{1}{2} \tan^2 \beta)$	$0.4F((m-1)/m)(1 + \frac{1}{2} \tan^2 \beta)$	$4F((m - 1)/m)(1 + \frac{1}{2} \tan^2 \beta)$
90° SIDE SCATTER	$\frac{2 \pi (D/\delta)}{4F}$	3.45F	0.282F	2.82F
NEAR BACK SCATTER	$\frac{\pi (D/\delta)}{4F(1 + \frac{1}{2} \tan^2 \beta)}$	$4.88F(1 + \frac{1}{2} \tan^2 \beta)$	$0.4F(1 + \frac{1}{2} \tan^2 \beta)$	$4F(1 + \frac{1}{2} \tan^2 \beta)$

TABLE II

COMPARISON OF APPROXIMATE AND NUMERICAL PREDICTIONS FOR  $D/\delta$   
VALUES AT FIRST ZERO IN VISIBILITY FUNCTION

OBSERVATION ANGLE (DEGREES)	COLLECTION APERTURE F/NO.	INDEX-OF- REFRACTION	FIRST ZERO IN VISIBILITY APPROXIMATE SOLUTION	NUMERICAL SOLUTION	% DIFFERENCE APPROXIMATE-NUMERICAL NUMERICAL
10	2.8 (1)	1.33	3.47	3.65 (1)	- 4.9 (1)
10	2.8	1.5	4.63	4.70	- 1.5
20	2.8 (1)	1.33	3.64	4.0 (1)	- 9.0 (1)
20	2.8	1.5	4.86	5.0	- 2.9
30	2.8	1.33	3.98	4.5	-11.5
30	2.8	1.4	4.55	4.8	- 5.2
30	2.8	1.5	5.31	5.3	+ 0.18
90	2.2	1.33	7.74	7.59 (1)	1.94 (1)

(1) Private communication with Bachalo indicates that the published values are incorrect. They are not consistent as reported in the publication.<sup>9</sup> The numerical values published here were computed using a program developed at UTSI.

## APPENDIX I

In this appendix a ray trace is developed to find the value of  $f$  for small angles of incidence ( $\theta_i \lesssim 20^\circ$ ) and spherical particles. Consider the two rays in figure 7. The assumption is made that Snell's law of refraction can be written as

$$\sin \theta_i = m \sin \theta_R \quad (a) \tag{56}$$

$$\begin{aligned} \theta_i &\approx m \theta_R \\ \theta_i &\lesssim 20^\circ \end{aligned} \quad (b)$$

Elementary geometrical arguments show that the angles of interest can be written as

$$\beta' = 2(\theta_i - \theta_{R1}) \tag{57}$$

$$\gamma' = 2\theta_{R1} - \theta_i \tag{58}$$

Using the approximation for Snell's law (equation 56b) equation 57 and 58 may be written as

$$\beta' \approx 2\theta_i \left( \frac{m - 1}{m} \right) \tag{59}$$

$$\gamma' \approx \theta_1 \left( \frac{2-m}{m} \right) \quad (60)$$

Inspection of figure 7 shows that p and q can be written as

$$p = r \sin \gamma' \quad (61)$$

$$q = p / \tan \beta' \quad (62)$$

$$q = r \sin \gamma' / \tan \beta' \quad (63)$$

For small angles

$$\sin \gamma' \approx \gamma' \quad (64)$$

$$\tan \beta' \approx \beta' \quad (65)$$

$$\cos \gamma' \approx 1 \quad (66)$$

Using equations 64 and 65 in equation 63 yields

$$q \approx \frac{r}{2} \left( \frac{2-m}{m-1} \right) \quad (67)$$

Equation 66 allows f to be written as

$$f \approx r + q \quad (68)$$

Substituting equation 67 into equation 68 produces the desired relationship:

$$f = \frac{r}{2} \left( \frac{m}{m-1} \right) \quad (69)$$



## REFERENCES

1. M. K. Mazumder, et.al, "Application of SPART Analyzer for Monitoring Real-Time Aerodynamic Size Distribution of Stack Emission," Laser Velocimetry and Particle Sizing, Hemisphere Press, 1979.
2. A. J. Yule, et.al., "Particle Size and Velocity Measurements by Laser Anemometry" AIAA Paper No. 77-214, Presented at the AIAA 15th Aerospace Sciences Meeting, Los Angeles, CA. January 1977.
3. W. M. Farmer, "Measurement of Particle Size, Number Density, and Velocity Using a Laser Interferometer" Appl. Opt. 11, 2603 (1972).
4. W. M. Farmer, "Observation of Large Particles with a Laser Interferometer," Appl. Opt. 13 610 (1974).
5. D. M. Robinson and W. P. Chu, "Diffraction Analysis of Doppler Signal Characteristics for a Cross-Beam Laser Doppler Velocimeter," Appl. Opt. 14, 2177 (1975).
6. N. S. Hong and A. R. Jones, "A Light Scattering Technique for Particle Sizing Based on Fringe Anemometry," J. of Phys. D. App. Phys. 9, 1839 (1976).
7. D. W. Roberds, C. W. Brasier and V. W. Bomar, "Use of Particle Sizing Interferometer to Study Water Droplet Size Distribution," Opt. Eng. 18, 236, (1979).
8. W. M. Farmer, "Measurement of Particle Size and Concentrations Using LDV Techniques" Proceedings of the Dynamic Flow Conference, 1978. Organizing Secretariat, P. O. Box 121, DK-2740, Skovlunde, Denmark.

9. W. D. Bachelo, "Method for Measuring the Size and Velocity of Spheres by Dual Beam Light Scatter Interferometry," Appl. Opt., 19, 363 (1980).
10. J. R. Hodgkinson and I. Greenleaves, "Computations of Light Scattering and Extinction by Spheres According to Diffraction and Geometrical Optics and Some Comparisons with Mie Theory," J.O.S.A., 53, 577 (1963).

## LIST OF FIGURES

1. Probe volume co-ordinate system geometry for interferometric particle size analysis.
2. Co-ordinate system geometry for visibility estimate for refracting spheres.
3. 114 micrometre glass sphere in a fringe pattern and the resulting scattered field pattern.
4. Ray trace system for estimation of focal point separation.
5. Example signal phase and visibility for a large refracting sphere.
6. Ray trace co-ordinate for the estimation of  $f$ .

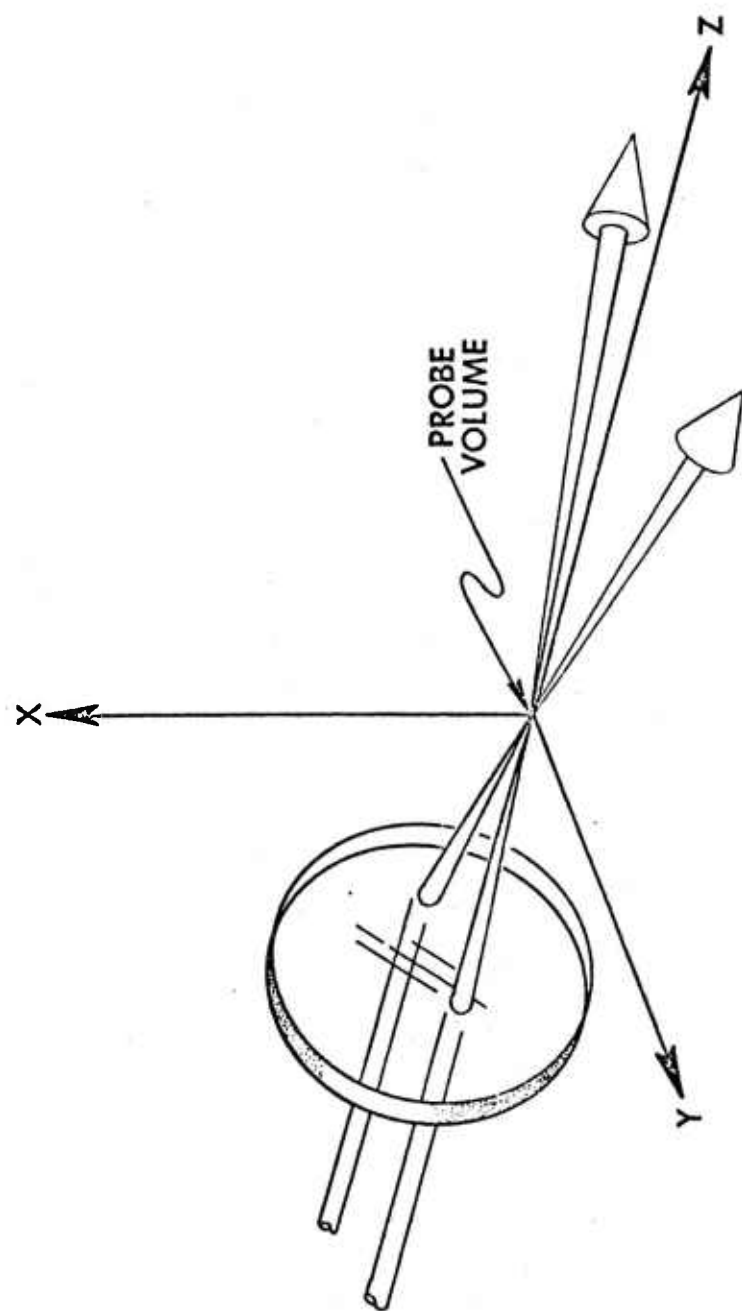


Figure 1. Probe Volume Co-ordinate System Geometry for Interferometric Particle Size Analysis.

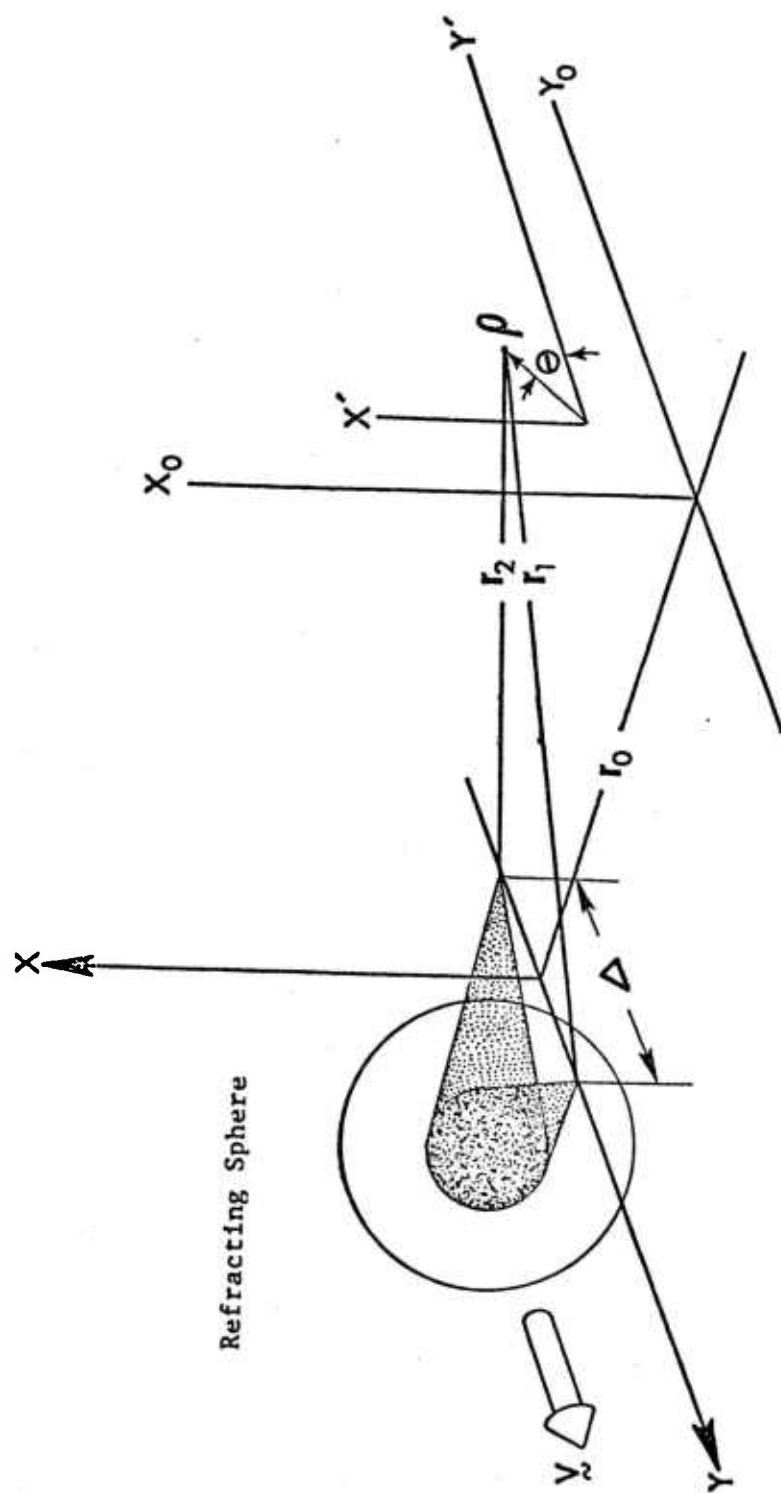


Figure 2. Co-ordinate System Geometry for Visibility Estimate for Refracting Spheres.

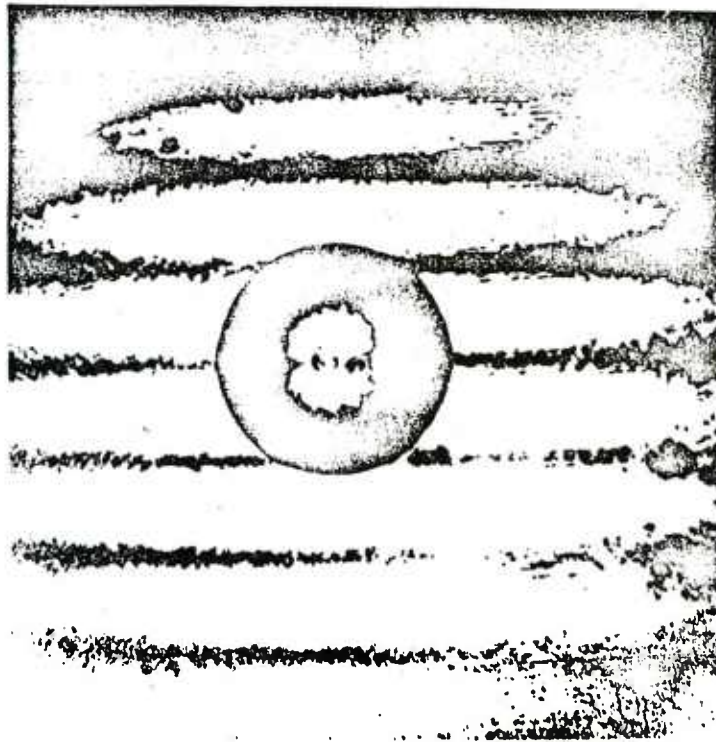


Figure 3. 114 micrometre glass sphere in a fringe pattern and the resulting scattered field pattern.

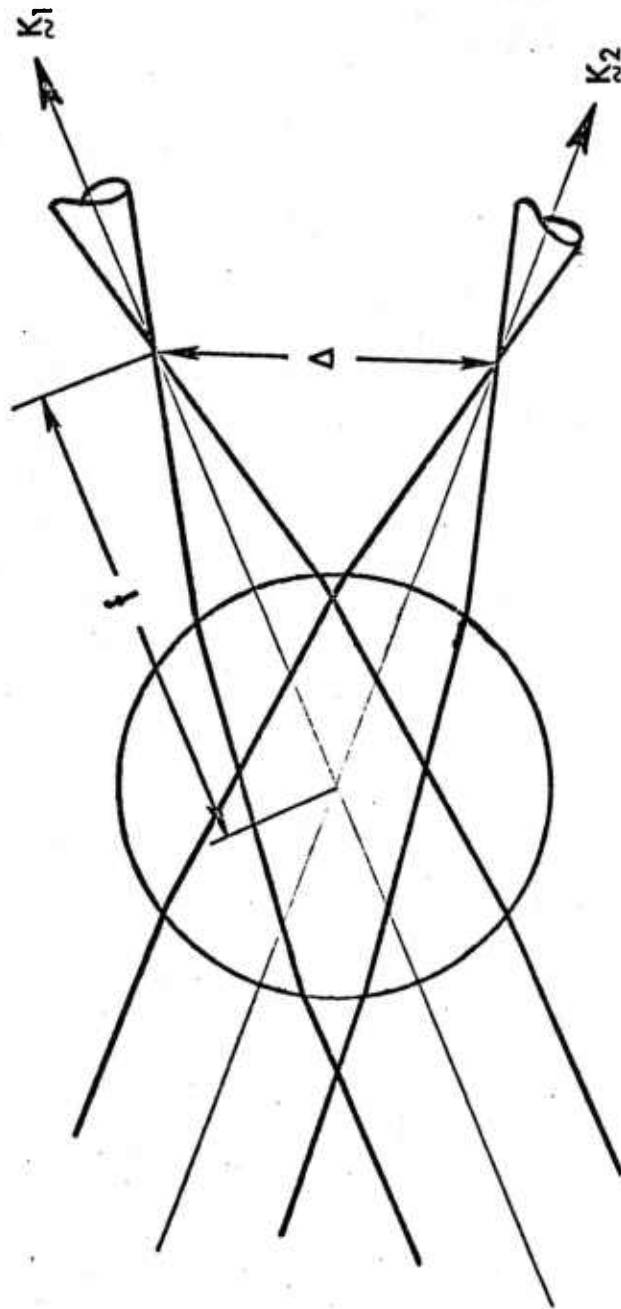


Figure 4. Ray Trace System for Estimation of Focal Point Separation.



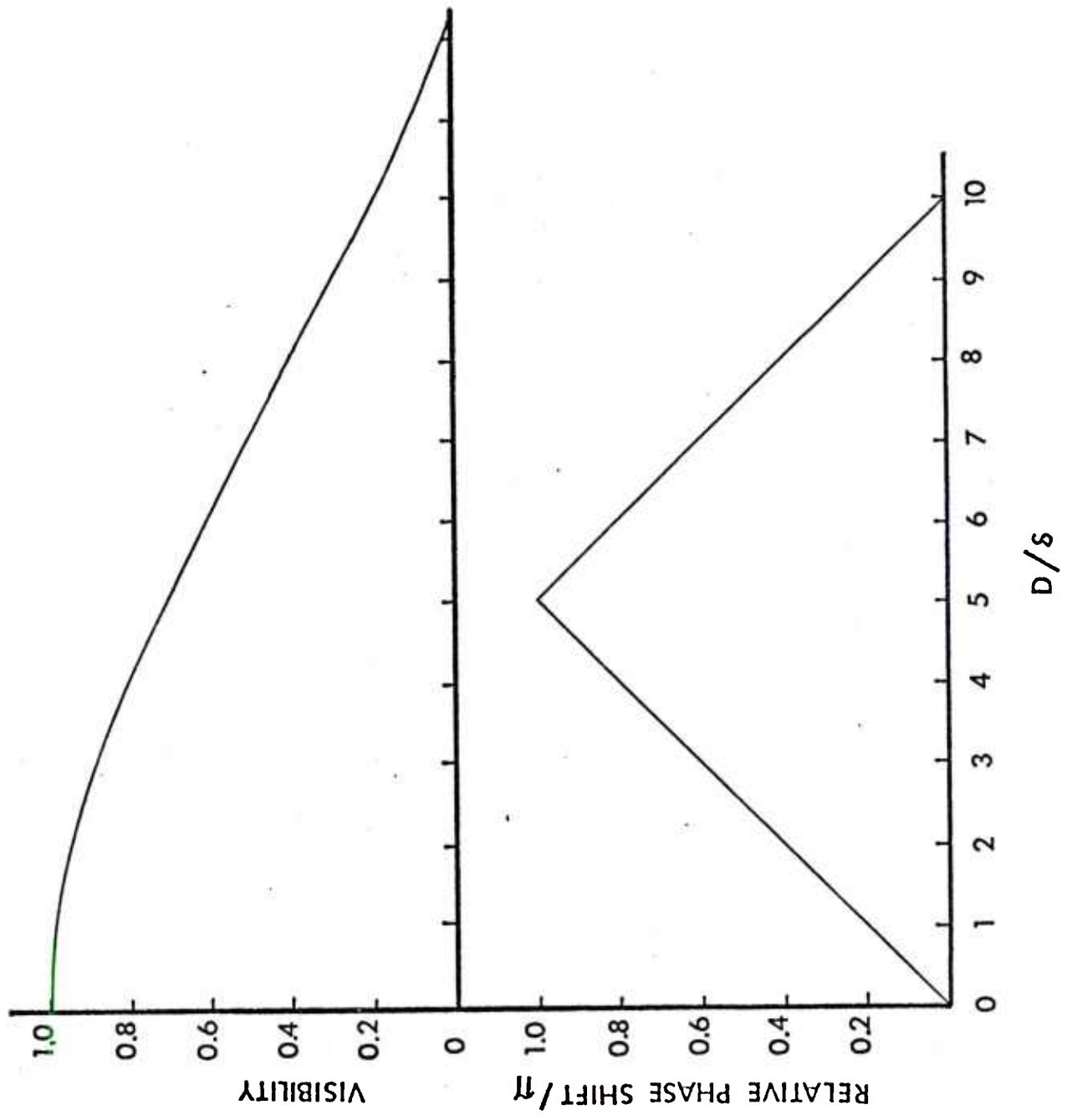


Figure 5. Example Signal Phase and Visibility for a Large Refracting Sphere.

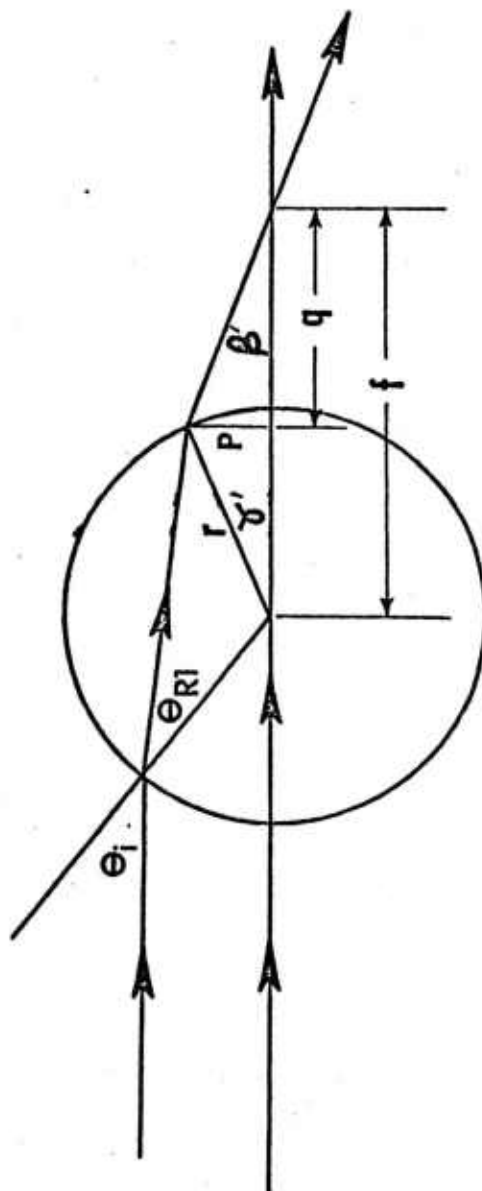


Figure 6. Ray Trace Co-ordinates for the Estimation of  $f$ .

## APPENDIX II

A MODEL FOR ESTIMATING PARTICLE  
NUMBER DENSITY USING DIFFERENTIAL  
DOPPLER LASER VELOCIMETERS

W. M. Farmer

ABSTRACT

A model is developed which may be used to predict particle number density using data from currently available differential Doppler laser velocimeter optical systems and burst counter signal processors. The results may also be used to predict relative system performance as the LDV system parameters used in the model change.

INTRODUCTION

The estimation of particulate number density in a moving fluid is a particularly difficult experimental problem subject to numerous sources of error. For example, mechanical sampling systems such as cascade impactors must sample isokinetically and at a fixed flow rate. These kinds of measurements yield number density estimates from computations involving weight measurements for each stage of the impactor corresponding to "equivalent" aerodynamic particle diameters.<sup>1,2</sup> The resulting estimate is thus not a direct numeric count but rather an "equivalent" number density. Because mechanical samplers often introduce unacceptable perturbations in the flows being measured, optical and other more exotic techniques have been developed, each having its own peculiarities and limitations.<sup>3</sup> These methods have ranged from multiple wavelength transmissometer schemes to sophisticated multiple scatter angle techniques

involving highly sophisticated inversion schemes and considerable computational effort. Single particle optical counters which determine a particle size from a scattered light measurement and maintain an accurate particle count rate for a fixed sample flow rate are among the most accurate devices for estimating numeric number densities. They are, however, cumbersome to use except in the most benign environments because of the need to draw a fluid sample through their optically sensitive region. Furthermore, when number densities become "large", it is necessary to dilute the concentration in order to reduce the probability that more than one particle will exist in the sample volume during a measurement interval. In hostile environments, such as encountered in combustion or chemically active flows or in flows with particles that may be affected by the sampling system, it is not practical to use these kinds of optical counters. Differential Doppler laser velocimeter systems are appropriate for use in these kinds of particle climates. The sampling volumes of these devices may be modeled as periodic structures resulting from sets of localized interference fringes. The number of cycles and signal shape in a signal generated by a particle scattering light from this fringe structure may be related both to the size and the trajectory of the particle. As a result, signal processing electronics has been developed which can test signals in terms which can at least be heuristically related to trajectory through the sample volume or the presence of two or more particles generating the signal. Thus, these optical systems do not rely on plumbing or dilution to restrict particle flow through the sampling volume. Rather, it is common practice

to focus these devices into particle laden flows and to let the particle flux arrive as the flow velocity, concentration, and spatial distribution dictate. The signal processing electronics and signal test logic then sample the particle flux in a manner analogous to the functions imposed by the sampling and dilution plumbing of single particle optical counters. The purpose of this paper is to present a model that shows how data obtained with a differential Doppler laser velocimeter (LV) may be used to estimate particle number density in otherwise inaccessible flow fields. The method utilizes data which is readily available from most existing LV systems and should therefore be straightforward to implement on a wide variety of experiments where these devices are in use and number density data are of interest. In addition to providing a number density estimate from LV data, the method may also be used to address a problem often encountered in the application of the LV. The problem is to estimate how often data can be acquired for a specified number density given the constraints of the optical and signal processing system.

Because the approach taken in this paper is somewhat different than normally encountered in dealing with number density limitations on LV system performance, a review is first given of the results of a typical LV system measurement of a particle laden flow. Next, statistics normally associated with this process are examined in the various limits which might be encountered experimentally. Factors which affect the applicability of these statistics are examined. A model is then proposed to circumvent the difficulty imposed by these factors. Finally, experimental results are presented which suggest that the proposed model can be effectively

used to estimate particle number density.

#### TYPICAL LV EXPERIMENT

A typical LV experiment might involve an optical system of the type shown in figure 1. Two coherent beams are made to cross and focus at some position in a particle laden flow. The scattered light collector will be assumed to be sufficiently large that individual particles can be detected as they traverse the beam cross region. This region is commonly called the probe volume. For TEM<sub>00q</sub> laser beams and angles between the beams of about  $10^\circ$  or less, this volume will appear to be an ellipsoid of revolution. In most experiments, the flow velocity is not constant but varies randomly about some mean value. Normally, the particles in the flow may be distributed in particle size, shape, and composition. Depending on the drag coefficients which may be ascribed to the ensemble of particles measured and the fluid velocity parameters, the particles may follow the fluid velocity or "slip" relative to it. Normally, it is assumed that the particles follow the fluid velocity well within the uncertainties acceptable for the experiment. In a typical experiment, the photodetector is set to a fixed gain level which is commensurate with amplifier linearity used in the signal processor electronics. A signal threshold level is set for a value that minimizes or eliminates the time spent by the signal processor attempting to measure sources of non flow related noise. If it is assumed that the threshold is set such that the processor does not spend time attempting to measure noise, then for a sample time  $\Delta t$ , with  $N_1$  valid measurements



(valid in the sense that all signal processor requirements are met)

the following factors account for the value of  $\Delta t$ .

1. The amount of time required for  $N_1$  particles to traverse the sample volume  $-\Delta t_1$
2. The amount of time during which no particles are present in the sample volume  $-\Delta t_2$
3. The amount of time due to 2 or more particles are simultaneously in the sample volume  $-\Delta t_3$
4. The amount of time due to single particles producing signals with too few cycles to be measureable (normally associated with very small particles or particles passing near the edge of the sample volume)  $-\Delta t_4$
5. The amount of reset time required by the signal processor and data acquisition system after each measurement attempt  $-\Delta t_R$

Thus  $\Delta t$  may be expressed as:

$$\Delta t = \Delta t_1 + \Delta t_2 + \Delta t_3 + \Delta t_4 + \Delta t_R \quad (1)$$

$\Delta t_1$  may be expressed as:

$$\Delta t_1 = \sum_{i=1}^n N_{Li} \tau_i \quad (a)$$

or

$$\Delta t_1 = \Delta t P(1) \quad (b)$$

where  $N_{Li}$  is the number of cycles generated in the  $i$ th signal and  $\tau_i$  is the signal time period.  $P(1)$  is the probability of 1 particle being present in the sample volume.  $\Delta t_R$  may be expressed as:

$$\Delta t_R = (N_E - 1) \tau_R \quad (3)$$

where  $\tau_R$  is the signal processor reset time and  $N_E$  is the total number of attempted measurements made by the signal processor. No similar simple relationships exist for  $\Delta t_2$ ,  $\Delta t_3$ , and  $\Delta t_4$ . These times can be estimated using statistical estimators. For example,  $\Delta t_2$  may be written as:

$$\Delta t_2 = \Delta t P(0) \quad (4)$$

where  $P(0)$  is the probability that zero particles are present in the sample volume. Similarly,  $\Delta t_3$  might be written as:

$$\Delta t_3 = \Delta t P(n \geq 2) \quad (5)$$

where  $P(n \geq 2)$  is the probability that two or more particles are present in the sample volume.  $\Delta t_4$  might be computed using  $P(1)$  and a weighting factor to account for the fact the sample volumes over which these measurements can be made is probably much smaller than that corresponding to  $\Delta t_1$  or  $\Delta t_3$ .

Experimentally, it is not unusual to find  $N_E \gg N$  and  $\tau_R \ll N_{Li} \tau_i$ . It is thus possible that  $\Delta t_R$  can make a significant contribution to  $\Delta t$ . It is often observed that in flows with moderate number densities of particles that  $\Delta t_1 / \Delta t \ll 1$ , and that  $N_1 / N_3$  ( $N_3$  being the number of signals generating  $\Delta t_3$ ) generally varies between 0.1 - 0.8 and seems to depend on number density. This suggests that a statistical model might relate particle number density to  $N_1 / N_3$ . The next section examines a statistical model commonly used to analyze LV optical systems.

# COMMON STATISTICAL ANALYSIS OF FINDING $n$ PARTICLES IN THE LV SAMPLE VOLUME

It is generally assumed that the probability of finding  $n$  particles in the LV sample volume is fully equivalent to that posed by Chandrasekhar for  $N$  particles randomly distributed in a volume  $V$  which is sampled by a small volume  $v$ .<sup>4,5</sup> In this case, Chandrasekhar, starting from the Bernoulli distribution, derives the Poisson distribution for simultaneously obtaining  $n$  particles in  $v$  as

$$P(n) = \frac{(Np)^n}{n!} e^{-Np} \quad (6)$$

where  $p$  is the probability of finding a particular particle in  $v$ . If the particles are randomly distributed throughout  $V$  then by definition of a random variable<sup>6</sup>

$$p = v/V \quad (7)$$

The value  $Np$  is usually written as  $\rho_N v$  where  $\rho_N$  is the number of particles per unit volume.  $P(n)$  may then be written in the form normally seen for equation 6

$$P(n) = \frac{(\rho_N v)^n}{n!} e^{-\rho_N v} \quad (8)$$

For later reference it is to be noted the probability of obtaining 2 or more particles in the sample volume may be written as

$$P(2) = 1 - e^{-\rho_N v} - \rho_N v e^{-\rho_N v} \quad (9)$$

Note that

$$\lim_{\rho_N v \rightarrow \infty} P(2) = 1 \quad (10)$$

$$\lim_{\rho_N v \rightarrow 0} P(2) = 0 \quad (11)$$

In the case where  $\rho_N v \gg 1$ , the Poisson distribution approaches a Gaussian distribution. Chandrasekhar shows that  $P(n)$  can be expressed as

$$P(n) = \frac{1}{\sqrt{2\pi\rho_N v}} e^{-(n - \rho_N v)^2 / 2\rho_N v} \quad (12)$$

These equations are relatively straightforward and present no interpretational difficulties until attempts are made to apply them to experimental LV data. The fundamental experimental parameter in equations 8 and 12 is

$$\rho_N v = N v/V \quad (13)$$

$v$  and  $V$  are well defined quantities in the mathematics. Experimentally, this may not be so. Consider the fact that  $v$  may be a time dependent variable. For example,  $v$  for a single particle can be defined as

$$v = \underline{v} a_{pv} t \quad (14)$$

where  $\underline{v}$  is the particle velocity component normal to the sample volume cross sectional area  $a_{pv}$  and  $t$  is the particle transit time across the sample volume. If account is

taken of the fact that the particles sampled may have a speed distribution as well as a size distribution, then the sample volume for a particle having the  $i$ th velocity and  $j$ th particle size is

$$v_{ij} = v_i a_{pvj} t_{ij} \quad (15)$$

$a_{pv}$  and  $t$  have  $j$  subscripts because it is presently understood that an LV sample volume depends on the particle size (or more specifically the scattering cross-section) producing the signal.<sup>7</sup> Hence, it is to be expected that  $v$  will vary from one particle to the next. A second difficulty arises in attempting to define the total volume of aerosol sampled,  $V$ . For example, if  $V$  were defined in a fashion similar to equation 14, then

$$V = \int \int_{\sigma} v (a_{pv1} \Delta t_1 + a_{pv2} \Delta t_2 + a_{pv3} \Delta t_3 + a_{pv4} \Delta t_4) f(v) f(\sigma) d\sigma dv \quad (16)$$

where  $f(v)$  and  $f(\sigma)$  are the probability density functions for the velocity and extinction cross-sections for the measured ensemble. The resolution of equation 16 depends not only on assuming functions for  $f(v)$  and  $f(\sigma)$  but also in defining  $a_{pv}$  when no particles are present or when 2 or more occupy the sample volume.

Equation 15 shows that the sampling volume varies particle to particle as a function of both particle size and speed. Except for artificially contrived cases, it is not constant in value. Equation 16 illustrates the problem associated with attempting to estimate  $V$  from experimental data and models for the velocity and size distributions.

Erdmann and Gellert have pointed out that when the velocity is distributed the Poisson distribution describing the arrival rate of particles crossing the sample volume must be replaced by the compound Poisson distribution.<sup>5</sup> In their case, the compound Poisson distribution for some distribution of velocity  $f(\underline{v})$  is given by

$$Q(n, \lambda T) = \int_{\underline{v}} \left\{ \frac{(\lambda T)^n \exp(-\lambda T)}{n!} \right\} f(\underline{v}) d\underline{v} \quad (17)$$

where  $\lambda$  is the mean particle arrival rate and  $T$  is the sample time of interest. Feller indicates how compound Poisson distributions lead to solutions for Brownian motion and "randomized random" walk problems.<sup>8</sup> For the application under consideration here, the compound Poisson process yields

$$Q(n, \rho_N v) = \int_v \left\{ \frac{(\rho_N v)^n}{n!} e^{-\rho_N v} \right\} \phi(v) dv \quad (18)$$

where  $v$  is the sample volume and  $\phi(v)$  is the sample volume distribution which may depend on both the particle scattering cross-section and velocity distribution. Hence,  $Q(n, \rho_N v)$  will be a strong function of experimental conditions and instrumentation response. To formally solve equation 18, it is necessary to assume a functional dependence for  $\phi(v)$ . In this work, rather than directly postulating a  $\phi(v)$  function, a somewhat different approach will be taken which has been found to yield reasonably good agreement with experiment and provides some physical insight into the measurement process. In this approach, it is first assumed that at some

instant in time the particle ensemble to be measured is randomly distributed in the total measured volume. As the sample volume is moved through the ensemble, it will be assumed to vary (because of velocity and particle size) in a fashion that can be described by a random walk process. Such a sample volume will be called a "Random Walk Sample Space." In the following section, the probability of two or more particles existing within some distance of each other for each of three orthogonal coordinates in the random walk sample space is computed. It will be assumed that the logic circuits of the LV signal processor are sufficiently accurate to reject all signals resulting from two or more particles. Obviously, the accuracy with which this can be accomplished is a major limitation to the accuracy of this model. (Our experience has been that such circuits are fooled by broadband Gaussian noise in less than 1% of the measurement attempts which might correspond to a multiple particle signal). The resulting probability distribution for particle separation in three dimensions and assuming accurate multiple particle detection lead to the definition of a signal acceptance ratio, A. "A" specifies the ratio of number of particles measured to those detected. "A" is then taken as the sampling efficiency of the LV and is a quantitative measure of how well the LV performs as a function of number density. Conversely, if the LV optical system parameters and signal processor characteristics are carefully specified, then a measurement of "A" can be used to estimate particle number density.

## PROBABILITY OF TWO PARTICLES SIMULTANEOUSLY IN THE RANDOM WALK SAMPLE SPACE

The development of the probability density distribution for two particles simultaneously in a random walk sample space is based on the well known random walk analysis commonly found in text books on statistics.<sup>6,8</sup> Because the functional dependences of the resulting distribution are not immediately evident, the steps leading to the result are briefly sketched.

Because the particles are assumed to be randomly distributed in space and a random walk is performed to reach one, the probability  $P(x,y,z)$  of a particle existing at some  $x,y,z$  position in a rectangular coordinate system may be written as

$$P(x,y,z) = P(x) P(y) P(z) \quad (19)$$

where  $P(x)$  etc., is the probability that the particle position is at the coordinate  $x$ . Consider figure 2, a dimension in the  $x, y, z$  coordinate system, is divided into a set of cells of dimension  $\epsilon$ . The occupied cell is approached by advancing or retreating in unit cells with equal probability, i.e. the probability of advancing a unit cell is  $1/2$ . Let some arbitrary cell be chosen as the origin and count cells to the left until a cell is found which is occupied. Let this number of cells be  $p$ . Next, let  $q$  be the number of cells counted from the origin before the next successive occupied cell is found. Define the total number of cells involved as given by  $n$  while the number of cells between the particles is  $m$ , then



$$p + q = n \quad (18)$$

$$p - q = m \quad (19)$$

The probability that a sequence  $n$  leads to a value of  $m$ ,  $P_{n,m}$  is given by the Bernoulli equation

$$P_{n,m} = \frac{n!}{p!q!} \left(\frac{1}{2}\right)^n \quad (20)$$

Applying Stirling's formula for  $n!$  and manipulating variables, there results the Laplace de Moivre limit<sup>6</sup>

$$P_{n,m} \approx \left(\frac{2}{\pi n}\right)^{1/2} \exp(-m^2/2n) \quad (21)$$

$$|m| \ll n$$

It is convenient to make the following identities

$$x = m\epsilon \quad (22)$$

$$X = \frac{n\epsilon}{2} \quad (23)$$

where  $x$  is the spatial displacement between particles and  $X$  is the arithmetic average of the distance between the particles. Substituting Equations 22 and 23 into Equation 21 results in

$$P_{n,m} \approx \left(\frac{\epsilon}{\pi X}\right)^{1/2} \exp\left(\frac{-x^2}{4\epsilon X}\right) \quad (24)$$

Let  $P(x,X)dx$  be the probability of a distance  $x$  to  $x + dx$  existing between particles when the average distance is  $X$ . For small  $dx$ ,  $P_{n,m}$  is approximately constant. Then  $P(x,X) dx$  is  $P_{n,m}$  multiplied by the number of values of  $m$  occurring in  $dx$  for fixed  $n$ ,

$$P(x,X)dx = P_{n,m} \frac{dx}{\epsilon} \left( \frac{1}{2} \right) \quad (25)$$

A factor of  $\frac{1}{2}$  enters since for fixed values of  $n$ , values of  $m$  are either all odd or all even. Equation 24 can now be expressed using Equation 25 as

$$P(x,X)dx = \frac{1}{(\pi 4 \epsilon X)^{1/2}} \exp \left( \frac{-x^2}{4 \epsilon X} \right) dx \quad (26)$$

It is assumed that the arithmetic average distance between particles along a specified direction for a given number density  $\rho_N$  is given by

$$X = \rho_N^{-1/3} \quad (27)$$

The cell length  $\epsilon$  is chosen to be the fringe period  $\delta$  of the LV system since this is the basic resolution element through which the logic circuits in the LV processor must decide if two or more particles occupy the sample volume. With these identifications

$$P(x,X)dx = \left[ \frac{\rho_N^{1/3}}{4\pi\delta} \right]^{1/2} \exp \left( \frac{-\rho_N^{1/3} x^2}{4\delta} \right) dx \quad (28)$$

It is convenient to define  $a$  as

$$a \equiv \rho_N^{1/3} / 4\delta \quad (29)$$

With these results and definitions, the probability of finding 2 or more particles in some increment of space  $\Delta x \Delta y \Delta z$  when the particles are separated by some average distance  $X$  is given by

$$P(\Delta x \Delta y \Delta z) = \int_0^{\Delta x} \int_0^{\Delta y} \int_0^{\Delta z} P(x,X) P(y,X) P(z,X) dx dy dz \quad (30)$$

Because the integrals are separable and identical in form, differing only in the limits of interest, only one is explicitly evaluated. Using Equations 28 and 29 for this evaluation gives

$$\int_0^{\Delta x} P(\Delta x, X) dx = \sqrt{\frac{a}{\pi}} \int_0^{\Delta x} \exp(-ax^2) dx \quad (31)$$

which readily yields

$$\int_0^{\Delta x} P(x, X) dx = \frac{1}{2} \operatorname{erf}(\sqrt{a} \Delta x) \quad (32)$$

An accurate approximation for a closed form solution to Equation 32 may

be obtained by using an approximation due to Menzel<sup>9</sup>

$$\text{erf}(b) = \left[ 1 - \exp(-4b^2/\pi) \right]^{1/2} \quad (33)$$

Therefore, the solution to the integral is

$$\int_0^{\Delta x} P(x, X) dx \approx \frac{1}{2} \left[ 1 - \exp \left( \frac{-4a\Delta x^2}{\pi} \right) \right]^{1/2} \quad (34)$$

In the limit as  $\Delta x \rightarrow \infty$ , the integral has a value of  $\frac{1}{2}$ . Since in the limit it is required that the particles be somewhere in the box  $\Delta x \Delta y \Delta z$ , the probability of finding the particles separated by some distance  $\Delta x$  is normalized to the value for infinite separation.

$$p(\Delta x) = \frac{\int_0^{\Delta x} P(x, X) dx}{\int_0^{\infty} P(x, X) dx} \quad (a)$$

$$p(\Delta x) = 2 \int_0^{\Delta x} P(x, X) dx \quad (b)$$

$$p(\Delta x \Delta y \Delta z) = \frac{P(\Delta x \Delta y \Delta z)}{P(\infty, \infty, \infty)} \quad (c)$$

Using Equations 34 and 35 in Equation 30 and manipulating variables, a functional relationship for  $p(\Delta x \Delta y \Delta z)$  is obtained

$$p(\Delta x \Delta y \Delta z) = \left[ \left[ 1 - \exp\left(-\frac{\rho_N^{1/3} \Delta x^2}{\pi \delta}\right) \right] \left[ 1 - \exp\left(-\frac{\rho_N^{1/3} \Delta y^2}{\pi \delta}\right) \right] \left[ 1 - \exp\left(-\frac{\rho_N^{1/3} \Delta z^2}{\pi \delta}\right) \right] \right]^{1/2} \quad (36)$$

$p(\Delta x \Delta y \Delta z)$  can be simplified to a somewhat more convenient form

$$p(\Delta x \Delta y \Delta z) = 8^{1/2} \exp \left[ \frac{\rho_N^{1/3}}{4\pi\delta} (\Delta x^2 + \Delta y^2 + \Delta z^2) \right] \times \left[ \sinh \left( \frac{\rho_N^{1/3} \Delta x^2}{2\pi\delta} \right) \sinh \left( \frac{\rho_N^{1/3} \Delta y^2}{2\pi\delta} \right) \sinh \left( \frac{\rho_N^{1/3} \Delta z^2}{2\pi\delta} \right) \right]^{1/2} \quad (37)$$

$p(\Delta x \Delta y \Delta z)$  represents the probability that 2 or more particles will be found in a volume  $\Delta x \Delta y \Delta z$ . By using values of  $\Delta x$ ,  $\Delta y$  and  $\Delta z$  appropriate to the LV probe volume or sample space, an estimate can be made of how often two or more particles may be expected in the probe volume. Note that Equation 36 or 37 shows that

$$\begin{aligned} \lim_{\rho_N \rightarrow \infty} p(\Delta x \Delta y \Delta z) &= 1 & (a) \\ \lim_{\rho_N \rightarrow 0} p(\Delta x \Delta y \Delta z) &= 0 & (b) \end{aligned} \quad (38)$$

which is a result predicted by Poisson statistics and should also be reasonably predicted for these statistics. It should also be noted that while  $\Delta x$ ,  $\Delta y$ ,  $\Delta z$  appear separately in equation 37 and not directly as a volume, equation 37 does not predict that  $p(\Delta x \Delta y \Delta z)$  is shape dependent.  $p(\Delta x \Delta y \Delta z)$  is perfectly symmetric in  $\Delta x$ ,  $\Delta y$ ,  $\Delta z$ . As a result, there is no preferred shape dependence for any one dimension or equivalently for a particular volume shape.

#### THE ACCEPTANCE RATIO

The results from the previous section can now be used to define an experimental parameter called the acceptance ratio,  $A$ .  $A$  is defined as

$$A = \frac{\text{Number of Signals Accepted for Measurement}}{\text{Number of Signals Detected}} \quad (39)$$

where "number of signals detected" is understood to mean those which generate sufficient signal cycles to be measured - both those resulting from single particles and those resulting from 2 or more particles. If it is assumed that the logic circuits in a burst type LV signal processor are totally effective in rejecting all multiple particle signals, then if  $N$  is the total number of signals detected, the number of signals rejected is  $Np(\Delta x \Delta y \Delta z)$  where  $\Delta x$ ,  $\Delta y$ ,  $\Delta z$  are appropriate probe volume or sample space dimensions. With these assumptions and definitions, Equation can be used to express  $A$  as

$$A = 1 - p(\Delta x \Delta y \Delta z) \quad (a) \quad (40)$$

$$A = P(0) + P(1) \quad (b)$$

where  $P(0)$  and  $P(1)$  are the probabilities of finding no particles and a single particle in  $p(\Delta x \Delta y \Delta z)$ . In order to explicitly express  $A$  in terms of LV system parameters, it is convenient to make the following identifications. Assume an LV system similar to that in Fig. 1 capable of measuring one velocity component, then let  $\Delta y$  be the dimension parallel to the velocity component measured. Express  $\Delta y$  as

$$\Delta y = N_L \delta \quad (41)$$

where  $N_L$  is taken to be the average number of observable cycles generated in the LV signal. Let  $\Delta x$  be the dimension perpendicular to  $\Delta y$  and the bisector between the beams (i.e. in the fringe model of the LV it is parallel to the fringe planes). Write  $\Delta x$  as

$$\Delta x = k N_L \delta \quad (42)$$

where  $k$  is a constant which specifies the relative size of  $\Delta x$  and  $\Delta y$ . In practice  $\Delta x \leq \Delta y$ . This may result, for example, from logic constraints in the signal processor or slit apertures placed in the receiver optics to limit the size of the probe volume.  $\Delta z$  is assumed parallel to the bisector between the beams and may be expressed in terms of  $\Delta x$  and  $\Delta y$ . For most LV systems currently in use,  $\Delta z \gg \Delta y$ . For example, if  $\Delta z$  were made to correspond to the length of the transmitted probe volume

corresponding to the average  $e^{-2}$  intensity contour, then

$$\Delta z = \frac{4N_L \delta}{\alpha} \quad (43)$$

where  $\alpha$  is the angle between the beams. A typical value of  $\alpha$  is less than 0.1 making  $\Delta z = 40\Delta y$ . When  $\rho_N^{1/3} \Delta z^2 / 2\pi\delta$  is computed for the range of values commonly encountered in most LV systems and applications, (i.e.  $\Delta z \gtrsim 100\delta$ ,  $\rho_N > 5\text{cc}^{-1}$ ,  $\delta \gtrsim 6 \mu\text{m}$ ) it is found that

$$\sinh \left( \frac{\rho_N^{1/3} \Delta z^2}{2\pi\delta} \right) \approx \exp \left( \frac{\rho_N^{1/3} \Delta z^2}{2\pi\delta} \right) / 2 \quad (44)$$

and

$$\frac{\rho_N^{1/3} \Delta z^2}{2\pi\delta} > 2 \quad (45)$$

It follows for many applications that A will be independent of  $\Delta z$ . With these definitions and approximations, A can be explicitly expressed as

$$A = 1 - 2 \exp \left( \frac{-\gamma}{2} (1 + k^2) \right) \left[ \sinh (\gamma) \sinh (k^2 \gamma) \right]^{1/2} \quad (46)$$

$$\gamma = \frac{\rho_N^{1/3} N_L^2 \delta}{2\pi} \quad (47)$$



Equations 46 and 47 show that if  $N_L$ ,  $\delta$ , and  $k$  (all experimental constants for a given LV system) are known, then a determination of  $A$  can be used to compute  $\rho_N$ . Conversely, specification of  $\rho_N$  with a required  $k$ ,  $N_L$ , and  $\delta$  provides an estimation of the acceptance ratio. If  $A$  is taken as a measure of system performance, then examination of the response of  $A$  for variation in system parameters will show how to optimize the system for expected operational conditions.

#### LV SYSTEM PERFORMANCE

Figure 3 plots  $A$  as a function of  $\gamma$  for selected values of  $k$  between 1.0 and 0.2. As the figure shows, for fixed  $N_L$  and  $\delta$ , significant increases in acceptable  $\rho_N$  for given values of  $A$  can be achieved by reduction of the probe volume cross-section through apertures (a fact well known to anyone who has used an LV). Figure 4 graphically illustrates this dependence by plotting  $\gamma$  as a function of  $k$  for selected values of  $A$ . The figure shows, for example, that if  $A = 0.1$ , then reducing  $k$  from 1 to 0.2 when  $N_L$  and  $\delta$  are held constant results in an effective increase of acceptable  $\rho_N$  by a factor of nearly 8,000.

In applying an LV to a turbulent flow measurement, it may be necessary to add particles to the flow to satisfy sampling rate requirements. However, Fig. 3 shows that as the particle number density (i.e.  $\gamma$ ) increases, the acceptance ratio decreases. Eventually, the number density will reach a level where the data rate actually decreases with increasing number density because the acceptance ratio has become so small. As the number density increases, a point will be reached where

numerous particles always exist in the sample space and either it becomes expedient to switch to a local oscillator optical system or to use signal processors which optimally function with continuous type signals. The above analysis can be used to estimate the maximum number density which can continue to increase the data rate when all other system parameters are fixed. Note that the data rate  $\dot{\eta}$  can be written as

$$\dot{\eta} = \dot{N}A \quad (48)$$

where  $\dot{N}$  is the rate at which particles pass through the sample volume. Assume that the time scales involved are such that  $A$  can be assumed constant and that the flow velocity,  $\tilde{V}$ , is constrained to the dimension normal to the cross-sectional area  $a_{pv}$  of the sample space, then  $\dot{N}$  can be written as

$$\dot{N} = \rho_N \tilde{V} a_{pv} \quad (49)$$

combining Equations 48 and 49, taking the derivative with respect to  $\rho_N$ , and making use of Equation 47, there results

$$\frac{\partial \dot{\eta}}{\partial \rho_N} = \tilde{V} a_{pv} \left[ A + \frac{\gamma}{3} \frac{\partial A}{\partial \gamma} \right] \quad (50)$$

$\dot{\eta}$  is an extreme when the bracketed term in Equation 50 is zero. Using Equation 48 and performing the indicated algebra in Equation 50, it is found that  $\frac{\partial \dot{\eta}}{\partial \rho_N}$  is an extreme when

$$A = \frac{\frac{\gamma}{6} (1 - \coth(\gamma)) + k^2 (1 - \coth(k^2\gamma))}{\frac{\gamma}{6} (1 - \coth(\gamma)) + k^2 (1 - \coth(k^2\gamma)) - 1} \quad (51)$$

Figure 5 plots A as a function of  $\gamma$  for various values of k for optimum data rate. The figure shows the interesting result that after k reaches about 0.5, A becomes nearly constant. This means that the acceptance ratio or equivalently the LV sampling efficiency cannot be improved by, for example, further reduction of the sample space cross-section via apertures. However, further reduction of k will provide an increase in the data rate for increasing number density.

For the case where A is chosen to yield a maximum value for  $\dot{\eta}$  as a function of  $\rho_N$ ,  $\gamma$  is assumed constant. Solving Equation 47 for  $\rho_N$  with  $\gamma$  constant yields

$$\rho_N = \frac{(2\pi\gamma)^3}{N_L^6 \delta^3} \quad (52)$$

Equation 52 shows this extreme value of  $\rho_N$  is much more drastically affected by the number of signal cycles generated by a scattering particle than by the absolute magnitude of the LV fringe period. Hence, in seeking to optimize data rates for a particular LV geometry, it is most expedient to reduce the number of cycles in the signal rather than to change the fringe period.

## NUMBER DENSITY DETERMINATION

In this section, the results of experimental applications of the expression derived for A in the previous section are described. It is very difficult to produce a direct quantitative comparison of experiment with theory since there are no generally accepted calibration standards for number density. In this section, the results of three experimental comparisons are described. The results, while inferential, suggest that the previously computed expression for the acceptance ratio does yield reasonably good results.

The first set of results reported here were obtained with a particle sizing interferometer (PSI) in a laboratory chamber test and in an outdoor field test. Details of these tests may be found elsewhere.<sup>10</sup> Only a brief sketch of the experiments is presented here.

The optical geometry for the PSI is shown in figure 6. The system was arranged to measure a particle size range of 0.3 - 6.0 micrometres. The smallest particle size detectable with the system was estimated to be approximately 0.2 micrometres for water droplets. This PSI used a 5 milliwatt HeNe laser and F/2.2 receiving lens. Data obtained with the PSI signal processor and data acquisition system in these experiments were recorded on magnetic disks for hard copy presentation and data storage. The PSI measured particle velocity, signal magnitude (which is also a measure of particle size), the PSI size parameter-visibility, and the acceptance ratio.

The laboratory measurements were conducted in a sealed box with an atmosphere initially at ambient temperature and humidity conditions.

The PSI system was placed directly inside the chamber. Filter samples and samples obtained with an Andersen Cascade Impactor were obtained via samples drawn from wall ports.

Phosphorus and HC smokes were generated by igniting small samples at one end of the chamber. Fog oil, while not hygroscopic, was easy to generate using a small commercially available fog oil generator and it also was measured using both PSA systems. Mass concentration as a function of time was obtained using filter samples which trapped a portion of the smoke withdrawn from the chamber at a fixed flowrate.

Figure 7 shows a comparison of concentration estimates obtained mechanically by weight and that obtained using PSI acceptance ratio data. The concentration,  $C$ , was computed from

$$C = \frac{\pi}{6} \rho \mu_3 \rho_N \quad (53)$$

where  $\rho$  is the material density, and  $\mu_3$  is the third moment of the size distribution. A major uncertainty in the comparison is the material density of the smokes measured. Orthophosphoric acid (density = 1.28 gm/cc at 82% RH) is assumed for red phosphorus and for fog oil a density of 0.9 gm/cc is assumed.

As Figure 7 shows, agreement between the concentration estimate using the acceptance ratio data and that determined by weighing is surprisingly good.

It is of interest to compare the number density determined by the acceptance ratio using equation 46, i.e. for a random walk sample space

for the data in figure 7 and that obtained using commonly used Poisson or Gaussian statistics. Poisson statistics yield an acceptance ratio given by

$$A(P) = (1 + \rho_N v) e^{-\rho_N v} \quad (54)$$

Gaussian statistics ( $\rho_N v \gg 1$ ) yield

$$A(G) = 1 - \frac{\exp(-(2 - \rho_N v)^2 / 2\rho_N v)}{\sqrt{2\pi\rho_N v}} \quad (55)$$

The same parameters entering into the computation of  $\gamma$  were used to compute  $V$  and subsequently  $\rho_N$  using  $A(P)$  and  $A(G)$ . Figure 8 shows that  $A(P)$  and  $A(G)$  yield number density values which are significantly in excess of those estimated via the random walk sample space. If these  $\rho_N$  values were used with the PSI size distribution data, mass concentration would have been significantly overestimated for the data shown in figure 7. It may be argued that there may be compensating errors in the PSI data, i.e. it overestimates  $\mu_3$  and  $\rho_N$  is underestimated. However, comparison of PSI size data with that from other optical counters shows that third moments in the measured size distribution agree within 10%. Compensating errors would require that  $\mu_3$  be roughly a factor of 4 too large which seems unlikely in lieu of agreement between particle size analyzers.

The same PSI system was also used in a series of field measurements on the same kind of particles as those examined in the laboratory chamber tests. In the field measurements, the PSI was placed within 3m of a commercially available optical particle counter (Climet). This device

dilutes a sample of the aerosol in order to count individual particles. It is claimed that by dilution, this device can determine particle number densities approaching  $10^6 \text{ cc}^{-1}$ . The field tests involved measurements of spatially inhomogeneous clouds over times of 5 - 10 minutes. Figure 9 shows typical results of the two independent number density determinations in 14 separate test trials. A linear regression of these data shows that the two measurements are related by

$$\rho_N(\text{CLIMET}) = 0.2\rho_N(\text{PSI}) + 2.48 \cdot 10^4 \quad (56)$$

with a correlation coefficient of 0.58. The slope obtained for the linear regression is in surprisingly good agreement with the fact that 80 - 90% of the PSI measured size distribution was beyond the size range capability of the Climet. In view of the fact that the two devices 1) examined a spatially nonhomogeneous cloud with a separation of about 3m, 2) covered different size ranges, and 3) one device required aerosol dilution, agreement between the two sets of data is surprisingly good.

The third comparison is actually an examination of the internal consistency of a set of measurements. These data were obtained in a smelter operating at  $2760^\circ \text{ C}$ . The particles measured are believed to be slag particles from the walls of the smelter. The number density for these measurements has been estimated using the random walk sample space acceptance ratio and from the equation

$$\rho_N = N / \bar{v}_{pv} \Delta t \quad (57)$$

$\bar{v}_{pv} \Delta t$  will be called the standard volume.

N is assumed to be the number of measurements satisfying the requirement that the signal have a minimum number of cycles.  $\bar{V}$  is the average speed measured for the ensemble of measurements and  $\Delta t$  is the ensemble acquisition time. Water cooled probes were used to limit the probe volume length to approximately 2.5 cm. The fringe period of the system was 36.6 micrometres and signal observation with an oscilloscope showed that the maximum number of cycles in the probe volume was approximately 12. The signal processing electronics required the signal to have a minimum of 6 cycles. Assuming a rectangular cross-section, the maximum value of  $a_{pv}$  is computed to be approximately  $9.3 \cdot 10^{-2} \text{ cm}^2$ . For the optical geometry in these experiments,  $K = 1$ , and equation 46 reduces to

$$A = e^{-2\gamma} \quad (58)$$

Using equation 47 and solving equation 58 for  $\rho_N$ , there results

$$\rho_N = \left( \frac{\pi}{N_L^2 \delta} \right)^3 \ln^3(A^{-1}) \quad (59)$$

A value of 8 (as determined by oscilloscope observation) was assumed for  $N_L$ . Table I lists the experimental values used in the computation of  $\rho_N$  using equations 59 and 47. Note that by comparison with the first set of experiments, the A values are quite large. The number of particles producing signals with too few cycles to process was typically 25% more than N.

Comparison of  $\rho_N$  computed from equation 57 with that computed using equation 59 shows that when  $A \geq 0.88$  agreement between the two estimates



differs by no more than about 15%. In these cases,  $N$  was very close to all particles detected, the turbulence intensity (velocity distribution standard deviation/mean velocity) was about 20%, the observed size range was relatively narrow, and relatively few signals were due to multiple particles. As  $A$  decreases, the observed size distribution becomes broader (with several predominant mode sizes) and  $\Delta t$  becomes less representative of the time required to sample  $N$ . Hence, the greatest divergences in the estimates should occur when the true  $\rho_N$  is the largest. The standard volume calculation shows roughly the same particle concentration for all values of  $A$ . Experimentally, this is known not to be the case. When the random walk value of  $\rho_N$  is roughly greater than  $20 \text{ cc}^{-1}$ , the smelter was much cooler and the observed particle concentration was expected to be much higher than for conditions where the temperature was near  $2700^\circ \text{ C}$ . Finally, ultraviolet transmission measurements were found to yield consistent number densities predicted using the random walk sample space. Note in examining the values in Table I that very small changes in  $A$  correspond to rather large changes in  $\rho_N$ . This is consistent with the plot for  $K = 1$  in figure 3. What is surprising to this author is how well the model apparently predicts  $\rho_N$  when  $\rho_N$  is small. It is of interest to note that when Poisson statistics are used to estimate  $\rho_N$  for the measured values of  $A$ , that number densities of  $400 - 800 \text{ cc}^{-1}$  are predicted for the data. These values were found to be inconsistent with the UV transmission measurements.

## SUMMARY AND CONCLUSIONS

A random walk analysis has been used to predict how often two or more particles will appear in a randomly varying sample volume of an LV system. From this model, the acceptance ratio is defined and applied to the evaluation of fringe type LV system performance as a function of particle number density and the estimation of particle number density when the acceptance ratio is measured. This model leads to the following conclusions:

1. For coaxial optical systems, the acceptance ratio is a function of the probe volume cross-section geometry and is essentially independent of the optical system depth-of-field.
2. It is found that as number density increases, the acceptance ratio decreases. Thus, data rate for an LV cannot be increased indefinitely by increasing  $\rho_N$ . For a given optical system geometry, there exists an optimum acceptance ratio beyond which the data rate will decrease.
3. When the number density is constant, it is found that the acceptance ratio increases as  $k$ , the probe volume cross-section ratio, decreases.
4. When  $k$  reaches a value of about 0.5, the acceptance ratio will not significantly improve as the number density is increased and  $k$  is decreased. The data rate can be increased by decreasing  $k$  as number density increases.
5. Comparison of number density estimates via the random walk acceptance ratio with other experimental methods such as optical

particle counters and mass concentration measurements shows that the acceptance ratio method yields reasonable results.

6. The acceptance ratio was not found to yield number densities consistent with experiment when constant sample volumes were used with Poisson or Gaussian statistics which attempt to estimate the probability of two or more particles in the sample volume on the basis of mean numbers of particles in the sample volume.
7. The acceptance ratio method can be used to estimate number density with conventional LV fringe type optical systems and burst signal processors with modest modification and system calibration to determine  $k$ .

The limitations and potential modifications of this model should be clearly understood. The model does not directly account for number density as a function of particle size.  $N_L$  will ultimately be a function of particle size. Using an average  $N_L$  determined experimentally thus weights the number density estimate toward those sizes most frequently giving a measureable signal. In light of experimental results, this appears to be a reasonable approach. There is, however, considerable room for model refinement in this area. For example, this technique assumes all multiple particle signals are detected. This is known to not be the case when  $A$  is small and the model accuracy can be expected to hinge directly on signal processor efficiency in detecting such signals. It should also be realized that when the particle number density becomes so high that optical transmission becomes limited, the LV system cannot function and the model must fail.

Thus, future refinements must also include transmission effects.

Experimentally, it has been determined that the instrument and model appear to work well for transmittances as low as 80%.

## REFERENCES

1. Fuchs, N. A. The Mechanics of Aerosols, Pergamon Press, New York, (1964).
2. Liu, B. Y. H. (Editor), Fine Particles, Academic Press, New York, (1976).
3. McGregor, W., "Some Problems with Gas/Particle Diagnostics in Solid Propellant Combustion," AIAA Paper 79-0084, Presented at the 17th Aerospace Sciences Meeting, New Orleans, LA, January 15-17, 1979.
4. Chandrasekar, S., "Stochastic Problems in Physics and Astronomy," Rev. Mod. Phys. 15, 1-89 (1943).
5. Erdmann, J. C. and R. I. Gellert, "Particle Arrival Statistics in Laser Anemometry of Turbulent Flow," Appl. Phys. Letters, 29, 408-411 (1976).
6. Papoulis, A., Probability, Random Variables, and Stochastic Processes, McGraw Hill, New York, (1965).
7. Farmer, W. M., "Sample Space for Particle Size and Velocity Measuring Interferometers," Appl. Optics 15, 1984-1989 (1976).
8. Feller, W. An Introduction to Probability Theory and Its Applications, 2nd. ed., Wiley, New York, (1971).
9. Menzel, R. "Approximate Closed Form Solution to the Error Function," Am. V. Phys., 43, 366-367, (1975).
10. Farmer, W. M., R. D. Morris, F. A. Schwartz, and R. H. Doherty, "Optical Particle Size Measurements of Hygroscopic Smokes in Laboratory and Field Environments," Submitted to Applied Optics, June 1980.

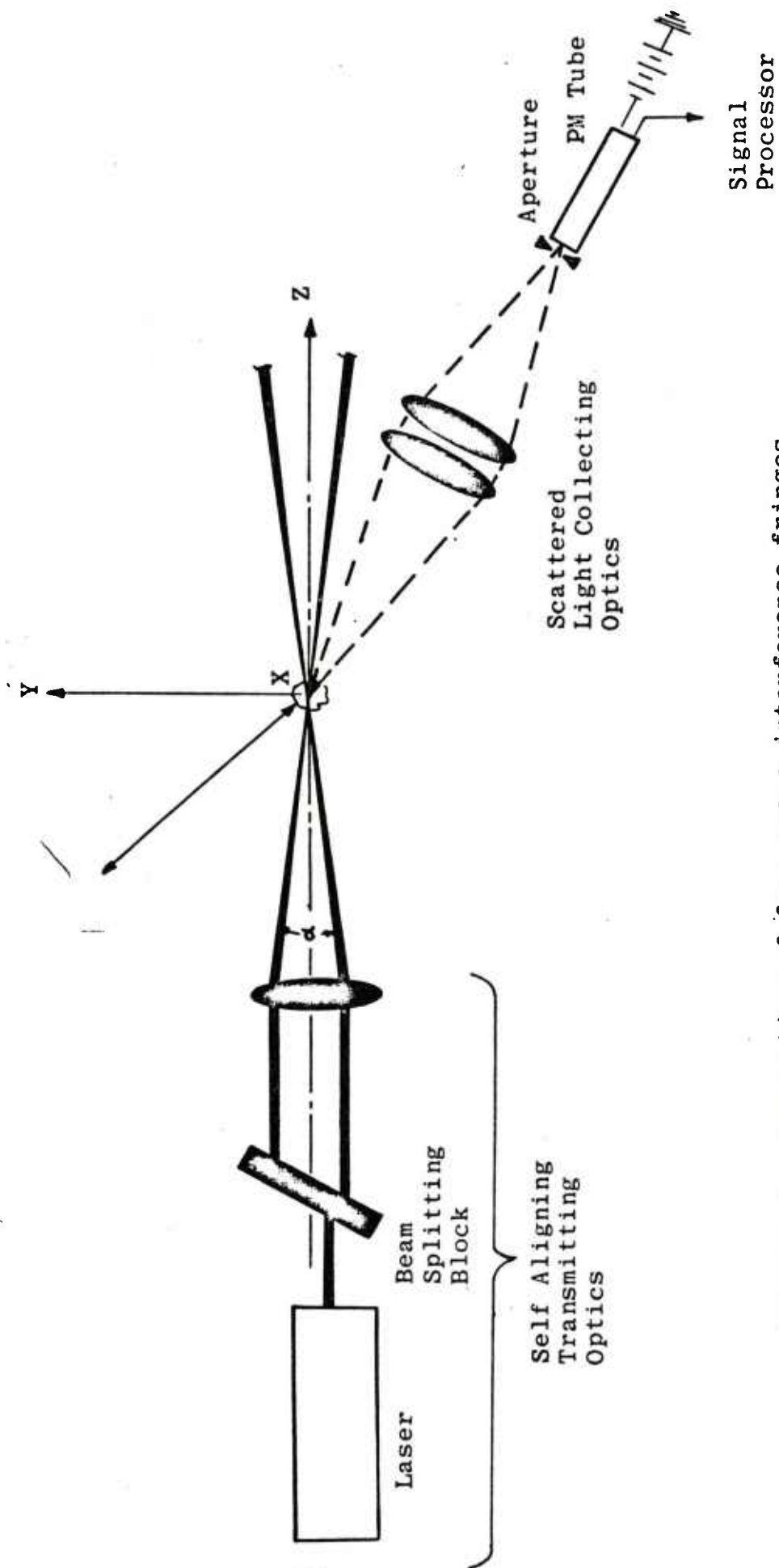


Figure 1. Generation of free space interference fringes with a laser Doppler velocimeter system.

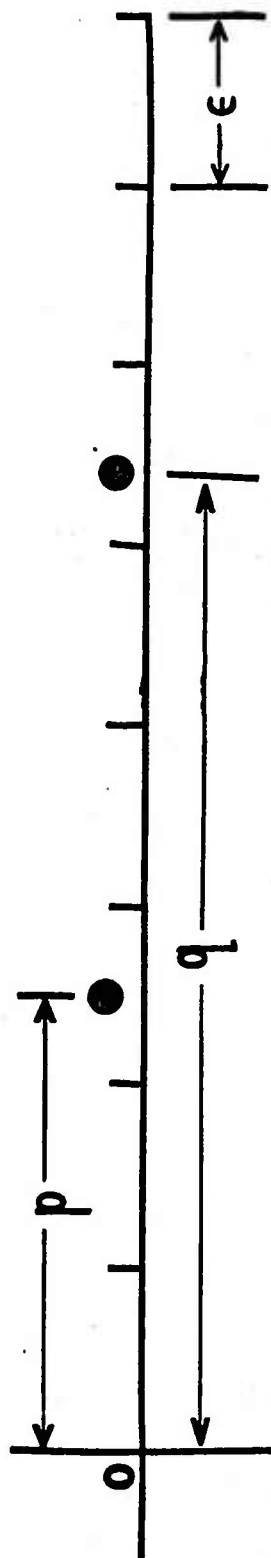


Fig 2 Visualization of  $p$ ,  $q$  and  $\epsilon$ .

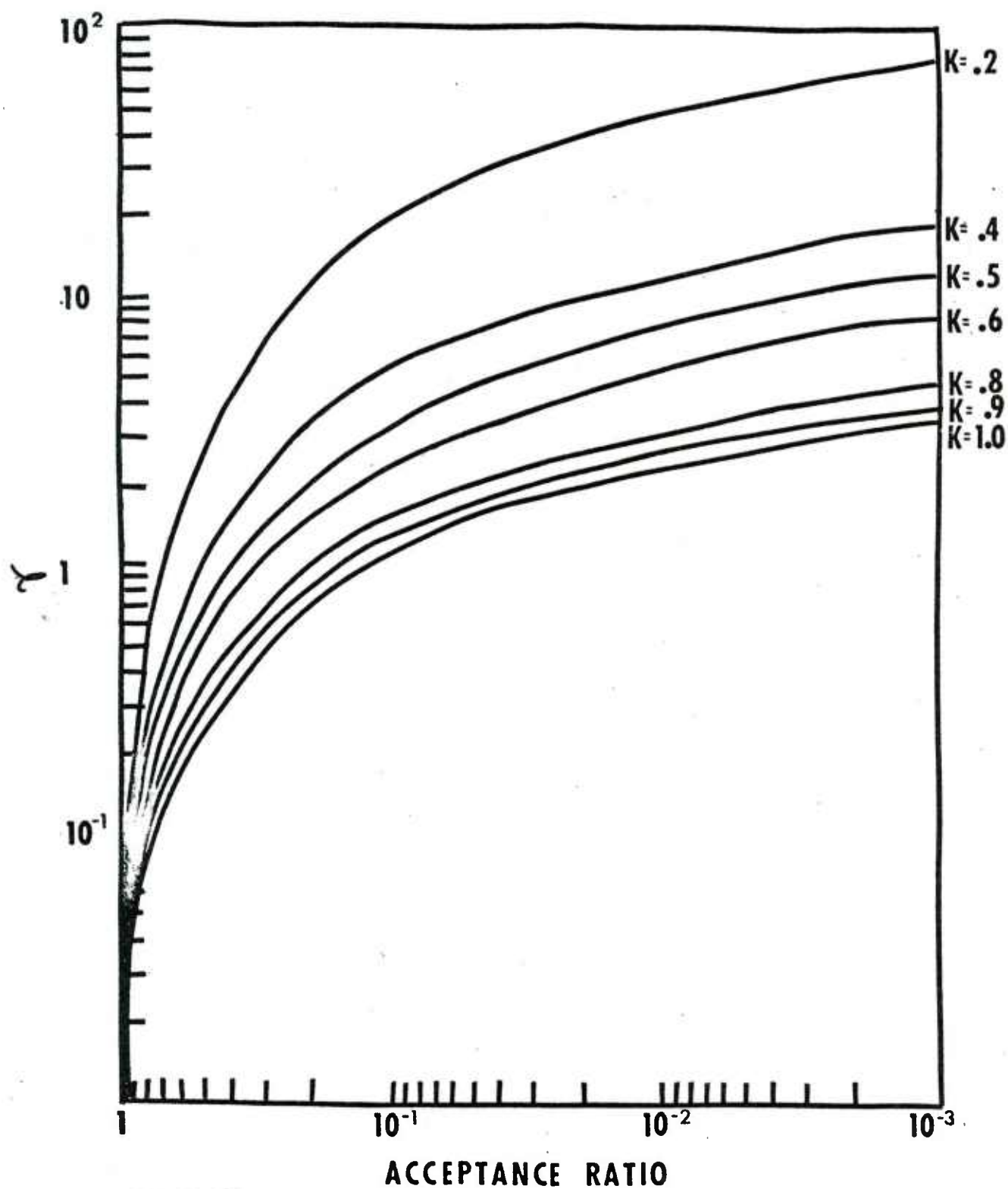


Fig. 3.  $A$  as a Function of  $\gamma$  With  $K$  as a Parameter.



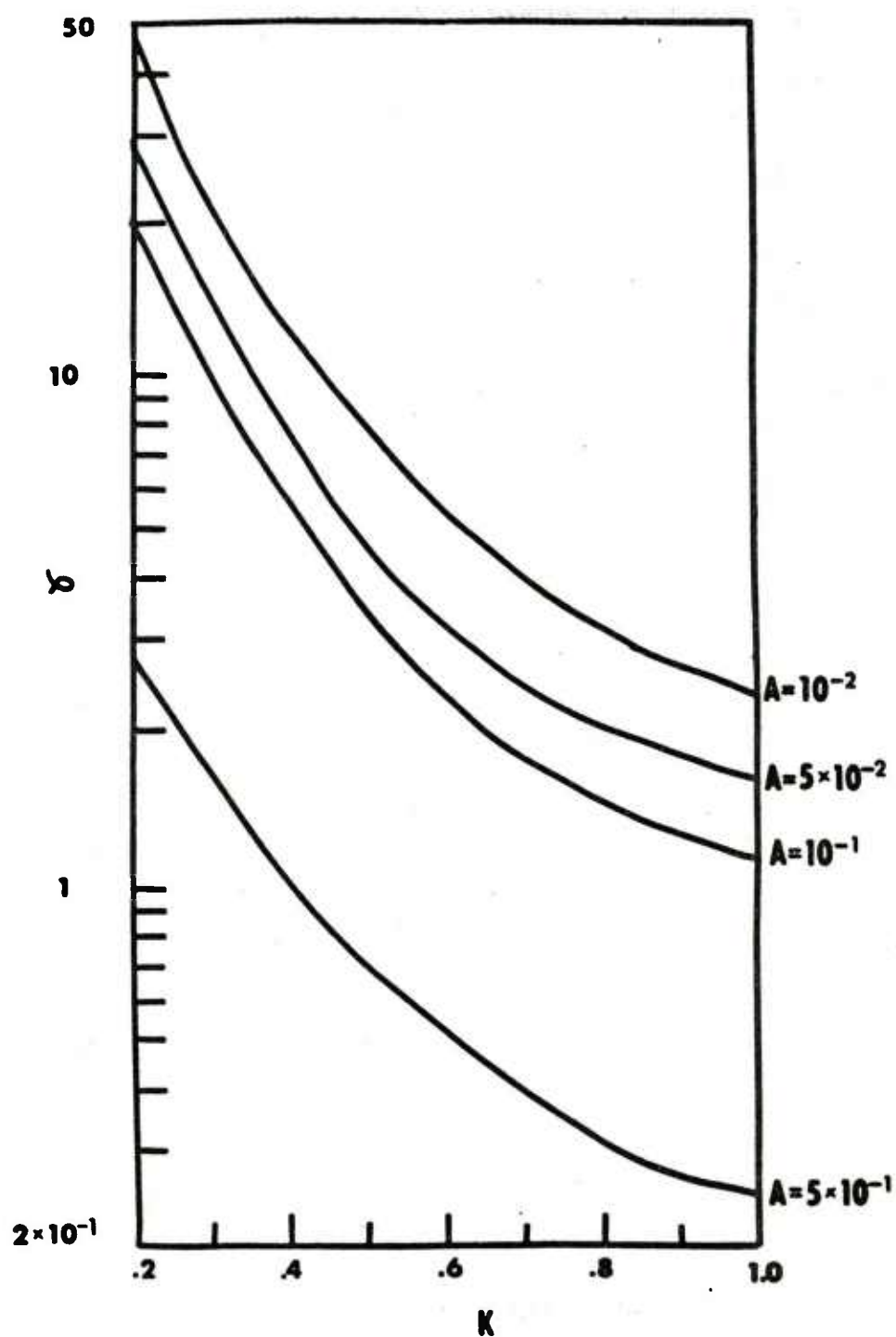


Fig. 4.  $\gamma$  as a Function of  $K$  With  $A$  as a Parameter.

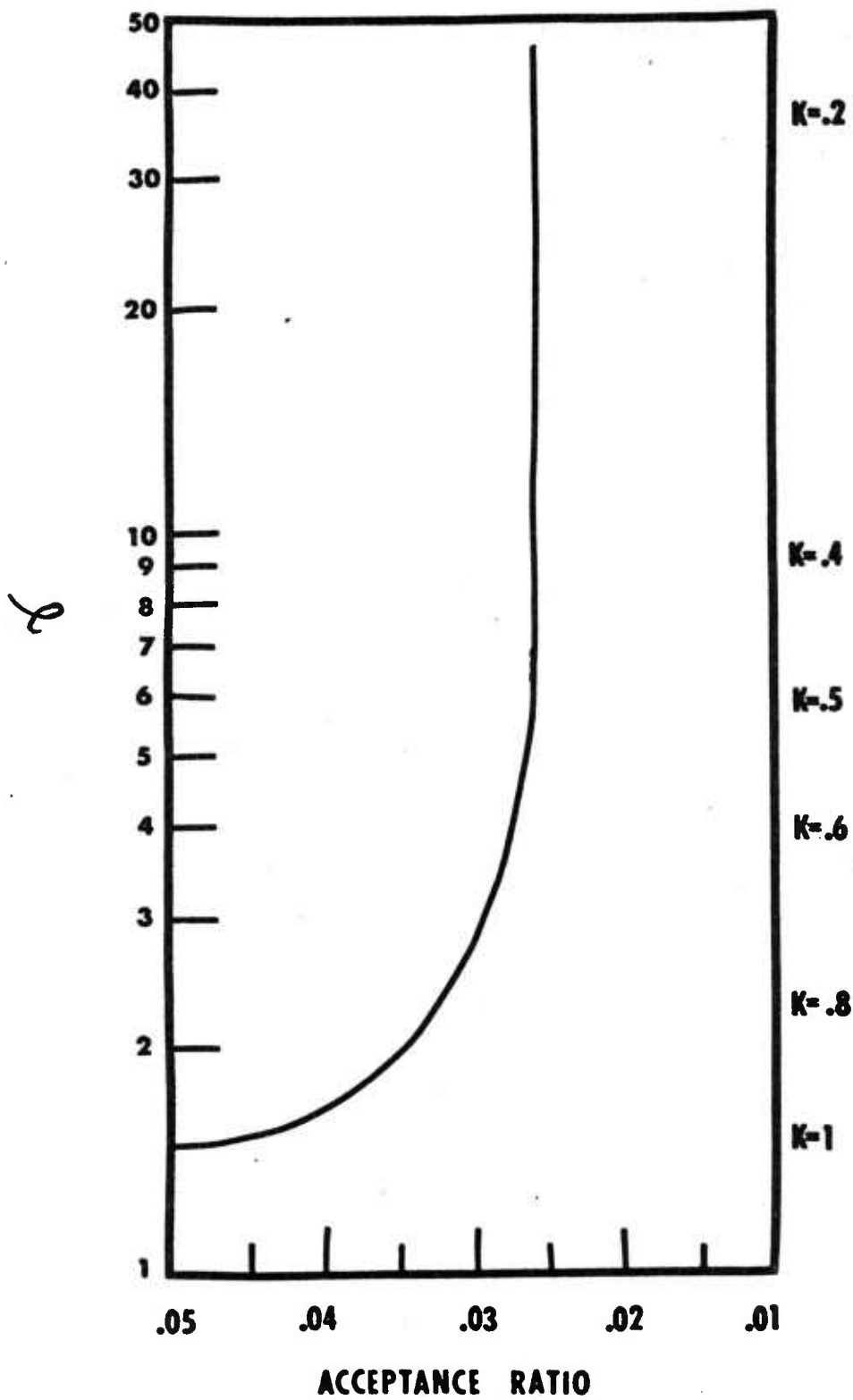


Fig. 5 Optimum A for Maximum Data Rate.

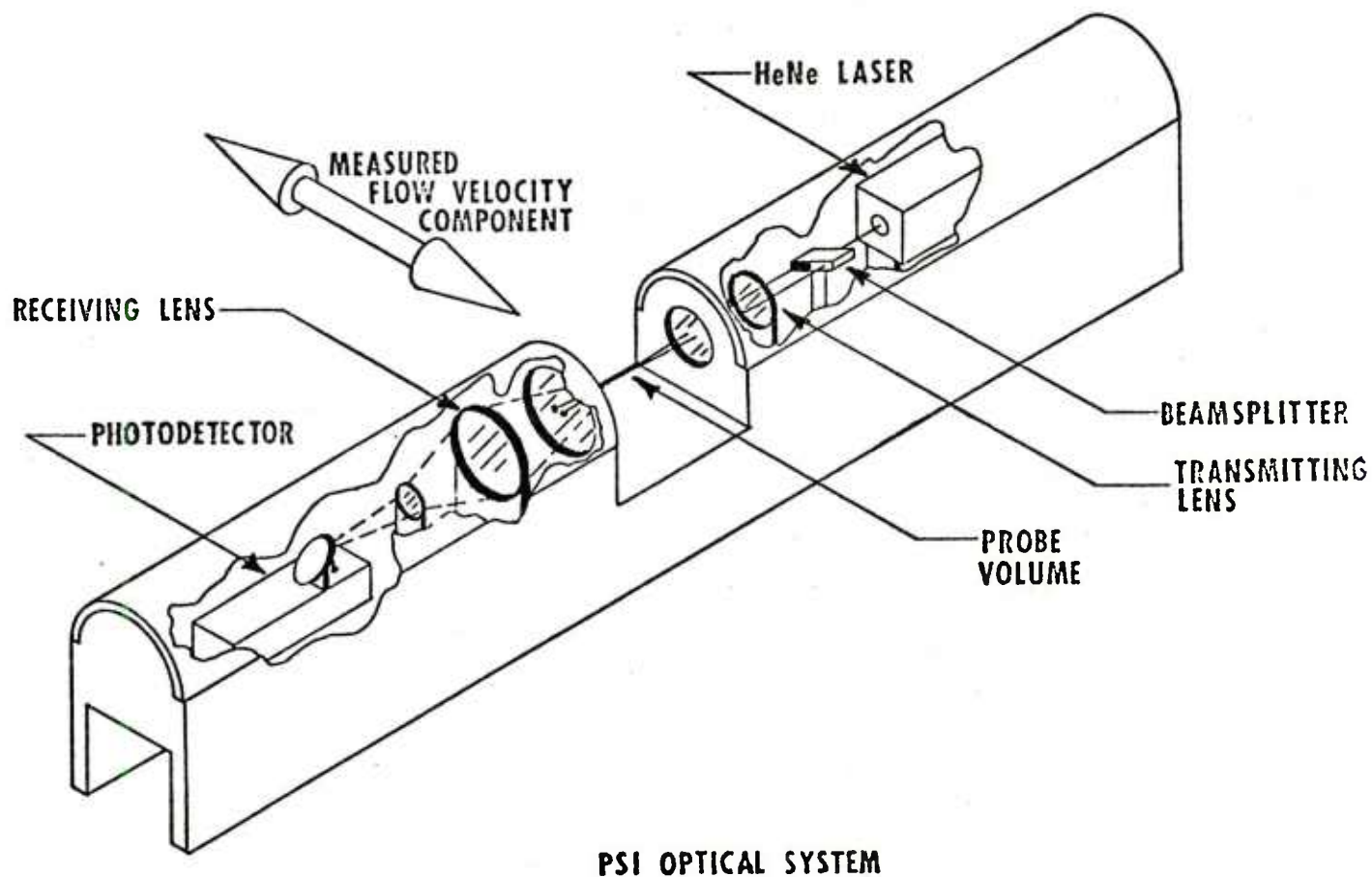


FIGURE 6. Schematic of the PSI optical system used in the laboratory and field measurements.

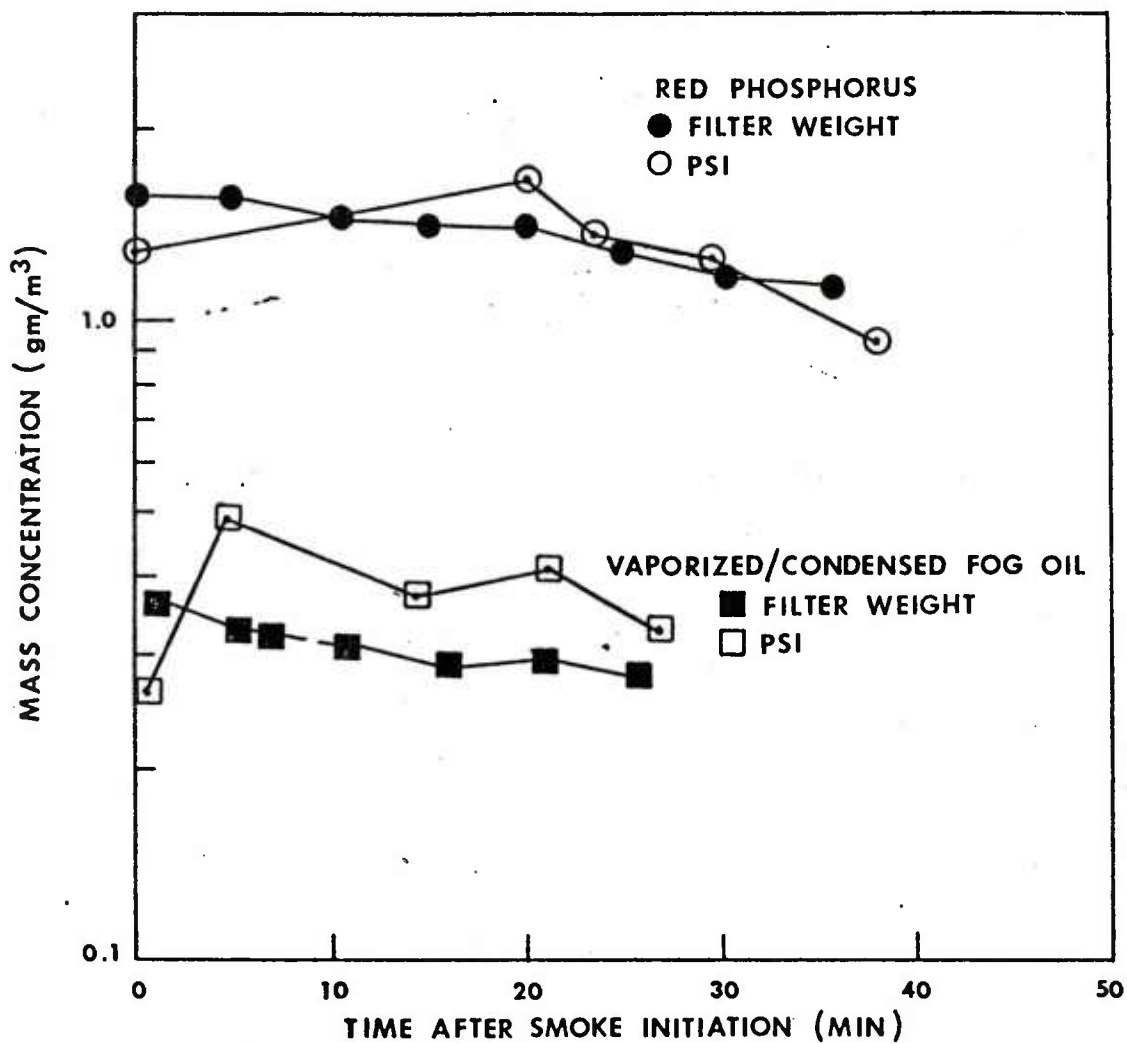


Fig. 7. Comparison of mass concentrations as determined by filter weights and PSI measurements for red phosphorus and vaporized condensed fog oil smokes.

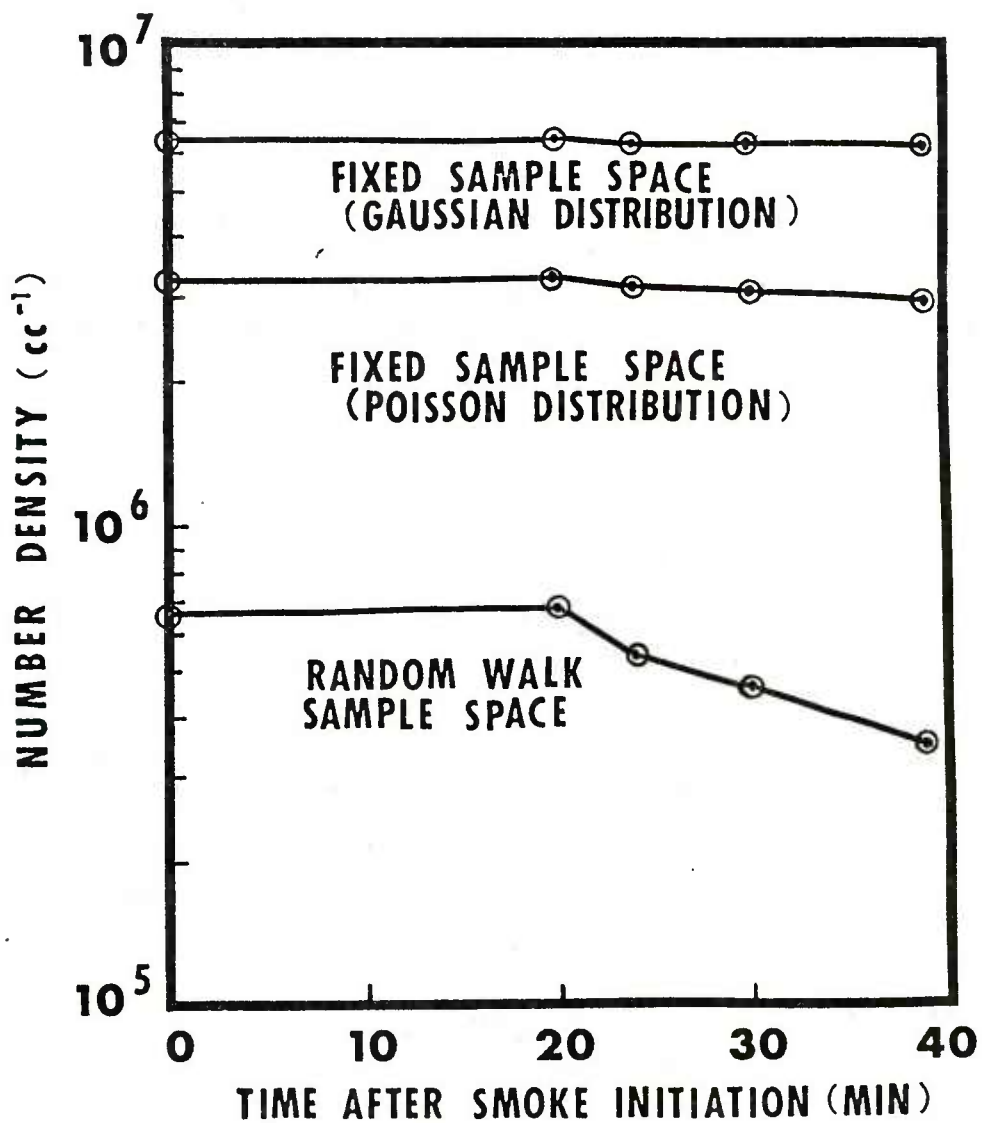


Fig. 8. Comparison of number densities for the smoke data in Fig. 1. as estimated using three statistical models.

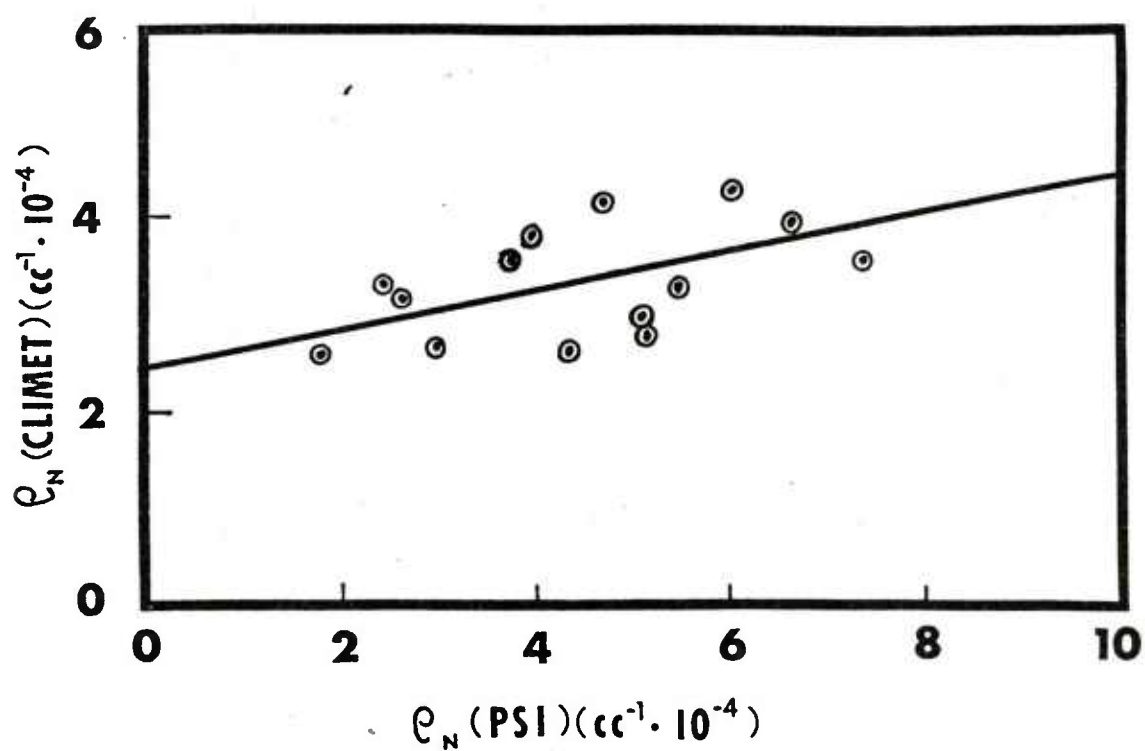


Fig. 9. Comparison of number densities as determined by a single particle counter and that using a random walk sample space model.

### APPENDIX III

OPTICAL PARTICLE SIZE MEASUREMENTS  
OF HYGROSCOPIC SMOKES IN  
LABORATORY AND FIELD ENVIRONMENTS

W. M. Farmer , R. D. Morris , F. A. Schwartz

ABSTRACT

Optical Particle Size Analyzer (PSA) measurements of hygroscopic smokes are reported from experiments conducted in laboratory chambers and in field tests. Three different instruments were used: a particle sizing interferometer, a Climet (model 211), and a Particle Measurements System CSASP-100-HC. Field measurements were made under relative humidity conditions ranging between 65 and 97%. The results indicate that the size distributions are at least bimodal - not log-normal - and that mean particle diameter does not appear to increase with increasing relative humidity.

INTRODUCTION

Hygroscopic smokes form a major portion of the conventional obscurants inventory of the U. S. Army. Additionally, there exist numerous other particle sources which are thought to be hygroscopic. Changes in the shape of the particle size distribution as relative humidity increases is of fundamental importance in describing the optical properties of these smokes. For example, predictive models hypothesize



that the particle sizes in the distribution increase as relative humidity increases.<sup>1</sup> As a result, optical transmission through such smokes may significantly decrease over a broad range of wavelengths.

In an attempt to produce a solid base of field test data on the performance of conventional hygroscopic smokes at RH values greater than 60% and to begin resolution of data differences, the U. S. Army PM Smoke Office conducted the High Humidity Hygroscopic Smoke ( $H^3S$ ) field test at the Edgewood Area of Aberdeen Proving Ground during July 1979.

During the  $H^3S$  test, particle size distribution data were obtained under conditions which allowed the results from the PSA systems to be reasonably compared (i.e. close spatial positions and similar size ranges). These particle sizing systems were 1) a particle sizing interferometer operated by the University of Tennessee Space Institute and 2) a Climet operated by Dugway Proving Grounds (DPG).

The initial intent was to compare the PSA systems in a small laboratory test chamber immediately before they were moved to the  $H^3S$  test. In this way specific differences in PSA data under controlled conditions could be identified and data could be obtained by the same instruments in both laboratory and field environments. Because of shipping difficulties, one of the PSA systems (a Climet operated by DPG) did not arrive in time for the laboratory comparison. However, the second PSA system (a Particle Sizing Interferometer operated by UTSI) was used in both the field test and in a laboratory comparison with a Particle Measuring Systems PSA (PMS CSASP-100-HC) operated by the Research Division of the Chemical Systems Laboratory. Direct comparison of laboratory and field test

results can thus be made only for data obtained with the particle sizing interferometer.

In reporting these results, the objectives of this paper will be to:

1. Compare hygroscopic particle size distribution data obtained from three (3) different optical PSA systems operating in laboratory and/or field conditions.
2. Present results for the measurement of size distributions of hygroscopic smokes under conditions of high RH.
3. Test the hypothesis that particle size increases with increasing RH.
4. Determine how well PSA concentration estimates compare with chemical impinger data.

To achieve these objectives, the pretest PSA comparison and subsequent results are first described. Next, PSA results obtained during  $H^3S$  and examples of size distributions as measured by the PSA systems are given. The measured effects of RH on mean particle size are shown and concentration estimates obtained with the particle sizing interferometer are compared with those obtained with a nearby chemical impinger.

#### PRETEST PSA COMPARISON

The optical geometry for the PSI is shown in Figure 1. The system was arranged to measure a particle size range of less than 0.3 - greater than 6.0 micrometres. The smallest particle size detectable with the system was estimated to be approximately 0.2 micrometres for water droplets.

This PSI used a 5 milliwatt HeNe laser, and F/2.2 receiving lens. A detailed description of the theory and operation of the PSI system is given in references 2-5. The PSI functions on the principle that particle sizes can be determined by measurement of a signal shape parameter from light scattered out of a localized fringe pattern called the probe volume. Both particle size and velocity data are obtained with a PSI. Data obtained with the PSI signal processor and data acquisition system in these experiments were recorded on magnetic disks for hard copy presentation and data storage. The PSI measured particle velocity, signal magnitude (which is also a measure of particle size), the PSI size parameter-visibility, and a particle number density parameter. The particle size histogram was divided into 21 bins corresponding to 0.3 micrometre size increments ranging from all detectable particles less than 0.3 to all greater than 6.0 micrometres.

The PMS CSASP-100-HC uses an intake horn to shape an air flow drawn through the instrument with a small fan. The device uses a 5 milliwatt HeNe laser and measures the scattered signal magnitude observed with a lens in the forward scatter direction. The signal magnitudes (corresponding to equivalent latex sphere diameters) are sorted into histogram bins beginning at 0.3 micrometres and increasing in 0.04 micrometre increments to 1.0 micrometre where the bin width increases to 0.1 micrometre. The last two histogram bins cover 1.8 - 2.1 and 2.1 - 2.4 micrometres. For this experiment the histogram bin counts were read and recorded manually from a panel display on the PMS data acquisition and signal processing system.

The laboratory measurements were conducted in a sealed box with an

atmosphere initially at ambient temperature and humidity conditions. Figure 2 schematically illustrates the experimental arrangement for the measurements. The PSI system was placed directly inside the chamber. Filter samples and samples obtained with an Andersen Cascade Impactor were obtained via samples drawn from wall ports. Since the PMS particle analyzer measurements become uncertain due to the probability of multiple particle signals when particle number density is high, it was necessary to first dilute the smoke by allowing it to enter a dilution chamber through a small hole (diameter approximately 3 mm) in the side of the main chamber.

Phosphorus and hexachloroethane (HC) smokes were generated by igniting small samples at one end of the chamber. Fog oil, while not hygroscopic, was easy to generate using a small commercially available fog oil generator and it also was measured using both PSA systems. After initial smoke generation, the smoke was given time to become evenly dispersed in the chamber. During this time the operating parameters for the PSI were set and the other instruments tested for operational readiness. A common clock was used to synchronize time for all instrument samples. Transmissometer recordings were made continuously on strip charts. As soon as filter samples were obtained they were weighed to minimize any evaporation losses. The PSI data acquisition system was instructed to obtain chronological histograms of  $10^3$  counts each and to record all data on magnetic disks. The PMS system was manually interrogated at approximately 10 minute intervals. A typical test might run 30 to 60 minutes, after which the chamber was exhausted in preparation for the next test.

Transmissometer measurements were used to compute an optical depth as a function of time after smoke initiation. Mass concentration as a function of time was obtained using filter samples which trapped a portion of the smoke withdrawn from the chamber at a fixed flowrate. Since it has been assumed that these smokes follow log-normal distributions, the geometric mean and standard deviations for the PSA data were estimated. The PMS data were plotted on log-probability paper to obtain the geometric mean diameter and logarithmic geometric standard deviation and to determine how closely the distribution approximated a log-normal distribution. PSI data were used to compute the probability density, geometric mean diameter, geometric standard deviation and particle number density. The method of estimating particle number density is new and described in a recent UTSI report.<sup>6</sup> By using the PSI measured distribution functions, a mean particle volume was computed which together with the particle number density estimates provided an estimate of the mass concentration.

#### EXPERIMENTAL RESULTS FROM LABORATORY MEASUREMENTS

Table I shows a comparison of typical data for the three smokes examined: HC, red phosphorus, and fog oil. Geometric mean diameter, geometric standard deviation and third moments are compared for the particle size distributions determined by the PSI and the PMS CSASP. It should be borne in mind when comparing these data that the PSI counted and recorded particles less than 0.3 micrometres in diameter while the PMS system began at 0.3 micrometres and the smoke entered a dilution chamber through a relatively small hole prior to measurement. There is surprisingly good agreement between the two measurements when the geometric means are compared.

The agreement is deceptive however. The PSI measurements include a large number of particles less than 0.3 micrometres in diameter. This becomes apparent when the logarithmic geometric standard deviations are compared. The PSI values are typically 20 - 30% greater than those measured by the PMS system. This results from the fact that the PMS system measured virtually no particles greater than 1.0 micrometres in diameter. The PSI, on the other hand, typically found 3 - 4% of the distribution was greater than 1.0 micrometre. This difference is significant when the third moments of the distribution are computed in order to estimate mass concentration. The PSI third moments are roughly a factor of 10 greater than the PMS values. A number density estimate could not be obtained from the PMS system since the smokes were diluted before measurement. The number density column in Table I is the estimate obtained with the PSI. In order to indicate the fraction of particles less than 0.3 micrometres measured by the PSI, a column labeled %  $\leq 0.3 \mu\text{m}$  provides the probability density amplitudes for this size fraction. Figure 3 shows a comparison of concentration estimates obtained mechanically by weight and that obtained using PSI data. A major uncertainty in the comparison is the material density of the smokes measured. Orthophosphoric acid (density = 1.28 gm/cc at 82% RH) is assumed for red phosphorus and for fog oil a density of 0.9 gm/cc is assumed. Agreement between the filter and the PSI estimates is remarkably good for the red phosphorus and fog oil when the large differences in the two methods to arrive at the concentrations are considered. The PSI technique is purely optical and subject to any localized variations in number density which may exist in



the test chamber. The filter method of determining the concentration is purely mechanical - the smoke is pulled to the filter at a fixed flowrate for a fixed time interval and weighed.

Figures 4 through 6 plot examples of the particle size distributions obtained with the PMS system. The deviations from the straight line fits to the data occur where the particle counts are relatively small and potential uncertainties large. As the figures show, the PMS size distributions are represented reasonably well by log-normal distributions with mean diameters and logarithmic standard deviations indicated in the figures.

Figure 7 shows representative probability density functions as measured by the PSI for the smokes and for the background aerosol present in the laboratory where the measurements were made. The data clearly show the contribution of the smokes to the small particle background. The strong multimodal characteristic of the fog oil smoke is a result consistently seen in a large number of different tests.

#### RESULTS OF PSA FIELD TEST MEASUREMENTS

After the pretest laboratory calibration, the PSI was moved to position in the  $H^3S$  field test. It was placed approximately 2 m off grid center, 1 m off ground level, and 3 m from the Climet PSA and a chemical impinger. Actually operated were two Climet PSA systems. The system data which will be reported here covered a size range of 0.3 to 3.0 micrometres in six unequal size increments. The second Climet system covered a range of 0.3 to 13 micrometres in six unequal increments. Typically, the second

system obtained measurements in only the three smallest size intervals (the largest size measured being 5.2 micrometres). This data was considered to be too poor in size resolution for the comparison with PSI data, although this data does provide some insight into the Climet and PSI data comparisons.

Unlike the PSI, the Climet PSA determines particle size by measuring the pulse magnitude of white light scattered in the forward direction by single particles withdrawn from the smoke cloud, diluted in number density and blown across the incident light beam at a fixed flowrate. This PSA is calibrated with latex spheres. As a result, the particle size measured by the Climet must be interpreted as an equivalent latex sphere diameter. Calculations given in reference show that when the particles are nonabsorbing dielectrics, the response function of this instrument is monotonic.

The results of the particle size distribution measurements as a function of RH will be presented as 1) sample moments of the size distribution, 2) mean particle diameters (geometric, volumetric and mass means) and 3) histograms of the size distribution for selected trials.

The means and moments of the particle size distribution are defined as follows. Let the data be grouped into  $n$  intervals with a frequency of occurrence in the  $i$ th interval given by  $f_i$ . The total number of measurements is then given by

$$N_t = \sum_{i=1}^n f_i \quad (1)$$



The kth sample moment of the size distribution,  $\mu_k$ , is then given by

$$\mu_k = \frac{1}{N_t} \sum_{i=1}^n f_i D_i^k \quad (2)$$

where  $D_i$  is defined as the largest diameter value in the size increment.

Using these definitions the following mean diameters can be written as:

1. Numeric Mean Diameter

$$D_1 = \mu_1 \quad (3)$$

2. Volumetric Mean Diameter

$$D_v = \mu_3^{1/3} \quad (4)$$

3. Mass Mean Diameter

$$D_{mm} = \mu_4 / \mu_3 \quad (5)$$

A log-normal size distribution is often assumed for analytical calculations. This distribution is characterized by the geometric mean diameter  $D_g$  and the logarithmic geometric standard deviation  $\sigma_g$ . These are defined by

$$D_g = \text{EXP} \frac{1}{N_t} \sum_{i=1}^n f_i \ln D_i \quad (6)$$

$$\sigma_g = \text{EXP} \frac{1}{N_t} \sum_{i=1}^n f_i \ln^2 (D_i / D_g) \quad (7)$$

If the size distribution can be approximated as a Gaussian distribution, then the second central moment,  $m_2$ , (often called the "variance") is used as a measure of the "spread" of the distribution.

$M_2$  is defined as

$$M_2 = \frac{1}{N} \sum_{i=1}^n f_i (D_i - \mu_1)^2 \quad (8)$$

The measurements reported here are for phosphorus smokes which were dispersed as either red phosphorus grenades or white phosphorus wicks or wedges.

Tables II and III summarize the computations for the means and moments for all PSA size measurements obtained during a specified trial. Table II additionally tabulates the proportion of the total particles detected by the PSI which were less than 0.3 micrometres in diameter. These particles, while too small to resolve for measurement, could be detected and were included in the total numeric count.

Figures 8-12 compare size distribution histograms obtained by the PSA systems for examples of data for each of the different kinds of munitions. The PSI data in these figures have had the smallest size bin ( $D \leq 0.3 \mu\text{m}$ ) artificially truncated in order to get a more direct comparison with the Climet data. The PSI data show a reasonable consistency in size distribution shape for all phosphorus trials. These data show that the distribution is at least bimodal with one mode occurring at less than 0.6 micrometres and the second occurring at around 3.0 micrometres in diameter.

The HC data show a multimodal distribution with a relatively large number being less than 0.6 micrometres. The Climet data generally shows a strong size mode for sizes less than 0.6 micrometres and a second mode which appears between 1.0 and 1.5 micrometres. The two instruments are therefore in agreement that the predominant size mode occurs below 0.6 micrometres. However, the PSI data indicates that the larger size mode should occur at about 3.0 micrometres and that significant numbers of particle sizes exist in the 3-5 micrometre range. The later results also seem to be verified by the second PSA which detected particles in the 1-5.2 micrometre range (see figure 8). As a result of the Climet not measuring a second mode with sizes as large as that observed with the PSI, Tables II and III show that significant differences exist in the computed moments for the two systems.

#### EFFECTS OF RELATIVE HUMIDITY ON MEAN PARTICLE SIZE

An assumption made in the analysis of hygroscopic smokes is that as the relative humidity increases the mean particle diameter will increase significantly.<sup>1</sup> It is of interest, therefore, to examine the PSA results for the effects of RH on mean particle diameter. Figures 13 and 14 plot mean particle diameter as a function of RH as measured by the two PSA systems. The PSA data do not show an increase in mean particle diameter with increasing RH. In fact, the data show a slight volumetric and geometric mean diameter decrease with increasing RH. Only the PSI mass mean appears to increase slightly. The geometric mean yields an average value close to the most frequently occurring size in the distribution.

The strongest PSI mode in all the data occurred for sizes less than 0.3 micrometres. Therefore, the PSI geometric mean is smaller than that for the Climet which begins counting only for sizes greater than 0.3 micrometres. The differences in the mass and volumetric means are due primarily to relative values of the second mode in the size distributions. As a result, the PSI values for volumetric and mass mean diameters are roughly a factor of 2 greater than those measured by the Climet. It is interesting to note that in the case of the mass mean measurements, the PSA data is a factor of 2 to 4 times greater than that assumed in the analytical computations.<sup>1</sup> This assumption was based on data obtained with an Andersen cascade impactor measuring smokes in a laboratory test cell. However, if a log-normal distribution is assumed, then the geometric mean and standard deviation values yield mass mean diameter values which are very near those assumed for the analytical calculations.

The apparent decrease in mean particle diameter with increasing humidity is unexpected. However, the PSI data may provide a clue in explaining this anomalous behavior. Figure 15 plots the detected particles smaller than 0.3 micrometres in diameter as a function of humidity. The trend shown by this figure is for the number of small particles detected by the PSI is to increase with increasing relative humidity. Also shown is the equation obtained for a logarithmic curve fit with a correlation coefficient of 0.68. From this data it is hypothesized that very small particles released by the munition source (which otherwise could not be detected by the PSI and are evidently always present in the size

distribution) grow to measurable size as the humidity increases.

As the numbers of detectable small particles increase with increasing humidity, there is a shift in the distribution which apparently balances any detectable size increase in the larger sizes. If a PSA system were used which could respond to the small size tail of the distribution then Figure 15 suggests that particle growth would indeed be observed.

#### PSA CONCENTRATION ESTIMATES

The PSA systems produce data which can be used with the obscurant's material density to obtain an estimate of mass concentration. Pretest comparison indicated that the PSI could obtain concentration estimates which were in reasonable agreement with weighed samples withdrawn from the test chamber (see Figure 3). It is of interest therefore to determine how well PSI concentration estimates agree with those obtained by chemical impingers. It should be expected that the PSI data should yield concentration values which are larger than the dosage values obtained with the chemical impingers. To obtain concentration from a chemical impinger, a yield factor multiplies the dosage value to account for water absorbed by the elemental phosphorus. By ratioing the PSI concentration and the chemical impinger dosage an "experimental" yield factor for the field data is obtained.

To compare PSI concentration estimates with dosage estimates it is necessary to compute the trial time average PSI concentration. This is given by

$$\langle C(\text{PSI}) \rangle = \frac{\pi}{6} \langle \mu_3 N \rangle \quad (9)$$

where  $\langle \rangle$  indicates a time average,  $C(\text{PSI})$  is the concentration as determined from PSI data,  $\mu_3$  is the third sample moment and  $N$  is the corresponding number density. Number density data from the Climet PSA was not available for this calculation. Time averaged dosage data were obtained for the chemical impinger located nearest the PSI during the field test. The values for  $\rho$  were computed using equation 25 in reference 1. Values of  $\langle C(\text{PSI}) \rangle$  and  $\langle D^*(\text{CI}) \rangle$ , the time average dosage value for the chemical impinger nearest the PSI, are listed in Table IV for the phosphorus trials. Table IV lists the theoretical yield factor used to compute the concentration from the dosage. An experimental yield factor  $YF_e$ , is listed and is computed from

$$YF_e = \frac{\langle C(\text{PSI}) \rangle}{\langle D^*(\text{CI}) \rangle} \quad (10)$$

Comparison of the experimental with the theoretical yield factor shows large differences with a few points showing close agreement. In general, the dosage values are much closer to the PSA determined concentration values than the values obtained by using the theoretical yield factors.

## CONCLUSIONS

Examination of the data shown in the previous sections leads to the following conclusions.

1. Size distributions measured by the PSA's are usually bimodal. One mode occurs for sizes less than 0.6 micrometres. The second mode

appears for sizes between 1.0 - 1.5 micrometres or at about 3.0 micrometres depending on which PSA data is used.

2. Size distributions measured in the laboratory and field by the PSI have similar mode characteristics.

3. Although the measured size distributions are not log-normal, mass mean diameters computed from geometric mean and standard deviations assuming a log-normal distribution are close to previously assumed values.

4. PSI size distribution data indicates that most of the detected particles are less than 0.3 micrometres in diameter.

5. The numbers of particles less than 0.3 micrometres in diameter appear to increase as relative humidity increases.

6. Measured mean particle diameters (geometric, volumetric, or mass) do not appear to increase as relative humidity increases.

7. Measured mass means are a factor of 2 to 4 times greater than those assumed in a previous analytical computation.

8. Concentration estimates made with PSI data are generally smaller than those obtained using a theoretical yield factor and dosage data.

#### ACKNOWLEDGEMENT

The authors wish to acknowledge the invaluable support provided by personnel in the Gas Diagnostics Division of UTSI during the preparation of this paper. Mr. Mark Binkley and Mr. Chris Layne provided the illustrations and Ms. Susan Carpenter typed the manuscript. From the PM Smoke Office, Mr. Gene Bowman and Mr. Joseph Steedman provided test direction during the  $H^3S$  test and the authors are especially grateful for numerous helpful comments by Mr. Gary Nelson and Mr. Sidney Gerard on portions of the manuscript. However, the authors are solely responsible for its contents. This work was supported under U. S. Army Contract DAAK-11-78-C-0124 with the PM Smoke Office.

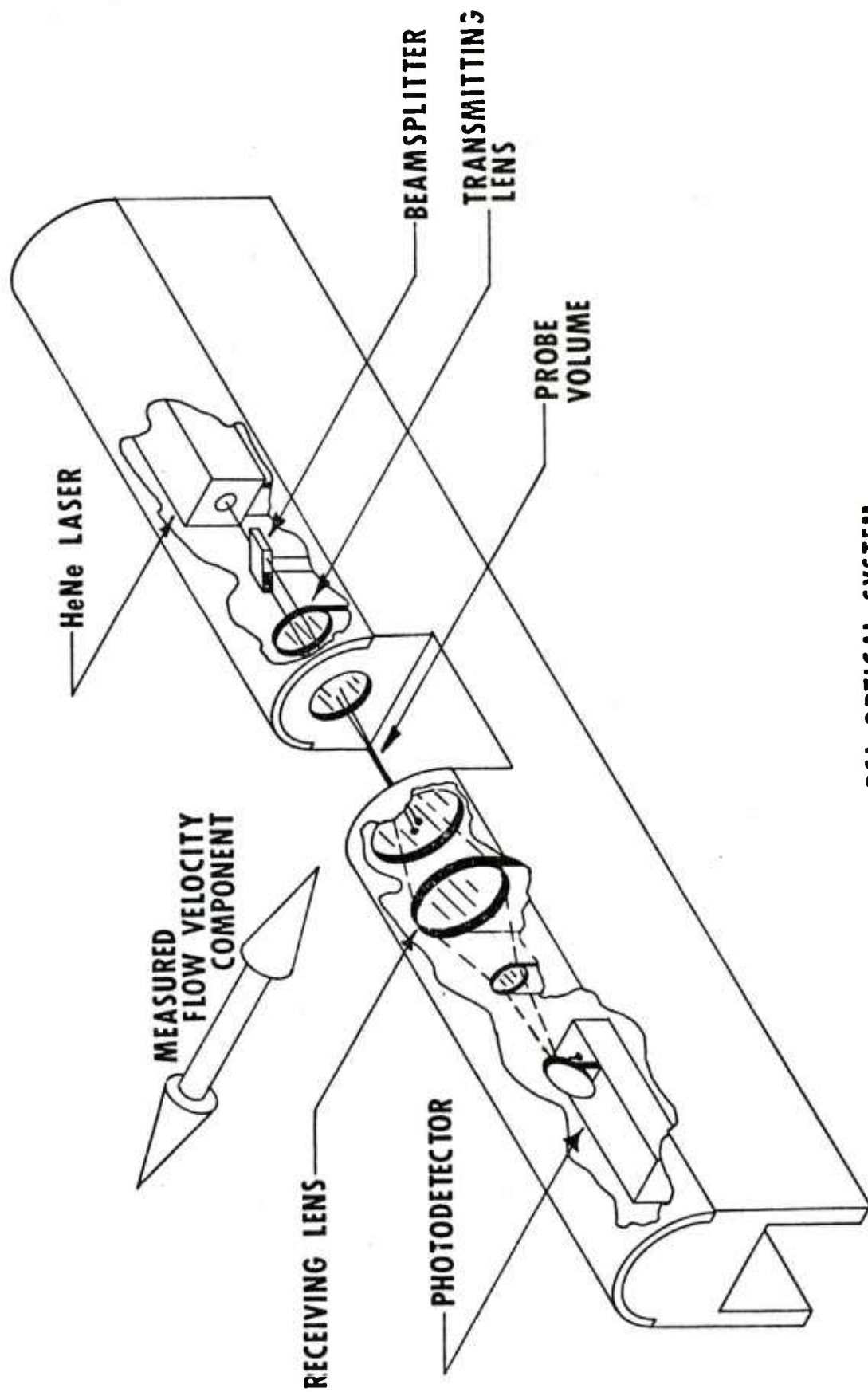


## REFERENCES

1. Frickel, R. H., G. O. Rubel, and E. W. Stuebing, "Relative Humidity Dependence of the Infrared Extinction by Aerosol Clouds of Phosphoric Acid" Proceedings of Smoke/Obscurant Symposium III, Harry Diamond Laboratories, Adelphi, MD, April 24-25, 1979. p. 571.
2.  $H^3S$  Data to be published by Dugway Proving Ground.
3. Farmer, W. M., "An Evaluation of Data Obtained During the  $H^3S$  Test" Proceedings of Smoke/Obscurant Symposium IV, Harry Diamond Laboratories, Adelphi, MD, April 22-23, 1980.
4. Farmer, W. M., K. E. Harwell, J. O. Hornkohl, and F. A. Schwartz, "Laser Particle Sizing Interferometer in Solid Propellant Exhaust Plumes" JANNAF 11th Plume Technology Meeting, Redstone Arsenal, Huntsville, AL, May 1979.
5. Farmer, W. M., "Particle Number Density Estimates Using a Laser Velocimeter," UTSI Gas Diagnostics Division Report, GDTP-79-100 1979.
6. Cooke, Deery D. and Milton Kerker, "Response Calculations for Light Scattering Aerosol Particle Counters" Appl. Opt. 14, 734, 1975.

## LIST OF FIGURES

- Figure 1. Schematic of the PSI optical system used in the laboratory and field measurements.
- Figure 2. Schematic of the smoke chamber for laboratory comparisons.
- Figure 3. Pretest comparison of mass concentration estimates obtained using filter sampling and PSI measurements.
- Figure 4. PMS measured size distribution for HC.
- Figure 5. PMS measured size distribution for red phosphorus.
- Figure 6. PMS measured size distribution for fog oil
- Figure 7. Examples of the probability density distributions obtained in laboratory measurements.
- Figure 8. Climet and PSI particle size histogram comparison for trial 9.
- Figure 9. Climet and PSI particle size histogram comparison for trial 4.
- Figure 10. Climet and PSI particle size histogram comparison for trial 10.
- Figure 11. Climet and PSI particle size histogram comparison for trial 10.
- Figure 12. Climet and PSI particle size histogram comparison for trial 11.
- Figure 13. Mean particle diameter as a function of relative humidity as determined by the PSI.
- Figure 14. Mean particle as a function of relative humidity as determined by the Climet.
- Figure 15. Detected number of particles less than  $0.3\ \mu\text{m}$  as determined by the PSI.



## PSI OPTICAL SYSTEM

Figure 1. Schematic of the PSI optical system used in the laboratory and field measurements.

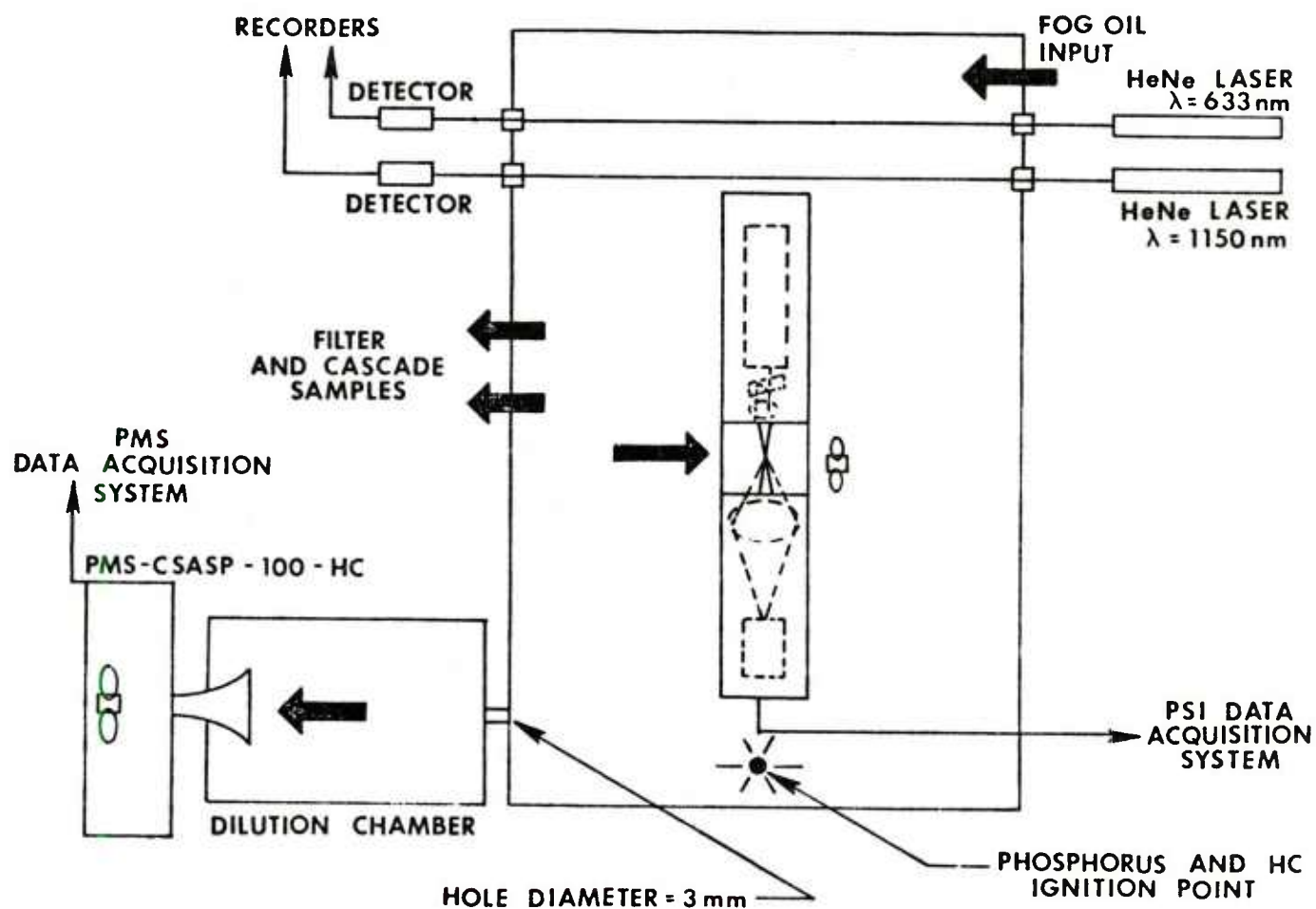


Figure 2. Schematic of the smoke chamber for laboratory comparisons.

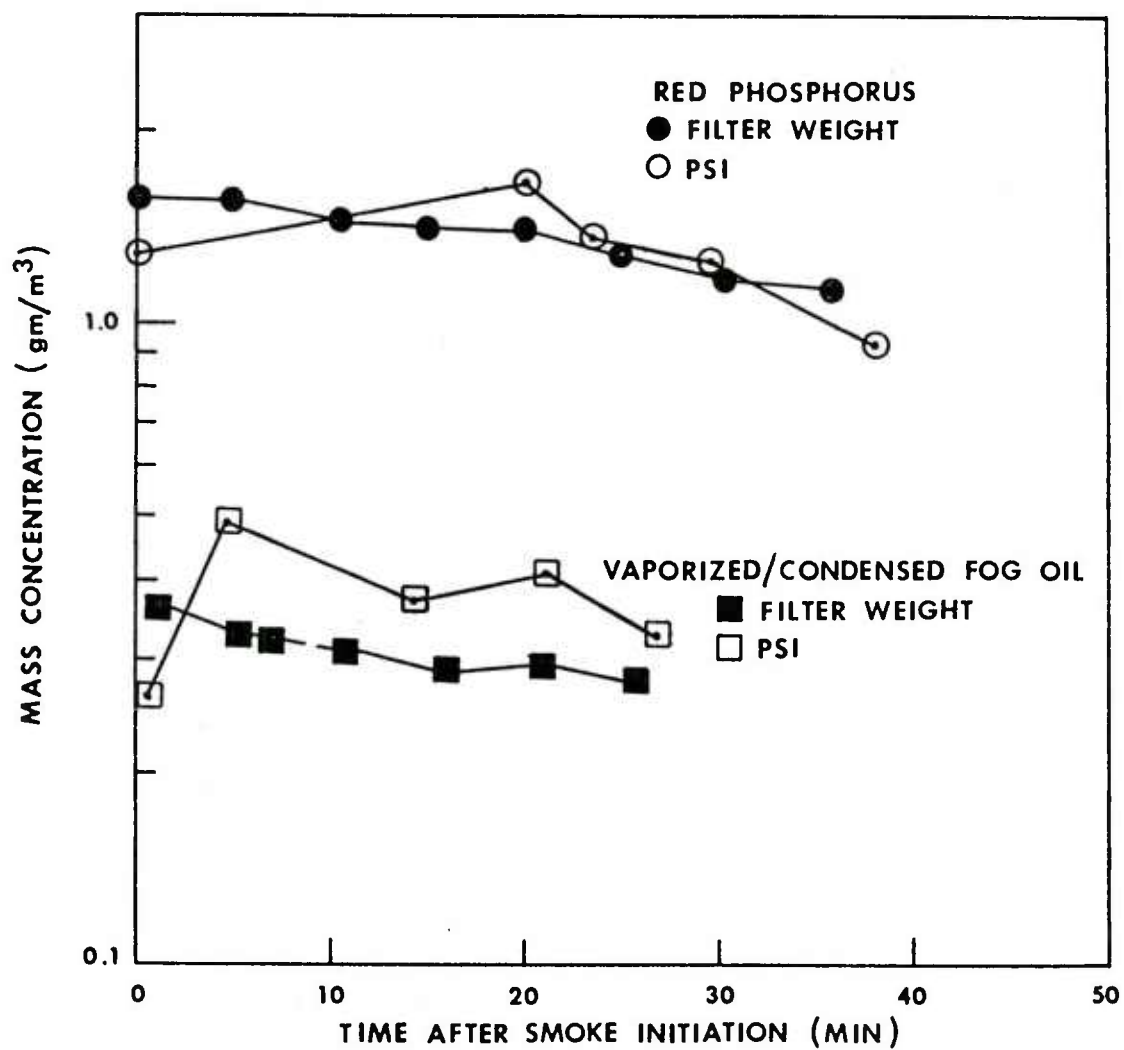


Figure 3. Pretest comparison of mass concentration estimates obtained using filter sampling and PSI measurements.

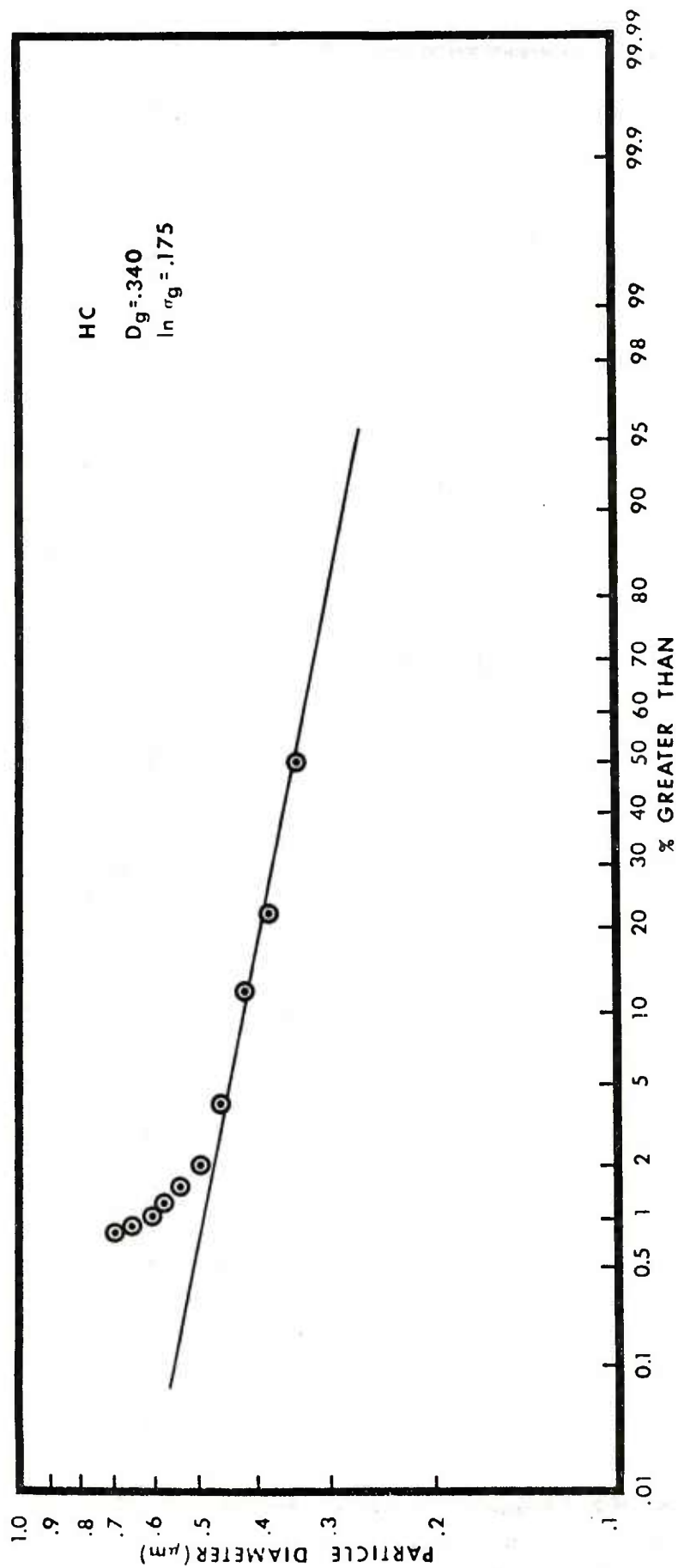


Figure 4. PMS measured size distribution for HC.

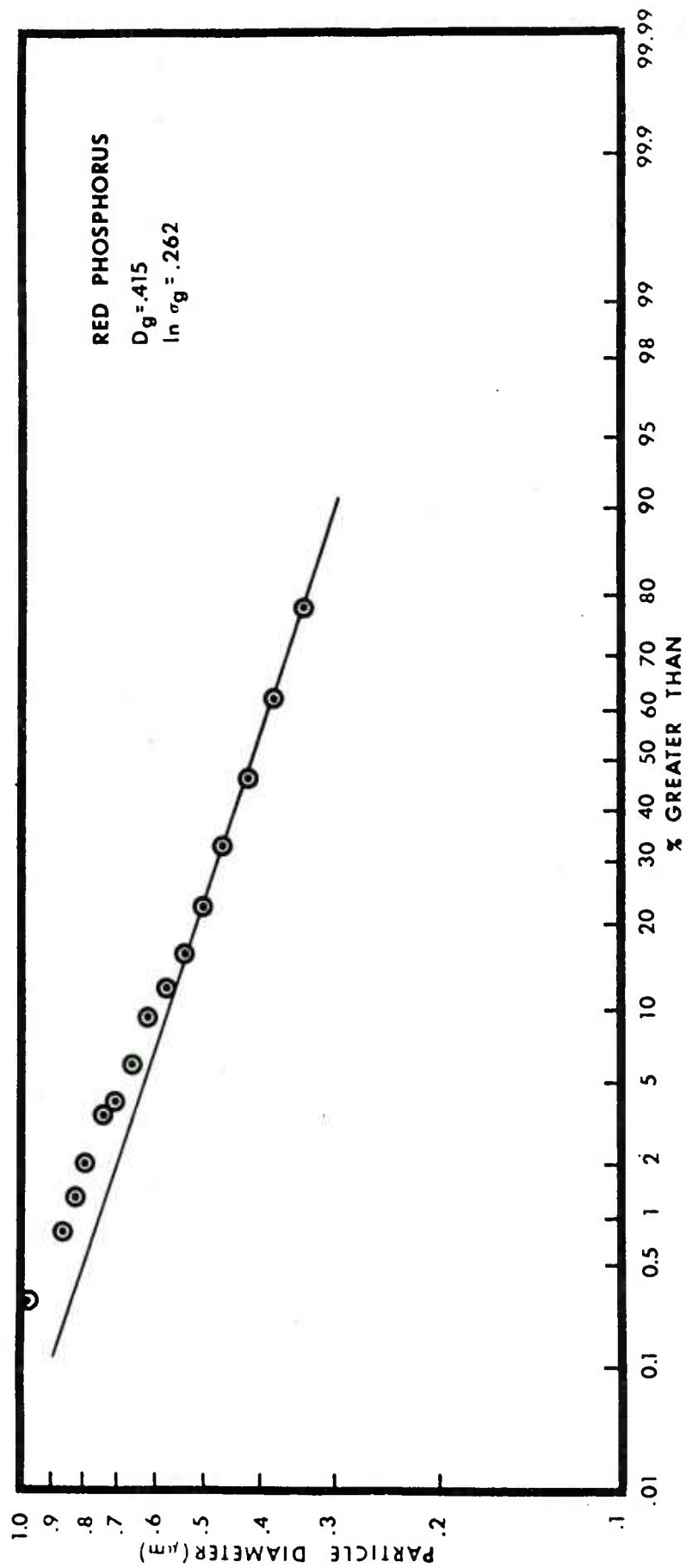


Figure 5. PMS measured size distribution for red phosphorus.

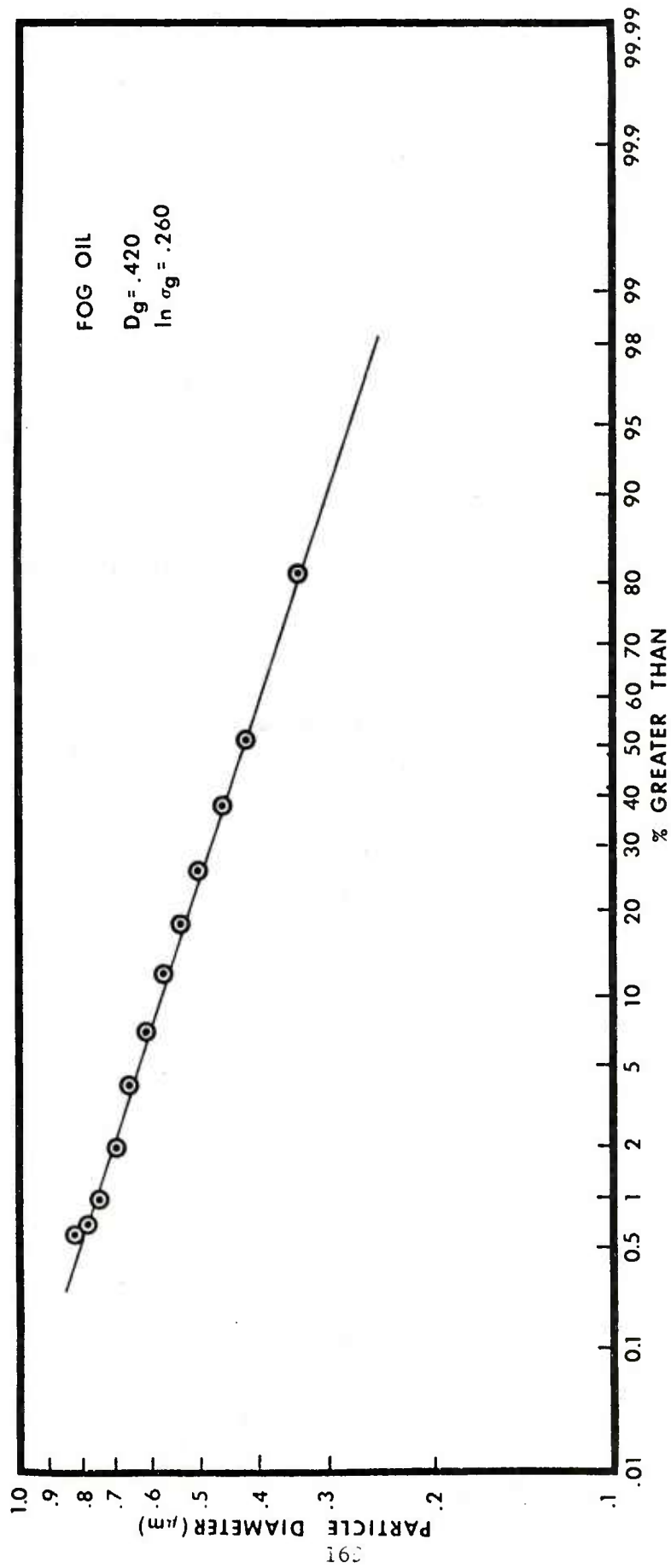
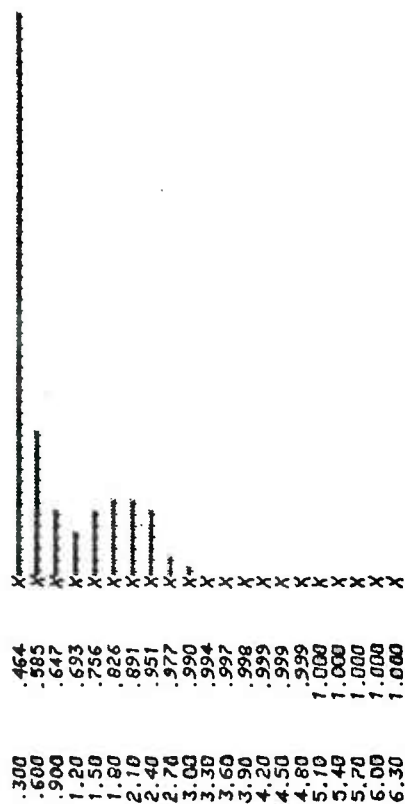
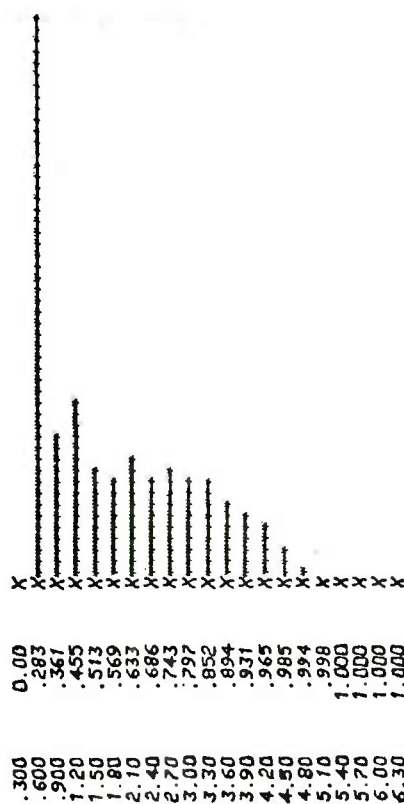


Figure 6. PMS measured size distribution for fog oil.

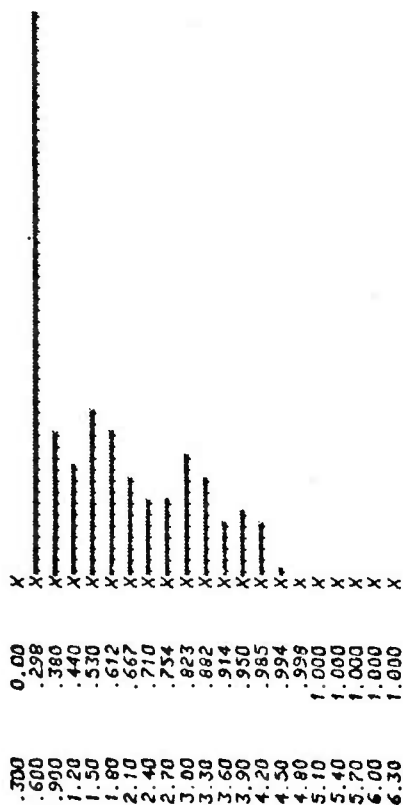




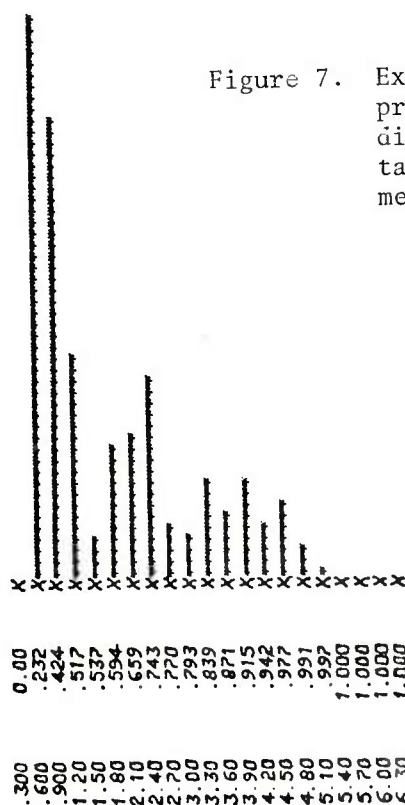
\*\*\* BACKGROUND AIR MEASUREMENT \*\*\*



\*\*\* FIRST PHOSPHORUS CALIBRATION TEST \*\*\*

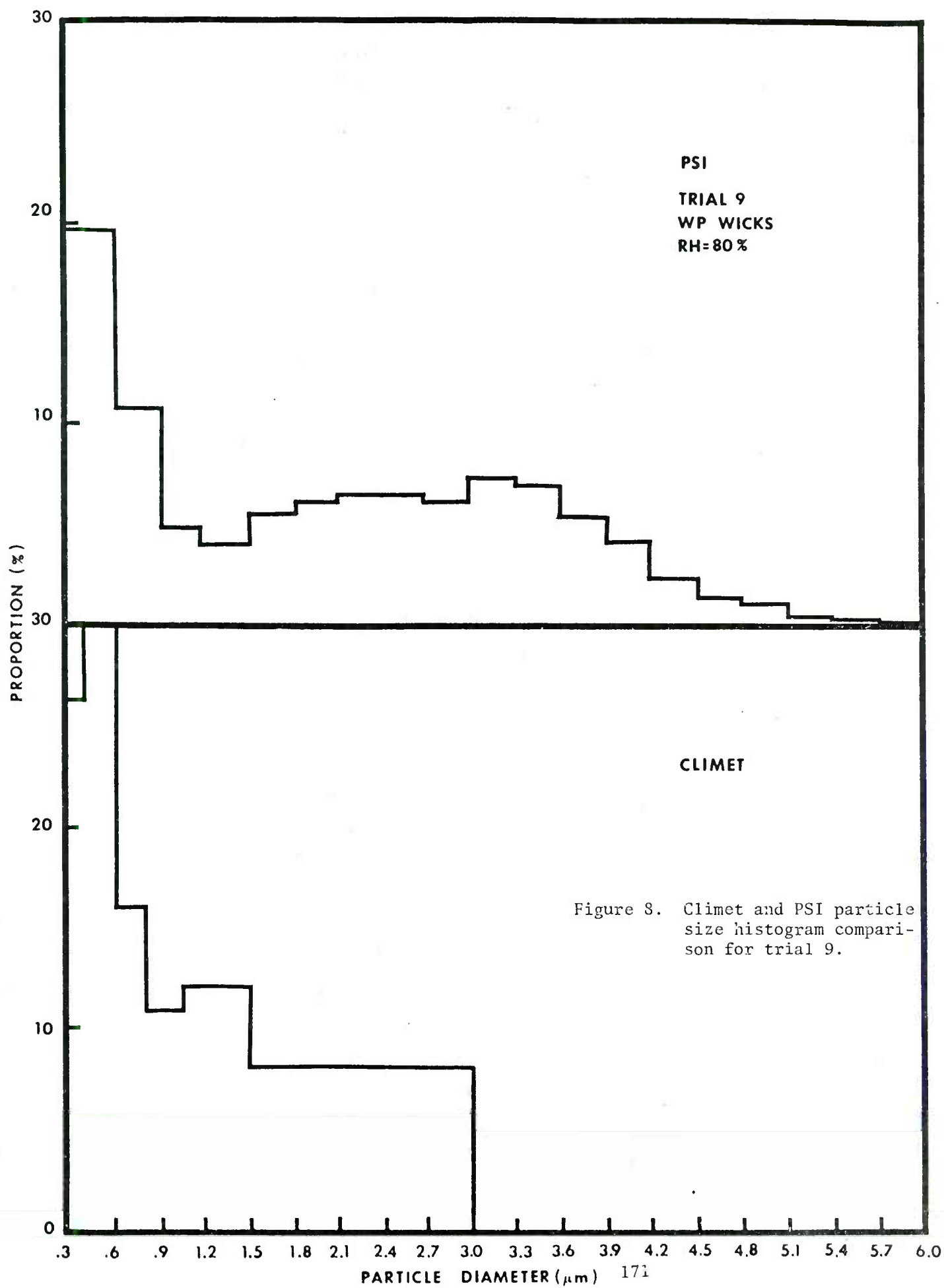


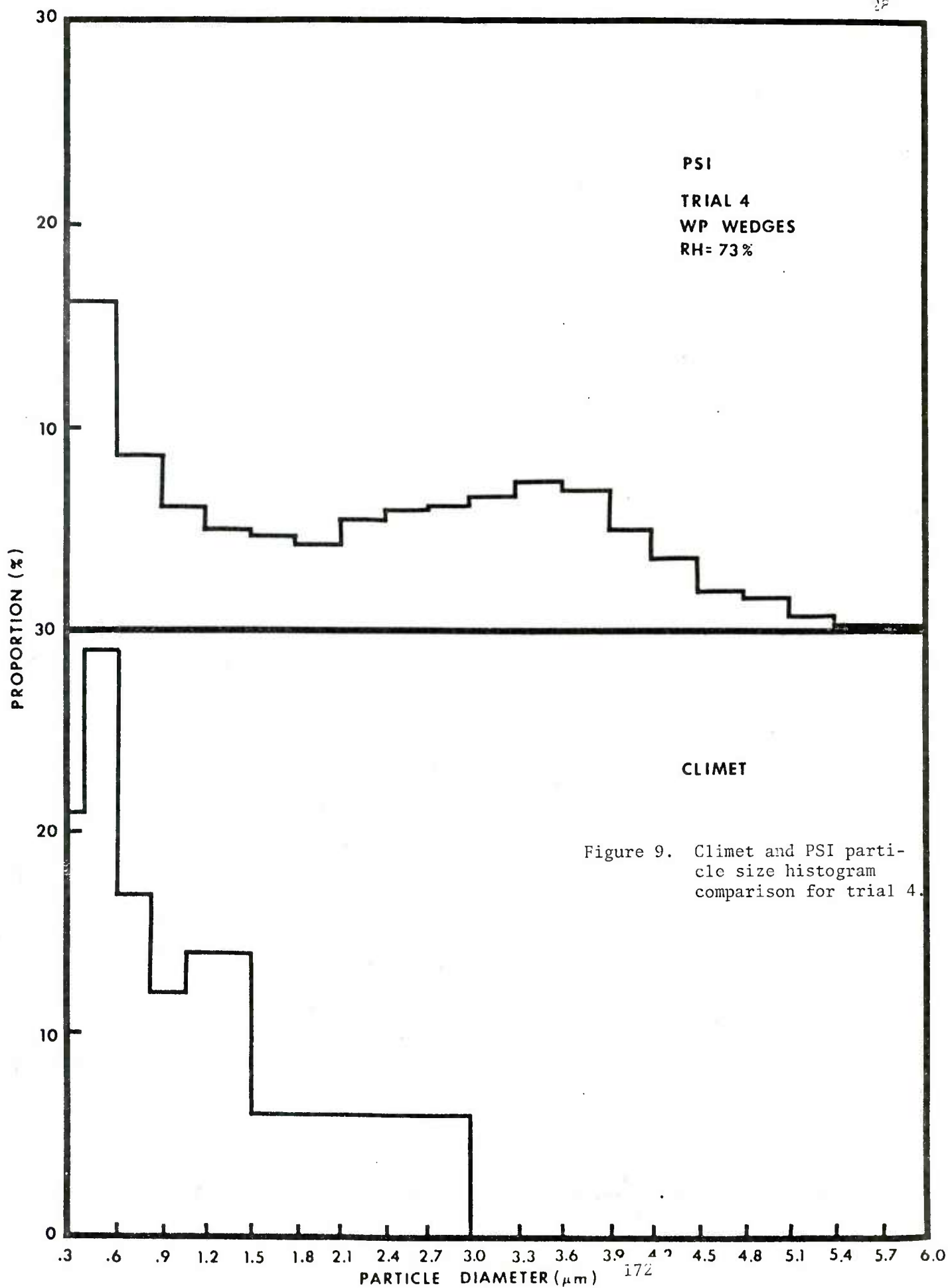
\*\*\* FIRST HC CALIBRATION TEST \*\*\*



\*\*\* SECOND F06 OIL CALIBRATION TEST \*\*\*

Figure 7. Examples of the probability density distributions obtained in laboratory measurements.





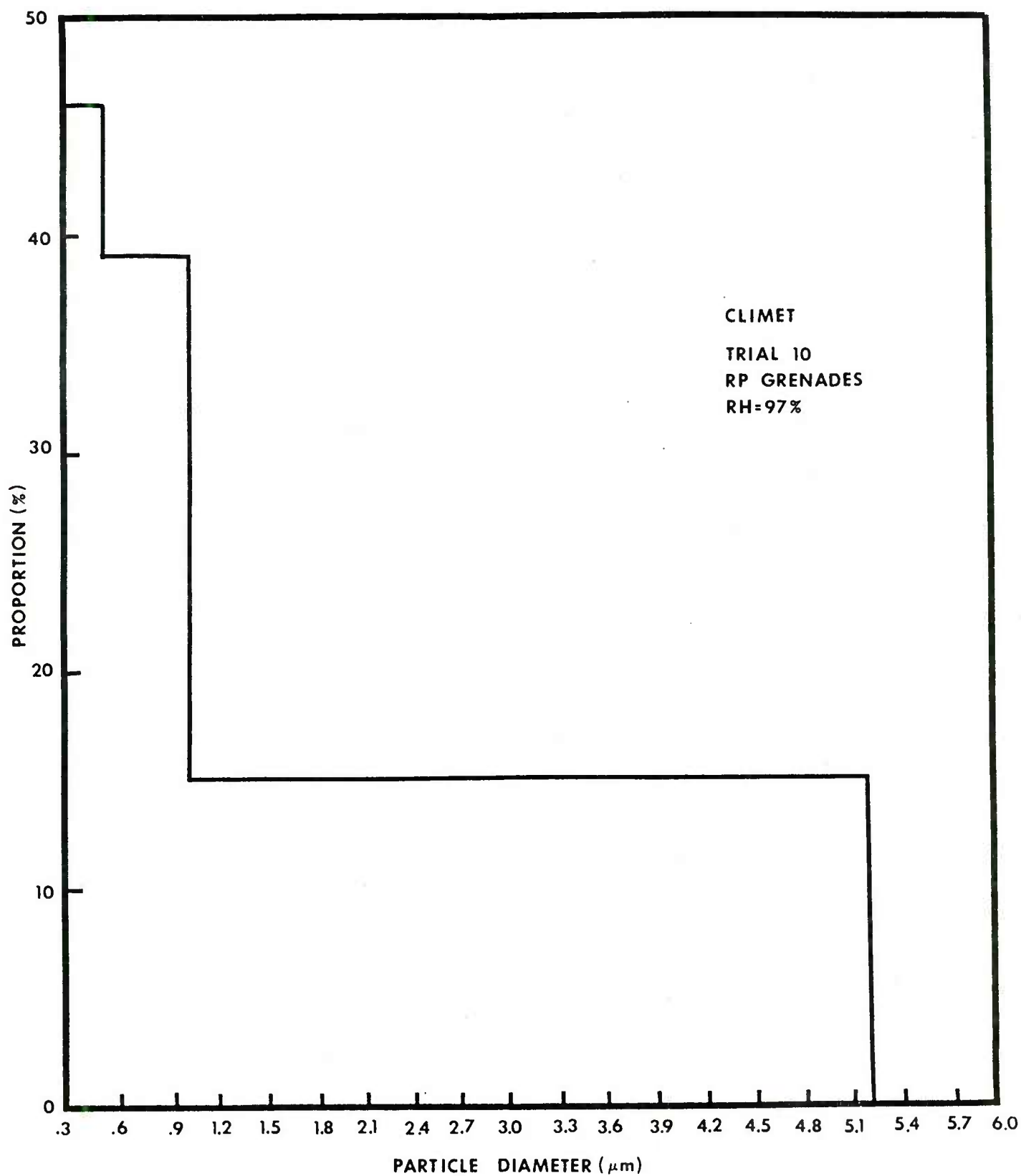


Figure 10. Climet and PSI particle size histogram comparison for trial 10.

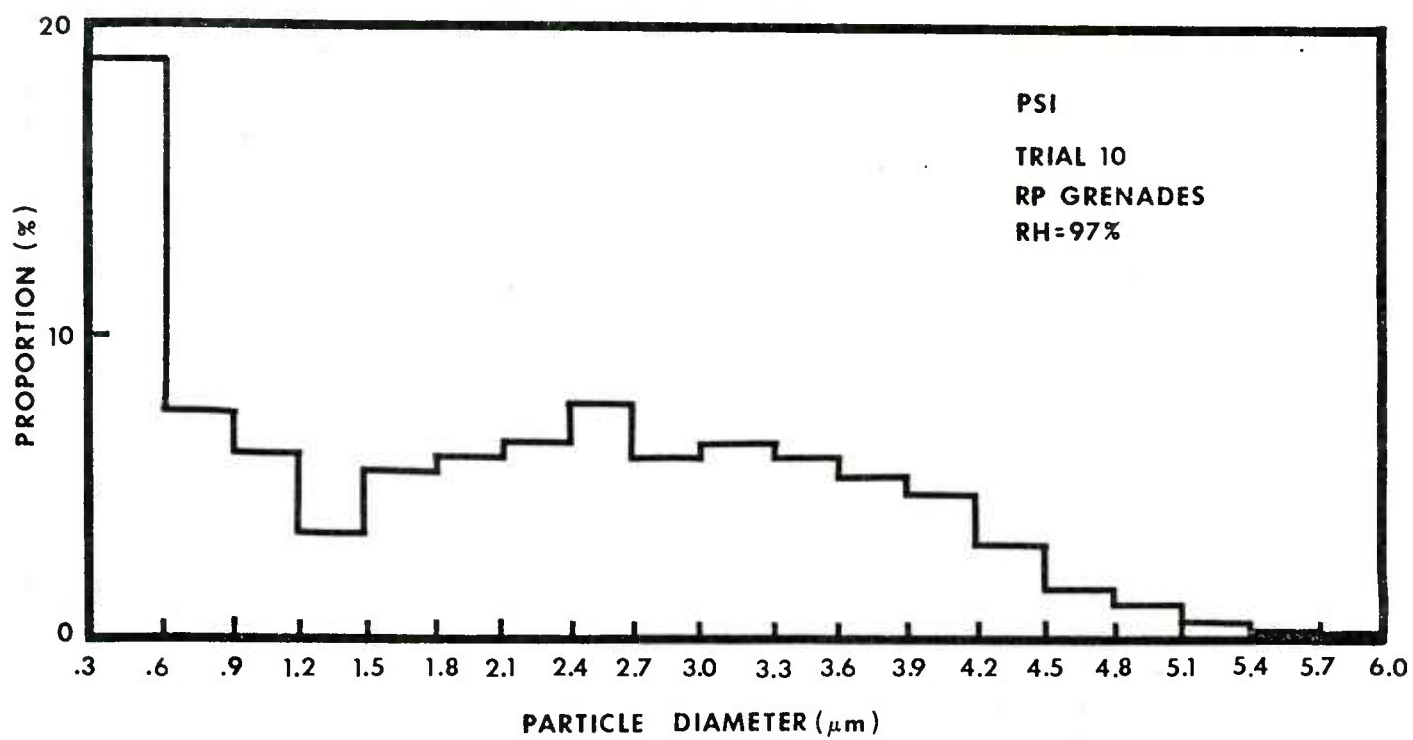
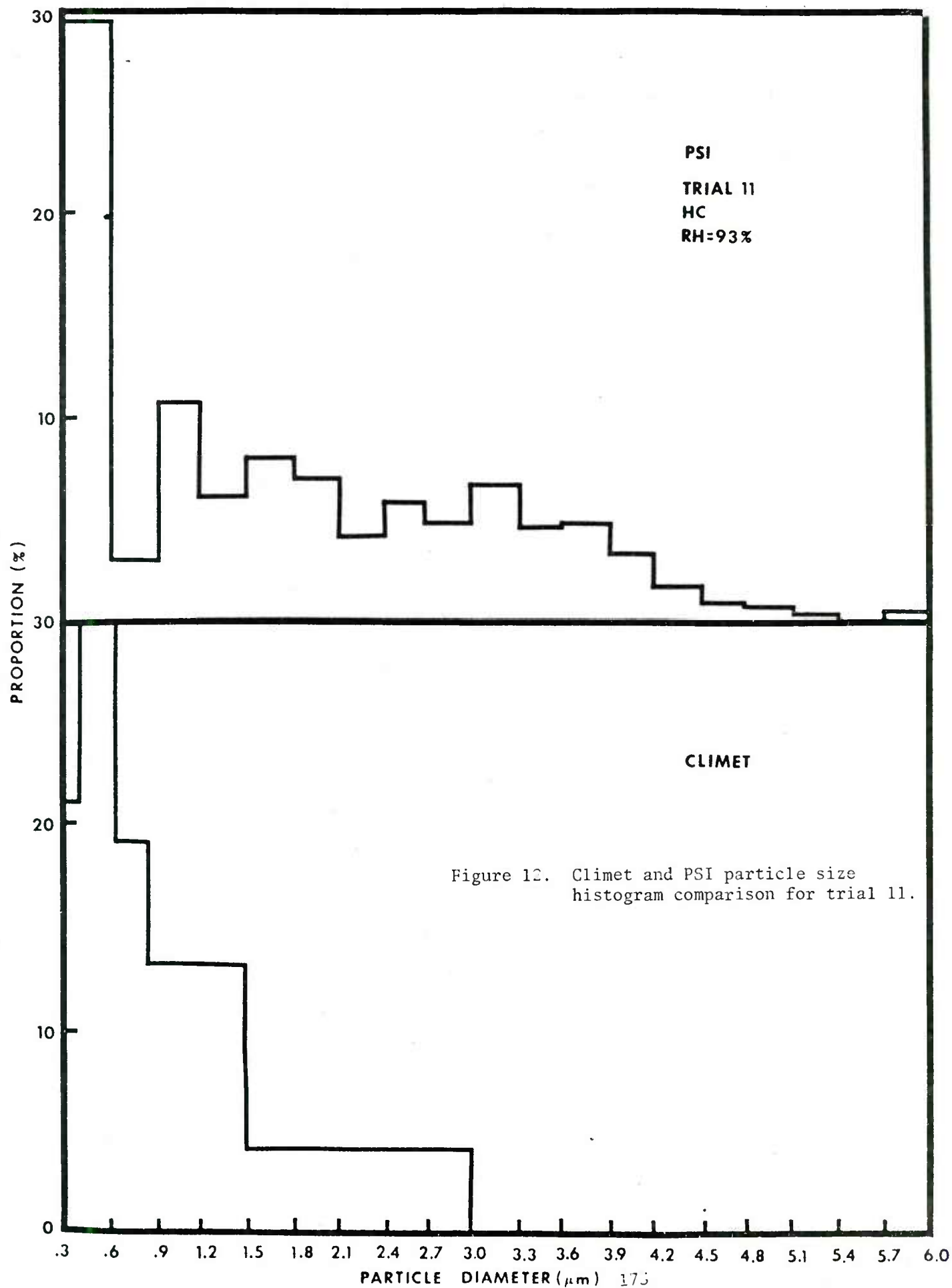


Figure 11. Climet and PSI particle size histogram comparison for trial 10.



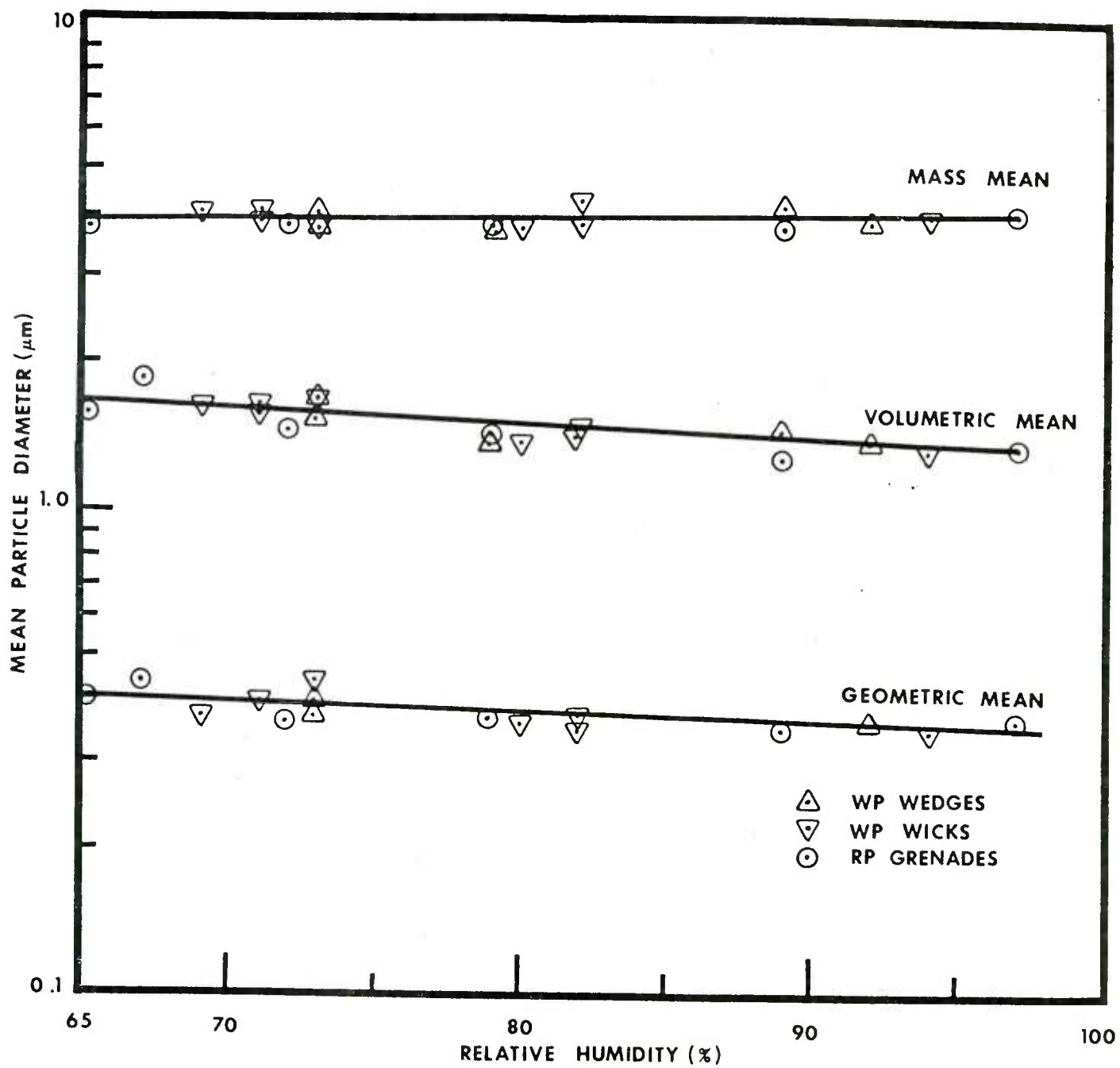


Figure 13. Mean particle diameter as a function of relative humidity as determined by the PSI.

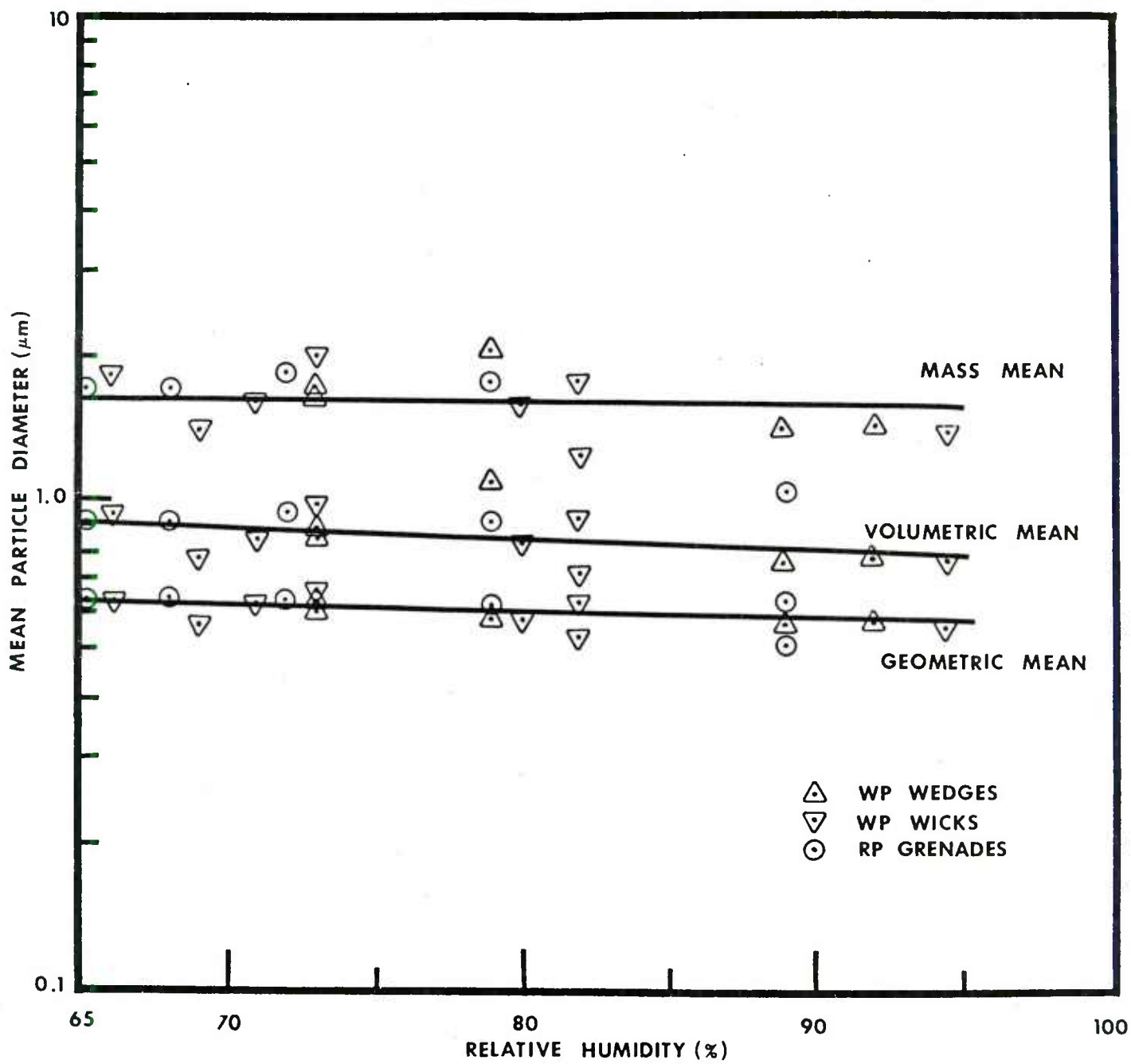


Figure 14. Mean particle as a function of relative humidity as determined by the Climet.



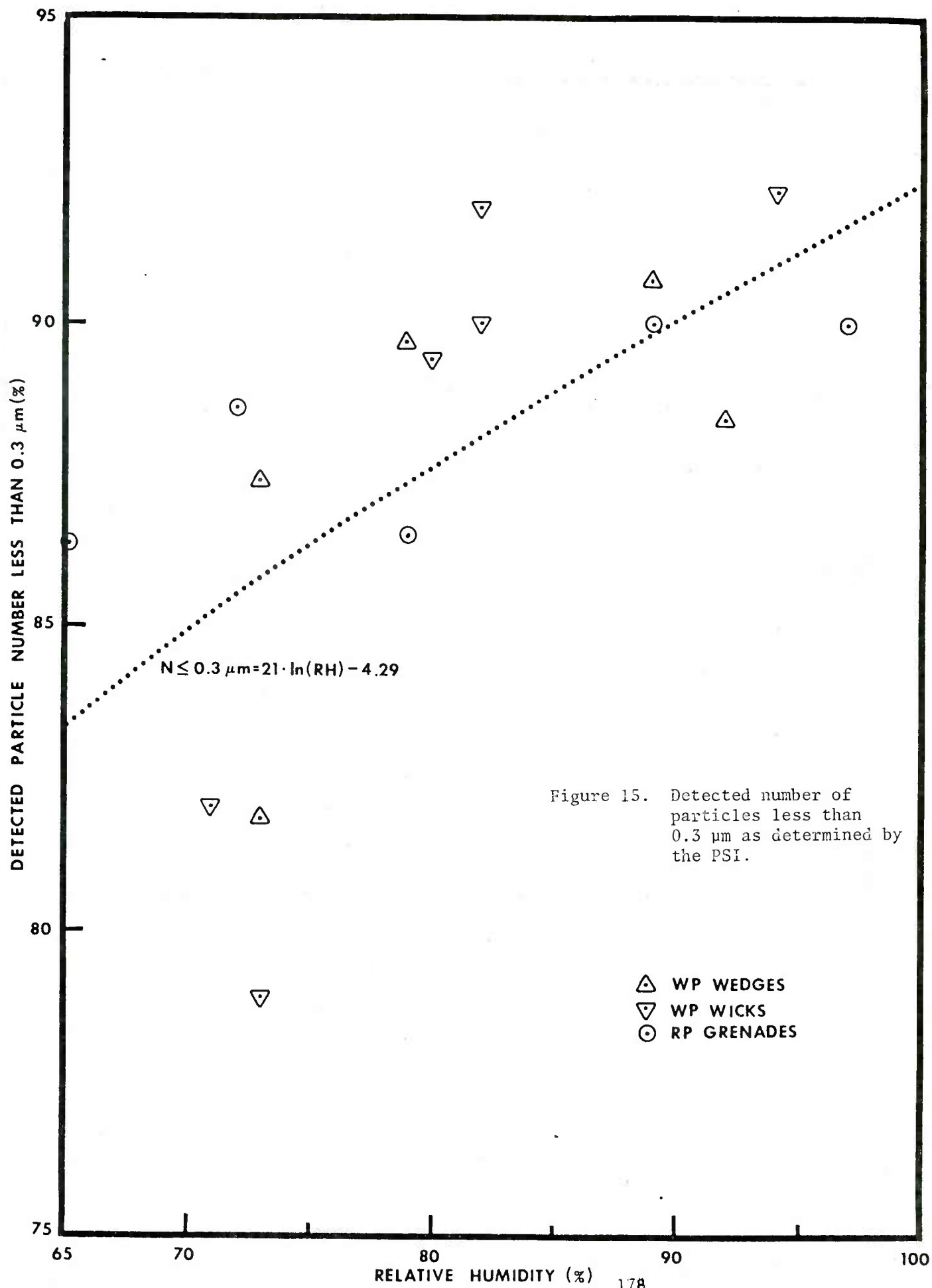


Figure 15. Detected number of particles less than 0.3 μm as determined by the PSI.

- △ WP WEDGES
- ▽ WP WICKS
- RP GRENADES

TABLE 1

COMPARISON OF TYPICAL LABORATORY  
PSA DATA FOR 81 - 83% RELATIVE HUMIDITY

	GEOMETRIC MEAN DIAMETER ( $\mu\text{m}$ )				GEOMETRIC STANDARD DEVIATION				THIRD MOMENT ( $\mu\text{m}^3$ )		TYPICAL NUMBER DENSITY ( $\text{cc}^{-1} \cdot 10^{-6}$ )	% $\leq 0.3 \mu\text{m}$
	PSI	CSASP	PMS		PSI	CSASP	PMS		PSI	CSASP		
HC	0.334	0.34			1.52		1.19		0.72	0.045	0.576	93
RED PHOSPHORUS	0.328	0.415			1.538		1.3		0.97	0.097	1.62	$94.8 \pm 0.8$
FOG OIL	0.326	0.42			1.54		1.29		0.969	0.099	1.07	$95.2 \pm 0.9$

TABLE II  
PARTICLE SIZING INTERFEROMETER  
PARTICLE SIZE DISTRIBUTION DATA  
OBTAINED DURING THE H<sub>2</sub>S TEST

TRIAL NO.	OSCURANT SOURCE MASS (μg)	RELATIVE HUMIDITY (%)	$\mu_1$ (μm)	$\mu_2$ (μm <sup>2</sup> )	$\mu_3$ (μm <sup>3</sup> )	$\bar{D}_g$ (μm)	$\bar{D}_v$ (μm)	$\bar{D}$ (μm)	$m_2$ (μm <sup>2</sup> )	$1 \text{ no}_g$	$\Sigma \pm 0.3 \mu\text{m}$	
RP GRENADES												
10	2.17	97	0.502	0.79	2.547	0.361	1.366	4.036	0.538	1.59	90.0 ± 3.1	
15	1.45	89	0.479	0.69	2.152	0.355	1.291	3.802	0.464	1.57	90.0 ± 2.5	
3	1.45	79	0.522	0.86	2.832	0.370	1.415	3.880	0.591	1.59	86.5 ± 2.3	
7	2.90	72	0.531	0.91	3.010	0.369	1.444	3.835	0.629	1.60	88.6 ± 2.6	
19	1.45	67	0.751	1.77	6.401	0.439	1.857	4.014	1.21	1.74	81.5	
18	2.90	65	0.620	1.21	4.024	0.401	1.591	3.798	0.822	1.64	86.4	
WP WEDGES												
17	6.21	92	0.505	0.80	2.664	0.363	1.386	3.968	0.544	1.58	88.4 ± 2.4	
12	6.21	89	0.503	0.85	3.028	0.358	1.447	4.232	0.600	1.59	90.7 ± 1.7	
8	6.21	79	0.506	0.82	2.646	0.362	1.383	3.796	0.560	1.59	89.7 ± 1.9	
4	6.21	73	0.559	1.04	3.625	0.377	1.536	4.036	0.730	1.62	87.4 ± 5.2	
27	12.42	73	0.672	1.43	4.946	0.417	1.704	3.880	0.980	1.68	81.8 ± 8.08	
WP WICKS												
16	0.95	94	0.465	0.69	2.281	0.347	1.316	4.014	0.473	1.57	92.2 ± 2.0	
2	2.85	82	0.485	0.78	2.757	0.354	1.402	4.336	0.542	1.58	91.9 ± 1.1	
13	1.91	82	0.514	0.85	2.799	0.364	1.409	3.897	0.585	1.59	90.0 ± 2.0	
9	1.91	80	0.505	0.80	2.574	0.362	1.371	3.811	0.546	1.59	89.4 ± 1.7	
28	1.91	73	0.734	1.58	5.248	0.446	1.738	3.723	1.04	1.71	78.9 ± 0.9	
25	1.91	71	0.631	1.25	4.194	0.407	1.613	3.807	0.850	1.65	82.0 ± 4.5	
22	0.95	69	0.573	1.11	3.882	0.376	1.572	4.020	0.782	1.64	-	
20	1.91	66	NO DATA									
HC												
11	4.9	93	0.419	0.49	1.499	0.337	1.144	4.055	0.318	1.54	93.1 ± 0.3	
23	4.9	87	0.515	0.77	2.176	0.367	1.296	3.322	0.507	1.59		
14	2.45	84	0.587	1.03	3.519	0.402	1.521	4.288	0.690	1.60		
26	9.8	75	NO DATA									
6R	4.9	72	0.687	1.59	5.899	0.407	1.807	4.217	1.12	1.72		
5	2.45	70	NO DATA									
21	4.9	68	NO DATA									
1R	4.9	59	1.32								2.19	

1. Geometric mean diameter averaged over the trial.
2. Volumetric mean diameter averaged over the trial.
3. Mass mean diameter.
4. Second central moment or variance.
5. Geometric standard deviation averaged over the trial.

TABLE III  
OUCHAY PROVING GROUND PARTICLE SIZE ANALYZER  
PARTICLE SIZE DISTRIBUTION DATA OBTAINED  
DURING THE H<sub>2</sub>S TEST

TRIAL NO.	OBSCURANT SOURCE MASS (kg)	RELATIVE HUMIDITY (%)	$\mu_1$ (um)	$\mu_2$ (um <sup>2</sup> )	$\mu_3$ (um <sup>3</sup> )	$D_g$ (um)	$D_v$ (um)	$D_{nm}$ (um)	$m_2$ (um <sup>2</sup> )
RP GRENADES									
10	2.17	97	0.679	0.745	21.531 (PSA1) <sup>5</sup>	0.611	2.782 <sup>5</sup>	5.11 <sup>5</sup>	0.284
15	1.45	89	0.534	0.329	0.630	0.506	0.857	1.87	0.043
3	1.45	79	0.685	0.613	2.958	0.617	1.436	2.52	0.143
7	2.90	72	0.704	0.651	3.288	0.631	1.487	2.55	0.155
19	1.45	67	0.698	0.624	2.732	0.631	1.398	2.46	0.137
18	2.90	65	0.698	0.626	2.756	0.630	1.402	2.46	0.139
WP WEDGES									
17	6.21	92	0.608	0.454	1.420	0.561	1.124	2.22	0.084
12	6.21	89	0.602	0.443	1.387	0.556	1.115	2.24	0.081
8	6.21	79	0.630	0.495	1.765	0.577	1.209	2.31	0.099
4	6.21	73	0.664	0.562	2.3996	0.602	1.339	2.44	0.122
27	12.42	73	0.682	0.583	2.58	0.630	1.372	2.54	0.118
WP WICKS									
16	0.95	94	0.610	0.455	1.411	0.563	1.122	2.22	0.084
2	2.85	82	0.691	0.622	2.987	0.622	1.44	2.52	0.144
13	1.91	82	0.573	0.392	1.023	0.535	1.008	2.10	0.064
9	1.91	80	0.631	0.504	2.030	0.576	1.266	2.40	0.106
28	1.91	73	0.715	0.672	3.890	0.651	1.573	2.69	0.161
25	1.91	71	0.668	0.544	2.008	0.621	1.262	2.42	0.098
22	0.95	69	0.613	0.460	1.425	0.566	1.125	2.22	0.084
20	1.91	66	0.709	0.658	3.290	0.637	1.487	2.55	0.155
HC									
11	4.9	93	0.660	0.539	1.824	0.604	1.222	2.28	0.104
23	4.9	87	0.745	0.767	5.307	0.669	1.744	2.78	0.212
14	2.45	84	0.647	0.520	1.796	0.593	1.216	2.30	0.101
26	INSUFFICIENT DATA				INSUFFICIENT DATA				
6R	4.9	72	0.822	0.980	7.369	0.707	1.946	2.80	0.304
5	2.45	70	NO DATA						
21	4.9	68	0.781	0.840	5.454	0.686	1.760	2.72	0.231
1R	4.9	59	0.694	0.624	2.966	0.625	1.437	2.52	0.143

1. Geometric mean diameter averaged over the trial.
2. Volumetric mean diameter averaged over the trial.
3. Mass mean diameter.
4. Second central moment or variance.
5. PSA size range 0.3 - 13  $\mu$ m

TABLE IV

COMPARISONS OF CONCENTRATION ESTIMATES  
OBTAINED WITH THE PARTICLE SIZING INTERFEROMETER  
AND CHEMICAL IMPINGERS DURING THE H<sup>3</sup>S TEST

TRIAL NO.	OBSERVANT SOURCE MASS (kg)	RELATIVE HUMIDITY (Z)	$\langle C(PSI) \rangle^1$ (gm/m <sup>3</sup> )	$\langle D^*(CI) \rangle^2$ (gm/m <sup>3</sup> )	DPG YIELD FACTOR	$\langle C(CI) \rangle^*$ (gm/m <sup>3</sup> ) (YF $\cdot \langle D(CI) \rangle$ )	EXPERIMENTAL YIELD FACTOR
RP GRENADES							
10	2.17	97	0.0946	0.0035	23.89	0.083	27.03
15	1.45	89	0.0362	0.003	10.82	0.032	12.06
3	1.45	79	0.074	0.0041	7.25	0.03	18.05
7	2.90	72	0.134	0.0125	6.16	0.077	10.72
19	1.45	67	0.0779	0.0027	5.66	0.015	28.85(3)
18	2.90	65	0.0694	0.0073	5.49	0.04	97.506
VP WEDGES							
17	6.21	92	0.0618	0.006	13.28	0.08	10.3
12	6.21	89	0.477	0.0138	10.82	0.15	34.5
8	6.21	79	0.0402	0.00206	7.25	0.015	19.5
4	6.21	73	0.129	0.0099	6.29	0.062	13.03
27	12.42	73	0.127	0.0054	6.29	0.034	23.5
WP WICKS							
16	0.95	94	0.0536	0.005	15.94	0.08	10.72
2	2.85	82	0.3176	0.0068	7.95	0.054	46.7
13	1.91	82	0.121	0.018	7.95	0.143	6.7
9	1.91	80	0.0351	0.0039	7.46	0.029	9
28	1.91	73	0.196	0.006	6.29	0.038	32.66
25	1.91	71	0.0804	0.0055	6.05		14.6
22	0.95	69	0.0682		5.84		
20	1.91	66			5.57		

## NOTE:

1. PSI concentration estimate obtained using equation 9.
2. Time average dosage computed using chemical impinger data nearest PSI and dividing by official trial time.
3. Yield factor is not realistic because of poor sampling statistics.
4. Note: All values of  $\rho$  above 90% are extrapolated from equation 28, section 3.

EXTINCTION COEFFICIENT AND CONCENTRATION -  
PATHLENGTH MEASUREMENTS OBTAINED  
DURING H3S TEST

TRIAL NO.	OBSCURANT SOURCE MASS (kg)	RELATIVE HUMIDITY (%)	EXTINCTION COEFFICIENT (m <sup>2</sup> /gm)			CONCENTRATION - PATHLENGTH <sup>2</sup> (gm · min/m <sup>2</sup> )	CONCENTRATION		SAMPLE TIME (min.)
			0.4 - 0.7	WAVELENGTH (μm)	3.4		8 - 12	NEAREST PSI	
RP GRENADES									
10	2.17	97	0.84	0.33	0.10	0.05	82.20	.67	8.0
15	1.45	89	1.57	0.60	0.20	0.15	24.87	.32	10.0
3	1.45	79	1.83		0.24		12.26	.15	5.03
7	2.90	72	2.21	0.76	0.22		21.12	.40	5.25
19	1.45	67	2.16		0.16	0.27	5.68	.08	5.25
18	2.90	65	1.92	0.63	0.24		9.46	.15	3.75
WP WEDGES									
17	6.21	92	0.94	0.59	0.15	0.10	83.24	.98	10.00
12	6.21	89		0.83	0.19	0.18	64.65	1.2	8.0
8	6.21	79	1.96	0.73	0.21		24.62	.17	11.00
4	6.21	73	2.42	0.99	0.33		46.38	.64	10.25
27	12.42	73	1.32	0.49	0.26	0.20	45.98	.48	14.0
WP WICKS									
16	0.95	94	0.78		0.12	0.09	30.99	.82	10.25
2	2.85	82	1.56	0.74	0.29		28.11	.43	8.0
13	1.91	82	1.16	0.85	0.19	0.15	28.92	1.14	8.0
9	1.91	80	1.21		0.16		18.80	.29	10.0
28	1.91	73	2.10	0.55	0.23	0.18	8.38	.23	6.0
25	1.91	71	1.83	0.68	0.25	0.17	15.42	.3	9.0
22	.95	69	2.21	0.58	0.14	0.36	4.66	0	9.0
20	1.91	66	2.81		0.40	0.34	5.85	.11	6.5
HC									
11	4.9	93	0.81		0.11	0.06	11.48	.49	3.0
23	4.9	87	1.49	0.88	0.05	0.01	8.91	.08	5.0
14	2.45	84	0.99		0.10	0.04	6.36	.11	3.0
26	9.8	75	2.87		0.15	0.04	8.19	.10	6.0
6R	4.9	72	1.46	0.72	0.07		12.43	.71	3.0
5	2.45	70	3.14	0.82	0.11		4.72	0	2.75
21	4.9	68	2.05	0.99	0.11	0.05	5.87	.05	3.0
1R	4.9	59					19.7	.06	3.0

#### APPENDIX IV

NUMERICAL CALCULATIONS OF VISIBILITY USING  
MIE THEORY OR REFRACTION THEORY OF GEOMETRICAL OPTICS

by

J. David Pendleton

The University of Tennessee  
Space Institute  
Energy Conversion Division

Tullahoma, Tennessee 37388

June 1980



NUMERICAL CALCULATIONS OF VISIBILITY USING MIE THEORY  
OR REFRACTION THEORY OF GEOMETRICAL OPTICS

Mie theory numerical calculations of the visibility parameter for the interference fringe Laser Doppler Velocimeter (LDV) have been made by Adrian and Early,<sup>1</sup> Adrian and Orloff<sup>2</sup>, Chu and Robinson<sup>3</sup>, Hong and Jones<sup>4</sup>, and others. These calculations have typically considered only a paraxial forward or back scatter configuration. An exception was the work of Hong and Jones<sup>4</sup> which achieved a more flexible program which allowed the calculation of visibility with the photomultiplier tube (PMT) located in any direction from the probe volume. However, the published calculations of Hong and Jones were only for small rectangular apertures. The approach of Hong and Jones has been extended in this research to develop a computer code for a more realistic configuration: a circular aperture of the sizes used in actual experimental work. Calculations of visibility may be made with or without beam stops with the PMT aperture in any direction from the probe volume. For aperture locations and particle sizes where refraction theory is adequate, refraction theory may replace the Mie theory subroutine by following the work of Bachalo.<sup>5</sup>

Figure 1 shows the scattering geometry of the two laser beams with the z axis defined as the bisector of the angle between the beams. The y-axis is in the plane of the beams aligned normal to the z axis. Polarization of the incident beams is in the x direction. Associated with the (x,y,z) system is an (r,  $\theta$ ,  $\phi$ ) system as shown. It is assumed with that all light which is scattered into the solid angle of the PMT aperture is delivered to the PMT.

Following this assumption, the intensity resulting from the sum of scattered fields is calculated in the plane of the aperture, and integration of this intensity over the aperture determine radiant power delivered to the PMT. The vector  $\underline{r}$  locates the field points in the aperture plane.

The scattering process of the LDV was discussed briefly by Chu and Robinson<sup>3</sup>. Adapted versions of their equations (1) through (12) are given below as background to the development of an explicit expression for the visibility which may be evaluated by numerical integrations. Far from the scattering region at position  $\underline{r}$  and time  $\underline{t}$  the electric field scattered by the particle is

$$\underline{E}_{1,2}(\underline{r}, t) = \underline{E}_{1,2}(\underline{r}) \exp [i(\omega + \Delta\omega_{1,2}) t] \quad (1)$$

where the subscript 1 or 2 indicates one of the two incident laser beams as shown in Figure 1. The Doppler frequency shift is  $\Delta\omega_{1,2}$ . Born and Wolf<sup>6</sup> discuss an averaging procedure for the Poynting flux which results in the expression

$$\underline{S}(\underline{r}, t) = \frac{1}{2} \text{Re} \left\{ \{ \underline{E}_1(\underline{r}, t) + \underline{E}_2(\underline{r}, t) \} \times \{ \underline{H}_1(\underline{r}, t) + \underline{H}_2(\underline{r}, t) \}^* \right\} \quad (2)$$

where  $\underline{H}_{1,2}(\underline{r}, t)$  are the magnetic fields scattered by the particle from beams 1 and 2. Defining

$$\underline{S}_{\alpha\beta} = \underline{E}_\alpha \times \underline{H}_\beta^* \quad \alpha, \beta = 1, 2 \quad (* \text{ indicates complex conjugation}) \quad (3)$$

allows (2) to be written as

$$\underline{S}(\underline{r}, t) = \frac{1}{2} \text{Re} \left\{ \underline{S}_{11}(\underline{r}) + \underline{S}_{22}(\underline{r}) + \underline{S}_{12}(\underline{r}) \exp(i\omega_d t) + \underline{S}_{21}(\underline{r}) \exp(-i\omega_d t) \right\} \quad (4)$$

where  $\omega_d = \Delta\omega_1 - \Delta\omega_2$  is the Doppler modulation frequency.

Use of the subscripts  $\alpha$  and  $\beta$  will indicate the quantity in question to be a function of position  $\underline{r}$  only.

The energy per unit time that is scattered into the solid angle of the PMT aperture is given by

$$W(t) = \int r^2 d\Omega e_r \cdot \underline{S}(\underline{r}, t) \quad (5)$$

where the integral is taken over the solid angle of the aperture and where  $e_r$  is the radial unit vector. Substituting Eq. (4) into Eq. (5) gives

$$W(t) = \frac{1}{2} \operatorname{Re} (W_{11} + W_{22} + W_{12} \exp(i\omega_d t) + W_{21} \exp(-i\omega_d t)) \quad (6)$$

with  $W_{\alpha\beta}$  defined as

$$W_{\alpha\beta} = \int r^2 d\Omega e_r \cdot \underline{S}_{\alpha\beta}(\underline{r}) \quad (7)$$

Eq. (6) may then be expressed as

$$W(t) = W_{dc} + W_{ac} \cos(W_d t + \phi) \quad (8)$$

$$\text{where } W_{dc} = \frac{1}{2} \operatorname{Re} (W_{11} + W_{22}) \quad (9)$$

$$W_{ac} = \frac{1}{2} \left( \{ \operatorname{Re} (W_{12} + W_{21}) \}^2 + \{ \operatorname{Im} (W_{12} - W_{21}) \}^2 \right)^{\frac{1}{2}} \quad (10)$$

$$\phi = \tan^{-1} \frac{\operatorname{Im} (W_{12} - W_{21})}{\operatorname{Re} (W_{12} + W_{21})} \quad (11)$$

The visibility function  $V$  is defined as

$$V = \frac{W_{ac}}{W_{dc}} \quad (12a)$$

For a plane wave propagating in a medium with intrinsic impedance  $Z$

$$\underline{H}_\beta = (\underline{e}_r \times \underline{E}_\beta) / Z$$

where

$$Z = \left( \omega\mu / (\omega\epsilon + i\sigma) \right)^{\frac{1}{2}} \quad (13)$$

where  $\mathbf{e}_r$  is the unit vector in the direction of propagation.

For a medium with electrical conductivity  $\sigma = 0$ ,  $\gamma = (\mu/\epsilon)^{1/2}$  is a real quantity. Substituting Eq. (13) into Eq. (3) gives

$$\underline{S}_{\alpha\beta} = \underline{E}_\alpha \times (\mathbf{e}_r \times \underline{E}_\beta^*) / Z \quad (14)$$

If we require that the aperture be located adequately far from the probe volume,

$\underline{E}_\alpha \cdot \mathbf{e}_r = 0$  at the aperture and it follows that

$$\underline{S}_{\alpha\beta} = \mathbf{e}_r (\underline{E}_\alpha \cdot \underline{E}_\beta^*) / Z \quad (15)$$

Inserting Eq. (15) into Eq. (7) gives

$$W_{\alpha\beta} = \int r^2 d\Omega (\mathbf{e}_r \cdot \mathbf{e}_r) (\underline{E}_\alpha \cdot \underline{E}_\beta^*) / Z \quad (16)$$

With the electrical conductivity of the medium equal to zero, the intrinsic impedance is real, and it may be noted that  $W_{\beta\alpha} = W_{\alpha\beta}^*$  so  $W_{11}$  and  $W_{22}$  are real and

$$W_{12} + W_{21} = 2 \operatorname{Re} W_{12} \quad (17)$$

$$W_{12} - W_{21} = i 2 \operatorname{Im} W_{12} \quad (18)$$

Substituting Eqs. (17) and (18) into (10) and (11)

$$W_{ac} = \{(\text{Re } W_{12})^2 + (\text{Im } W_{12})^2\}^{1/2} \quad (19a)$$

$$W_{dc} = \frac{1}{2} (W_{11} + W_{22}) \quad (19b)$$

$$\text{and } \phi = \tan^{-1} \left( \frac{\text{Im } W_{12}}{\text{Re } W_{12}} \right) \quad (19c)$$

$$V = \frac{2 \{(\text{Re } W_{12})^2 + (\text{Im } W_{12})^2\}^{1/2}}{(W_{11} + W_{22})} \quad (20)$$

In Mie theory or refraction theory, the formulas which give the solutions to scattering of an incident plane wave are written in terms of a coordinate system defined by the directions of propagation and polarization of the incident wave with Z the direction of propagation and X the direction of polarization. In matrix form, the electric field components of far-field Mie scattering in a spherical coordinate system  $(r, \theta, \phi)$  associated with an  $(x, y, z)$  coordinate system may be expressed as

$$\begin{bmatrix} E_{\theta}(\theta, \phi) \\ E_{\phi}(\theta, \phi) \end{bmatrix} = \frac{iE_0}{kr} \exp(-ikr) \begin{bmatrix} -\cos \phi S_2(\theta) \\ \sin \phi S_1(\theta) \end{bmatrix} \quad (21)$$

where  $E_0$  is the magnitude of the incident electric field of either beam.

$S_1(\theta)$  and  $S_2(\theta)$  are the amplitude functions of Mie theory.

Eq. (21) may be written as

$$\begin{bmatrix} E_{\theta}(\theta, \phi) \\ E_{\phi}(\theta, \phi) \end{bmatrix} = \epsilon C(\theta, \phi) \quad (22).$$

$$\text{with } \epsilon = E_0 \exp(-ikr)/kr \quad (23)$$

$$C(\theta, \phi) = \begin{bmatrix} -\cos \phi S_2(\theta) \\ \sin \phi S_1(\theta) \end{bmatrix} \quad (24)$$

Now introduce an alternate coordinate system for each beam as shown in Figure 2. Considering the scattering of beam 1 and 2 as separate events in their own spherical coordinate frames  $(\theta_1, \phi_1)$  and  $(\theta_2, \phi_2)$  gives

$$\begin{bmatrix} E_{\theta_1}(\theta_1, \phi_1) \\ E_{\phi_1}(\theta_1, \phi_1) \end{bmatrix} = \epsilon C(1) \quad (25)$$

and

$$\begin{bmatrix} E_{\theta_2}(\theta_2, \phi_2) \\ E_{\phi_2}(\theta_2, \phi_2) \end{bmatrix} = \epsilon C(2) \quad (26)$$

$$\text{where } C(1) = C(\theta_1, \phi_1) = \begin{bmatrix} -\cos \phi_1 S_2(\theta_1) \\ \sin \phi_1 S_1(\theta_1) \end{bmatrix} \quad (27)$$

$$\text{and } C(2) = C(\theta_2, \phi_2) = \begin{bmatrix} -\cos \phi_2 S_2(\theta_2) \\ \sin \phi_2 S_2(\theta_2) \end{bmatrix} \quad (28)$$

The scattered electric fields as measured in the principal coordinate system  $(\theta, \phi)$  are the  $\underline{E}_\alpha$  and  $\underline{E}_\beta$  of Eq. (15).

$$\underline{E}_1 = E_{1\theta} \underline{\theta} + E_{1\phi} \underline{\phi} \quad (29)$$

$$\text{and } \underline{E}_2 = E_{2\theta} \underline{\theta} + E_{2\phi} \underline{\phi} \quad (30)$$

where  $\underline{\theta}$  and  $\underline{\phi}$  are unit vectors.

The magnitude of these components as measured in the  $(\theta, \phi)$  system may be obtained by orthogonal transformations on the components as measured in the beam coordinate systems  $(\theta_1, \phi)$  and  $(\theta_2, \phi_2)$ .

$$E_1 = \begin{bmatrix} E_{1\theta} \\ E_{1\phi} \end{bmatrix} = A \begin{bmatrix} E_{\theta_1}(\theta_1, \phi_1) \\ E_{\phi_1}(\theta_1, \phi_1) \end{bmatrix} \quad (31)$$

$$E_2 = \begin{bmatrix} E_{2\theta} \\ E_{2\phi} \end{bmatrix} = B \begin{bmatrix} E_{\theta_2}(\theta_2, \phi_2) \\ E_{\phi_2}(\theta_2, \phi_2) \end{bmatrix} \quad (32)$$

$$\text{where } A = \begin{bmatrix} a_{11} & a_{12} \\ a_{21} & a_{22} \end{bmatrix} \quad B = \begin{bmatrix} b_{11} & b_{12} \\ b_{21} & b_{22} \end{bmatrix} \quad (33)$$

A and B are the real orthonormal matrices of the transformation with

$a_{22} = a_{11}$ ,  $a_{21} = -a_{12}$ ,  $b_{22} = b_{11}$ , and  $b_{21} = -b_{12}$  which results in

$$A^+ A = B^+ B = I \quad (34)$$

Formulas for elements of A and B were given by Hong and Jones and are also given in the Appendix. Substituting Eqs. (25) and (26) into (31) and (32) gives

$$E_1 = A \epsilon \quad C(1) \quad (35)$$

$$E_2 = B \epsilon \quad C(2) \quad (36)$$

Matrix equations may now be obtained for  $\underline{E}_\alpha \cdot \underline{E}_\beta$  which allow the calculation of  $W_{\alpha\beta}$  by numerical evaluation of Eq. (16). This is accomplished by noting that

$$\underline{E}_\alpha \cdot \underline{E}_\beta = \underline{E}_\beta \cdot \underline{E}_\alpha \quad (35)$$

where  $\underline{E}_{\alpha,\beta}$  are the vectors as given by Eqs. (29) and (30) and  $E_{\alpha,\beta}$  are the matrices as given by Eqs. (31) and (32).  $E_{\alpha}^+$  is the complex conjugate of the transpose of  $E_{\alpha}$ .

$$\begin{aligned} \text{for } (\alpha, \beta) &= (1, 1) \\ \underline{E}_1 \cdot \underline{E}_1^* &= E_1^+ E_1 = \left( A \epsilon C(1) \right)^+ \left( A \epsilon C(1) \right) \\ &= \epsilon^* \epsilon C^+(1) A^+ A C(1) \\ &= \epsilon^* \epsilon C^+(1) C(1) \end{aligned} \quad (36)$$

since  $A^+ A = I$ .

For  $(\alpha, \beta) = (2, 2)$

$$\begin{aligned} \underline{E}_2 \cdot \underline{E}_2^* &= E_2^+ E_2 = \left( B \epsilon C(2) \right)^+ \left( B \epsilon C(2) \right) \\ &= \epsilon^* \epsilon C^+(2) B^+ B C(2) \\ &= \epsilon^* \epsilon C^+(2) C(2) \end{aligned} \quad (37)$$

since  $B^+ B = I$

For  $(\alpha, \beta) = (1, 2)$

$$\underline{E}_1 \cdot \underline{E}_2^* = E_2^+ E_1 = \left( B \epsilon C(2) \right)^+ \left( A \epsilon C(1) \right)$$

Substituting Eqs. (23), (36), (37), and (38) into (16) gives

$$W_{\alpha\beta} = \frac{|\underline{E}_0|^2}{Z K^2} I_{\alpha\beta} \quad (39)$$

where

$$I_{\alpha\beta} = \int d\Omega f_{\alpha\beta} \quad (40)$$

$$f_{11} = C^+(1) C(1) \quad (41)$$

$$f_{22} = C^+(2) C(2)$$

$$f_{12} = C^+(2) B^+ A C(1)$$

Inserting Eq. (39) into Eq. (20) gives

$$V = 2 \frac{\left( (\text{Re} I_{12})^2 + (\text{Im} I_{12})^2 \right)^{1/2}}{(I_{11} + I_{22})} \quad (42)$$



For Mie theory, it is seen to be necessary to evaluate three integrals:

$$\operatorname{Re} I_{12} = \int d\Omega \operatorname{Re} f_{12} = \int d\Omega F_1$$

$$\operatorname{Im} I_{12} = \int d\Omega \operatorname{Im} f_{12} = \int d\Omega F_2$$

$$(I_{11} + I_{22}) = \int d\Omega (f_{11} + f_{22}) = \int d\Omega F_3$$

For the actual evaluation of these integrals, define a rectangular coordinate system  $(x', y')$  in the plane of the aperture with origin at the center of the aperture as shown in Figure 3 with  $(\rho', \phi')$  as the corresponding polar coordinate system. The numerical computation of the visibility function over the range of geometrical configurations encountered in practice requires a numerical integration formula which may attain arbitrarily high polynomial accuracy by the addition of points. Figures 4 and 5 show the location of points for a Legendre-Gaussian scheme. Figure 4 has 16 points and Figure 5 has 36 points. This numerical integration scheme over a circle in the  $x'-y'$  plane may be expressed as

$$\iint dx' dy' f(x', y') = \pi \rho_{\max}^2 \sum_{i,j} w_{ij} f(\rho'_i, \phi'_j)$$

where  $\rho_{\max}$  is the radius of the circle and  $w_{ij}$  is the weighting factor for point  $(\rho'_i, \phi'_j)$ .

The integrals of immediate interest are of the form  $\int d\Omega F_K(\theta', \phi')$ .

$$\int d\Omega F_K(\theta', \phi') = \int \frac{dx' dy'}{r^2} F_K(\theta', \phi')$$

$$= \frac{1}{r_0^2} \int dx' dy' \left(\frac{r_0}{r}\right)^2 F_K(\theta', \phi')$$

$$\cos \theta' = \frac{r_0}{r}$$

$$\int d\Omega F_K(\theta', \phi') = \frac{1}{r_0^2} \int dx' dy' \cos^2 \theta' F_K(\theta', \phi')$$

$$= \frac{1}{r_o^2} \pi \rho_{\max}^2 \sum_{i,j} w_{ij} \cos^2 \theta'_{ij} F_K(\theta'_i, \phi'_j)$$

$$= \pi \left( \frac{\rho_{\max}}{r_o} \right)^2 \sum_{i,j} w_{ij} \cos^2 \theta'_i F_K(\theta'_i, \phi'_j)$$

$$\int d\Omega F_K(\theta', \phi') = \pi \tan^2 \theta'_{\max} \sum_{i,j} w_{ij} \cos^2 \theta'_i F_K(\theta'_i, \phi'_j)$$

$i$  = number of circle

$j$  = number of point on a particular circle

$$\tan \theta'_i = \frac{\rho_i}{r_o}$$

$$\tan \theta'_{\max} = \frac{\rho_{\max}}{r_o}$$

$$\frac{\tan \theta'_i}{\tan \theta'_{\max}} = \frac{\rho_i}{\rho_{\max}}$$

$$0 < \frac{\rho_i}{\rho_{\max}} < 1$$

The ratio  $\rho_i/\rho_{\max}$  is specified by the numerical integration scheme. Note

$$\text{that the } F/\# \text{ of the aperture is given by } F/\# = \frac{r_o}{2 \rho_{\max}} = \frac{1}{2 \left( \frac{\rho_{\max}}{r_o} \right)} = \frac{1}{2 \tan \theta'_{\max}}$$

$$\tan \theta'_{\max} = \frac{1}{2 F/\#}$$

$$\theta'_i = \tan^{-1} \left( \frac{\rho_i}{\rho_{\max}} \tan \theta'_{\max} \right)$$

$$\theta'_i = \tan^{-1} \left( \frac{\rho_i}{\rho_{\max}} \cdot \frac{1}{2 F/\#} \right)$$

$$\int d\Omega F_K(\theta', \phi') = \frac{\pi}{4(f/\#)^2} \sum_{ij} w_{ij} \cos^2 \theta'_i F_K(\theta'_j, \phi'_j)$$

The procedure for numerical computation of the visibility function is outlined in Figure 6.

The original motivation for development of the UTSI Mie theory visibility code was to provide the capability for critical review of the published work of other researchers. Such review is possible only if all details of the scattering geometry is available for a particular set of data.

Calculation of visibility for paraxial forward scatter to an aperture with beam stops was reported by Roberds.<sup>7</sup> Roberds' calculation was accomplished using scalar diffraction theory and a numerical integration over the aperture excluding the beam stops. His theoretical and experimental data for a twin beam stop configuration using water drops was presented in his Figure 8. The UTSI Mie code recently calculated the visibility for this experiment both with and without the beam stops with results as shown in Figure 7. As reported by Robinson and Chu, a real index of refraction results in an oscillatory phenomena for visibility calculated by the Mie theory in paraxial forward or back scatter. For the case under consideration this phenomenon is again observed. However, the UTSI Mie results using beam stops are very close to Roberd's scalar calculation. Both these calculations are observed to be slightly lower than the experimental data. The Mie calculation without beam stops agrees quite closely with the closed form for visibility as given by Farmer.<sup>8</sup> Roberds' Figure 10 reported backscatter data for water drops with fringe periods of 38.1 $\mu$ m

and  $66.6\text{ }\mu\text{m}$  with F number of collecting aperture not specified. This visibility data showed the oscillatory phenomenon that has led many researchers to question whether the LDV may be used for paraxial back-scatter. A UTSI Mie computation for fringe period of  $50\text{ }\mu\text{m}$  with  $f/4.0$  aperture also shows these oscillations in Figure 8.

However, Figure 9 for fringe period of  $20\text{ }\mu\text{m}$  shows a distinctly more monotonic behavior. This is also the case for Figure 10 for fringe period of  $10\text{ }\mu\text{m}$ . Figures 11, 12, 13, and 14 show the result of adding absorption (imaginary index of refraction) to the particles of Figure 9.

The UTSI Mie code has also been used to review the work of Bachalo<sup>5</sup> for large particles using an off-axis location with aperture centered in the x-z plane which is normal to the plane of the beams. Bachalo computed the visibility using refraction theory in a numerical integration over the aperture and also reported experimental data for angle  $\beta$  of  $30^\circ$ . His experimental data for  $\beta = 30^\circ$  shows excellent agreement with his computer calculation as does the Mie calculation of Figure 15. Mie and refraction calculations have since been made at UTSI (figures 16-23) which indicate that the refraction calculations are quite good for angles of  $\beta$  between  $20^\circ$  and  $60^\circ$  and a reasonably broad range of fringe periods. However, for angles of less than  $20^\circ$  and greater than  $70^\circ$  the Mie theory begins to deviate somewhat from the refraction theory. It is believed that this is due to diffracted light for the small angles and due to reflected light for the large angles.

## REFERENCES

1. R. J. Adrian and W. L. Earley, "Evaluation of LDV Performance Using MIE Scattering Theory," Symp. on Laser Anemometry, Univ. of Minnesota, Oct., 1975.
2. R. J. Adrian and K. L. Orloss, "Laser Anemometer Signals: Visibility Characteristics and Application to Particle Sizing," Appl. Opt., 16, 677 (1977).
3. W. P. Chu and D. M. Robinson, "Scattering From a Moving Spherical Particle by Two Crossed Coherent Plane Waves," Appl. Opt. 16, 619 (1977).
4. N. S. Hong and A. R. Jones, "A Light Scattering Technique for Particle Sizing Based on Laser Fringe Anemometry," J. Phys. D: (British) Appl. Phys., 9, 1839 (1976)
5. W. D. Bachalo, "Method for Measuring the Size and Velocity of Spheres by Dual-Beam Light Scatter Interferometry," Appl. Opt., 19, 363 (1980).
6. M. Born and E. Wolf, Principles of Optics, (Pergaman, New York, 1975) p. 33.
7. D. W. Roberds, "Particle Sizing Using Laser Interferometry," Appl. Opt. 16, 1861 (1977).
8. W. M. Farmer, "Measurement of Particle Size, Number Density, and Velocity Using a Laser Interferometer," Appl. Opt. 11, 2603 (1972).

## APPENDIX

The equations which relate the various coordinate systems are:

$$\begin{aligned} x &= r \sin \theta \cos \phi & x_{1,2} &= x \\ y &= r \sin \theta \sin \phi & y_{1,2} &= y \cos \gamma \pm z \sin \gamma \\ z &= r \cos \theta & z_{1,2} &= \pm y \sin \gamma + z \cos \gamma \end{aligned}$$

which give

$$\sin \theta_{1,2} \cos \phi_{1,2} = \sin \theta \cos \phi$$

$$\sin \theta_{1,2} \sin \phi_{1,2} = \sin \theta \sin \phi \cos \gamma \pm \sin \gamma$$

$$\cos \theta_{1,2} = \pm \sin \theta \sin \phi \sin \gamma \pm \cos \theta \cos \gamma$$

$$\begin{aligned} a_{11} &= (\sin \theta \cos \gamma \pm \cos \theta \sin \phi \sin \gamma) / \sin \theta_{1,2} \\ b_{11} & \end{aligned}$$

$$\begin{aligned} a_{12} &= \pm \cos \phi \sin \gamma / \sin \theta_{1,2} \\ b_{12} & \end{aligned}$$

$$a_{22} \quad a_{11} \quad a_{21} = -a_{12} \quad b_{22} = b_{11} \quad b_{21} = b_{12}$$

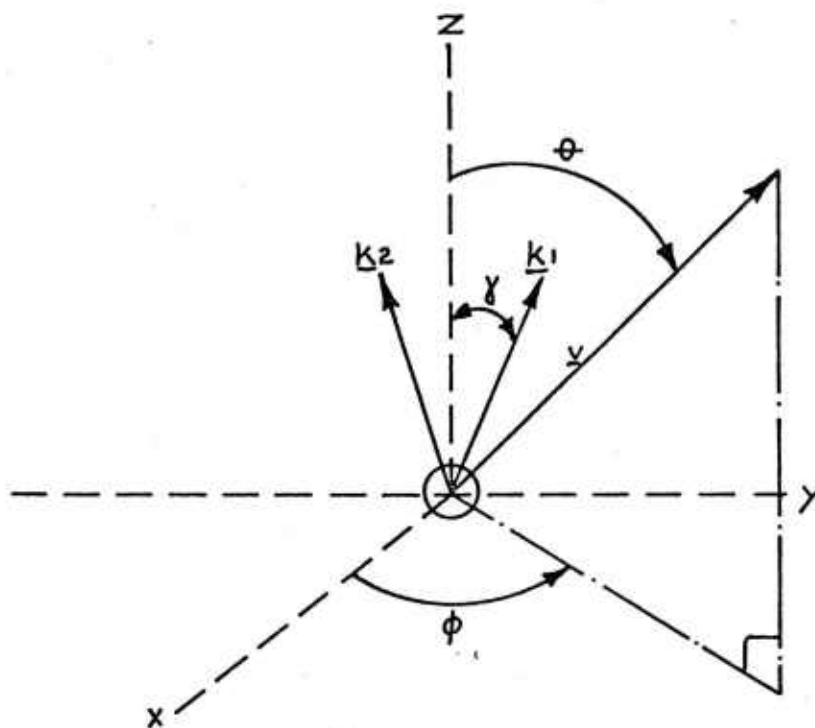


Figure 1. Scattering geometry.  $\underline{k}_1$  and  $\underline{k}_2$  are the propagation vectors of the incident Laser beams in the  $(y,z)$  plane.

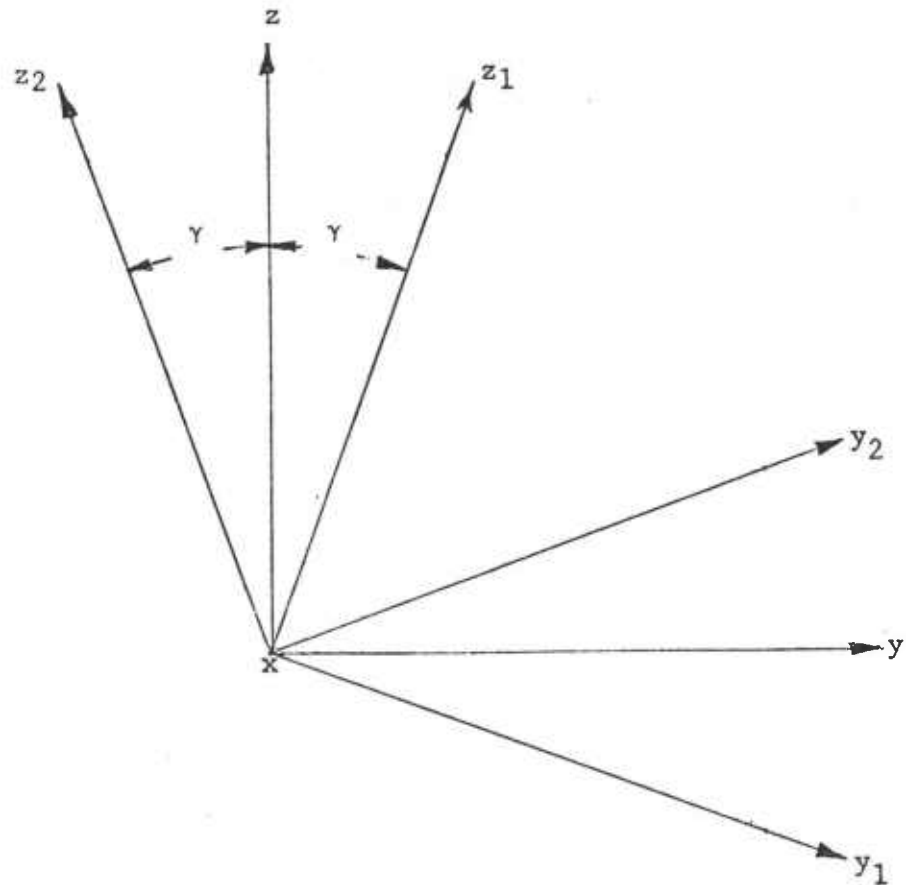


Figure 2. The beam coordinate systems with  $x = x_1 = x_2$  normal to the  $(y, z)$  plane



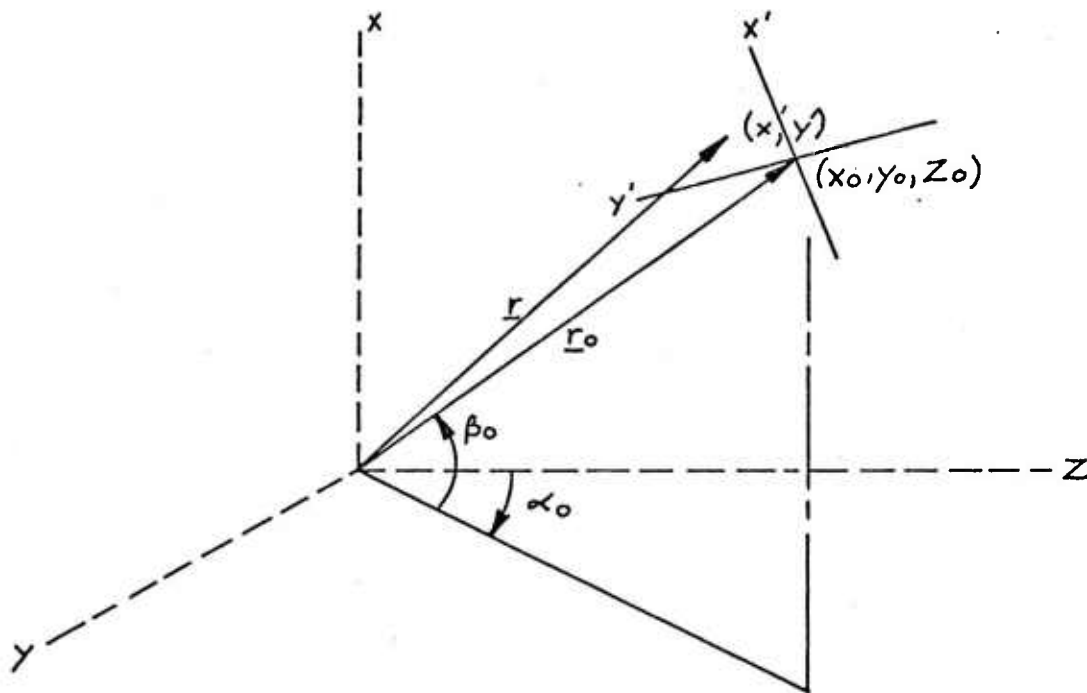


Figure 3. The vector  $\underline{r}_0$  locates the center of the aperture and the  $(x', y')$  plane is normal to  $\underline{r}_0$ .

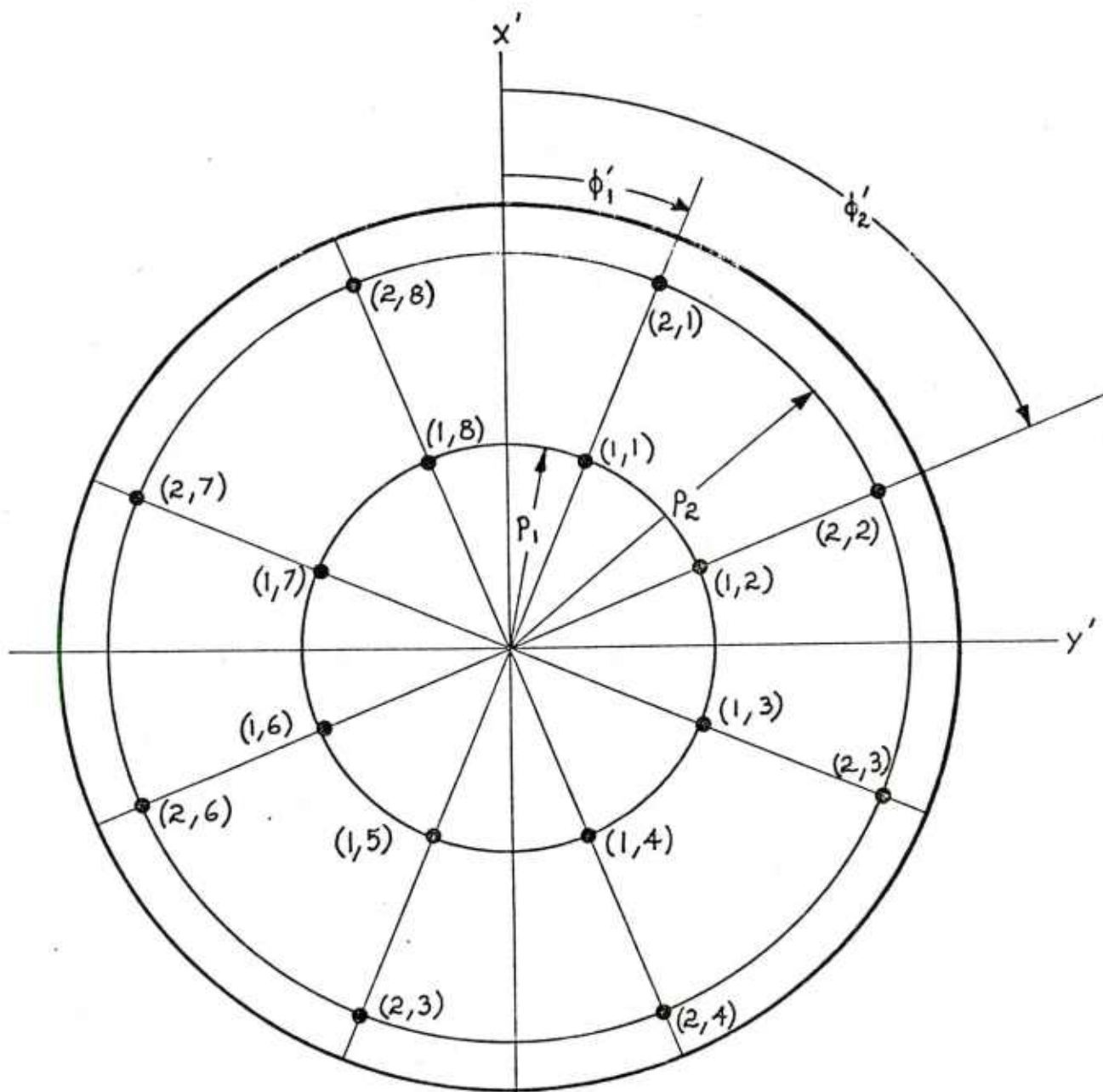


Figure 4. Location of points for Legendre-Gaussian numerical integration using 16 points.

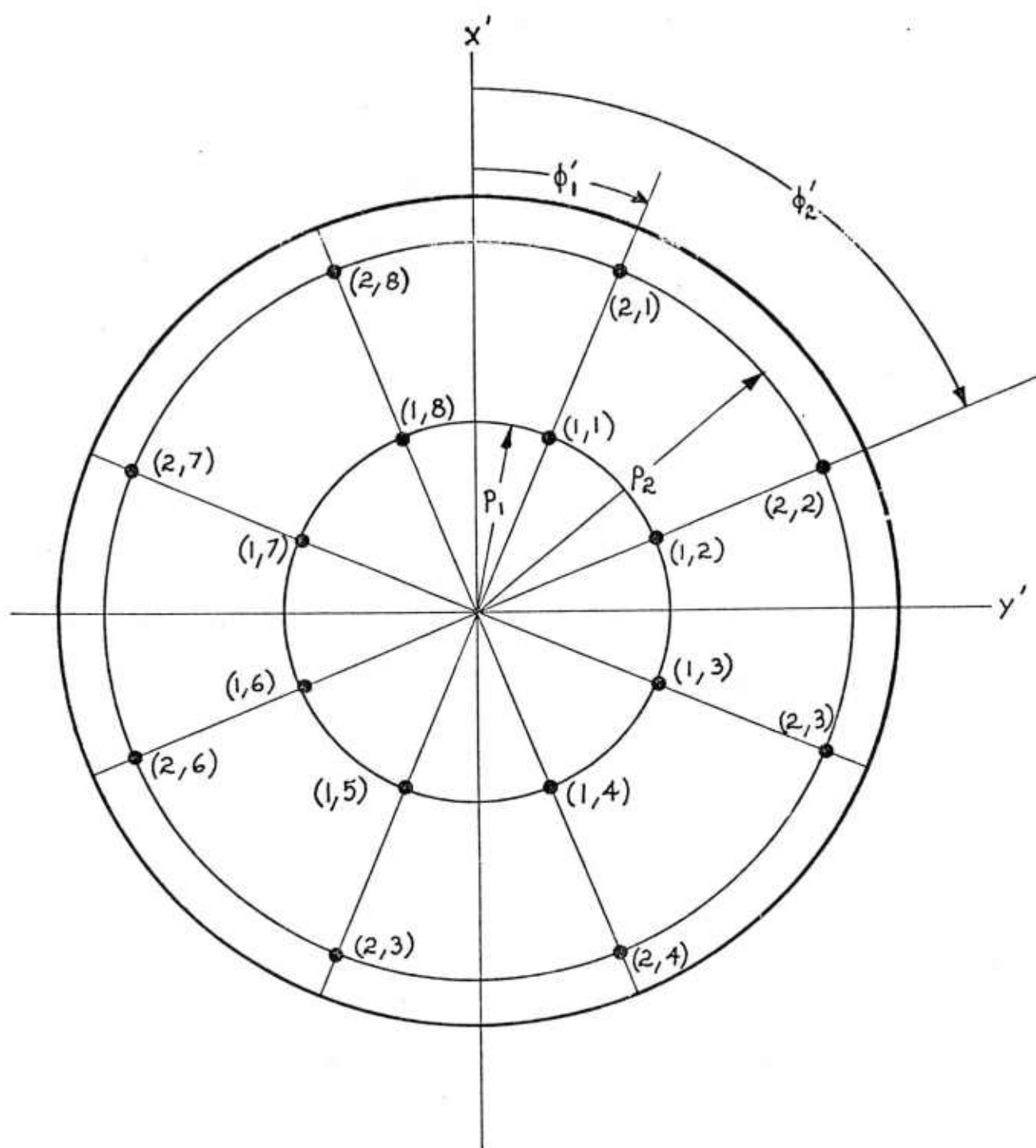


Figure 5. Location of points for Legendre-Gaussian numerical integration using 36 points.

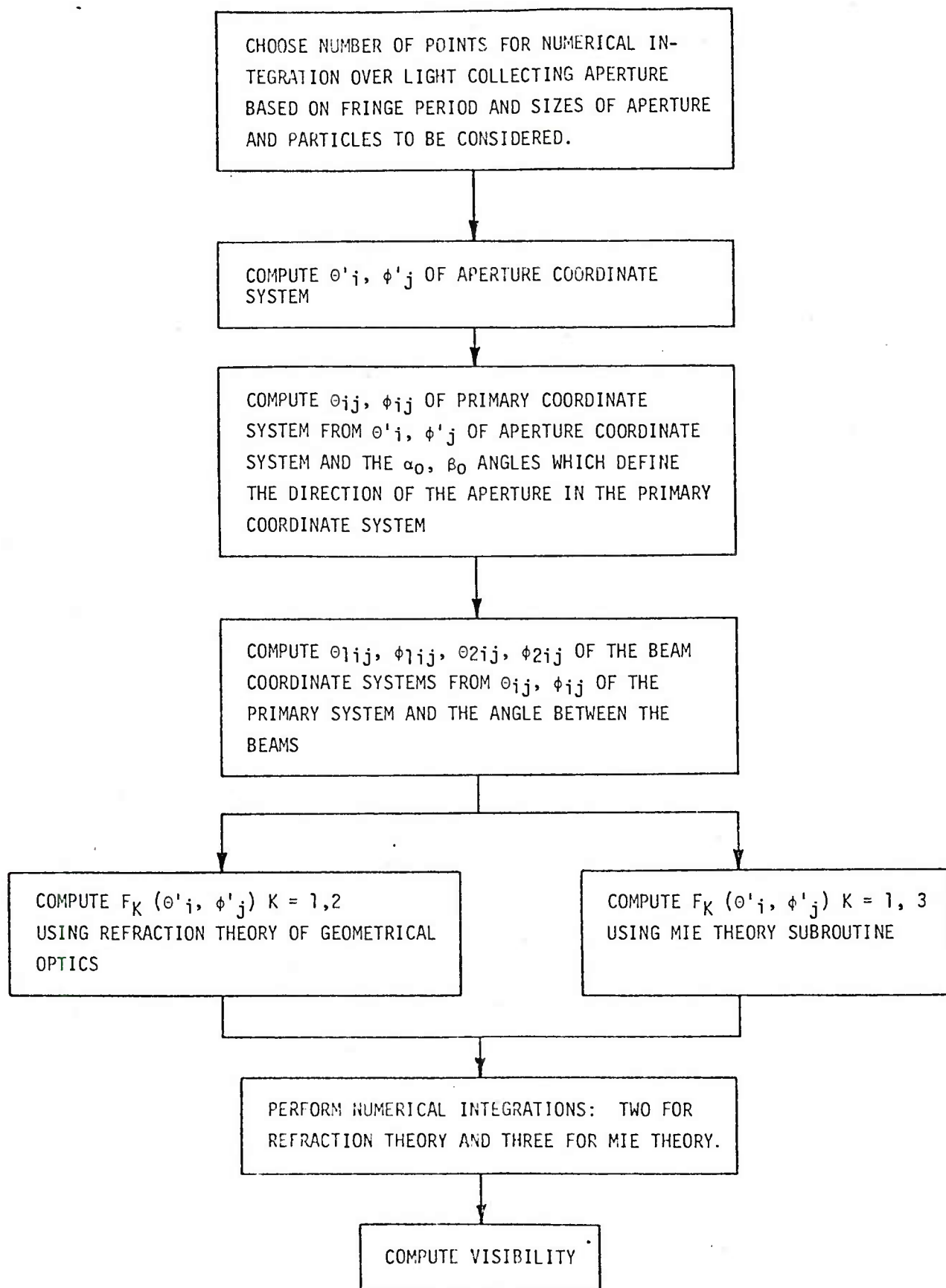


Figure 6. Flow Chart for Calculation of Visibility

# VISIBILITY VERSUS PARTICLE DIAMETER/FRINGE PERIOD

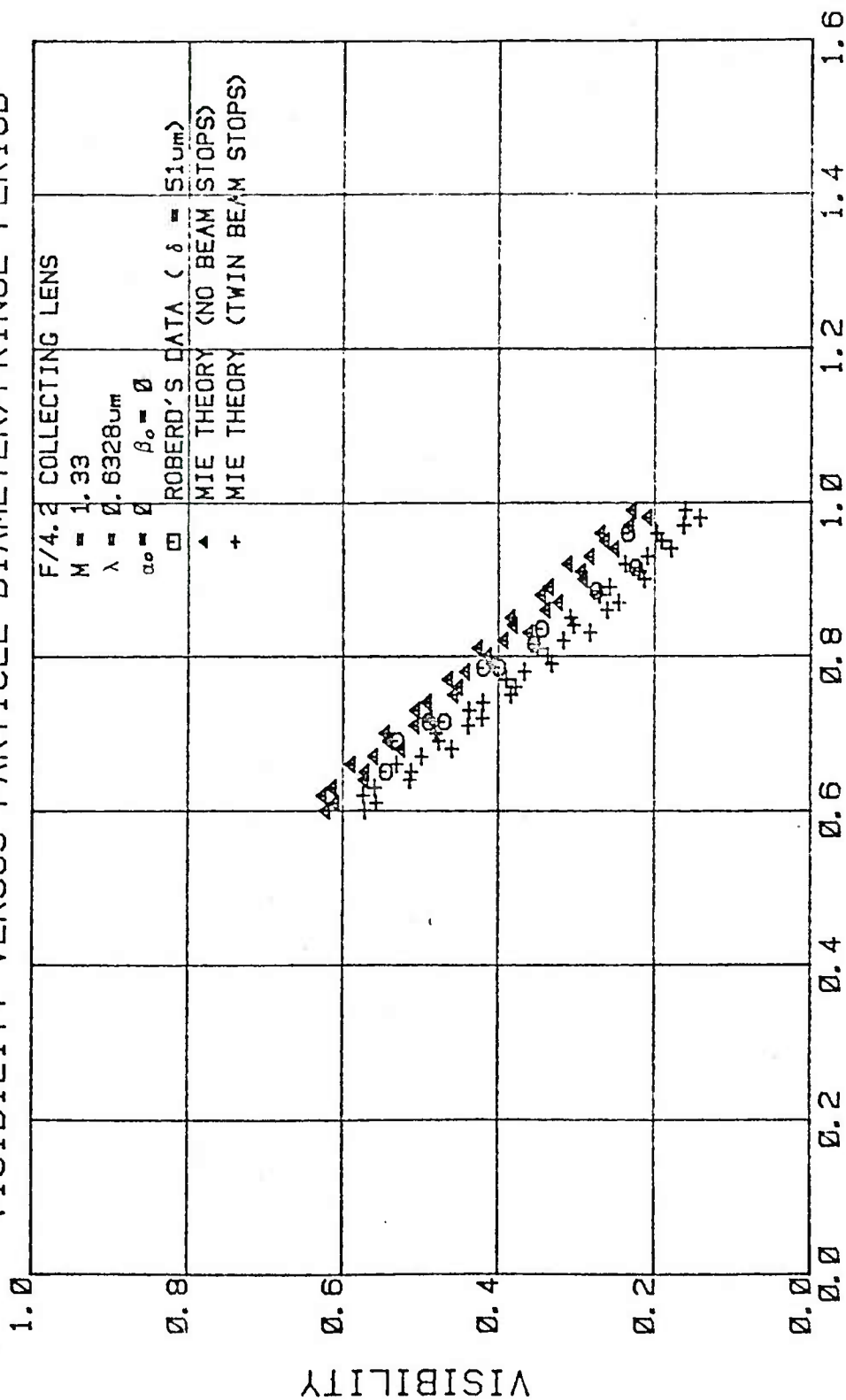


FIGURE 7

# VISIBILITY VERSUS PARTICLE DIAMETER/FRINGE PERIOD

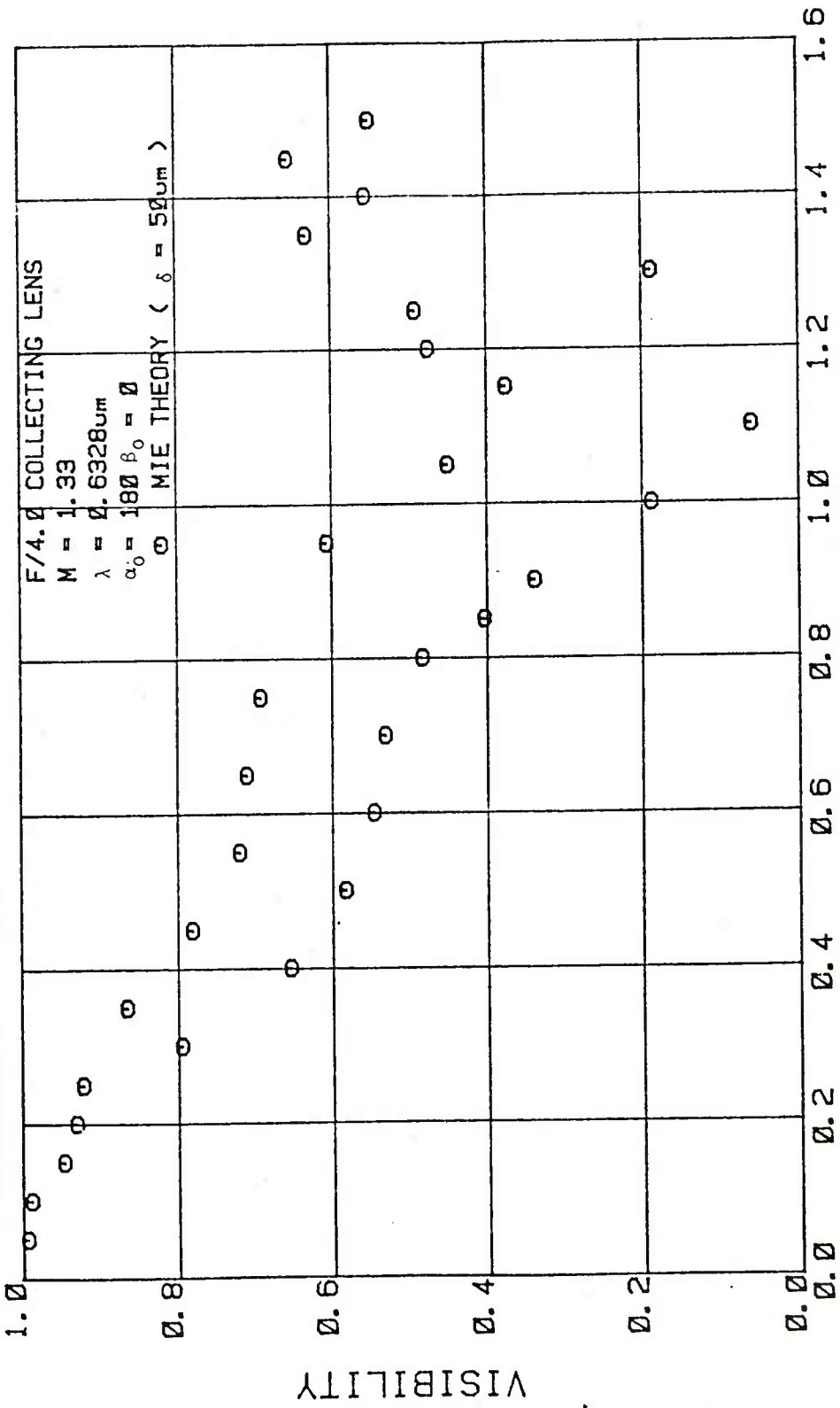


FIGURE 8

# VISIBILITY VERSUS PARTICLE DIAMETER/FRINGE PERIOD

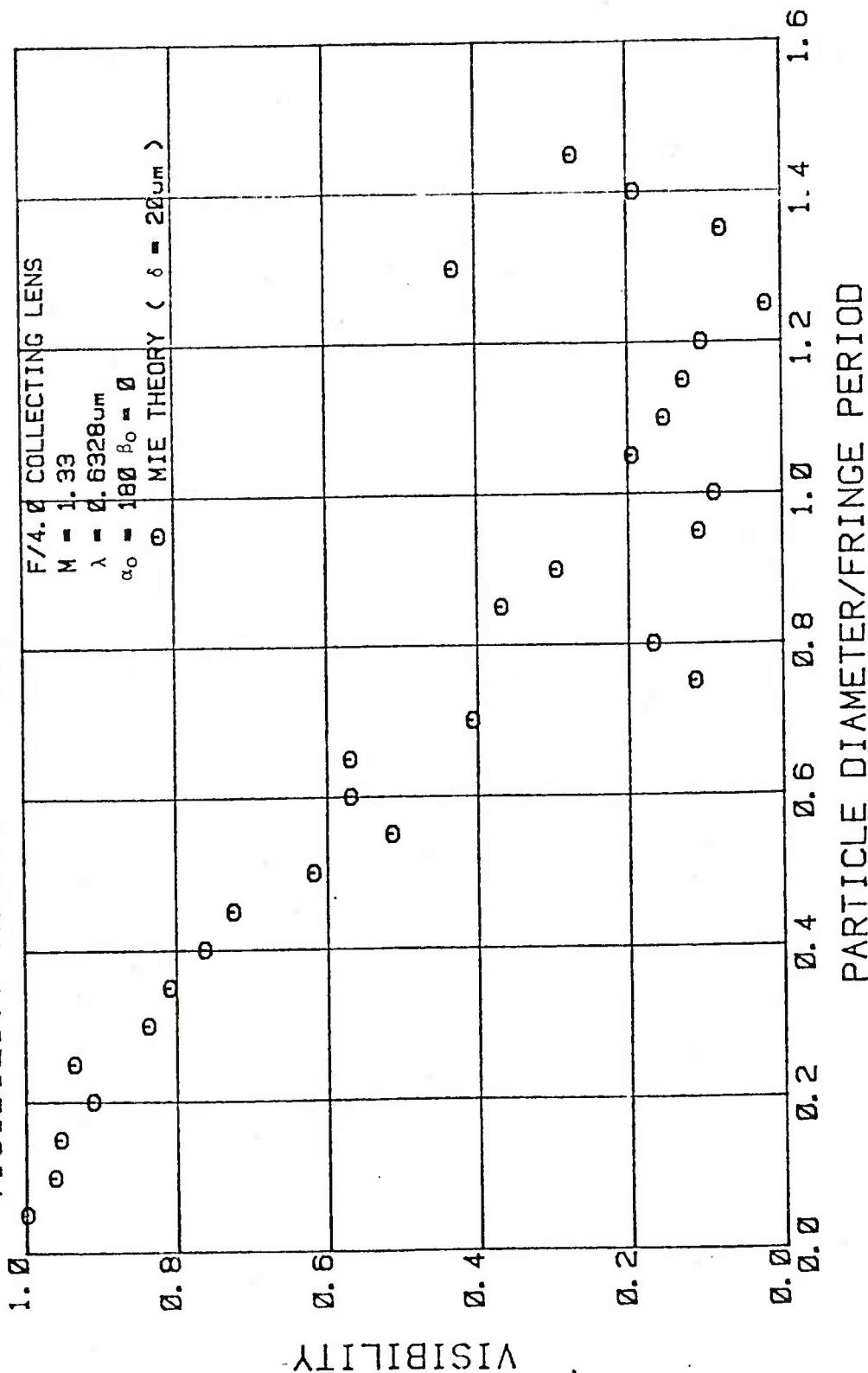


FIGURE 9

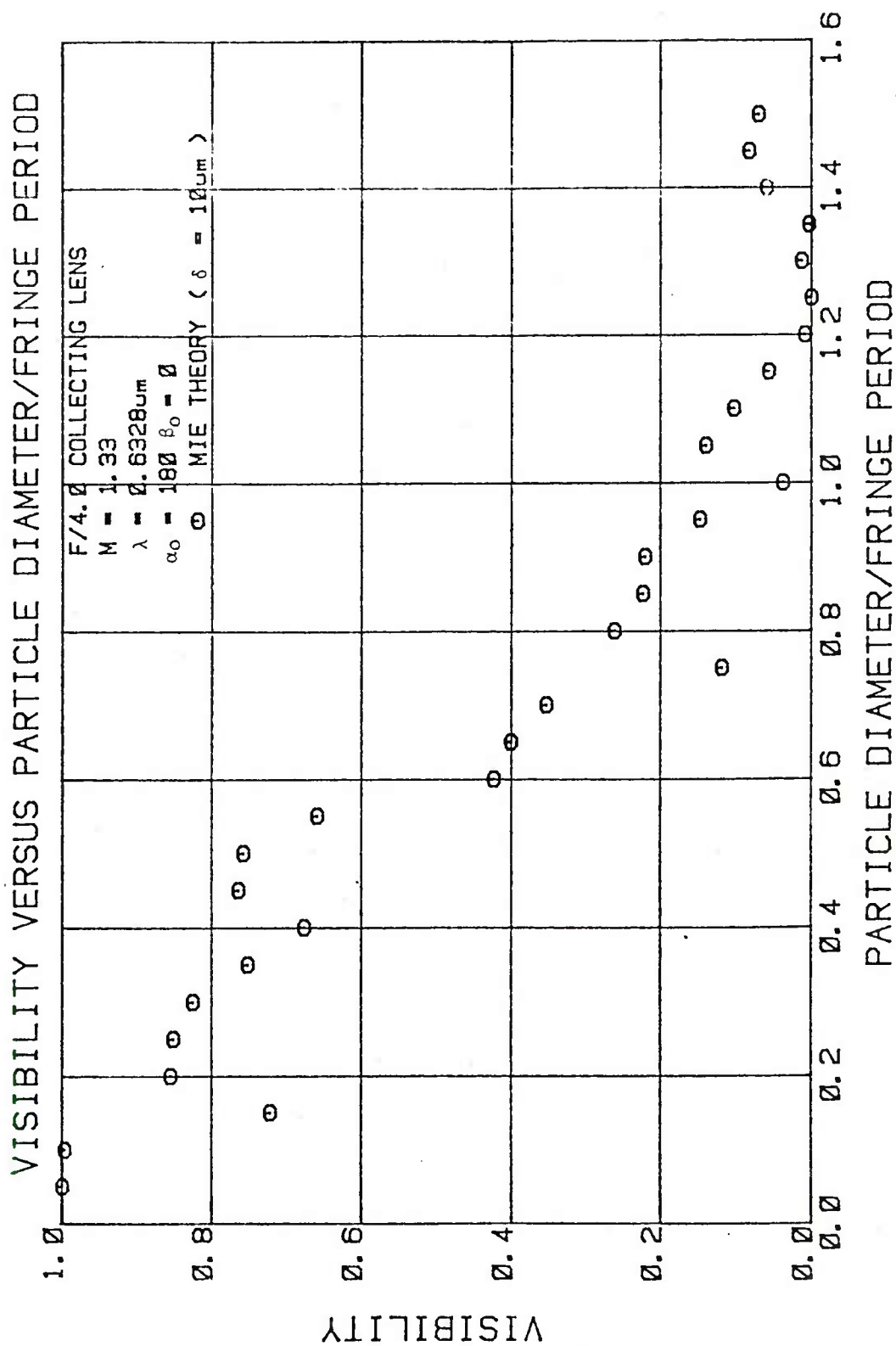


FIGURE 10



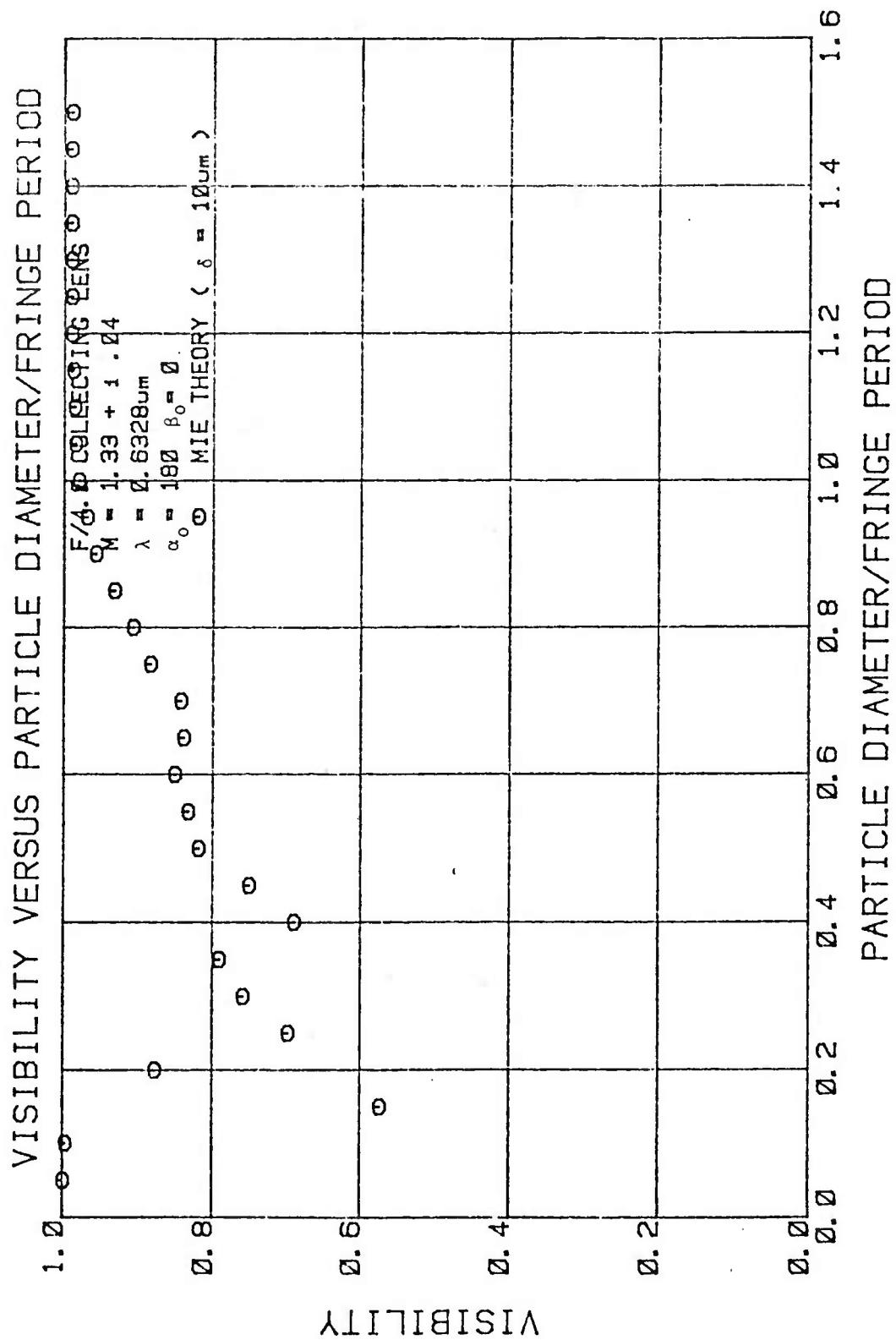


FIGURE 11

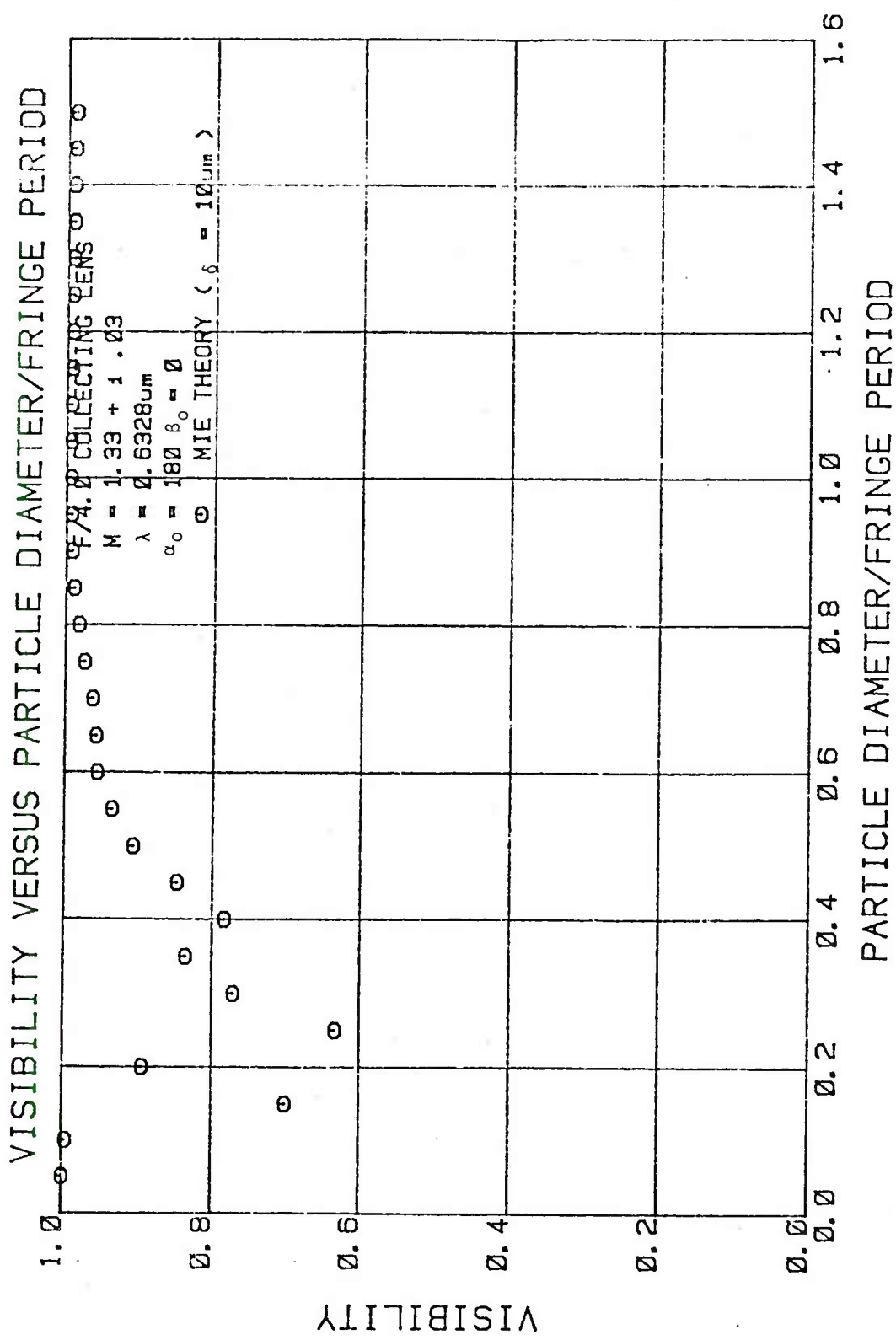


FIGURE 12

VISIBILITY VERSUS PARTICLE DIAMETER/FRINGE PERIOD

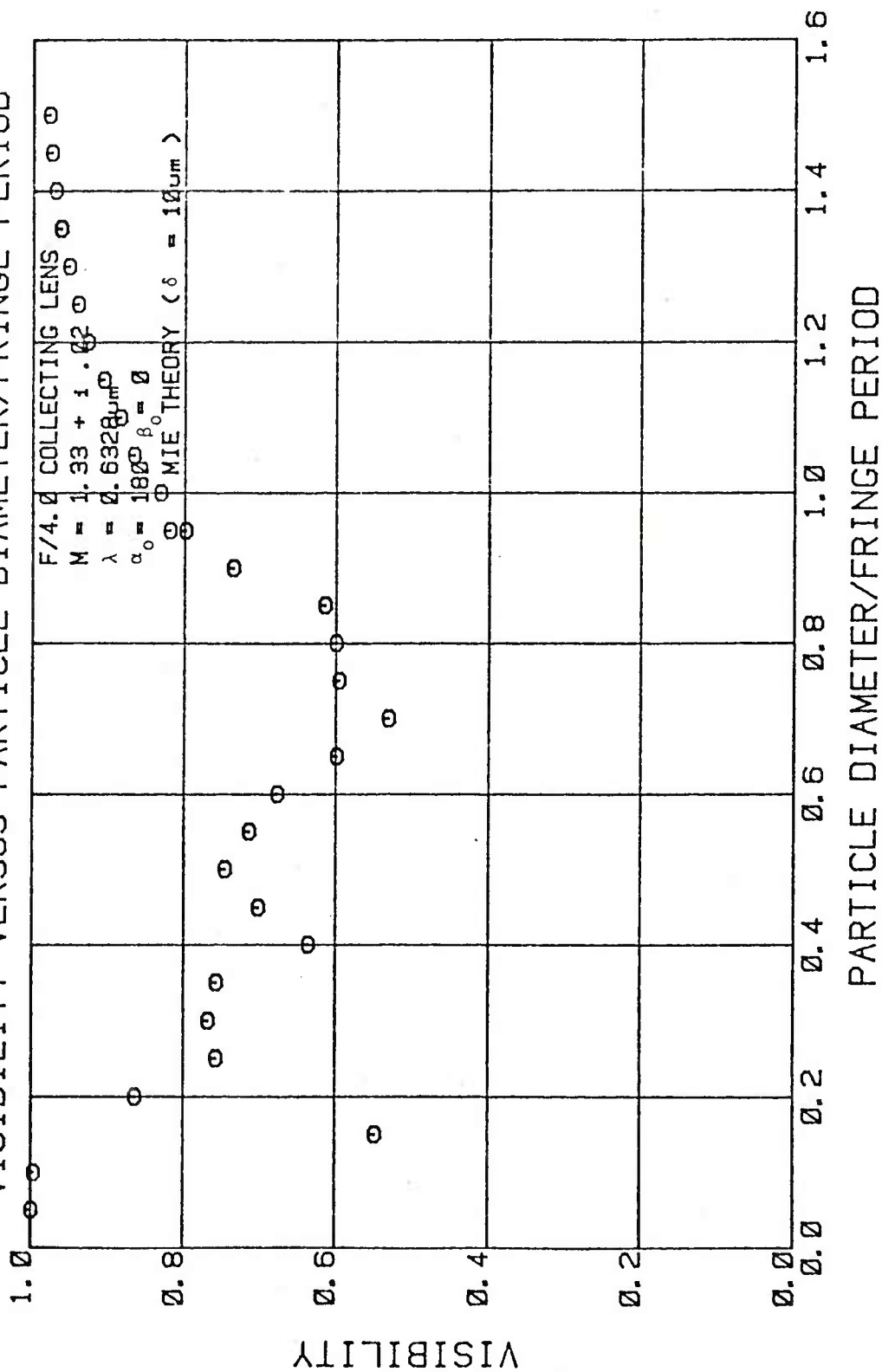


FIGURE 13

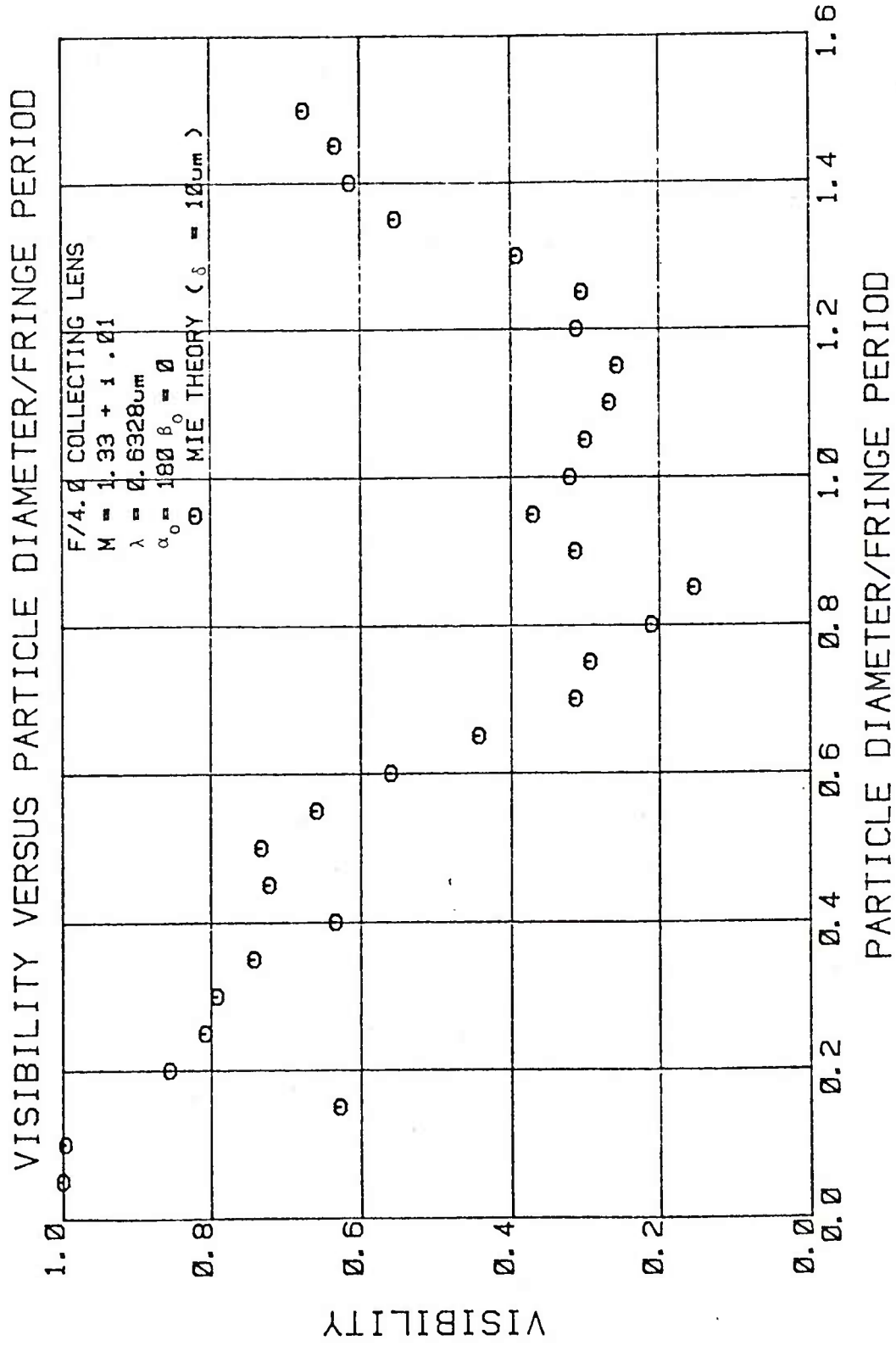


FIGURE 14

# VISIBILITY VERSUS PARTICLE DIAMETER/FRINGE PERIOD

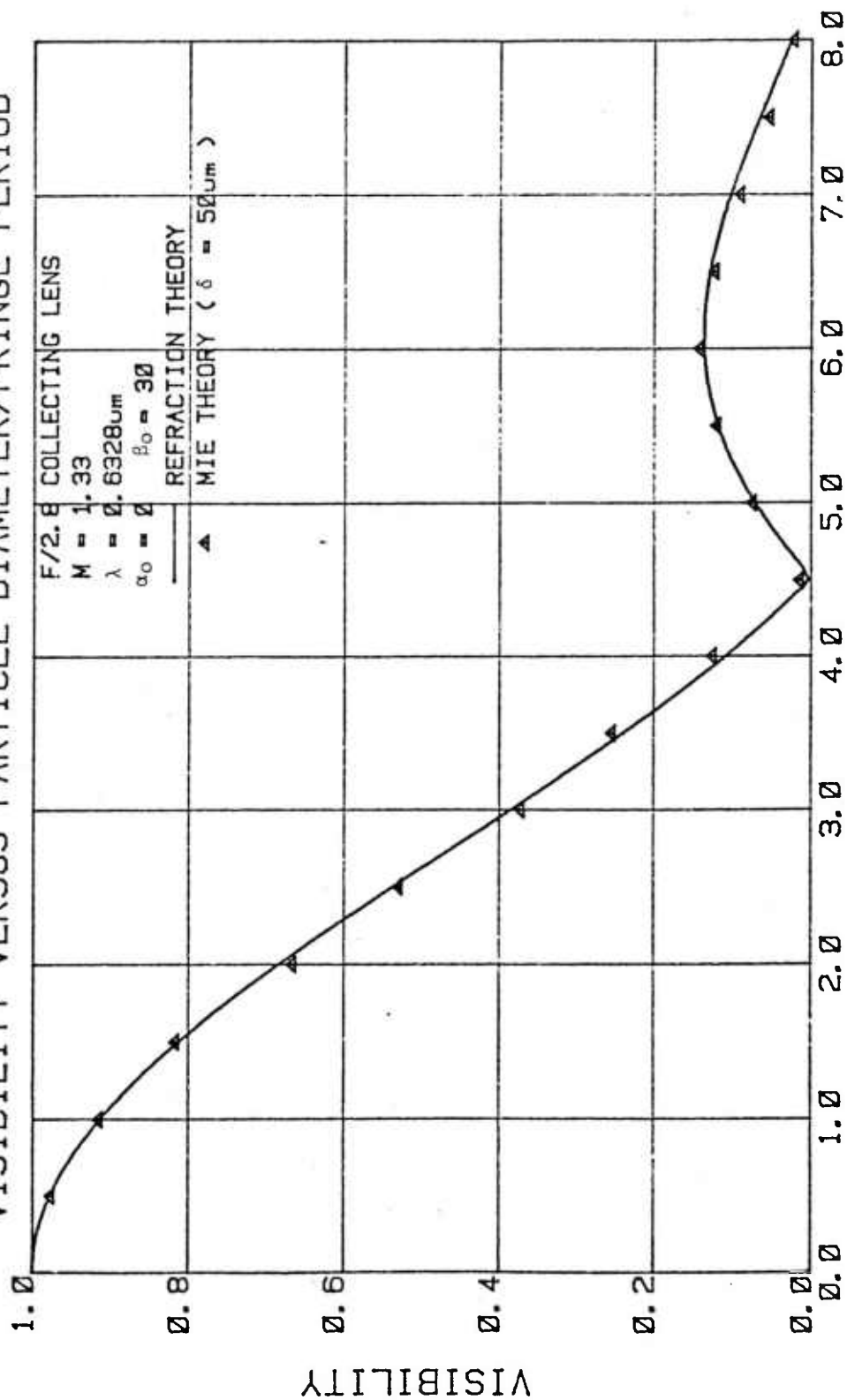


FIGURE 15

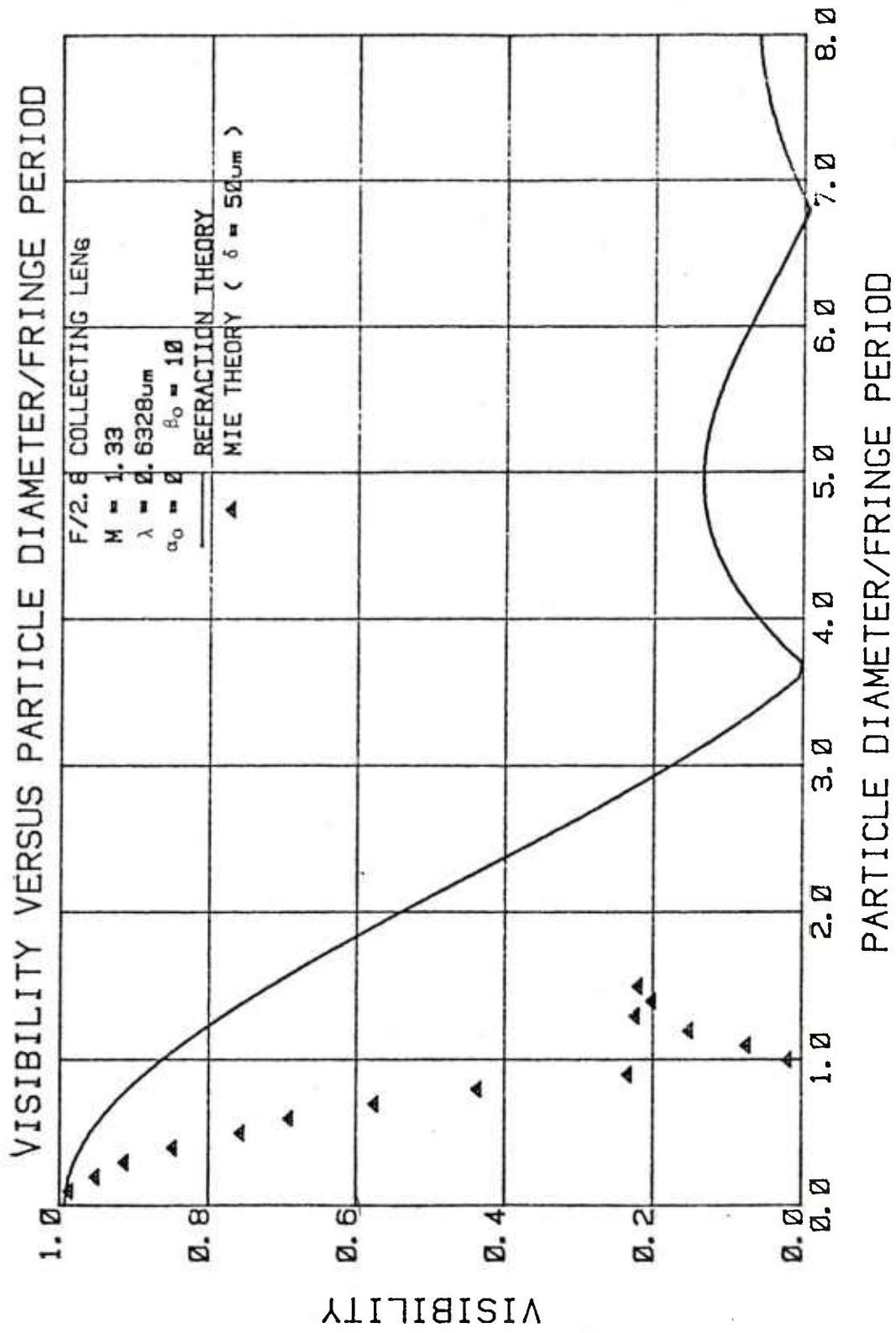


FIGURE 16

# VISIBILITY VERSUS PARTICLE DIAMETER/FRIDGE PERIOD

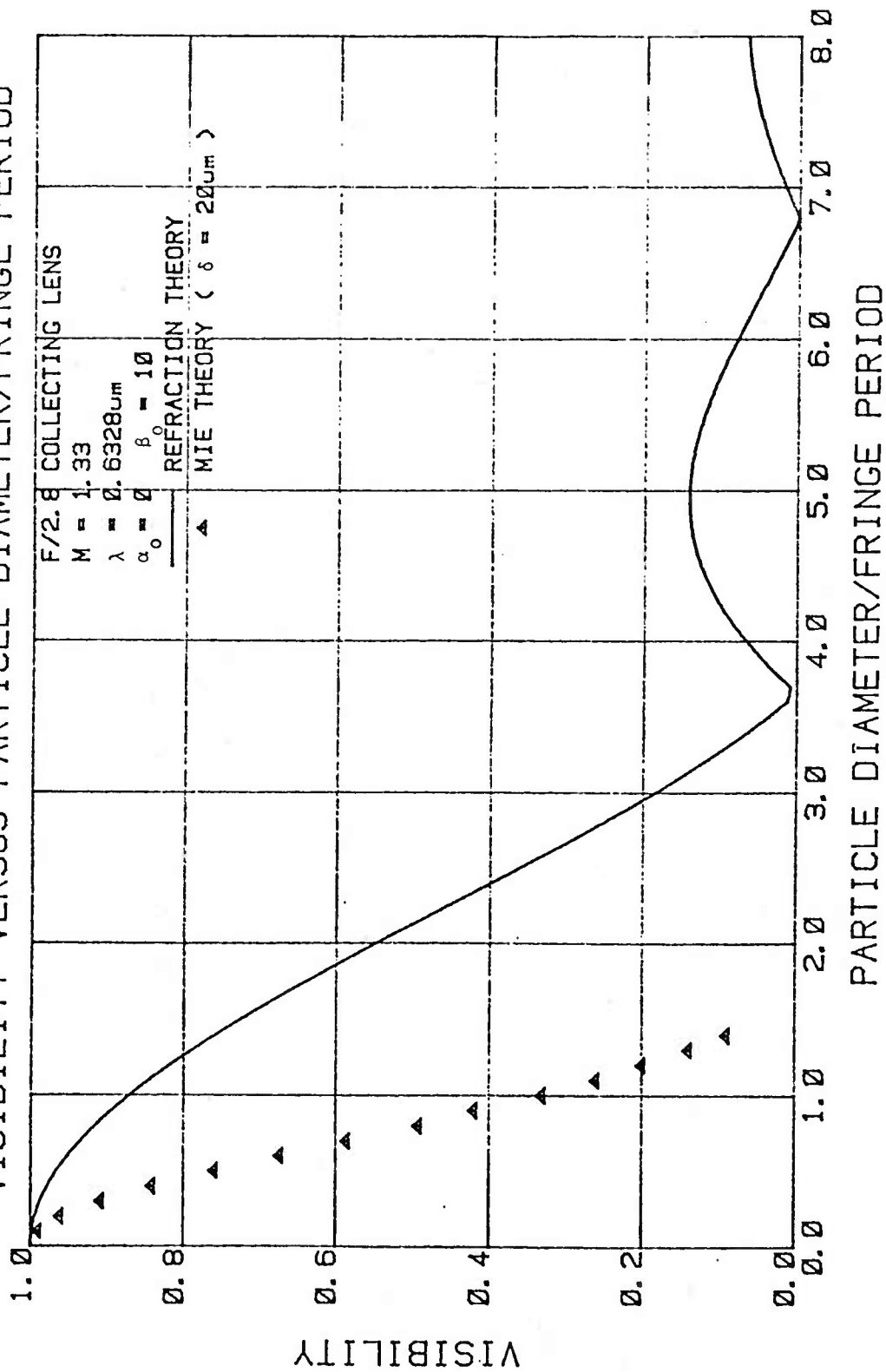


FIGURE 17

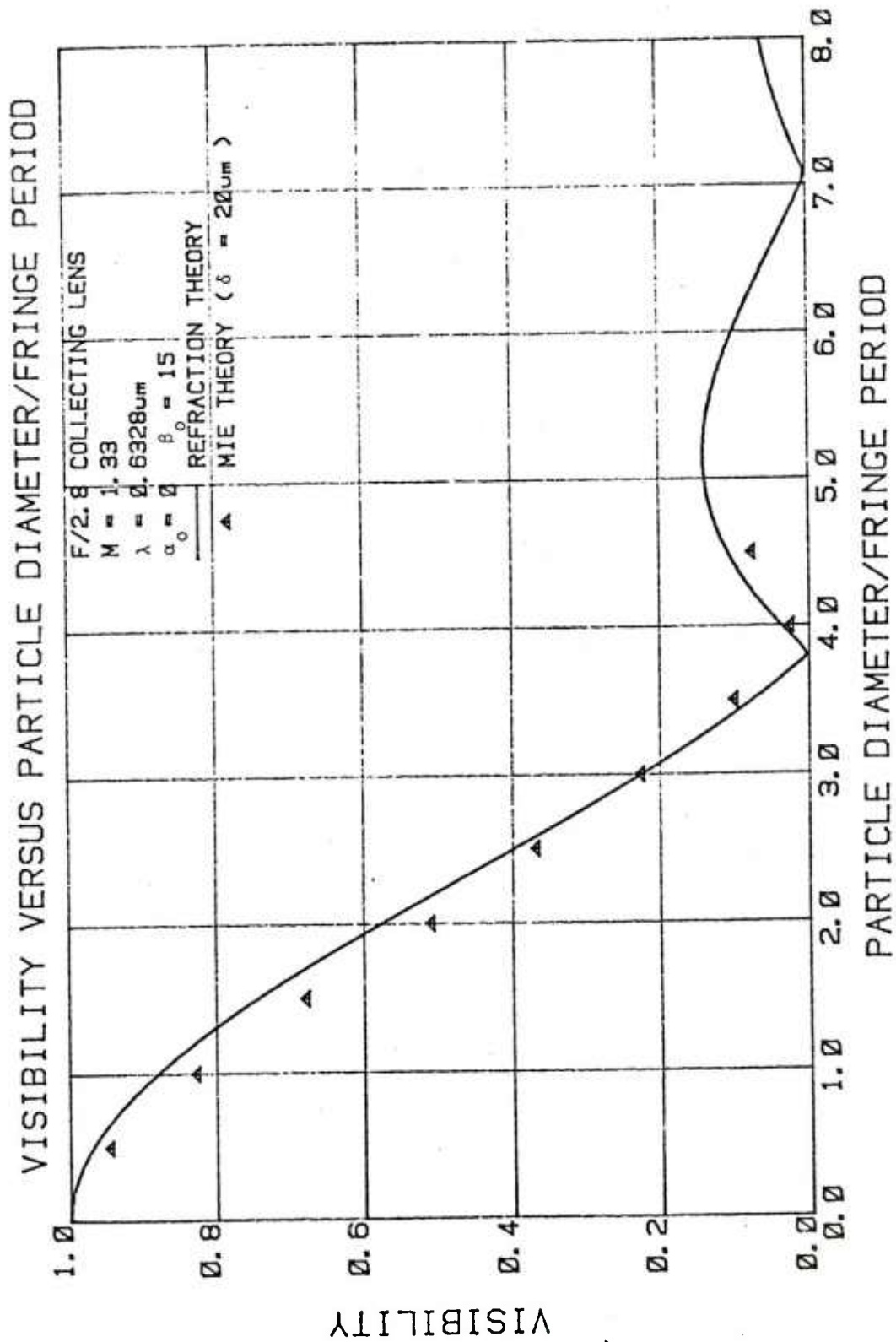


FIGURE 18



# VISIBILITY VERSUS PARTICLE DIAMETER/FRINGE PERIOD

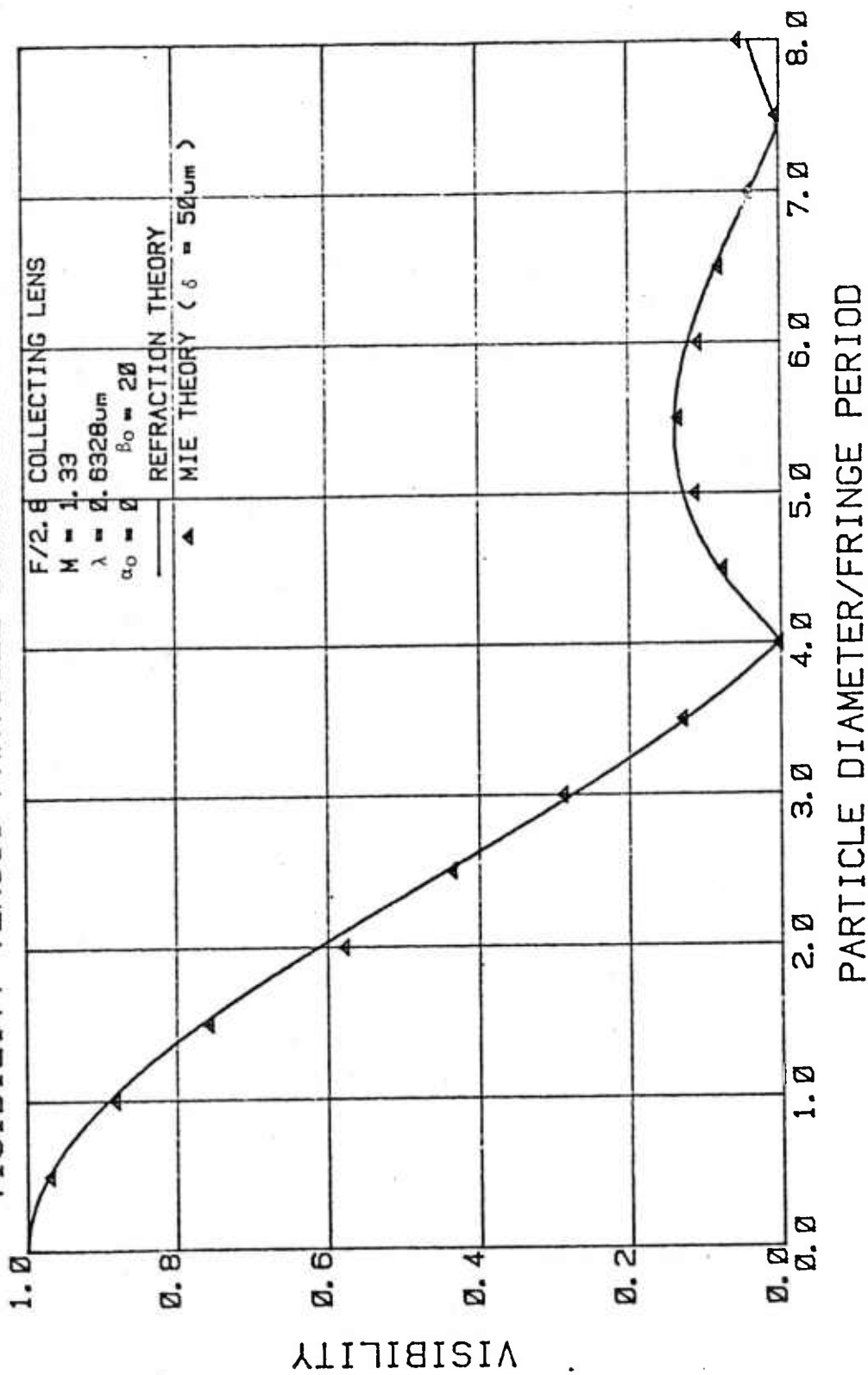


FIGURE 19

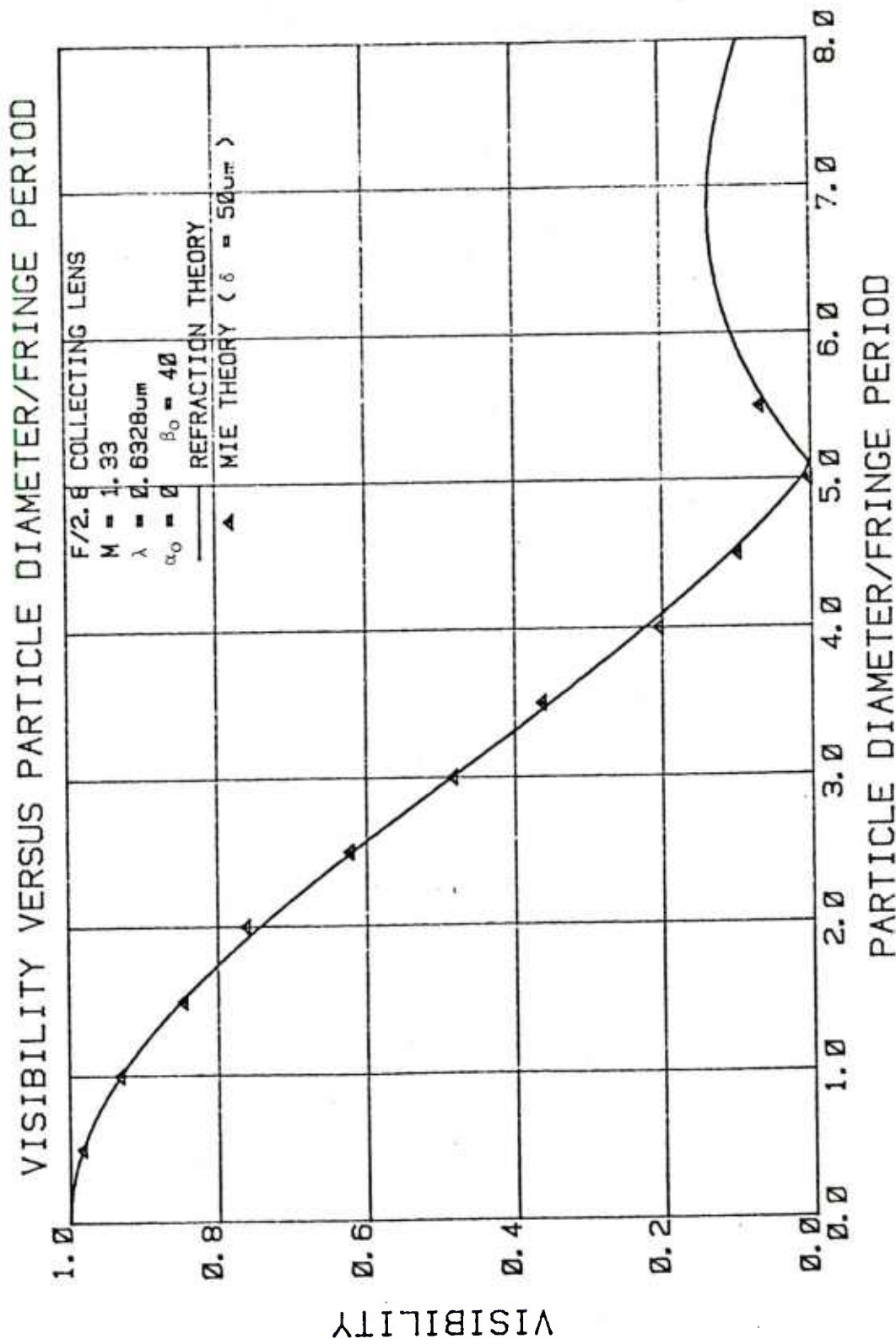


FIGURE 20

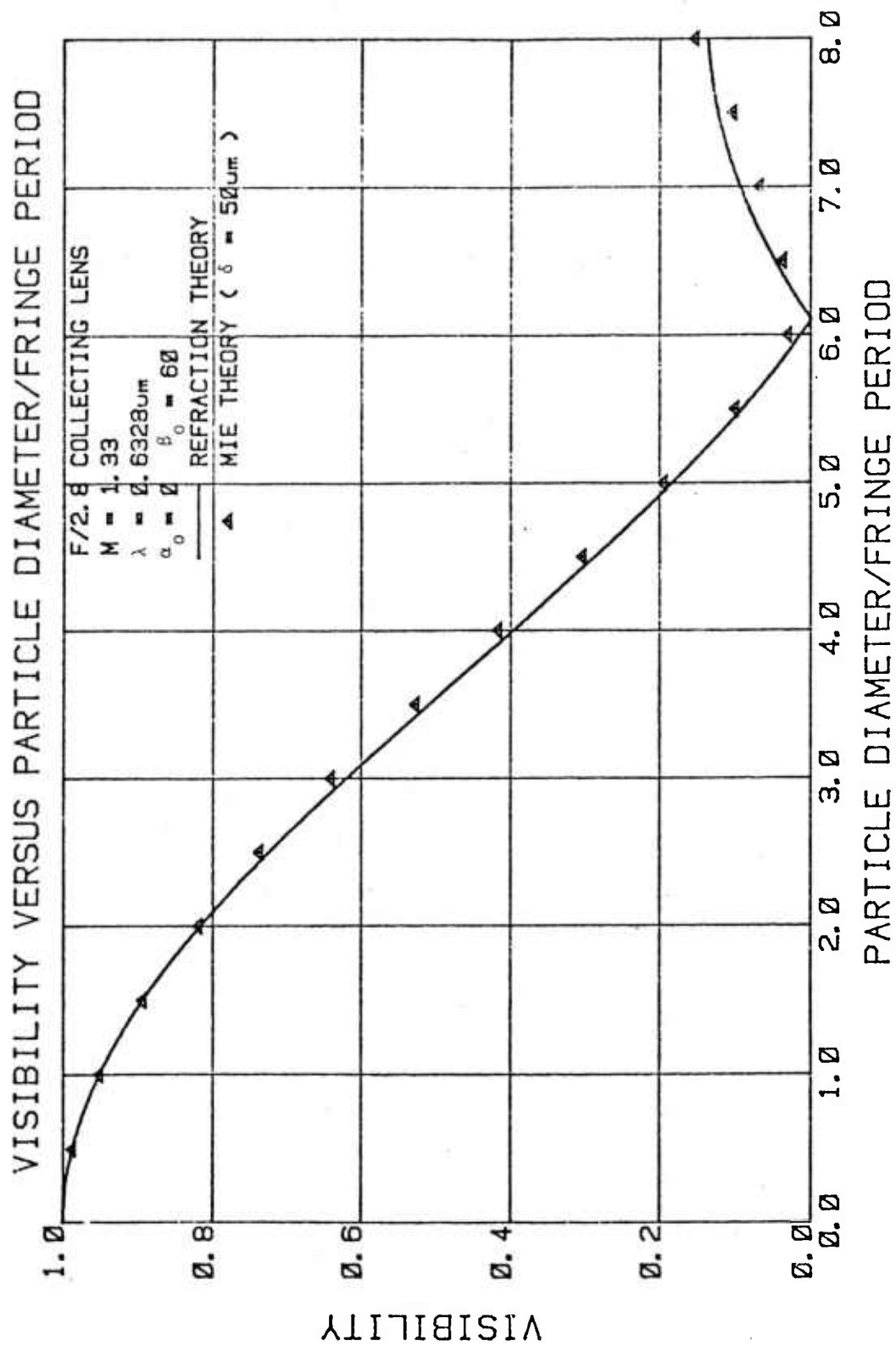


FIGURE 21

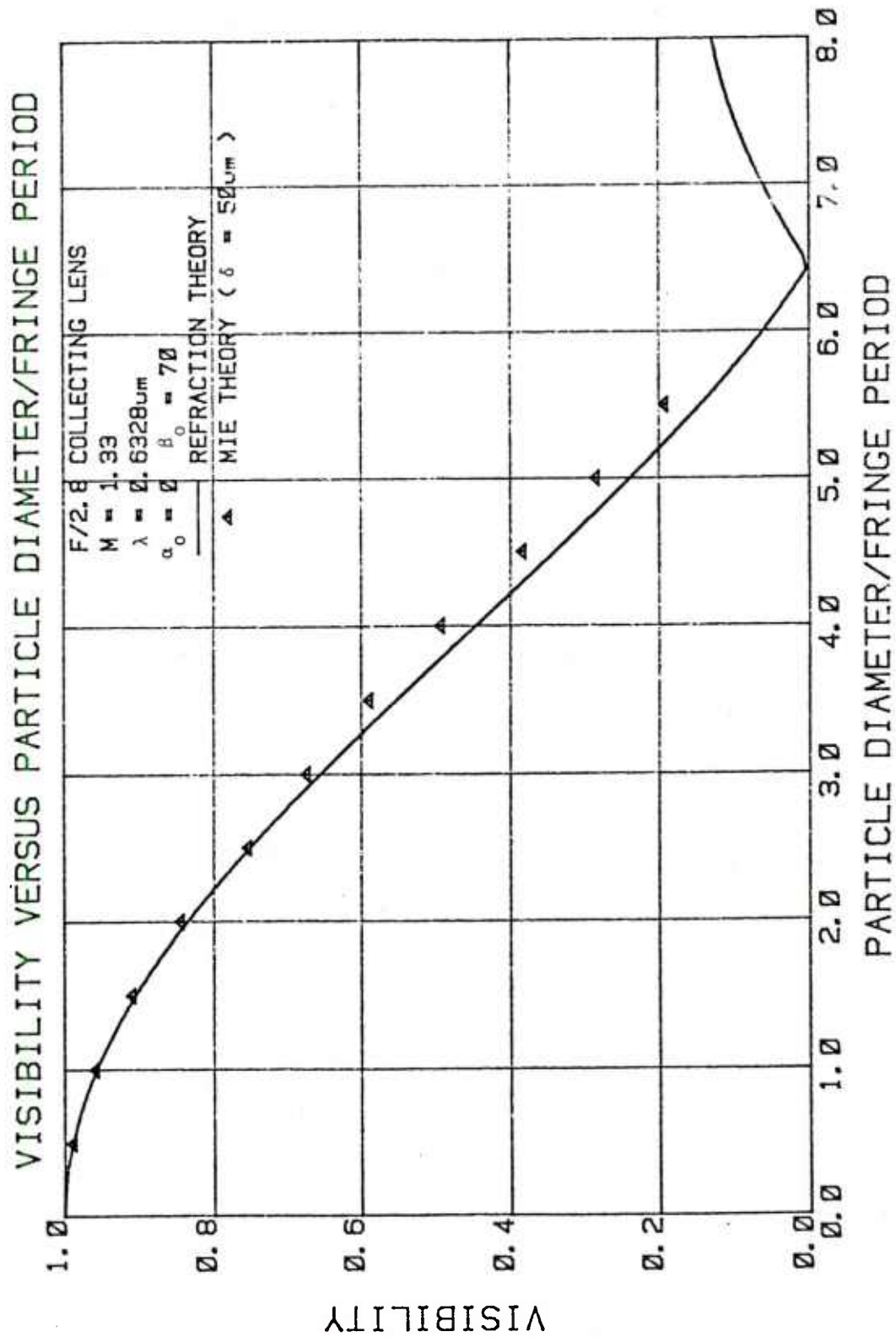


FIGURE 22

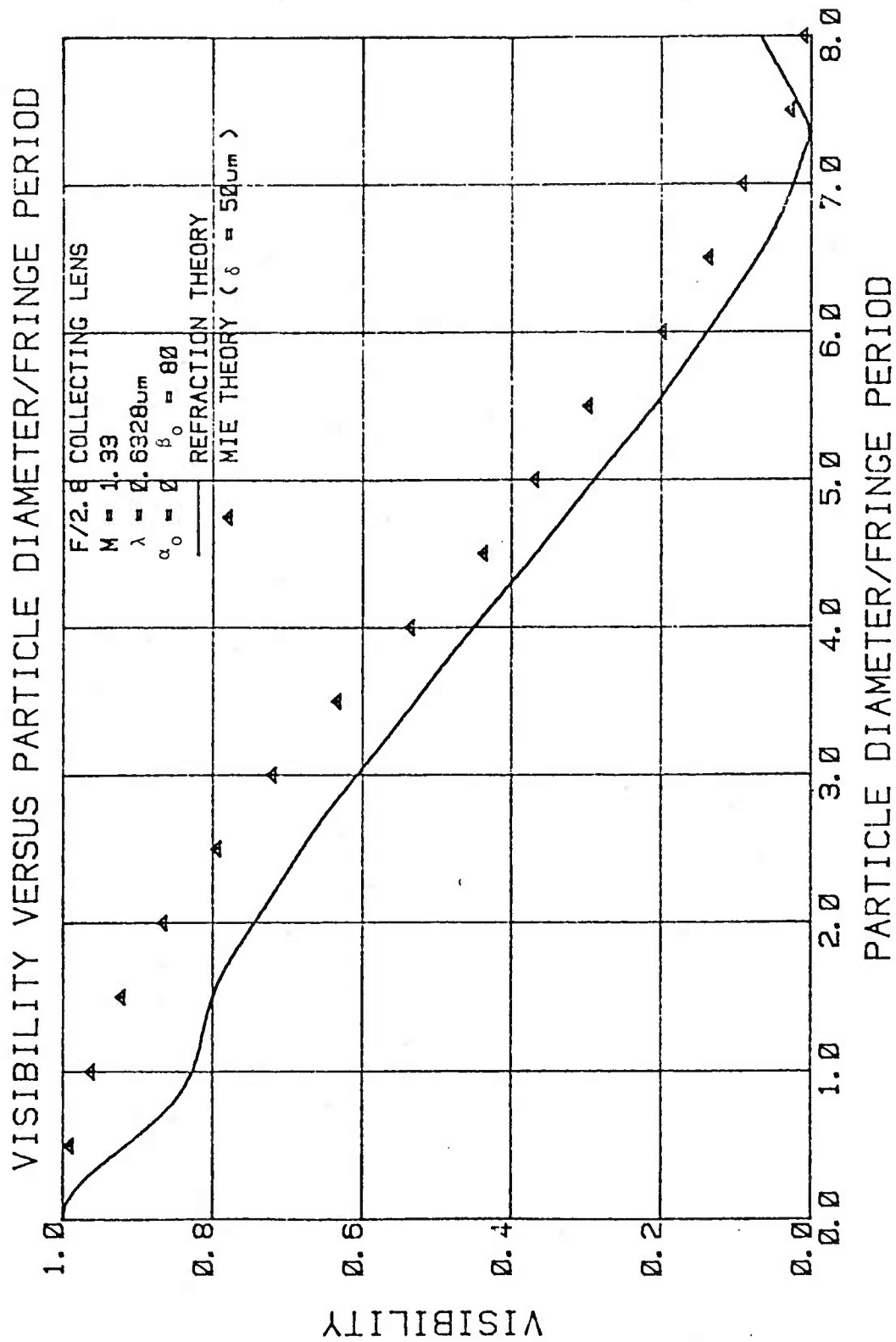


FIGURE 23

# NOMENCLATURE

A	Acceptance ratio
$A_p$	Particle cross sectional area
$a_s$	Cross-sectional area of spray
$b_o$	$e^{-2}$ Gaussian beam intensity radius
$\langle C \rangle$	Time averaged mass concentration
D	Particle diameter
$D_g$	Geometric mean diameter
$D_{gi}$	Geometric mean diameter in ith size distribution mode
$D_{mm}$	Mass mean diameter
$D_s$	Sauter mean diameter
$D_v$	Volumetric mean diameter
f	Fraction of particles in a mode size
$f_i$	Number of measurements in the ith size increment
F	Receiver F number
$G_i$	ith size increment scatter gain
$I_o$	Illuminating beam intensity distribution
$J_1( )$	First order Bessel function of first kind
$l$	Depth of field limit in visibility approximation
L	Transmittance path length
$L_c$	Cylindrical particle length
m	Dimensionless probe volume length in Z direction
$M'$	Particle index of refraction
$\dot{M}$	Mass flow rate
$\dot{N}$	Number of particles per second crossing a plane

# NOMENCLATURE (cont.)

$N_L$	Average number of signal cycles
$N_t$	Total number of measurements in a size distribution
$P(D)$	Probability density distribution
$Q_E$	Extinction efficiency
$r$	Calibration wheel radius
$T$	Transmittance
$v$	Particle velocity
$V$	Signal visibility
$V_o$	Off axis probe volume
$V_R$	Receiver limited probe volume
$V_T$	Transmitter limited probe volume
$V_{\sim z}$	Spray droplet velocity normal to $a_s$
$W_i$	$i$ th size increment weighting factor
$x, y, z$	Probe volume coordinates. $z$ parallel to bisector between the beams, $y$ perpendicular to $z$ and in plane of beams, $x$ perpendicular to $yz$ . Origin at the intersection of beam centerlines
$\Delta x$	width of PSI sample volume in $x$ direction
$\Delta y$	width of PSI sample volume in $y$ direction
$\Delta z$	width of PSI sample volume in $z$ direction
$Z$	Axial distance from spray nozzle outlet
$Z(0)_{\max}$	$Z$ distance corresponding a transmittance value of 0.8 and a monodisperse size distribution
$Z(1)_{\max}$	$Z$ distance corresponding a transmittance value of 0.8 and a single mode log-normal distribution
$Z(2)_{\max}$	$Z$ distance corresponding a transmittance value of 0.8 and a bimodal log-normal distribution

# NOMENCLATURE (cont.)

$\alpha$	Angle between illuminating beams
$\beta$	Receiver orientation for off axis observation
$\delta$	Fringe period
$\delta_e$	Equivalent fringe period
$\rho_o$	Material density (specific gravity)
$\rho_N$	Number density
$\rho_N^{(0)}$	Number density in a monodisperse size distribution
$\rho_N^{(1)}$	Number density in a single mode log-normal size distribution
$\rho_N \Big _{\text{max.}}$	Maximum measurable number density based on an acceptance ratio of 0.1
$\rho_N \Big _{\text{max.tran.}}$	Maximum measurable number density for a transmittance of 0.8.
$\rho_N \Big _{\text{max.tran.}}^{(0)}$	Maximum measurable number density for a transmittance of 0.8 and a monodisperse size distribution.
$\rho_N \Big _{\text{max.tran.}}^{(1)}$	Maximum measurable number density for a transmittance of 0.8 and a single mode log-normal size distribution
$\rho_N \Big _{\text{max.tran.}}^{(2)}$	Maximum measurable number density for a transmittance of 0.8 and a bimodal log-normal size distribution
$\theta$	Droplet spray cone half angle
$\overline{\sigma}$	Mean extinction cross section
$\sigma_g$	Geometric standard deviation
$\sigma_{gi}$	Geometric standard deviation in the ith size distribution mode
$\tau$	Doppler signal time period
$\mu_i$	ith moment in a size distribution
$\nu_{D \text{ min}}$	Minimum Doppler frequency accepted by the data acquisition system.
	Wavelength



# DISTRIBUTION LIST

<u>No. of</u> <u>Copies</u>	<u>Organization</u>	<u>No. of</u> <u>Copies</u>	<u>Organization</u>
12	Administrator Defense Technical Info Center ATTN: DTIC-DDA Cameron Station Alexandria, VA 22314	2	Commander US Army Armament Research and Development Command Benet Weapons Laboratory ATTN: DRDAR-LCB-TL P. Votis Watervliet, NY 12189
1	Director Defense Advanced Research Projects Agency ATTN: H. Fair 1400 Wilson Boulevard Arlington, VA 22209	1	Commander US Army Armament Materiel Readiness Command ATTN: DRSAR-LEP-L, Tech Lib Rock Island, IL 61299
1	HQDA (DAMA, C. Church) Washington, DC 20310	1	Commander US Army Aviation Research and Development Command ATTN: DRDAV-E 4300 Goodfellow Blvd. St. Louis, MO 63120
1	Commander US Army Materiel Development and Readiness Command ATTN: DRCDMD-ST 5001 Eisenhower Avenue Alexandria, VA 22333	1	Director US Army Air Mobility Research and Development Laboratory Ames Research Center Moffett Field, CA 94035
5	Commander US Army Armament Research and Development Command ATTN: DRDAR-TSS (2) DRDAR-SCA, M. Devine D. Adams B. Brodman Dover, NJ 07801	1	Commander US Army Communications Research and Development Command ATTN: DRDCO-PPA-SA Fort Monmouth, NJ 07703
4	Commander US Army Armament Research and Development Command ATTN: DRDAR-LCA, D. Downs A. Beardell DRDAR-LCE, N. Slagg DRDAR-LCS, W. Quine Dover, NJ 07801	1	Commander US Army Electronics Research and Development Command Technical Support Activity ATTN: DELSD-L Fort Monmouth, NJ 07703
1	Commander US Army Armament Research and Development Command ATTN: DRDAR-TDC, D. Gyorog Dover, NJ 07801	1	Commander US Army Harry Diamond Labs ATTN: DELHD-TA-L 2800 Powder Mill Road Adelphi, MD 20783

# DISTRIBUTION LIST

<u>No. of Copies</u>	<u>Organization</u>	<u>No. of Copies</u>	<u>Organization</u>
1	Commander US Army Missile Command ATTN: DRSMI-R Redstone Arsenal, AL 35898	1	Commander Naval Surface Weapons Center Dahlgren, VA 22448
1	Commander US Army Missile Command ATTN: DRSMI-YDL Redstone Arsenal, AL 35898	2	Commander Naval Surface Weapons Center ATTN: O. Dengel K. Thorsted Silver Spring, MD 20910
2	Commander US Army Mobility Equipment Research and Development Cmd ATTN: DRDME-WC DRSME-RZT Fort Belvoir, VA 22060	2	Commander Naval Weapons Center ATTN: C. Mallory S. Wood China Lake, CA 93555
1	Commander US Army Tank Automotive Research and Development Cmd ATTN: DRDTA-UL Warren, MI 48090	2	Commander Naval Ordnance Station ATTN: K. Mueller G. Poudrier Indian Head, MD 20640
1	Army Research Office Durham ATTN: R. Singleton P.O. Box 12211 Research Triangle Park, NC 27709	1	Superintendent Naval Postgraduate School Monterey, CA 93940
1	Director US Army TRADOC Systems Analysis Activity ATTN: ATAA-SL, Tech Lib White Sands Missile Range NM 88002	2	AFATL/ATWG, O. Heiney DLD, D. Davis Eglin, AFB, FL 32542
1	Chief of Naval Operations Department of the Navy ATTN: Code NOP-351G Washington, DC 20350	1	AFOSR/NA (L. Caveny) Bldg. 410 Bolling AFB, DC 20332
1	Commander Naval Sea Systems Command ATTN: J.W. Murrin (SEA-62R2) National Center Building 2, Room 6E08 Washington, DC 20362	2	US Bureau of Mines ATTN: R.A. Watson 4800 Forbes Street Pittsburgh, PA 15213
		1	Director Los Alamos National Laboratory ATTN: T. D. Butler P.O. Box 1663 MS B216 Los Alamos, NM 87545

# DISTRIBUTION LIST

<u>No. of</u> <u>Copies</u>	<u>Organization</u>	<u>No. of</u> <u>Copies</u>	<u>Organization</u>
1	Director Jet Propulsion Laboratory ATTN: Tech Lib 4800 Oak Grove Drive Pasadena, CA 91103	2	General Electric Company Armanent Systems Department ATTN: E. Ashley M. Bulman Burlington, VT 05401
2	Director National Aeronautics and Space Administration ATTN: MS-603, Tech Lib MS-86, Dr. Povinelli Lewis Research Center 2100 Brookpark Road Cleveland, OH 44135	1	Pulsepower Systems, Inc. ATTN: L.C. Elmore 815 American Street San Carlos, CA 93555
1	Director National Aeronautics and Space Administration Manned Spacecraft Center Houston, TX 77058	1	AFELM, The Rand Corporation ATTN: LibraryD 1700 Main Street Santa Monica, CA 90406
1	The BDM Corporation ATTN: Dr. T.P. Goddard P.O. Box 2019 2600 Cearden Road Monterey, CA 93940	1	Science Applications, Inc. ATTN: R. Edelman 23146 Cumorah Crest Woodland Hills, CA 91364
1	Calspan Corporation ATTN: E. Fisher P.O. Box 400 Buffalo, NY 14225	1	Shock Hydrodynamics ATTN: W. Anderson 471016 Vineland Avenue N. Hollywood, CA 91602
1	Food & Machinery Corporation Northern Ordnance Division ATTN: J. Oberg Columbia Heights Post Office Minneapolis, MN 55421	1	TRW Systems Group ATTN: R11032, E. Fishman One Space Park Redondo Beach, CA 90278
3	General Electric Ordnance Dpt ATTN: J. Mandzy R.E. Mayer H. West 100 Plastics Avenue Pittsfield, MA 01203	1	Director Applied Physics Laboratory The Johns Hopkins University Johns Hopkins Road Laurel, MD 20707
		2	Director Chemical Propulsion Information Agency The Johns Hopkins University ATTN: T. Christian Tech Lib Johns Hopkins Road Laurel, MD 20707

# DISTRIBUTION LIST

<u>No. of Copies</u>	<u>Organization</u>
1	Pennsylvania State University Dept. of Mechanical Engineering ATTN: K. Kuo University Park, PA 16802
2	Princeton Combustion Research Laboratories, Inc. ATTN: N.A. Messina M. Summerfield 1041 US Highway One North Princeton, NJ 08540
1	SRI International ATTN: Code L3106, G.A. Branch 333 Ravenswood Avenue Menlo Park, CA 94025
1	The University of Tennessee Space Institute ATTN: J. W. Farmer Tullahoma, TE 37388

## Aberdeen Proving Ground

Dir, USAMSAA  
ATTN: DRXSY-D  
DRXSY-MP, H. Cohen  
Cdr, USATECOM  
ATTN: DRSTE-TO-F  
Dir, USACSL, Bldg. E3516, EA  
ATTN: DRDAR-CLB-PA

### USER EVALUATION OF REPORT

Please take a few minutes to answer the questions below; tear out this sheet, fold as indicated, staple or tape closed, and place in the mail. Your comments will provide us with information for improving future reports.

1. BRL Report Number \_\_\_\_\_
2. Does this report satisfy a need? (Comment on purpose, related project, or other area of interest for which report will be used.)  
\_\_\_\_\_  
\_\_\_\_\_  
\_\_\_\_\_
3. How, specifically, is the report being used? (Information source, design data or procedure, management procedure, source of ideas, etc.) \_\_\_\_\_  
\_\_\_\_\_  
\_\_\_\_\_
4. Has the information in this report led to any quantitative savings as far as man-hours/contract dollars saved, operating costs avoided, efficiencies achieved, etc.? If so, please elaborate.  
\_\_\_\_\_  
\_\_\_\_\_  
\_\_\_\_\_
5. General Comments (Indicate what you think should be changed to make this report and future reports of this type more responsive to your needs, more usable, improve readability, etc.) \_\_\_\_\_  
\_\_\_\_\_  
\_\_\_\_\_  
\_\_\_\_\_
6. If you would like to be contacted by the personnel who prepared this report to raise specific questions or discuss the topic, please fill in the following information.

Name: \_\_\_\_\_

Telephone Number: \_\_\_\_\_

Organization Address: \_\_\_\_\_  
\_\_\_\_\_  
\_\_\_\_\_